MICROFLUIDIC-BASED CONTINUOUS SELF-ASSEMBLY, ALIGNMENT, AND PRINTING OF OLIGOPEPTIDES WITH π-CONJUGATED CORES ACCOMPANIED BY ADVANCED SINGLE MOLECULE CHARACTERIZATION

BY

LAWRENCE RENE VALVERDE

DISSERTATION

Submitted in partial fulfillment of the requirements
for the degree of Doctor of Philosophy in Materials Science and Engineering
in the Graduate College of the
University of Illinois at Urbana-Champaign, 2018

Urbana, Illinois

Doctoral Committee:

Professor Moonsub Shim, Chair
Professor William L. Wilson, Director of Research, Harvard University
Professor Kimani C. Toussaint
Assistant Professor Christopher Evans
Assistant Professor Cecilia Leal

ABSTRACT

Organic semiconducting materials exist in an immense and complex space that, despite decades of extensive exploration, still has unexplored regions with exciting potential. The mysteries of this science lie in the myriad combinations in which organic building blocks can be arranged and how these geometric conditions impact the bulk electronic properties of materials. Furthermore, the ability to physically manipulate reactants via intelligently engineered extensional flows has presented interesting avenues for control in directed assembly of biomimetic materials. Several years ago, we began to apply these new microfluidic techniques to a new class of functionalized peptides. Soon after its inception, I took over that work and have continued efforts to optimize devices and hone the techniques of their use in order to create a platform for high-throughput production of exceptionally aligned oligomer fibers. Early efforts have suggested that the optoelectronic properties of these aligned materials differ significantly and advantageously from their quiescently assembled analogs. Having developed a method for continuous assembly of oligopeptide, I sought collaboration with members of the Mechanical Engineering department to investigate the next step toward using these aligned materials in advanced functional devices, continuous printing and aligned deposition. We have achieved preliminary results with both continuous-line and dot printing with microscopic resolution that demonstrate the potential for optimizing printing techniques once specific device applications for these materials are determined.

In collaboration with peers in both the Materials Science and Engineering and Chemical Engineering departments, I simultaneously turned to characterizing three aspects of these materials with the goal of ultimately comparing quiescently assembled material to its aligned counterparts assembled in flow. One project was geared toward understanding the kinetics of the material's

self-assembly reaction through the use of fluorescence correlation microscopy. I measured fluctuations in fluorescence of a stimulated femtovolume to calculate diffusion constants, and thus particle size as a function of time during reaction. We correlated these findings with molecular dynamics simulations to gain surprising insight into the early timescales of these reactions. In short, it was discovered that the hitherto used method of acid-mediated self-assembly for creating functional peptide fibers operates in a pre-nucleated regime and, in fact, the early stages of assembly begin independent of protonation at concentrations as low as 100 nM, but no lower than 10 nM.

Second, I utilized a recently developed nearfield optical microscopy system to conduct nanoFourier transform infrared spectroscopy at sub-diffraction-limited spatial resolution, probing structural details and optoelectronic properties of several biohybrid materials at the single fibril level. We can identify infrared absorption features corresponding molecular secondary structure, and the calculation of complex indices of refraction and dielectric constants for these materials should be a facile operation with the collected data.

Third, I used conductive probe atomic force microscopy techniques in conjunction with lithographic techniques for single-molecule transistor architectures to characterize charge carrier transport and other optoeletronic properties. Finally, through collaboration with peers conducting tangential research on the same biomimetic materials, I used optical fluorescence microscopy to characterize fluorescence spectra and polarization macroscopically aligned peptide fibers. This body of work on microfluidic device and printer fabrication along with detailed characterizations can help to inform the suitable applications for these materials in semiconductor devices.

To Rikki, a constant support, my companion in every adventure

To my parents, without whom I would never have reached this distinction.

ACKNOWLEDGEMENTS

I would like to thank Dr. J. D. Tovar and Tejaswini Kale for providing the peptide material for this study and Gianni Pezzarossi for use of computational resources. Special thanks are due to Dr. Julio Soares for assistance with confocal microscopy and for advice and commiseration in operating the nanoIR equipment, Dr. Kathy Walsh for similar assistance and commiseration over Conductive Probe Atomic Force Microscopy, and Dr. Mayandi Sivaguru for assistance with *in situ* Fluorescence Lifetime IMaging and polarization microscopy.

We also thank the Frederick Seitz Materials Research Laboratory, the Beckman Institute for Advanced Science and Technology, and the Carl R. Woese Institute for Genomic Biology for facilities and instrumentation. This material is based upon work supported by the U.S. Department of Energy Basic Energy Science Award No. SC-0011847 and the National Science Foundation to Andrew L. Ferguson under Grant No. DMR-1729011.

TABLE OF CONTENTS

CHAPTER 1:

INTRODUCTION

The burgeoning field of organic and supramolecular electronics promises the development of cheaper devices with greater flexibility both in physical structure and in application as compared to traditional solid-state electronics. While tissue engineering, drug delivery, and reparative and regenerative medicine are natural applications of such bio-inspired phenomena, semiconductor and photovoltaic technologies also have much to gain [1,4,5]. Just a few of the myriad possibilities are: synthetic scaffolds for cell adhesion and growth with properties regulated by external stimuli (such as Polypyrrole-based cell scaffolds and artificial muscles) [2], semiconductors with readily tunable electronic and optoelectronic properties [1,4], π-conjugated chromophores to encourage energy migration, and bioactive ligands for eliciting cell adhesion [5]. Thus, the π-electron functionality of micro and nanostructured, self-assembling π-conjugated molecules is of increasing interest for nanotechnology [1–3]. However, the great disorder of organic materials in contrast to their crystalline counterparts lies at the root of most challenges to increased performance.

Naturally occurring polymers such as DNA, RNA, and peptides can deterministically self-assemble into complex hierarchical three-dimensional (3D) structures such as nanowires with specific structure-mediated functionality. Findings such as the formation of β-amyloid plaques due to the assembly of misfolded proteins into fibrils 10-50 nm wide by several microns long have inspired the use of similar biomimetic nanomaterials, such as synthetic polypeptides and peptide-polymer conjugates, as model systems for the design of bio-inspired building blocks with predictable hierarchical structure and functional properties [1,2,4]. Advances in the control of chemical residue profile, chain length, and functional group placement in these biomimetic

materials have facilitated the development of new avenues toward building supramolecular structures and highlight the importance of control over each level of morphological complexity [4,6]. Primary oligopeptide sequences can determine secondary structures such as alpha helices and beta sheets, which in turn result in tertiary or higher order structures with a staggering degree of complexity [7–9]. Furthermore, peptide sequences can be customized and appended to functional synthetic units, such as π-conjugated molecules, thereby creating deliberately engineered foldamers [6,7]. Generally, these functionalized oligopeptides are processed in solution and deposited using a variety of methods including spin coating, electrospinning, electrochemical deposition, vacuum vapor deposition, Langmuir-Blodgett, and reel-to-reel template printing; all with the potential to create functional devices [4,10,11]. In conjunction with collaborators from a variety of materials science subfields, I have investigated a particularly promising family of such biomimetic functional materials and have provided a brief exposition of their properties below. I have furthermore utilized novel designs and applications of microfluidic devices to move beyond the thermodynamic control of typical solution processing methods to a more physical approach of manipulating fibril nanomaterials into ordered superstructures as will be introduced following the materials' description. Finally, this work will discuss the efforts made toward characterizing this material both with respect to changes in functional properties as a result of the order achieved via microfluidic assembly as well as with respect to unprecedented materials insight from single-molecule characterization.

SYMETRIC PEPTIDES WITH π-CONJUGATED CORES

A promising subset of biomimetic systems are peptide/amide-based self-assembling molecules. Collaborator Prof. J.D. Tovar at Johns Hopkins University has conducted significant research on incorporating a variety of electronic structures in the synthesis of such compounds [2,4,5,12–16]. Prior work on fluidic-directed assembly of oligopeptides focused on a system with π-conjugated oligo(p-phenylenevinylene) (OPV) cores symmetrically flanked on either side with peptide sequences DFAA—in order from outermost to innermost: aspartic acid, phenylalanine, alanine, alanine—and DFAG (aspartic acid, phenylalanine, alanine, glycine) [4]. These peptides assemble into supramolecular fibers via beta sheet formation due to pH-triggered electrostatic screening of aspartic acid residues that become protonated below the pK_a of the residue side chain, thereby facilitating hydrogen bonding and van der Waals interactions between peptide monomers. Beta sheet formation can be further influenced by the solvation and π-π interactions of the cores, depending on the chemical identity of the π-conjugated core [2,4,12,14]. In addition to impacting the structural properties of self-assembling oligopeptides, π-π interactions within and among engineered oligomers facilitate electronic communication and serve as pathways for charge transport. Oligomers can be synthesized to include moieties known for their properties as electron donors or acceptors, thus functionalizing the resulting superstructures with p-type or n-type semiconducting properties [17].

The changes in π-π interactions that come with self-assembly affect the molecular energy levels and can manifest as shifted absorption and emission peaks and/or changes in fluorescence intensity. In a framework originally developed by Kasha and coworkers and expanded upon in more recent years by Spano and coworkers, oligopeptide aggregates can be roughly divided into

two species: H-aggregates, which stack laterally, forming ladder-like ribbons (in the simplest configuration each rung is one monomer) (Figure 1.1); and J-aggregates, which interact head to tail [4,18,19]. The former tend to exhibit blue-shifted absorption and quenched emission, while the latter conversely exhibit red-shifted absorption and super-radiance.

In short, these properties are due to the vibrational coupling between constituent subunits and the fact that side to side orientations require phonon-exciton coupling in order to radiatively couple to the ground state due to the S_0-S_1 vibrationless ground state radiative transition being symmetry-forbidden whereas head to tail coupling leads to optically allowed transitions down in energy from the lowest energy excited state [18]. Furthermore, it is well established that J-aggregates exhibit shorter fluorescence lifetimes compared to their unassembled monomer constituents due to a greater degree of exciton or excited state delocalization across several core species [1,20–22]. In practice, most oligomers exist as a superposition of H-like and J-like characteristics.

Despite recent progress, solution-based assembly generally lacks the requisite control to optimally align ordered domains such as π-conjugated units at the molecular scale [4], one step above the order governing individual fiber structure. Without such nano- to mesoscale ordering, organic semiconductor devices cannot fully realize the potential of optoelectronic properties that are encoded at the molecular level. To this end, there is a need for continued development of new methods for the directed assembly of precisely engineered bio-inspired and biomimetic materials. Further developing the initial efforts of Marciel et al., we have primarily used sequence-defined DFAG oligopeptides functionalized with OPV3 and quaterthiphene (4T)—well known for their p-type properties—as well as perylene-diimide (PDI)—an established n-type semiconducting organic compound (Figure 1.2). Additionally, we have investigated properties of some related

nonsequence-defined materials with the hope of finding analogous systems that are even easier and cheaper to create.

MICROFLUIDICS CONTINUOUS MATERIAL SYNTHESIS AND ALIGNMENT

Microfluidic devices could play an increasingly important role in the fabrication of supramolecular organic semiconductor assemblies. In recent work, fluidic-directed assembly using laminar co-flowing streams has introduced a strategy for control over reaction kinetics through unprecedented regulation of reactants [23,24]. However, simple laminar co-flows rely solely on diffusion and thermally driven transport to mix reactants. Although complex microfluidic mixers based on this approach can be powerful tools for promoting rapid reactions between streams or for regulating the overall reaction, these strategies generally rely upon using manifold structures involving multiple streams to regulate diffusive boundaries [24–28]. Interestingly, recent work by Marciel and coworkers demonstrated that extensional flow can be used to achieve orientational alignment and ordering of supramolecular structures during assembly. By employing the dominant extensional flow axis of a 4-channel cross-slot microfluidic device, it was observed that aligned oligopeptide structures can be consistently generated for materials that otherwise form random fiber networks under quiescent assembly [4] (Figure 1.3). In this way, simple cross-slot microdevices can provide access to the degree of nanoscale control necessary for preparing synthetic functionalized peptides such as the OPV3, 4T, and PDI-functionalized sequence-defined DFAG oligopeptides described above.

In prior work, a cross-slot microdevice was used to assemble some of these synthetic oligopeptides composed of OPV cores flanked by symmetric DFAA or DFAG peptide sequences by directing an unassembled peptide oligomer stream and an acidic stream (10-100 mM HCl) to meet in a head-on fashion at the center of a cross-slot junction, thereby generating aligned, assembled material in two orthogonal outflow streams (Figure 1.3b). In the vicinity of the cross-slot, the fluid velocity is described by $v_y = \dot{\varepsilon} y$ and $v_x = -\dot{\varepsilon} x$, where $\dot{\varepsilon}$ is the strain rate and (x,y) are the distances along the inlet/outlet from the stagnation point at the center of the cross-slot. In this way, assembled peptide forms due to diffusive mixing at the interface between the unassembled peptide and acid streams in the cross-slot junction, whereas the extensional component of the flow aligns the products as they assemble [4,29].

Although this approach was effective in assembling and aligning peptides, the original implementation of the method suffered from several drawbacks. In a simple cross-slot microdevice, the oligopeptide assembly front extends from the ceiling to the floor of the outflow channel, which effectively exposes the peptide stream to a wide range of horizontal fluid velocities as a function of position orthogonal to flow (z-direction). In particular, the fluid velocity is exactly zero at the ceiling and floor, which results in undesirable non-specific adsorption of assembled material onto the device's top and bottom inner surfaces. Further, non-specific adsorption is aggravated by the parabolic flow profile in the z-direction. As slower moving unassembled oligomer becomes protonated near the top and bottom surfaces, the assembled material tends to drive additional buildup onto the material at the surfaces due to attractive forces mediated by modest solubility from the aromatic π-conjugated cores. In other words, near the top and bottom surfaces in the outflow channels, the reaction driving peptide assembly outcompetes convection of protonated oligomer, thereby resulting in device clogging (Figure 1.4).

Unwanted material buildup and channel obstruction reduces throughput and leads to uncertainty in the prior processing history of the assembled material exiting the effluent streams. In some cases, disordered aggregates and clumps that become dislodged from the surfaces were observed over the course of several minutes after the initial assembly event. For these reasons, this method precludes the continuous and potentially high-throughput assembly and alignment of peptide material in flow using a simple cross-slot microdevice. From this perspective, there is a clear need to implement new methods for 'flow sheathing' in the vertical direction to prevent surface contact, for example by 3-D confinement of the inlet reactant stream.

Methods for 3-D focusing of fluidic streams are an active area of investigation in the microfluidics community, often in pursuit of improved platforms for flow cytometry [27,30–38]. One approach involves implementing top and bottom focusing streams in an analogous fashion to more common 2-D lateral focusing streams: Flows are introduced to the left and right as well as above and below a sample inlet stream, which results in a focused central core. Despite the apparent simplicity, this method is challenging to implement due to the requirement of complicated 3-D lithographic techniques as well as the coordination of additional fluidic sources or pumps in order to control a large number of fluidic streams. To overcome these challenges, researchers have developed alternative methods of channel patterning to manipulate fluid flow within channels. Recent work by the Ligler group has examined the effect of grooves or chevron patterns in channel walls for low Reynolds number ($Re \lesssim 100$) flow, and these studies have demonstrated that these patterned microfluidic designs can be used to generate controllable sheathed flows without the need for complicated pumping systems (Figure 1.5) [27,30,31,33,35–42]. Diagonal groove patterns (chevrons) were used in the ceilings and floors of microdevice inlet channels to generate

a sheath flow consisting of an inner peptide stream enfolded in an outer sheath stream [30,31,33,35–37].

The sheath stream is introduced at a higher volumetric flow rate than the inner core stream so that sheath fluid is directed across the channel above and below the inner peptide stream, thereby inducing vertical displacement and compression of the inner fluid. Having experimented with various methods for *in situ* microfluidic 3D focusing, I have found the most success using designs based upon the Ligler group work; although, this success has not been without significant challenges.

Establishing a platform that converts the batch process nature of earlier devices to a continuous process is extremely appealing both for academic and industrial applications. The growing field of bioprinting has enjoyed an active exchange with the modern industry of flexible and organic semiconductor devices and the methods are well poised for integration with microfluidic platforms. A wide variety of bioinks and printing methods—including droplet-based and extrusion-based approaches—are currently under development toward the goal of creating *in vitro* biological systems that optimally mimic their natural counterparts [43] and already avail themselves of microfluidic designs. The continuous assembly and flow characteristics of our device permit the high throughput manufacture of aligned material, a necessary prerequisite for conducting thorough material investigation through a large suit of techniques—including many described in this work—and for the ultimate scale up toward commercial manufacture of devices. As an added boon, material that is aligned in our devices can be directly flowed from the outlet to a print nozzle for direct writing on a substrate.

There are many different printing modalities which I will describe in Chapter 3, including high-resolution electrohydrodynamic jet (e-jet) printing, high-speed continuous jet printing, and

the highly precise but relatively simple drop-on-demand method. The specific printing goals as well as ink properties all influence the ultimate choice [44,45]. Surface energy and substrate-ink interactions are also critical [43,45–48]. Ultimately, the choice and tuning of printing method, ink rheology, substrate wettability, and other parameters form a complex, interdependent optimization problem which is accomplished in practice through systematic trial and error [45]. We investigated a proof of concept demonstrating integration of our continuous flow microfluidic devices with an e-jet printing stage and controller for continuous assembly, alignment, and deposition of material under various conditions. Undoubtedly, a more thorough investigation into printing this material should yield the ideal parameters for the desired printing application; however, this optimization is a proof of concept, and this determination enables a more detailed characterization of our materials both in their aligned assembly state and in their quiescent assembly state.

NANOSCALE MATERIALS CHARACTERIZATION

As the ultimate goal in developing the materials describe in this work is their application in advanced organic semiconductor devices, and optoelectronic properties are critical in determining the suitability of a given material toward a specific application, I have embarked upon detailed nanoscopic characterization of the monomer and polypeptide material while developing the aforementioned microfluidics and printing platforms. The following chapters of this dissertation provide detailed descriptions of characterization work primarily concerned with three aspects of these materials: molecular assembly dynamics (Chapter 4), secondary and tertiary structure order (Chapter 5), and secondary and tertiary structure-defined optoelectronic properties (Chapter 6); meanwhile, all materials used in the microfluidic device experiments were at a

minimum characterized with a suite of fluorescence-based techniques to determine spectral and fluorescence lifetime properties, described further in this chapter. The three primary characterization goals also roughly correspond to three advanced, nanoscale probing techniques: fluorescence correlation spectroscopy (FCS), nanoFourier transform infrared (nanoFTIR) spectroscopy and apertureless scanning nearfield optical microscopy (s-SNOM), and conductive probe atomic force microscopy (CP-AFM). Notably, there is some overlap with infrared spectroscopy and the considerations in Chapter 5 providing some optoelectronic properties as well.

Fluorescence correlation spectroscopy plays a critical role in understanding the assembly dynamics in amyloid-forming systems, a valuable step toward understanding how best to control such systems. This is especially true for bio-inspired materials. Knowing what factors can be changed to best harness the potential of natural self-assembly will impact the choice of assembly strategies. In DFAG-π-GAFD (D,F,A, & G corresponding to aspartic acid, phenylalanine, alanine, & glycine)—where π is one of various π-conjugated systems including 4T, OPV3, and PDI—although the fibers resultant from acid-mediated assembly can be seen experimentally, very little is understood about their assembly dynamics. Theoretical models suggest a variety of mechanisms by which these amyloid structures may form, with the classic example being an initial nucleation stage followed by successive elongation stages [49,50]. However, reaction speed upon introduction of acid to this system has made characterization of the initial stages difficult.

Molecular dynamics simulations have been used to analyze the impact of peptide symmetry [16], concentration [51], pH, and fluid flow [52] on peptide assembly. Collaborator simulations using explicit and implicit solvent with the umbrella sampling method enabled probing of the thermodynamics, kinetics, and morphologies of peptide aggregation [49,50]. Computation of potential of mean force (PMF) as a function of center of mass separation between peptide

aggregates revealed a strongly favorable free energy well at ~15 k_BT for the dimerization of DFAG-OPV3-GAFD peptide in a low pH environment as well as evidence for continued aggregation being energetically favorable. In addition, spontaneous formation of self-assembled stacks in free energy simulations and the increasingly favorable changes in free energy upon further aggregation agree well with the suspected amyloid-like nucleation and monomeric addition and elongation into larger 1-D fibers that have been observed experimentally [4,12,14,53].

Yet, the most interesting results in relation to the FCS experiments described in Chapter 4 are the surprising simulations for high-pH conditions which also exhibited favorable dimerization and further elongation, albeit with decreasing favorability for larger aggregates [53]. These simulations suggest a paradigm in which early-stage assembly consists of light aggregates which rapidly assembly and subsequently reorganize into more thermodynamically stable β-sheet-like structures, which in turn grow and elongate as further oligomeric units are added and structurally relaxed in a low-pH environment. The predicted high-pH assembly furthermore implies that when acid-mediated assembly is induced, the peptide precursor solution exists in a pre-nucleated state, significantly impacting how one should view the assembly kinetics in acid-mediated assembly experiments when analyzing through the lens of amyloid formation dynamics. Recent microrheological observations with other collaborators demonstrate peptide assembly only down to concentrations of 0.1 mM with no evidence of assembly below that concentration [54]. However, microrheologically observed critical concentration for deprotonated fiber formation is likely due to limitations of the technique rather than actual physical phenomena. Fluorescence correlation spectroscopy, though, is a single-molecule technique that allows us to directly detect peptide fluorescence to measure molecule size and to distinguish between low order aggregates of different sizes.

Having gained insight into our materials' assembly dynamics, I also sought to better understand the results of that assembly through unique implementations of FTIR spectroscopy and conductive AFM. Complex protein structures with drastically different functions such as those of our materials are not only possible due to the myriad permutations of the amino acids available, but also multiplied by slight changes in the manifold conformations those structures can take. The Amide I infrared absorbance band, related to C=O stretching vibrations coupled with N-H bond in-phase bending and C-N bond stretching is located between 1700 and 1600 cm^{-1} and is of particular interest for our system as these vibrational modes are directly related to backbone conformation and are the least complex, highest intensity of the Amide bands [55–59]. Infrared radiation at the same frequency as one of a protein's vibrational modes can induce a vibrational energy transition if the molecular dipole moment changes when vibrated at resonance, and the strength of this absorption is geometry dependent [57] and is key to gaining detailed chemical bond, morphological, and/or secondary structural information from FTIR spectra [59].

However, bulk FTIR measurements only provide an average of the properties in a relatively large observation volume, but recent investigations have shown the assembly process of this material to yield polydisperse material at the molecular level, and we sought to elucidate the unique structures at play in our materials through a recently advanced implementation of FTIR spectroscopy describe in Chapter 5 that uses scattering, or apertureless, scanning near-field optical microscopy (s-SNOM) to measure IR spectra at 10 to 20 nm spatial resolution [59,60]. This new technique hinges upon the integration of the laser system and optical components with a vibrating sharp metal probe, such as a metalized AFM tip, which acts as an antenna. The electromagnetic field is concentrated at the metallic tip and leads to optical field enhancement on the scale of the tip radius of curvature [61] and IR absorbance can be deduced from differences in the

pseudoheterodyne demodulated scattered signal at different wavenumber or different spatial locations [60].

As our ultimate intention in developing self-assembling functionalized oligopeptides is to create semiconductor devices, we sought to thoroughly characterize their optoelectronic properties in a more device-like manner. Previous experiments on similar peptides assembled in flow were the first indications that shear-flow could induce optical properties such as uniform polarization and electrical properties such as increased conductance in these systems [5]. However, these early experiments were conducted by hand and difficult to repeat consistently. The increased intermolecular π-stacking and aligned microdomains lead us to expect enhanced electronic properties [62,63], and consistent assembly via microfluidics should lead to consistently reproducible optoelectronic properties. Thin film field-effect transistor (FET) architectures are ideal for characterizing hole transport and voltage equilibrium for organic semiconductors, but collaborators have only made bulk measurements on randomly oriented fibers [17].

Chapter 6 explains how with CP-AFM operation, though, it is possible to create an FET architecture with only one fiber as the active layer. We deposited pads of conducting material onto an insulating SiO_2 substrate which itself was grown on a conductive, highly n-doped Si wafer. The peptides were deposited such that when fibers formed, some draped over the edges of these conductive pads. Meanwhile, the AFM was outfitted with a specialized tip holder that allowed us to ground the tip and provide a bias to the conductive pad. With a voltage supply connected to the same ground as the tip, we could apply a gate bias at the n-doped Si and effectively create a mobile transistor with the tip acting as the mobile drain. We also conducted additional experiments to measure transverse and longitudinal electrical properties of the peptides without an applied gate bias. It is important to keep in mind that the complex morphology of the tip-sample interaction,

where the tip apex acts effectively like a sphere 10-20 nm in diameter, leading to tip contact areas with the sample on the order 100 nm^2 [64,65], and assumptions must be made with regards the electric field at the tip [66]. With these geometrical considerations, we could take current-voltage curves measured along the fibers at different applied gate biases to extrapolate the charge carrier mobilities.

Finally, Chapter 7 of this dissertation addresses some fluorescence polarization measurements made on peptide fibers macroscopically aligned through a very different flow device: capillary drawing of the material through micro channels of cracked polystyrene films and subsequent evaporative assembly of the material. This alternative method also warrants further investigation and would benefit from detailed investigation through nanoFTIR and s-SNOM-based spectroscopy as well as CP-AFM. This last project also further illustrates what is discussed toward the end of chapter 2 with regards alternative microfluidic devices designs: there is an incredible diversity not only in permutations of peptide sequences and functional cores, but also in the way these materials can be manipulated as they self-assemble. This dissertation deeply explores some viable options, and there are many paths toward final device integration and application. It is my hope that the work presented here has entailed progress down some of those paths and that future work will see their ultimate realization.

FIGURES

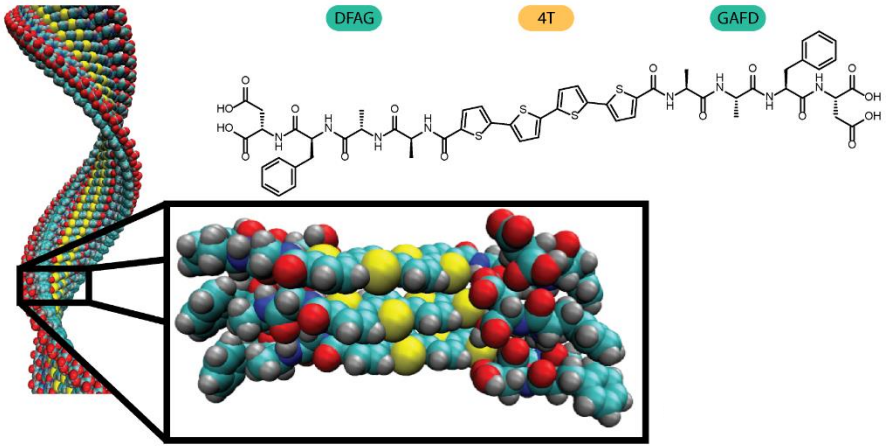

Figure 1.1 Example H-aggregate structure. The 3D structure represents an idealized H-stacked β sheet fibril which naturally adopts a chiral structure. The corresponding chemical structure diagram above shows the amino acid sequence: aspartic acid (D), phenylalanine (F), alanine (A), glycine (G), followed by quaterthiophene and then the same amino acid sequence in reverse order.

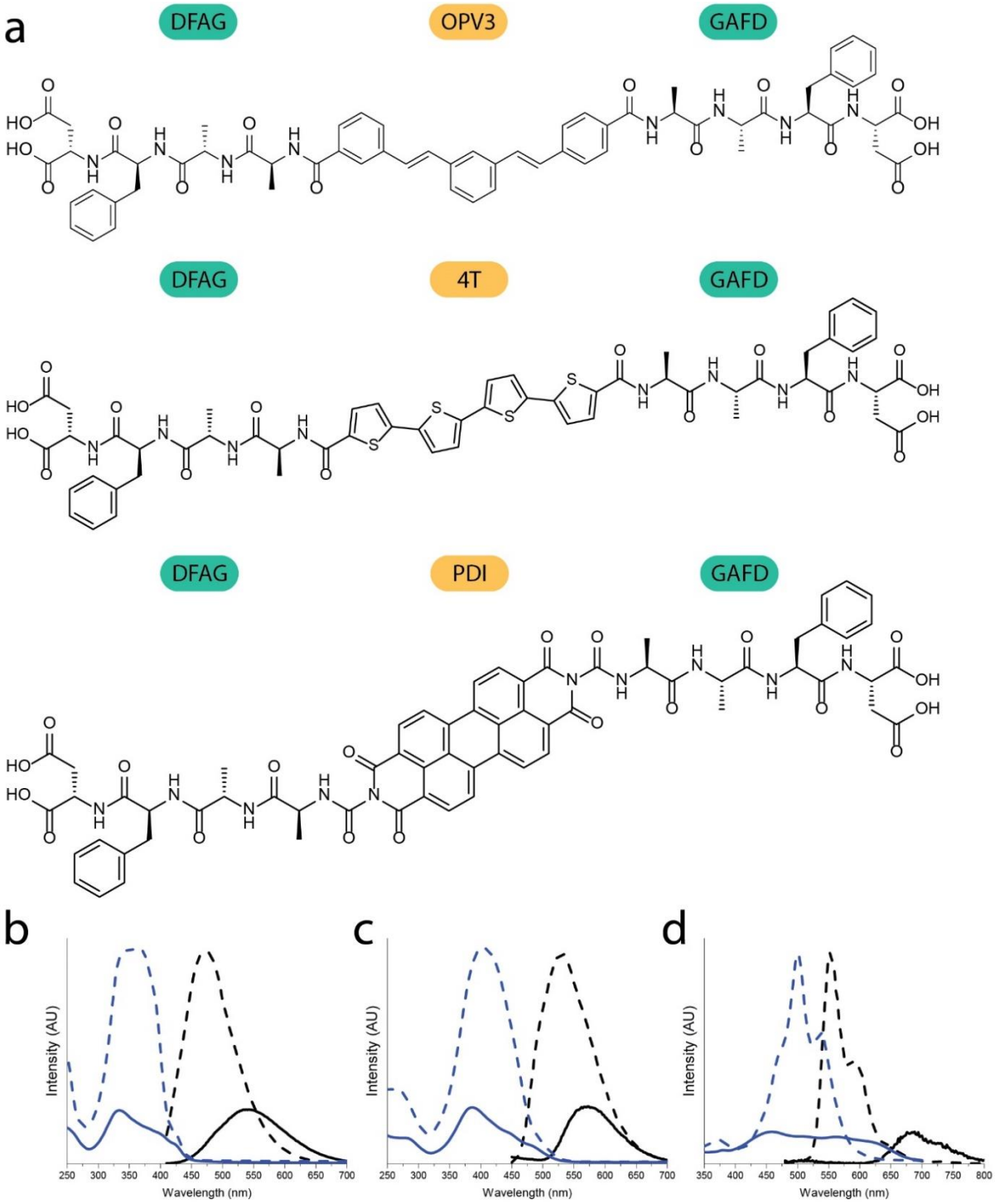

Figure 1.2 Photophysical properties of synthetic oligopeptides. (a) Structures and (b)-(d) bulk spectral properties of synthetic oligopeptides with different π-conjugated cores flanked by symmetric DFAG residues. Absorption and fluorescence emission spectra are shown for: (b) DFAG-OPV3, (c) DFAG-4T, and (d) DFAG-PDI. Absorption spectra (blue dashed lines) and fluorescence emission spectra (black dashed lines) are shown for oligopeptides under basic solution conditions prior to assembly. Under acidic conditions (pH < 3), these synthetic oligopeptides assemble into fiber-like networks that exhibit blue-shifted absorption peaks (solid blue lines) and red-shifted emission (solid black lines).

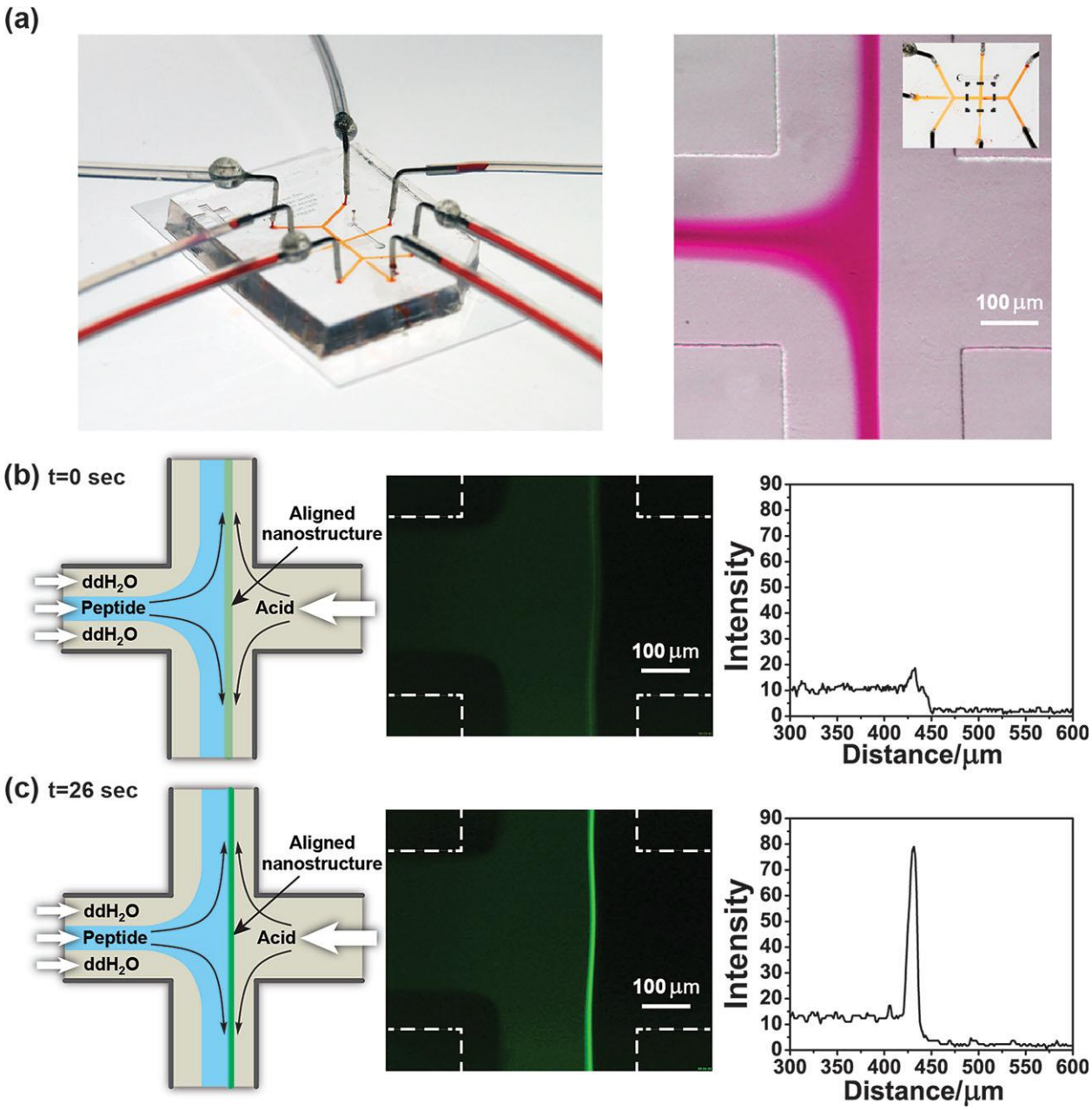

Figure 1.3 Example microfluidic device for oligopeptide alignment. (a) Photograph of device and optical micrograph of experimental setup. (b) Initial aligned nanostructure is formed at convergence of monomer and acid streams. (c) Increased structure formation at assembly axis. (from Marciel et al. 2013 [4])

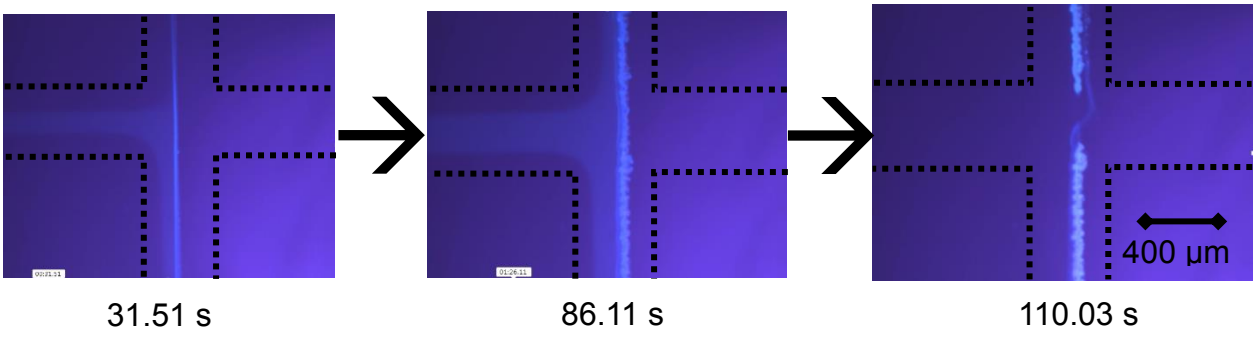

Figure 1.4 Typical peptide buildup in standard planar microfluidic devices. Fluorescence intensity images of one device over time indicate aggregation. Dotted lines are to clarify the device internal boundaries.

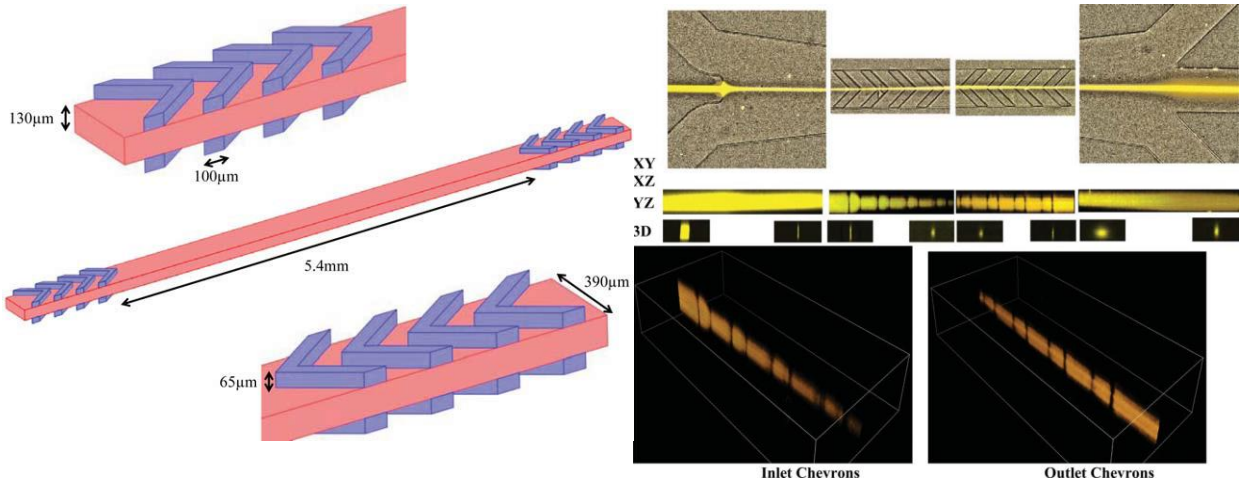

Figure 1.5 Example of 3D-focusing microfluidic using chevron-based design (from Hashemi et al. 2013 [33]). In this instance, Hashemi et al. utilize a microchannel with very similar geometry to the half of our device where peptide is introduced and focused. This result demonstrates not only that flow focusing is achieved, but that the laminar nature of the flow entails reversibility, and the focused stream can be defocused to its approximate initial shape by flowing the opposite direction through another set of identical chevrons.

CHAPTER 2:

CONTINUOUS ASSEMBLY USING 3D FOCUSING MICROFLUIDICS

Microfluidics are poised to play a key role in the directed assembly of advanced materials with ordered nano- and mesoscale features. Despite recent progress in the self-assembly of materials, there is a strong need for development of continuous processes for ordered assembly of materials that extend beyond discrete or batch methods. In this work, we describe a continuous microfluidic process for the assembly and alignment of synthetic oligopeptides with π-conjugated cores using three-dimensional (3D) flow focusing of inlet reactant streams. To achieve continuous assembly, poly(dimethylsiloxane) (PDMS)-based microdevices are fabricated with integrated chevron patterns in the ceiling and floor to generate a 3D focused sheath flow of the reactant peptide. Following 3D focusing, the peptide stream is directed toward an acidic triggering stream in a cross-slot geometry which mediates assembly into higher-order fiber-like structures. Using this approach, the focused peptide stream is assembled using a planar extensional flow, which ensures high degrees of microstructural alignment within the assembled material. We demonstrate the utility of this approach using three different synthetic oligopeptides, and in all cases, we observe efficient and continuous assembly of peptide without unwanted buildup of assembled material. *In situ* confocal fluorescence microscopy and *in situ* fluorescence lifetime imaging microscopy (FLIM) are used to characterize the integrity of peptides during the assembly process. In addition, finite element simulations are used to guide device design and to validate 3D focusing. Overall, this approach presents an efficient and effective method for the continuous assembly and alignment of ordered materials using microfluidics.

INTRODUCTION

Naturally occurring polymers such as DNA, RNA, and peptides can deterministically self-assemble into complex hierarchical three-dimensional (3D) structures that give rise to specific functions. In recent years, bio-inspired materials have been developed with the aim of harnessing natural self-assembly for precisely engineered functionality [1,2,4]. Development of new biomimetic materials has benefitted from advances in both synthetic organic chemistry and the improved synthesis of biological materials [1,2,4,5,12,14,15,67]. Recent advances in synthetic control over chemical residue profile, polymer molecular weight, and functional group placement have facilitated new assembly techniques that highlight the importance of controlling supramolecular structure [6]. Moreover, synthetic polymers can be created with a chemically diverse palette of non-natural monomers with a broad range of functionality. On the other hand, biological materials such as peptides and proteins allow for precise placement of monomers along a polymer backbone, albeit in the context of a small number of naturally occurring monomers. Primary amino acid sequences in peptides can determine secondary structures such as α-helices and β-sheets, which in turn result in higher order structures with a staggering degree of complexity [7,9,68].

A major challenge in the field is the development of systematic methods for controlling the nano- to mesoscale ordering of functional materials. To control structural ordering, bio-hybrid materials such as functionalized oligopeptides are typically processed in batch solutions and deposited onto surfaces to generate functional devices using a variety of methods including spin coating [4,10,20], electrospinning [4,30,31,69–71], and roll-to-roll template printing [10]. Despite recent progress, however, it can be challenging to use these methods to optimally align ordered

domains such as π-conjugated units at the molecular scale. Without such nano- to mesoscale ordering, organic semiconductor devices cannot be engineered to realize the full range of optoelectronic properties that are encoded at the molecular level. To this end, there is a need for continued development of new methods for the self-assembly and directed assembly of engineered materials for applications such as organic semiconductors.

Microfluidic devices have played an increasingly important role in the fabrication of supramolecular assemblies. In recent work, fluidic-directed assembly of materials using laminar co-flowing streams has introduced new routes for controlling reaction kinetics through unprecedented regulation of reactants [23,25]. However, simple laminar co-flows rely solely on diffusion to mix reactants. Although complex microfluidic mixers based on this approach can be used to promote rapid reactions, these strategies generally use manifold structures to regulate diffusive boundaries without providing orientational control of morphology [24–28]. Interestingly, recent work by Marciel and coworkers demonstrated that extensional flow can be used to achieve orientational alignment and ordering of supramolecular structures during assembly. By employing the dominant extensional flow axis of a 4-channel cross-slot microfluidic device, aligned oligopeptide structures were consistently generated for materials that otherwise form random fiber networks under quiescent assembly [4]. In this way, simple cross-slot microdevices can provide access to nanoscale control over sub-structure alignment.

Although the 4-channel cross-slot device was effective in assembling and aligning peptides, the original implementation of the method suffered from several drawbacks. In a simple cross-slot microdevice, the oligopeptide assembly front extends from the ceiling to the floor of the outflow channel, which effectively exposes the peptide stream to a wide range of fluid velocities in the direction orthogonal to flow (*z*-direction). Moreover, undesirable non-specific adsorption of

assembled material occurs on the device inner surfaces, which is aggravated by the parabolic flow profile in the *z*-direction. As slower moving monomer becomes protonated near the top and bottom surfaces, the assembled material tends to drive additional buildup onto the material at the surfaces due to attractive forces mediated by modest solubility due to aromatic π-conjugated cores. Unwanted material buildup and channel obstruction reduces throughput and leads to uncertainty in the prior processing history of the assembled material. For these reasons, the simple cross-slot method precludes the continuous, high-throughput assembly of peptides in flow. From this perspective, there is a need to implement new methods for 'flow sheathing' to prevent surface contact and to enable to continuous assembly of synthetic peptides in flow.

Microfluidic methods for 3D flow focusing are an active area of research, often in pursuit of improved platforms for flow cytometry [27,30–38]. One approach involves implementing top and bottom focusing streams in an analogous fashion to more common 2D lateral focusing streams, though this method can be challenging to implement due to the requirement of complicated 3D lithographic techniques as well as the need for additional fluidic sources or pumps. Recent work by the Ligler group has uncovered alternative methods for 3D focusing using patterned channel walls (grooves or chevron patterns) to generate sheath flows under low Reynolds number ($Re \lesssim 100$) conditions. These studies have demonstrated that patterned microfluidic designs can be used to generate controllable sheathed flows without the need for complicated pumping systems [27,30,31,33,35,36].

In this work, we implement 3D flow focusing of peptide streams using patterned microfluidic channels to achieve the continuous assembly of oligopeptides. In particular, we incorporate chevron structures into the ceiling and floor of the inlet channels in cross-slot microdevices such that the reactant peptide stream is focused *before* reaching the assembly zone

at the cross-slot region. For these devices, microfluidic channel designs are validated using computational fluid dynamics and chemical transport simulations in COMSOL [33,72]. Flow focusing and real-time assembly were characterized *in situ* using confocal fluorescence microscopy, polarized fluorescence microscopy, and *in situ* and *ex situ* fluorescence lifetime imaging (FLIM). In all cases, we observe the unobstructed continuous assembly and alignment of synthetic oligopeptides over long times. Taken together, our results show that the integrated chevron/cross-slot microdevices offer the potential for new microreactor designs with enhanced control over fluid flow to generate assembled materials in a high throughput, continuous flow format.

METHODS

Computational modeling

We performed a series of simulations of the flow process using computational fluid dynamics to assess the effect of chevron features on flow focusing in microfluidic channels. Moreover, simulations further served to inform the requisite number and spacing of chevrons for efficient 3D flow focusing. In particular, we used finite element analysis in COMSOL Multiphysics to analyze flow fields generated by grooved channel features. The computational algorithm considers the Navier-Stokes equations for incompressible flow in the laminar flow regime, for which non-linear inertial terms can be neglected:

$$-\frac{\partial p}{\partial x_i}+\mu\frac{\partial^2 u_i}{\partial x_j \partial x_j}=0$$

$$\frac{\partial u_i}{\partial x_i}=0 \tag{2.1}$$

where p is pressure, u_i is fluid velocity, and μ is the dynamic viscosity. Eqs. (2.1) are given in indicial notation such that subscripts refer to vector components. For the dilute aqueous streams, we used standard properties for water at ambient temperature with a no-slip boundary condition at the walls, a laminar inflow boundary condition at the inlets, and an open interface boundary condition at the outlets. The Transport of Dilute Species module of COMSOL was used to model diffusion via Fick's law:

$$\frac{\partial}{\partial x_j}\left[D\frac{\partial c}{\partial x_j}-cu_j\right]=0 \tag{2.2}$$

where D is the diffusion coefficient and c is the concentration of the focused species (small molecule dye or unassembled peptide oligomer). We assume a constant diffusion coefficient D and use a normalized concentration c such that $c=\tilde{c}/\tilde{c}_0$, where $\tilde{c}$ is the dimensional concentration and $\tilde{c}_0$ is the dimensional inlet concentration. It is assumed that the peptide monomer is sufficiently dilute such that the presence of dissolved peptide in the flowing streams does not influence fluid flow. In this way, we first solved the Navier-Stokes equations and then used the flow solution as the velocity field for solving the associated convection-diffusion problem.

Ligler and coworkers [35] previously investigated the impact of grooved chevron features in generating sheath flows in microfluidic channels. In particular, prior work provides a comprehensive analysis of the effects of both the number and spacing of chevrons on 3D flow focusing. In general, the number of chevrons controls the vertical compression (z-direction

focusing), whereas the sheath-to-core flow ratio controls the lateral focusing, with various permutations affecting the shape of the focused stream. Higher flow ratios of sheath-to-core change the cross-sectional shape of the core stream from bowtie-like to oblong to nearly circular focusing. In the present work, we were primary interested in generating a simple sheath flow in order to exclude the focused peptide stream from the top and bottom surfaces, hence the details of the shape of the focused stream were not critical for our purposes. For these reasons, we generally employed sets of four chevrons in our devices using a specific pattern that was found to be efficient for flow focusing in prior work (chevrons with a 90° angle, symmetrically centered along the top and bottom of the inlet stream, in the range of sheath-to-core flow ratios from 10:1 to 100:1, with similar dimensions to those used in this study). We found these microdevice geometries and operating parameters maintained sample stream symmetry at the cross-slot and generated coaxial flows fairly insensitive to the sheath-to-core flow rate ratio, in agreement with Ligler et al [30,35].

Microdevice fabrication

Microfluidic cross-slot devices with chevron patterns were fabricated using standard soft lithography techniques [73,74]. Microdevices consist of hybrid glass/poly(dimethylsiloxane) (PDMS) assemblies suitable for fluorescence microscopy. Chevrons were designed with a 90° angle and were symmetrically centered along the top and bottom of the inlet oligopeptide stream. Chevron dimensions were 50 μm high by 50 μm wide with a 200 μm pitch, and channel dimensions were 100 μm in height by 400 μm in width (Figure 2.1). Overall, the integrated PDMS device consists of three layers (top chevrons, center channels, bottom chevrons), which requires careful alignment of these features (Figure 2.2). Two different masters were created on silicon wafers using SU-8 photoresist (MicroChem) and exposed to UV light with a custom photomask (MRL photomask services). One master (Figure 2.2a) was created by first spin-coating a 100 μm thick

layer of SU-8 and exposing and developing the pattern for the main (center) channel features. Next, a 150 μm thick layer of SU-8 was deposited, and the chevron photomask was aligned with the monomer inlet channels using a stereomicroscope. The pattern was then exposed and developed to reveal a two-layer master containing the aligned channel and top-chevron features. The use of an FeO on soda lime photomask was instrumental in this alignment step (as opposed to the laser-printed plastic transparency sheets typically used by coworkers) because, while the FeO mask material is opaque at the UV wavelengths used for photoresist exposure, it is transparent in the visible range, facilitating the process of aligning the chevron masks above the already-developed channel pattern. Furthermore, adequate illumination while aligning the mask is critical because the channel pattern and the undeveloped photoresist with which it is coated are both the same, essentially clear, color. One must rely upon diffraction at the edges of the patterned channels to distinguish where they lie and to align the chevron mask such that the chevrons are positioned exactly centered on the unassembled peptide lead-in channel. While difficult, conducting this initial alignment at the master level was an optimal choice because it eliminated a major source of error from the PDMS fabrication process: Tens to hundreds of PDMS devices could be made from one set of photoresist-on-Si masters. Although there are advanced techniques available for PDMS layer alignment in multilayer devices [75], if all alignment occurred at the PDMS stage of device fabrication, that would mean tens to hundreds of opportunities to incorrectly align each layer. Creating a two-layer master eliminated the need to align those two layers each time PDMS was poured. The reason all three layers of the end device could not be implemented into a single master is due to the undercut nature of this design and the extreme difficulty and instability associated with suspending the 400 x 100 μm channels above the Si wafer in all places except where the four bottom chevrons would contact the surface.

A second master was created using standard techniques (Figure 2.2b) and contained a single layer of 100 μm tall chevrons, which would serve to create the bottom layer chevrons in the inlet channel. Both masters were then treated with chlorotrimethylsilane (Sigma-Aldrich) vapor to prevent PDMS adhesion. Approximately 30 g of PDMS mixed in a ratio of 10:1 base:crosslinker was poured into a standard petri dish containing the two-layer master. Separately, a 50 μm thick layer of the same PDMS solution was spin coated onto the second master, thereby resulting in the master's SU-8 chevron features protruding 50 μm above the PDMS layer. The excess 50 μm height of the one-layer chevron master served to ensure that the spin-coated PDMS did not seal off the chevron features and served to aid in the lateral alignment of layers by protruding slightly into the channel of the two-layer mold (Figure 2.2c). After baking both molds for ~20 min at 60 °C the two-layer portion was removed from the master, inlet and outlet holes were punched through the layers, and a stereomicroscope was used to align the channels and top chevrons of the two-layer PDMS mold with the chevron features of the 50 μm spin coated mold. After an overnight cure, the PDMS was removed from the master and bonded to glass coverslips by treatment in oxygen plasma.

Materials Synthesis

Sequence-defined synthetic peptides with π-conjugated cores were synthesized using solid phase peptide synthesis (SPPS), as previously reported [2]. The π-conjugated oligopeptides containing an oligo(p-phenylene vinylene) (OPV3), quaterthiophene (4T), or perylene-diimide (PDI) core were flanked by symmetric peptides with a primary amino acid sequence Asp-Phe-Ala-Gly (DFAG). The overall sequence of the π-conjugated oligopeptides were the same except for the functional core and can be written as, for example, HO-DFAG-OPV-GAFD-OH, abbreviated as DFAG-OPV.

Fluidic-directed assembly of synthetic oligopeptides

Flow-focused streams of unassembled oligopeptide at a concentration of 0.1 mM in deionized water (18.2 MΩ·cm) were introduced into cross-slot devices and directed against an opposing aqueous acidic stream of 10 mM HCl, such that these two streams meet at the cross-slot junction (Figure 2.1). The unassembled peptide stream (volumetric flow rate 10 μL/min) was first focused laterally using two flanking streams of deionized water (500 μL/min). The 2D focused peptide stream was then directed into the inlet channel containing chevron features in the ceiling and floor, thereby resulting in a 3D flow-focused coaxial flow. An aqueous acidic stream was introduced into the opposing inlet, flowing to the cross-slot junction at a volumetric flow rate of 500 μL/min and later slowed to 250 μL/min in order to shift the position of the oligomer assembly front (Figure 2.3). In order to facilitate assembly, we initiated flow conditions in the following order: focusing stream, unassembled peptide stream, aqueous acid stream, followed by terminating the process using the reverse procedure. This order of operations significantly reduces introduction of air bubbles in the cross-slot or chevrons and/or backflow of the acid stream into the monomer solution that could result in unwanted spontaneous assembly. Three Harvard Apparatus PHD ULTRA syringe pumps were used to generate fluid flow. Forked tubing was used to connect the two cross-slot outlets to a single outlet from which the effluent stream was collected.

Fluorescence and confocal microscopy

Microdevices were mounted on a Zeiss LSM 700 inverted microscope and imaged through a 5x EC Plan-Neofluar objective (NA = 0.16) onto a linear CCD array (512 x 512 pixels). The peptides investigated in this work exhibit a blue-shifted absorption and quenched red-shifted emission upon assembly. For this reason, images were acquired by splitting fluorescence emission into two channels using appropriate dichroic mirrors, band-pass filters, and long-pass filters to

distinguish assembled oligomer from unassembled peptide (Table 2.1). Confocal images were acquired through a slit approximately 1 Airy unit wide (~10 μm) with a galvo *y*-scan and raster laser line oriented in the *x*-direction and scanned in the *z*-direction using a fast-scanning piezo-collar objective.

Table 2.1 Optical setups for fluorescence microscopy and imaging.[a]

Functional Core	Beamsplitter [nm]	Channel 1 [nm]	Channel 2 [nm]	Excitation Wavelength [nm]
OPV3	490	BP 495-520 + BP 550-615	BP 415-480	405
4T	565	LP 495	BP 495-555	405 + 488
PDI	635	LP 495	BP 505-610	488

[a]*Dichroic mirror beam splitters and filter sets were chosen to achieve two-color fluorescence imaging by separating fluorescence emission from unassembled and assembled peptide into two channels. The absorption profile for 4T straddles both excitation wavelengths, so both excitation lasers were used to augment signal intensity.*

Ex situ *fluorescence lifetime imaging microscopy (FLIM)*

Samples were prepared by pipetting a small amount (~15 μL) of material collected from the outlet stream of a microfluidic device onto glass slides, followed by addition of a glass coverslip and sealing with clear nail polish. Glass microscope slides were then mounted on a Nikon Eclipse Ti inverted microscope in conjunction with an Alba FCS and scanning mirror module. A mode-locked Ti:Sapphire laser system (Tsunami and Millennia, Spectral Physics) was used for

two-photon illumination of the samples at 80 MHz pulse repetition rate with ~100 fs pulse width. Fluorescence emission was imaged using a Nikon Plan APO 60x objective lens (NA = 1.2) and a single-photon counting module with sensitivity from ~500-1100 nm (70% quantum efficiency peak at 650 nm, dark count = 50 counts s^{-1}). Data were analyzed for fluorescence lifetimes using ISS Vista Vision software.

In situ *fluorescence lifetime imaging microscopy (FLIM)*

Microdevices were mounted on a Zeiss LSM710 inverted microscope and imaged through a Zeiss Plan-Apochromat 20x objective (NA = 0.8). A Ti:Sapphire laser system (Mai-Tai, Spectra Physics) was used for two-photon illumination of the devices. The FLIM system was first calibrated using ISS Vista software and a Rhodamine 6G standard (lifetime = 4.03 ns). The edge of a drop of Rhodamine dye was focused onto one of two high sensitivity non de-scanned (GaAsP) detectors and then directed to single-photon counting modules (ISS) for system calibration. Following microdevice setup and flow initiation, the cross-slot device was imaged using a QUASAR 34 channel spectral detector, consisting of two standard PMTs and a 32 channel PMT array. Once assembly was verified, scan area and speed were decreased to a 256 x 256 array with a 6.3 μs pixel dwell time at a 2x zoom, and the light path was redirected toward the single-photon counting modules. Data were analyzed for fluorescence lifetimes using the ISS Vista Vision software, similar to *ex situ* data.

RESULTS AND DISCUSSION

Photophysics of synthetic peptides with different functional cores

In this work, we studied the fluidic-directed assembly of three different synthetic peptides containing the same flanking amino acid sequence but with three different cores: OPV3, quaterthiophene (4T), and perylene-diimide (PDI) (Figure 1.2). These materials consist of a π-conjugated core flanked on either side with symmetric peptide sequences DFAG (aspartic acid, phenylalanine, alanine, glycine). Under acidic conditions, these peptides assemble into supramolecular fibers (Figure 2.4) via beta sheet formation due to pH-triggered electrostatic screening of aspartic acid residues that become protonated below the pK_a of the residue side chain, thereby facilitating hydrogen bonding and van der Waals interactions between peptide monomers. Beta sheet formation can be further influenced by the solvation and π-π interactions of the cores, depending on the chemical identity of the π-conjugated core [2,4,12,14].

We began by characterizing the photophysical properties of these three synthetic oligopeptides with different π-conjugated cores: OPV3, 4T, and PDI (Figure 1.2a). Upon assembly, these peptides exhibit blue-shifted absorption peaks and quenched red-shifted fluorescence emission, which is consistent with H-aggregate formation in the framework originally developed by Kasha and coworkers and expanded upon by Spano and coworkers [4,18]. The red-shifted fluorescence emission for 4T-functionalized peptides is noticeably less pronounced compared to peptides with OPV3 and PDI cores, which necessitates the use of different optical configurations for fluorescence imaging of peptides with 4T cores (Figures 1.2b and 1.2c, Table 2.1). Furthermore, the PDI peptide exhibits a significantly quenched fluorescence emission relative to 4T or OPV3 peptides, which complicates detection of PDI assembled peptides (Figure 1.2d).

For these reasons, we primarily focused on OPV3-functionalized peptides for characterizing assembly dynamics via fluorescence spectroscopy, though all three are assembled using the new continuous flow microdevices.

Flow field characterization for 3D flow focusing

Before proceeding with assembly experiments, we assessed the performance of microdevice designs using computational fluid dynamics in COMSOL Multiphysics. Diagonal groove patterns (chevrons) were used in the ceilings and floors of microdevice inlet channels to generate a sheath flow consisting of an inner peptide stream enfolded in an outer sheath stream (Figure 2.1) [30,31,33,35–37]. The sheath stream is introduced at a higher volumetric flow rate than the inner core stream so that sheath fluid is directed across the channel above and below the inner peptide stream, thereby inducing vertical displacement and compression of the inner fluid. In particular, we used symmetric pairs of chevron patterns, four on top and four on bottom of the peptide inlet stream (Figure 2.1a and 2.1b), in order to maintain sample stream symmetry at the cross-slot and to generate coaxial flows that are fairly insensitive to the sheath-to-core flow rate ratio [30,35]. In particular, we evaluated the performance of these devices for 3D focusing using sheath-to-core flow ratios in the range of 10:1 to 100:1 (Figures 2.5a and 2.5b). We found that these microdevice geometries and operating parameters were suitable for achieving efficient sheathing of the inner peptide stream, which effectively prevents the peptide from interacting with the top and bottom surfaces of microdevices while maintaining lateral focusing (Figure 2.5b).

Following validation of microdevice designs, we next fabricated 3-layer integrated microfluidic devices containing the same chevron patterns as analyzed in the computational studies. Using these devices, we experimentally characterized the performance of the chevron-containing microdevices for vertical flow focusing of small molecule dye and peptide streams

using confocal microscopy. Before proceeding with real-time characterization of peptide assembly, we first introduced a small molecule fluorescent dye as the inner core stream and used water as the sheath stream to demonstrate proof-of-principle validation of 3D flow focusing. In all cases, we observed efficient vertical focusing and generation of a sheath flow (Figures 2.5c and 2.5d). Notably, we observed that higher volumetric flow ratios of sheath-to-core streams resulted in substantial compression of the inlet dye stream, in some cases reducing photon counts to a low level, thereby signifying efficient *z*-direction focusing (Figure 2.6). It should be noted that when chevrons were poorly aligned, no such useful flow focusing was achieved (Figure 2.7) Nonetheless, using this method, we observed long-term stability (minutes to tens of minutes) of vertically focused streams when operating in a continuous flow mode, which enables the data acquisition using confocal imaging for vertical *z*-stack image integration with suitably long exposure times.

Following flow focusing, the peptide stream is directed to a 4-channel microfluidic cross-slot. In the vicinity of the cross-slot, the field is planar extensional with a fluid velocity described by $v_y = \dot{\varepsilon} y$ and $v_x = -\dot{\varepsilon} x$, where $\dot{\varepsilon}$ is the strain rate and (*x*,*y*) are the distances along the inlet (or outlet) from the stagnation point at the center of the cross-slot. In this way, peptide assembles due to diffusive mixing at the interface between the unassembled peptide and acid streams in the cross-slot junction, and the extensional component of the flow aligns the products as they assemble [4,29]. Using this integrated microfluidic device, we effectively generated 3D flow-focused inlet streams for OPV, 4T, and PDI peptides, followed by peptide assembly and alignment in a continuous flow format over long times (Figures 2.1c-2.1e).

Oligopeptide assembly under continuous flow

Following microdevice characterization, we next moved to study the continuous flow assembly of synthetic oligopeptides (Figures 2.8 & 2.9). For these experiments, we introduced a deionized water stream into the sheath flow inlets, an aqueous solution of unassembled peptide oligomer (0.1 mg/mL) into the sample inlet stream, and an aqueous acidic stream (10 mM HCl) into the opposing inlet channel of the cross-slot junction, as shown in the schematic in Figure 2.1. For direct comparison, we characterized the assembly of peptides in microdevices without (Figure 2.8a) and with (Figure 2.8b) chevron features in floors and ceilings of the inlet peptide streams. In all cases, microfluidic devices without vertical focusing exhibited rapid peptide aggregation and adhesion to the channel surfaces (Figures 2.8a and 2.8c). For microdevices without chevrons, fluorescence intensity measurements in the outlet channels clearly demonstrate the uncontrolled accumulation of assembled peptide. On the other hand, microdevices containing chevrons allowed for the continuous and long-time assembly of oligopeptides without material accumulation (Figures 2.8b and 2.8d).

Figure 2.8e shows the time-dependent fluorescence emission intensity for microdevices with and without vertical flow focusing. In simple devices without chevrons, solutions containing OPV3-functionalized peptide showed dramatic accumulation of material with significant clumping after only 90 s of device operation. Prior work has demonstrated that assembled oligomer in solution will rapidly disassemble when pH is returned to neutral, non-aggregate-inducing conditions [4]. However, when the acid flow rate was reduced after two minutes from 500 µL/min to 250 µL/min, thereby moving the assembly front and enveloping the pre-assembled material in high pH solution, significant quantities of adhered oligomer aggregation remained, which indicates that the surface-bound or ‘clumped’ assembled material may be irreversibly adhered to the

microdevice surfaces (Figure 2.10). On the other hand, microdevices containing chevrons showed no evidence of aggregation or irreversible adhesion to device surfaces, even after continuous flow and peptide assembly in excess of 15 minutes. Figure 2.8d shows that a steady-state amount of assembled peptide formation is attained within the flow, and the lateral and vertical width of the assembly front does not change in the *x*-*y* plane or in the *z*-direction. This is further evidenced by the constant transient fluorescence emission intensity over long times in the assembled peptide region in microdevices containing chevron features (Figure 2.8e). Remarkably, Figure 2.3 shows evidence that the material assembling at the peptide-acid interface in 3D focused devices is not touching the device surfaces and instead is like a suspended rope, moving freely in response to disturbances in the flow. Moreover, we found that oligopeptides with 4T and PDI cores exhibited similar behavior to OPV3-functionalized peptides. In microdevices without chevrons, both peptide solutions show evidence of oligomer aggregation and clumping on the top and/or bottom surfaces after only ~150 s of device operation. In contrast, microdevices containing chevrons yield efficient continuous assembly of 4T and PDI peptides for long times (Figure 2.9).

Continuous fluidic-directed assembly in microdevices allows for the ability to directly characterize the properties of assembled materials in real-time using *in situ* FLIM. In brief, FLIM measurements provide the time delay between excitation and fluorescence emission, and lifetimes are determined by the available energy state transitions before radiative emission in the sample and are thus indicative of molecular scale order. In this way, FLIM can be used to probe π-π stacking interactions between adjacent π-conjugated cores in order to gain insight into the supramolecular structures formed during assembly. For example, the difference between pure H-stacked behavior and J-coupled behavior are spectrally distinct [18]. In particular, the S_0-S_1 vibration-less ground state radiative transition is symmetry-forbidden in pure H-aggregates, which

means that higher order transitions via phonon coupling are favored in these types of aggregates, leading to the quenched and blue-shifted absorbance as shown in Figure 1.2 [18,19]. In this way, fluorescence lifetimes can be used to probe oligomer assembly by revealing additional insight into non-ideal H-structures at the molecular level.

We directly studied oligopeptide assembly in continuous flow using spatially resolved *in situ* FLIM for both 4T- and PDI–functionalized oligopeptides (Figures 2.11 & 2.12). Histograms of fluorescence lifetimes show a clear bimodal distribution for both functional cores, with the long-time and short-time maxima consistently corresponding to the locations of unassembled and assembled oligopeptide, respectively. As a reference, the fluorescence lifetimes of unassembled oligopeptides with 4T and PDI cores are ~0.7 ns and ~3 ns, respectively. Fluorescence lifetime shortening in the assembled structures suggests some degree of J-like aggregate behavior due to a greater degree of exciton or excited state delocalization across several core species, as it is well established that J-aggregates exhibit shorter fluorescence lifetimes compared to their unassembled monomer constituents [1,20–22]. Furthermore, the number of coherently coupled molecules, known as the coherence length of an oligomer, is directly proportional to the radiative decay rate and thus inversely proportional to the fluorescence lifetime [19,76–78]. In this way, we can estimate the coherence length of the assembled fibrils to be on the order of two to five times larger than unassembled peptide.

The combination of partially H-like and J-like properties of the assembled oligopeptides could arise due to tertiary or quaternary structures of joined β-sheets in the assembled fibrils, which was elucidated by Fitzpatrick and coworkers [79]. Alternatively, the assembled structure could have π-conjugated functional cores in an “offset H” type of configuration, which would lead to a slightly larger effective transition dipole and therefore a shorter lifetime compared to unassembled

peptide while retaining the H-aggregate characteristics observed in Figure 1.2. In our experiments, the dichroic mirror in the optical detection path separates the two emission channels for the *in situ* FLIM system detectors (Figure 2.13). In this way, fluorescence emission from the 4T samples was split across two channels, with redder, shorter lifetime emission from assembled oligomer dominating channel 1 (Figures 2.11c & 2.11e) and bluer, longer lifetime emission from unassembled peptide dominating channel 2 (Figures 2.11d & 2.11f). Notably, the fluorescence lifetime maps clearly show which regions are dominated by the presence of unassembled and assembled oligopeptide fluorescence (Figure 2.12), even for images in which fluorescence intensity variations make it difficult to simultaneously view under- and over-exposed regions.

In order to further understand the photophysical behavior, we can consider the structure of the assembled supramolecular materials. Although the amino acid residues flanking the functional core are the primary structural determinants, beta sheet formation can be altered by π-π stacking interactions of the cores. The assembled supramolecular peptide structure takes the form of a twisted ribbon structure, with π-π stacking interactions between adjacent π-conjugated cores and hydrogen bonding and van der Waals interactions between adjacent beta sheets in the flanking peptides. Although π-π stacking interactions between cores generally aids in assembly, steric interactions in amino acid side groups or core structures can influence the distance between stacked peptides. Both 4T and PDI are larger and more hydrophobic core groups compared to OPV3. From this perspective, beta sheet formation for oligopeptides functionalized with larger π-conjugated cores may be hindered compared to the less bulky OPV3 core. Therefore, in some cases, these factors make it difficult to distinguish unassembled from assembled oligopeptide using only fluorescence emission spectra. However, FLIM can be used as an effective technique for high contrast imaging of oligopeptide assembly.

Characterization of assembled oligopeptides using ex situ FLIM

In order to further validate the generation of aligned oligopeptide in these integrated microdevices, we also used FLIM to analyze the assembled material collected from effluent streams. In these experiments, we studied the photophysical properties of the assembled peptide material collected in the outlet flow streams for microdevices with and without chevrons. Histograms of fluorescence lifetimes for assembled material acquired from both simple and chevron-containing devices appear as an approximately Gaussian distribution (OPV3 peptides in Figure 2.14, and PDI peptides in Figure 2.15). Moreover, fluorescence lifetimes are observed to be similar for PDI materials when comparing both *in situ* and *ex situ* FLIM (Figures 2.12 & 2.15). Fluorescence lifetimes are not observed to drastically change for materials assembled in simple (non-chevron) and chevron devices, which suggests that 3D flow focusing allows for continuous peptide assembly without negatively impacting the properties of assembled materials.

CONCLUSIONS

In this work, we demonstrate the continuous assembly and extrusion of aligned oligopeptides using integrated microfluidics. Confocal fluorescence microscopy is used to verify that microdevices containing chevron patterns in the ceilings and floors of inlet channels generate a sheathed peptide monomer stream. Following assembly, we further characterize the fluorescence emission properties of OPV3, 4T, and PDI-functionalized synthetic peptides. In particular, fluorescence emission spectra and changes in fluorescence lifetimes associated with amyloid formation in these materials are used to show that oligopeptide assembly is induced in a spatially-

confined 3D reaction zone contained along the extensional flow axis in a cross-slot microdevice. In particular, assembly occurs within a vertical distance around 50 μm from the center-plane of the microdevice when a flow-sheathed unassembled peptide stream is directed to interface with an opposing aqueous acid stream at a cross-slot junction. In this way, oligopeptides can be assembled and aligned into highly ordered structures without device clogging, thereby providing a known processing history of assembled materials collected in effluent streams.

Using this approach, microdevices are used to facilitate the continuous assembly of oligopeptide materials. Using chevron-equipped cross-slot devices, aligned and assembled oligopeptides can be extruded in a continuous manner that is limited (in a single experiment) only by the capacity of the fluid reservoirs (in our case, glass syringes). Under proper device operation, our results suggest that there should be no limit to the number of times the external syringe pumps can be refilled in order to continue oligomer production. Using this approach, it is possible to explore the wide chemical parameter space of peptide residue and functional core combinations in a rapid format. As the role of microfluidics continues to grow as a tool for controlling the assembly of micromaterials in flow, our approach of using 3D flow focusing patterns as a technique to avoid contact between assembled material and device surfaces should become increasingly valuable.

FUTURE WORK

The designs in this work were all based upon the previous success of a cross-slot geometry for achieving extensional flow. However, in addition to the chevron modifications, we also considered several modifications and alternative designs which could potentially be more effective

or easier to fabricate. Many of the designs below are based upon the realization that while there is extensional flow within the cross-slot, the strain rate rapidly decreases as material exits that region and that while the extension rate is well defined at the stagnation point, it decreases rapidly with distance from the center along the flow axes (Figure 2.16) [80].

Modified cross-slot

We experimented briefly with a cross-slot geometry that was modified for a constant, homogeneous extension rate along the cross-slot flow axes as shown in Figure 2.17. We acquired the data from Haward et al. to integrate the modified geometry into our cross-slot designs and created several samples. We did not notice any obvious difference in the assembly dynamics. It would, however, be interesting to more systematically compare the two cross-slot designs to determine if material assembly is greater controlled over a longer portion of the device in the modified version.

Non-chevron-based 3D flow focusing

While the obvious comparison to make with the chevron devices would be with the more straightforward 4-channel lateral vertical focusing technique whereby vertical (z) focusing is attained analogously to the lateral focusing with an additional focusing stream above and below the channels, we deemed this method overly complicated given our success with the chevrons. Nonetheless, there was another design which we investigated that may also have potential. The design by Lin et al., which attempted to verify with COMSOL simulation, involves passing what would in this case be the unassembled oligomer inlet channel through a much larger vertical channel of focusing fluid (Figure 2.18). The focusing fluid enters the vertical channel from above and is pierced by the relatively higher velocity peptide stream. Both flows exit through one channel, a continuation of the inlet peptide stream, but the focusing fluid wraps around the focused

stream leading to a very neatly symmetric coaxial flow [34]. While we did construct these devices, the different sized channels and the difficulty of keeping the vertical focusing channel's inlet line out of the microscope optics—due to the larger, stiffer tubing and its closer proximity to the device center as compared to the other inlet lines—posed short-term challenges. We were not able to view focusing as demonstrated by Lin et al. and indicated in our own simulations, and perhaps the conspicuous dearth of follow-up studies by Lin et al. using their own design is indicative of greater practical challenges than implied by Lin et al.'s 2012 *Lab on Chip* paper. Nonetheless, we would be interested in exploring the method further. Finally, we conducted follow-up simulations in COMSOL that included the cross-slot with the vertical channel focusing and found that while Z-focusing appeared to remain intact after the cross-slot, it was significantly degraded as compared to the pre-cross-slot values (Figure 2.19). Results such as these and implications for what may be happening even in chevron devices inspired us to investigate simpler methods of achieving controlled extensional flow with acid-induced assembly as elaborated upon in the following section.

Alternative routes toward controlled assembly

Concurrent to the work above we investigated the assembly dynamics of the peptides and found that it would be best to slow down the acid-mediated reaction in order to probe these dynamics. Furthermore, as we investigated different methods of slowing the process for triggering randomly oriented assembly via acid vapor, we found that slower assembly yields longer, more nicely formed peptide fibers. We thus investigated alternative microfluidic designs to achieve slower assembly with more control of the triggering reactions.

A review of the literature revealed several microfluidic designs that take advantage of cohesive and capillary forces to eliminate the ceilings from devices to create microcanals [81] or

even eliminate both the ceiling and floor, creating suspended microfluidics [82]. These semi-contained features could be implemented for the entirety of a device or for only certain parts. Perhaps devices construction would be simpler by removing 3D focusing features and instead implementing a suspended design along only the extensional flow axis of the device. This method would eliminate the surfaces to which we are concerned about assembled material sticking. A further advantage to such a design is that it opens the possibility of triggered, simultaneous assembly of coflowing streams of different peptides. Instead of flowing peptide from one end of the cross-slot and acid into the opposing end to trigger assembly, if only the extensional flow axis of the device were suspended and open to air, we could induce assembly via acid vapor. This method could also allow us have two different peptide streams flowed in opposition such that the extensional flow axis where assembly occurs would also be the material interface. For example, we could create interesting p-n junctions by flowing a material with an OPV core against a material with a PDI core and inducing assembly where they meet along the extensional flow axis.

A similar design that would support higher flow pressures and might be easier to fabricate than the open microfluidic designs would be to flow peptide against water, itself, or a different peptide as in the previous example but instead of having an open portion of the device for acid vapor convection and diffusion, there would be an enclosed channel running above and/or below the extensional flow axis containing a high concentration HCl solution. Only a thin layer of PDMS would separate the main flow channels from the acid channel and the natural porosity of the PDMS would allow free hydrogen radicals to diffuse through to the material at the extensional flow axis. Assuming a permeability for H_2 in PDMS of approximately 8E-8 Barrer [83] and other diffusivity properties of hydrogen gas [84–86] as good ersatz properties for modeling acid diffusion from across the PDMS boundary we conducted rudimentary simulations in COMSOL for variations of

this design, demonstrating its potential for future work (Figure 20). This enclosed design, however, would require flow focusing like the chevron design as it would not address the problems of device clogging.

Finally, our work with the modified cross-slot as detailed above also inspired investigation to alternative geometries for achieving controlled extensional flow over longer distances than provided by the cross-slot, even in its modified form. Recalling Bernoulli's principle that, all else being equal, the inevitable change in pressure due to a change in cross sectional area of a flow channel will result in a corresponding change in the fluid velocity, we determined that a channel with decreasing width should result in a monotonic increase in velocity along the channel, giving the extensional flow properties desired. We naïvely implemented an initial design that simply tapered linearly from inlet values on the order of 20 to 120 microns wide to 20 microns at the outlets. While these devices showed good promise for monotonically increasing velocity, the response was not linear. In fact, simulations showed exponentially increasing strain rates along the length of the channel from inlet to outlet. A more thorough review of the microfluidic literature revealed studies in which researchers used hyperbolically converging channels to study the deformability of biological samples [85] which yielded a linear increase in velocity with distance along the channel (Figure 2.21). These long, tapered extensional flow channels ideally could be paired with one of the above methods of acid exposure in order to trigger assembly (co-flows of different peptides could easily be prepared upstream). The most likely method for acid exposure would be that of the separate HCl channel above the peptide flow channel, but it would be necessary to investigate the best method for 3D focusing as this design would likely have the same issues as addressed in the above work for peptide sticking to the device surfaces.

Assembly kinetics

After realizing that the cross-slot microfluidics could be used to create aligned assembled peptide, one of our early goals was to understand the kinetics of these reaction in order to know how best to control the end products. Toward that end we attempted to model the assembly using COMSOL's Laminar Flow, Transport of Dilute Species, Reacting Flow, and Surface Reaction physics, assigning gel-like properties to assembled peptide versus aqueous properties to unassembled peptide and prescribing different reaction rates for conversion of unassembled to assembled peptide upon touching the acid flow stream. Ultimately, a combination of insufficient computing power and insufficient experimental information to feed simulation led us to postpone these studies. But, it is reasonable to expect that COMSOL could be used to model the above-described reactions as well as taking into account the change in diffusive properties for acid that must be taken into account after the assembly front develops and the acid must diffuse through assembled material before reaching the unassembled material for reaction.

Ultimately, other experiments described in later Chapters of this work have demonstrated that kinetics do play an important role in the end products of material assembly. In particular, we noticed while drying material for preparation of FLIM samples that peptide appeared to self-assemble evaporatively, and experiments with slowing down the rate of evaporation through different solvents or the rate of triggered assembly by using a buffer between the peptide and acid vapor yielded longer, more homogeneous fibers [87]. As such, it would be very interesting to revisit modeling the reaction kinetics in COMSOL for a more detailed exploration of differences in assembly for the devices used in this work compared what might be achievable using the proposed future devices.

FIGURES

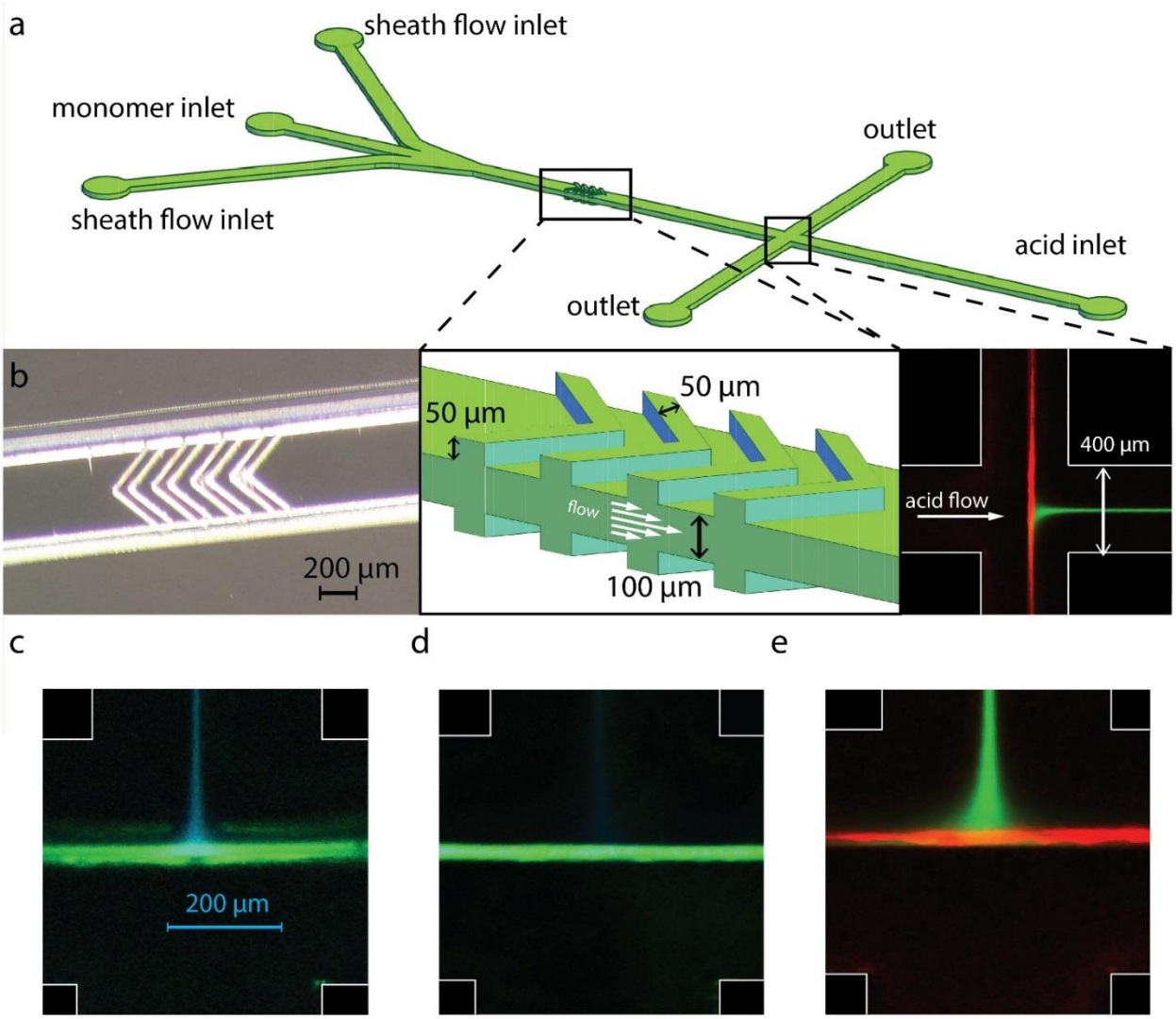

Figure 2.1 Integrated microfluidic device with cross-slot channel geometry and chevron features for 3D-focused oligopeptide assembly and alignment. (a) Schematic of the chevron microdevice. Channels are 400 µm wide by 100 µm tall. Top left inset: fluorescence image showing the cross-slot microdevice in operation as viewed under 50x objective. Bottom right inset: Close-up schematic of the chevron patterns. Chevrons are 50 µm tall and 50 µm wide with a 90-degree apex, intersecting the channel walls at a 45-degree angle. (b) Optical micrograph of the aligned chevrons. (c-e) False color images of the assembly process for (c) DFAG-OPV3, (d) DFAG-4T, and (e) DFAG-PDI. The inlet peptide stream (unassembled) is directed from the top down and appears as blue in parts (c) and (d) or green in part (e). Assembled peptide flows in the vertical outflow channels and appears with a red-shifted fluorescence emission. Green color (or red color) is used to illustrate emission wavelengths redder than the dichroic cutoff and blue color (or green) is used for emission that is bluer. Fluorescence emission was detected using the optical configurations described in Table 2.1.

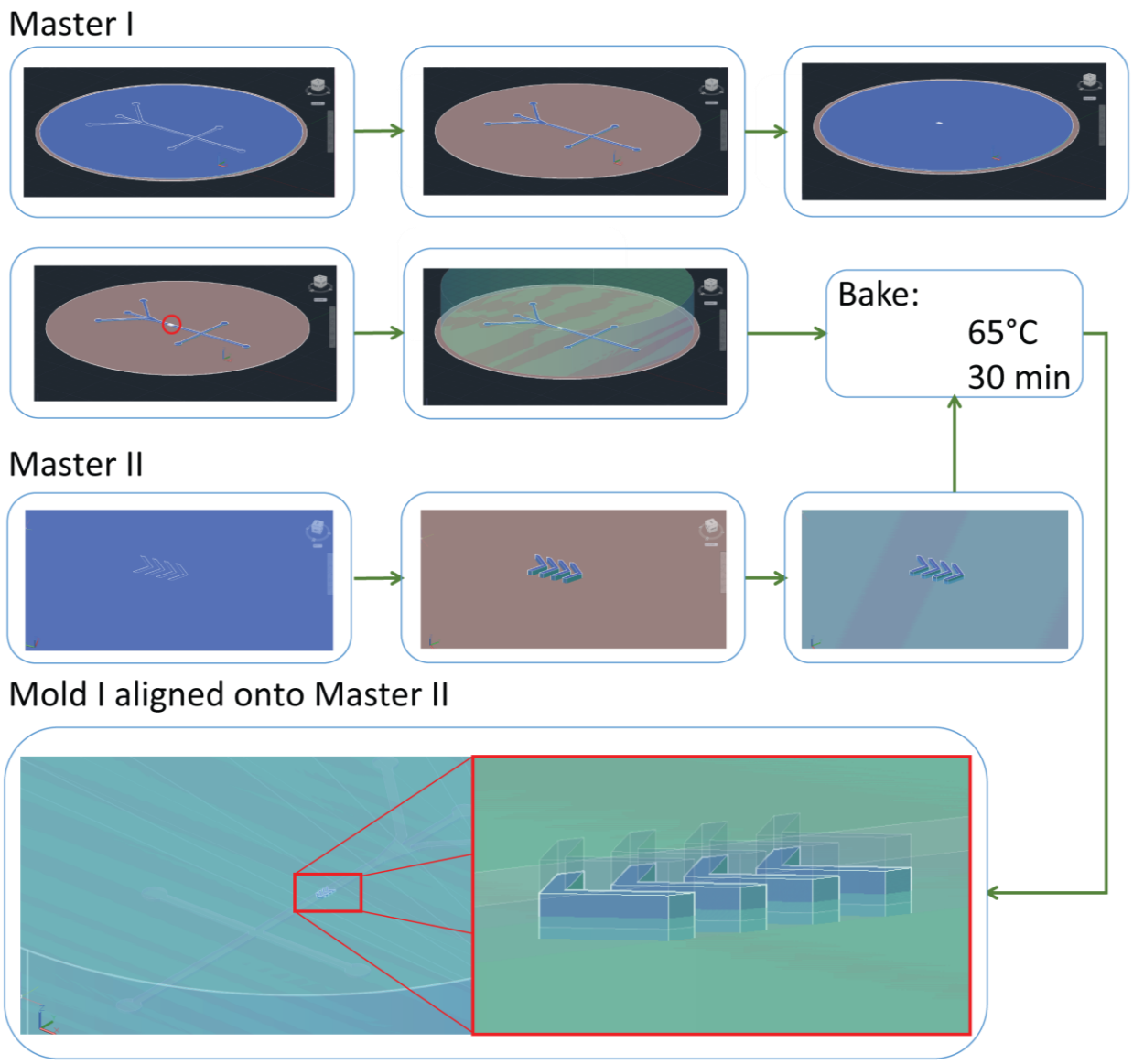

Figure 2.2 Fabrication process flow for multilayer microfluidic devices. Master I is created by iterative photolithographic steps to achieve a two layer master of cured photoresist; the first layer is the patter for the device channels and the second layer on top of that is for the top chevron patterns. PDMS is then poured onto this master to form one part of the device. Master II is created by spin coating photoresist to 100 µm thickness and patterning as chevrons. PDSM is then spin coated to 50 µm to define the 50 µm tall bottom chevrons of the device. The second half of the master structure protrudes from the PDMS to aid in alignment. Both PDMS molds are then partially cured in an oven at 65 °C for 30 min. After that point the PDMS from master I is removed from its master and aligned with the pattern on master II. The whole assembly is then allowed to finish curing overnight in the same oven, bonding to the two PDMS sections. Finally, the device is sealed by using oxygen plasma to pond the completed PDMS structure to a glass coverslip.

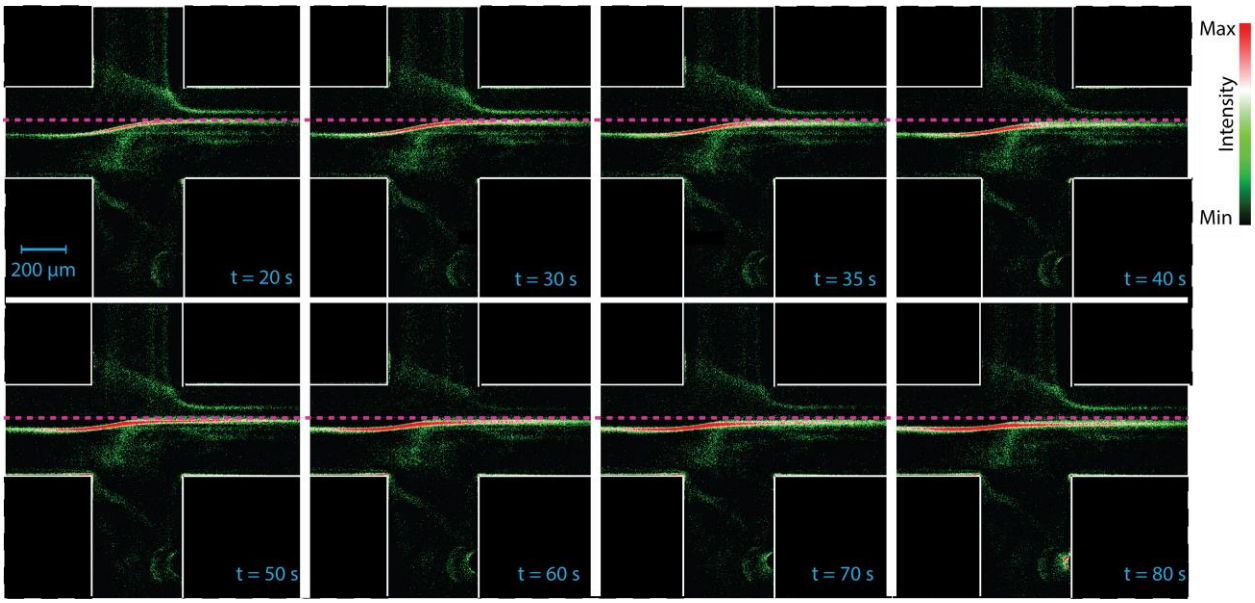

Figure 2.3 Observation of assembled, intact peptide materials suspended in flow over time, progressing left to right, top to bottom. The initial position of the assembly front, marked by highest intensity, is indicated by the horizontal dashed magenta line in each image. The assembly front gradually moves over time as an air bubble (out of view in the channel to the right) moves toward the outlet. The air bubble disturbs the flow, and its gradual progression out of the device is marked by corresponding changes in the flow lines at the cross slot. By the final timestamp at 80 s, the bright fluorescent line corresponding to the current assembly front has shifted completely below its position from the start of the time sequence. Notably, the entire process proceeds without leaving residual material on the ceiling or floor of the device, indicating complete focusing of material away from device surfaces.

.

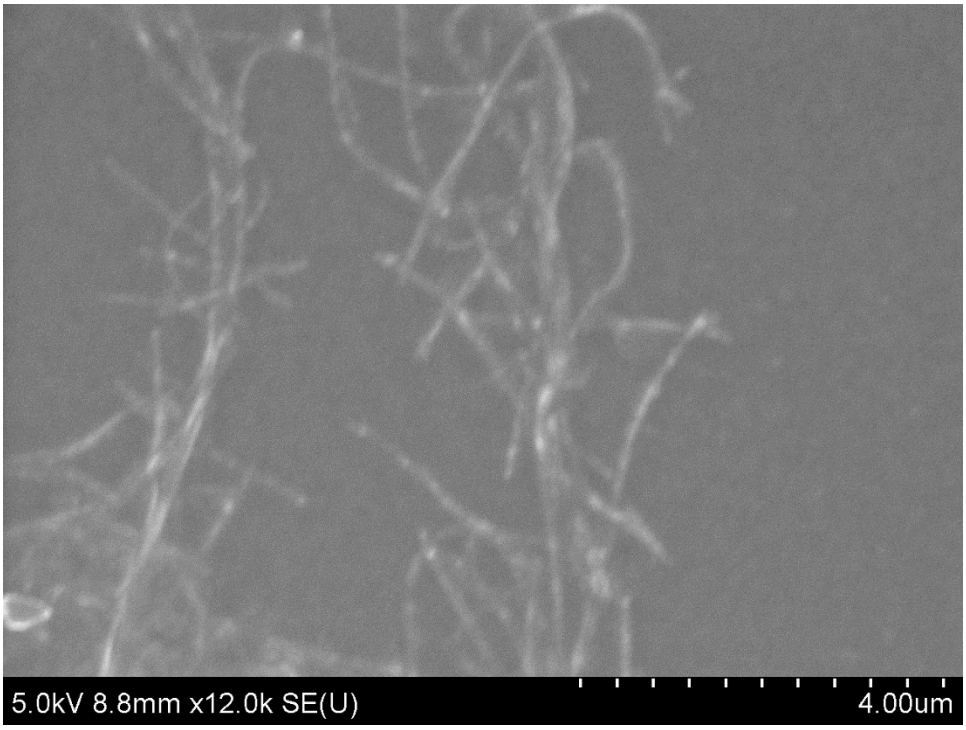

Figure 2.4 SEM image of DFAG-OPV3 fibers assembled via introduction of 100 mM HCl on silicon substrate.

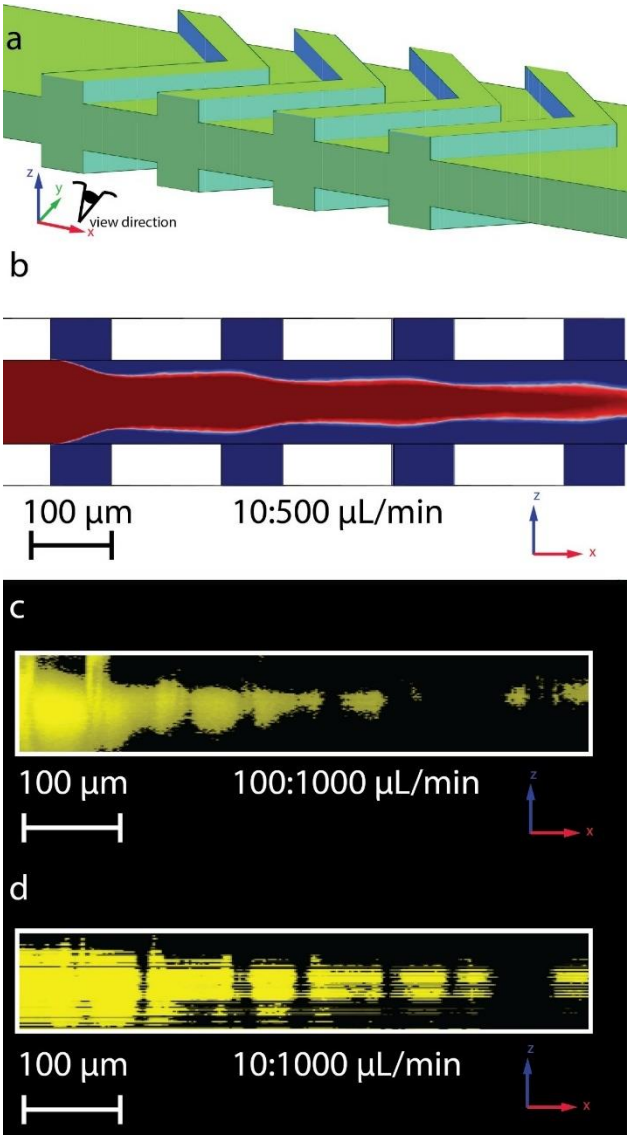

Figure 2.5 Computational and experimental validation of efficient vertical flow focusing using chevron-containing microdevices. a) Schematic of the microdevice showing orientation for cross sections in parts (b)-(d). Flow proceeds from the top left to the bottom right, in the direction that the chevrons are pointing. b) COMSOL simulation results showing vertical flow focusing of a core stream (red) using a sheath flow (blue). The results are displayed for a cross-sectional plane cut through (a)along the flow axis as indicated by the eye in (a). As flow passes through each subsequent chevron, seen as the 4 sets of symmetric rectangular protrusions, the red flow becomes progressively focused in the z-direction. c) Side view of a reconstructed confocal microscope 3D image of flow focusing for a fluorescent dye at a core:sheath flow ratio of 1:10. The plane of view is equivalent to the section in (b). d) Side view of reconstructed confocal microscope 3D image of flow focusing for a fluorescent dye at a core:sheath flow ratio of 1:100. Due to the higher core:sheath ratio and lower absolute flow rate of the dye, this image was acquired using a 3x longer exposure compared to the image in part (c).

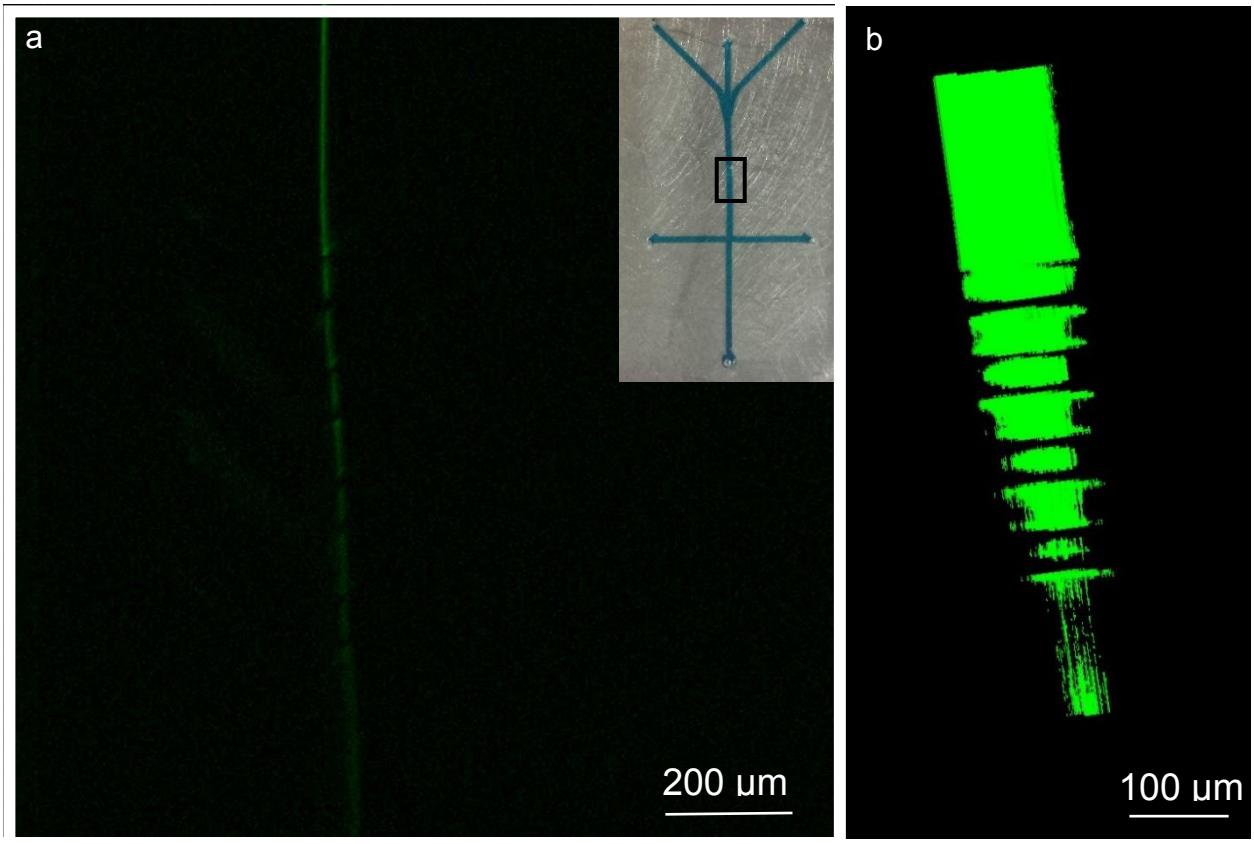

Figure 2.6 Successful flow focusing through well-aligned chevrons. a) Top down image of laterally focused fluorescent dye being vertically focused as it passes through chevrons. Focusing is visible in the steady decrease in intensity of the fluorescent line as it moves from top to bottom of the image. The region of observation is indicated by the black rectangle on the inset optical micrograph. b) Three-dimensional reconstruction of a Z-stack of fluorescent images taken at the chevrons.

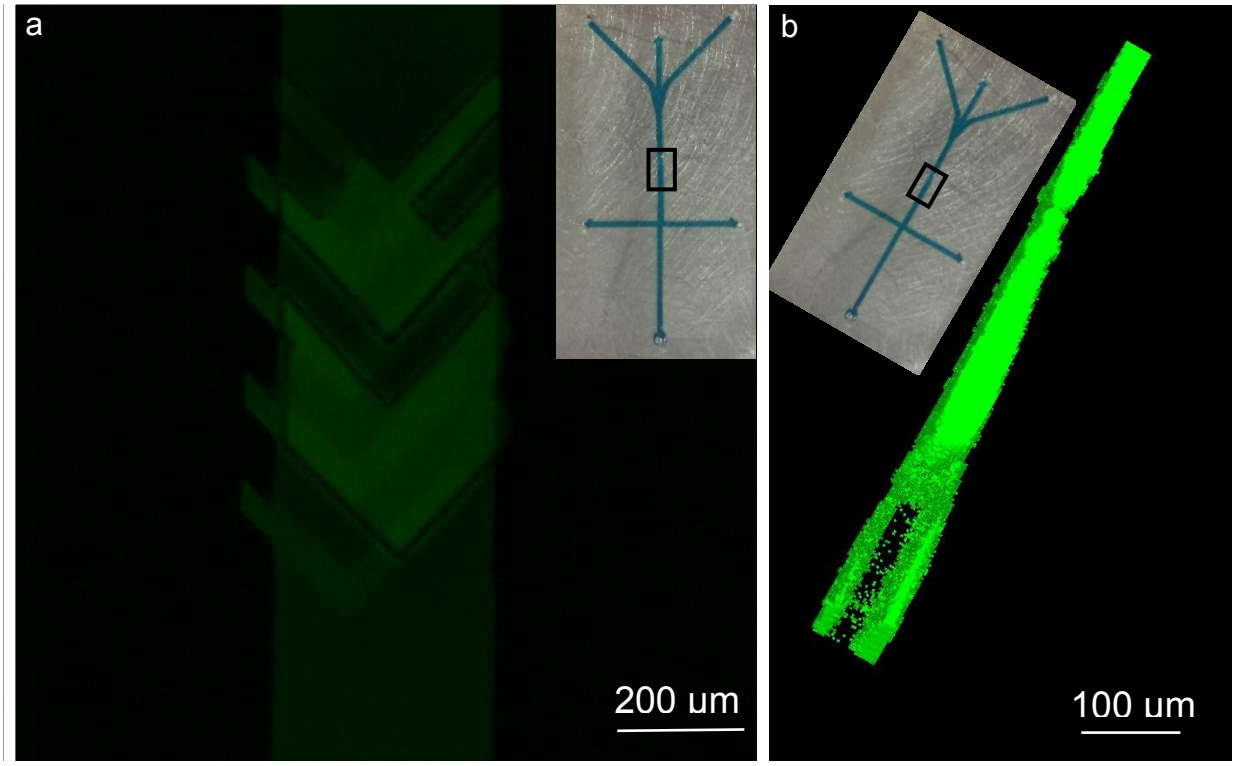

Figure 2.7 Poorly aligned chevrons lead to ineffective focusing. a) Top down image of poorly formed chevrons trapping fluorescent dye. When chevrons are poorly aligned or poorly formed, flow focusing is ineffective. The region of observation is indicated by the black rectangle on the inset optical micrograph. b) Three-dimensional reconstruction of a Z-stack of fluorescent images taken at the chevrons indicating splitting of the focused stream due to imperfections in the chevrons. The region of observation is indicated by the black rectangle on the inset optical micrograph. Flow is from top to bottom of the image.

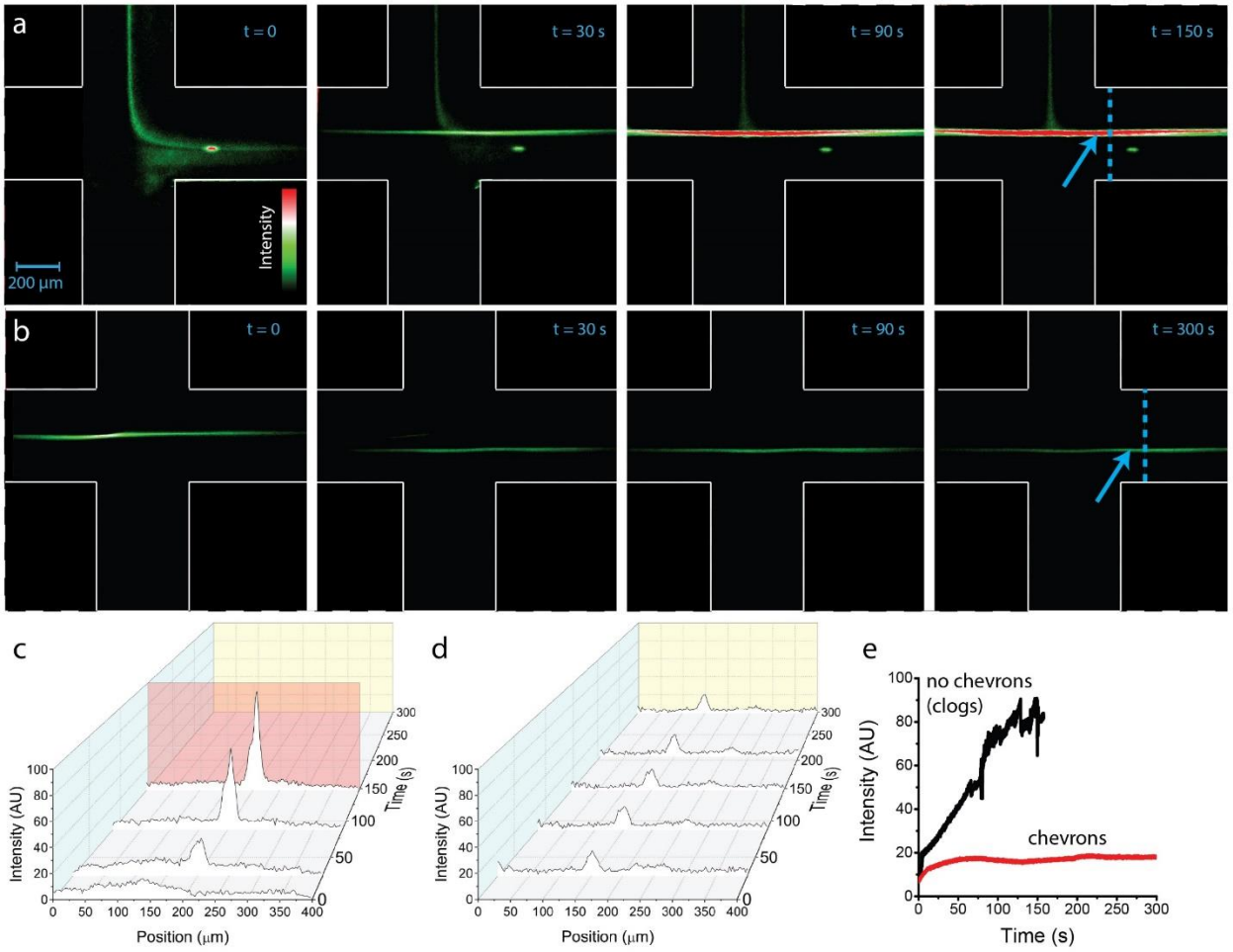

Figure 2.8 Assembly of oligopeptides in cross-slot microdevices. Images were collected on an inverted confocal microscope focused at the center plane of the device and excited with a 405 nm laser. (a) Time series of fluorescence images showing assembly of DFAG-OPV3 peptides in a simple cross-slot microdevice without chevrons. Assembled oligopeptide begins to form within the first minute and significant adhesion to channel surfaces is visible in less than 2 minutes. (b) Time series of fluorescence images showing assembly of DFAG-OPV3 peptides in a simple cross-slot microdevice with chevrons. At t = 0 s, flow rates are adjusted to be equal to the conditions in (a). At t = 30 s, the assembly front shows oligopeptide formation along new extensional flow axis. Continuous assembly can be achieved in microdevices with chevrons over the course of minutes to hours, much longer than for simple cross-slot devices without vertical flow focusing. Experiments in (a) and (b) were run under identical conditions in terms of peptide and acid concentrations (0.1 mg/mL and 10 mM, respectively) and volumetric flow rates (10 µL/min and 500 µL/min for sample and lateral aqueous focusing stream, respectively, and 500 µL/min for the acid stream). Images in (a) and (b) are shown in a false color intensity map normalized to the highest intensity across all images. (c) Fluorescence intensity line scan from the microdevice without chevrons across an outlet channel immediately downstream of the cross-slot indicated by a blue dashed line in the image in panel (a). (d) Fluorescence intensity line scan from a microdevice with chevrons across an outlet channel immediately downstream of the cross-slot indicated by a blue dashed line in the image in panel (b). (e) Fluorescence intensity of a 15 µm diameter spot centered on the assembly front, indicated by the blue arrow in the fluorescence images in (a) and (b) as a function of time.

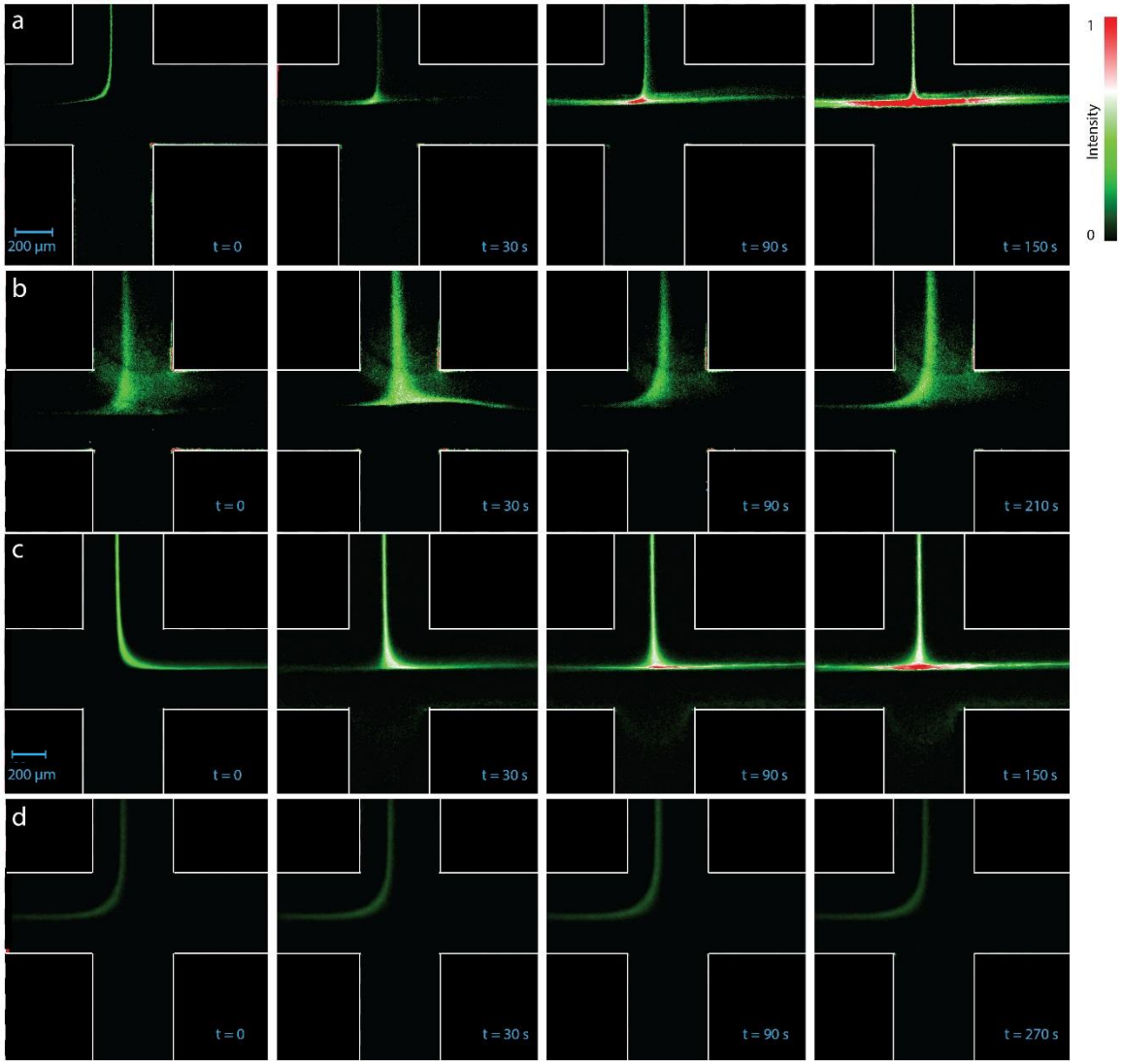

Figure 2.9 Continuous assembly of DFAG-4T and DFAG-PDI peptides in microdevices with chevrons. Images in (a), (b), (c) and (d) are shown in a false color intensity map normalized to the highest intensity across all images. Similar to the data in Figure 4, 0.1 mg/mL monomer solution is introduced at 10 µL/min, whereas the acidic stream (10 mM) and sheath flow are both introduced at 500 µL/min in all cases. (a) Assembly of 4T in a microdevice without chevrons. Oligopeptide adhesion is evident after two minutes. (b) Assembly of 4T in a microdevice with chevrons. No adhesion is observed and no change in fluorescence intensity is detected, indicating stable and continuous assembly of oligopeptide. (c) Assembly of PDI in a microdevice without chevrons. Oligopeptide adhesion is evident after two minutes. (d) Assembly of PDI in a microdevice with chevrons. No adhesion is observed and no change in fluorescence intensity is detected, indicating stable and continuous assembly of oligopeptide.

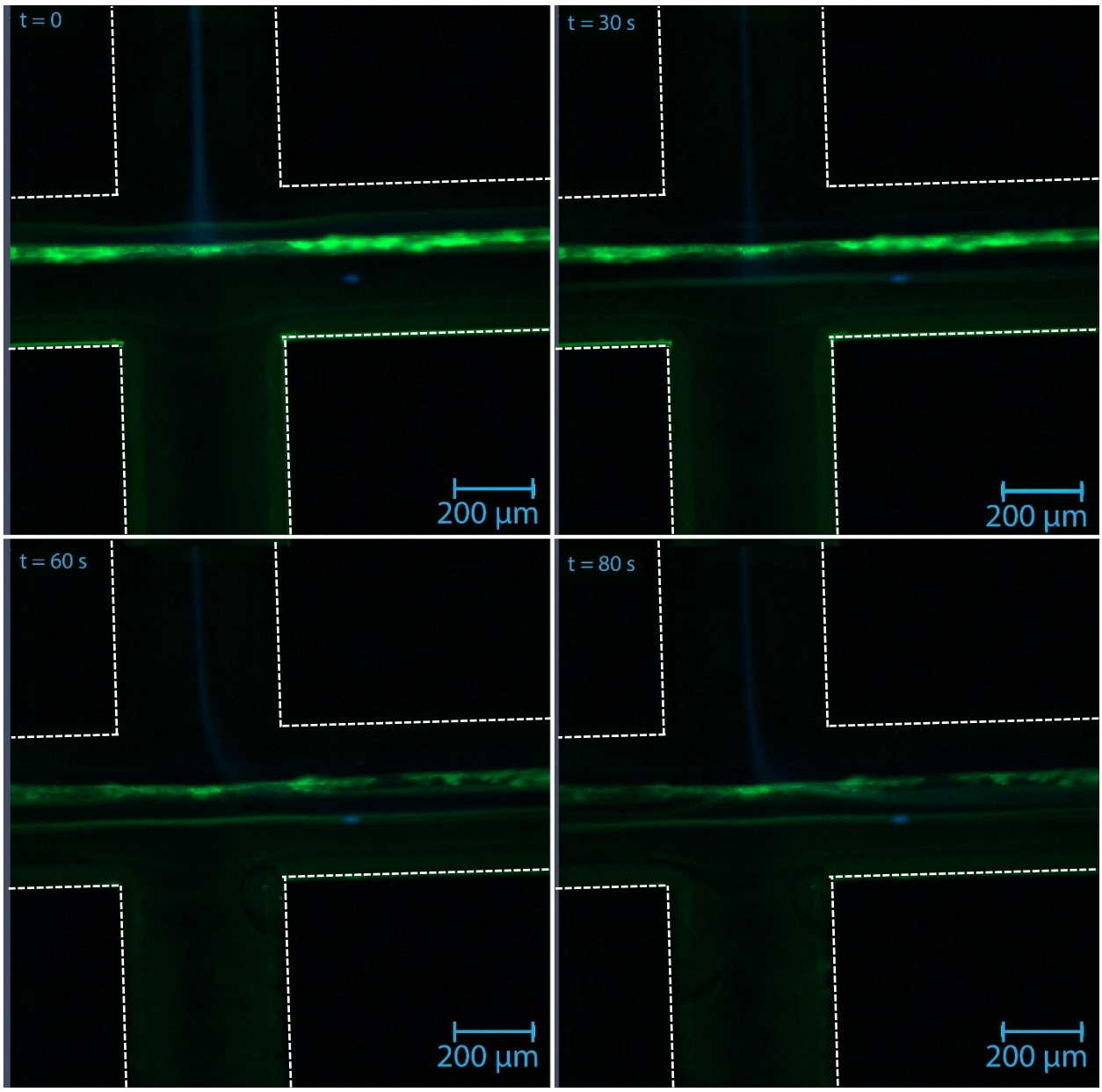

Figure 2.10 Persistence of clumped oligopeptide adhered to the top and bottom surfaces in microdevices without chevrons. At t = 0, the flow rate of the acidic stream is adjusted from 500 µL/min to 250 µL/min, causing the assembly front to recede and immersing the assembly front into neutral (high pH) peptide solution. By t = 80 s, assembled peptide begins to adhere to the device surfaces along the new assembly front while adhered material from the initial assembly front remains.

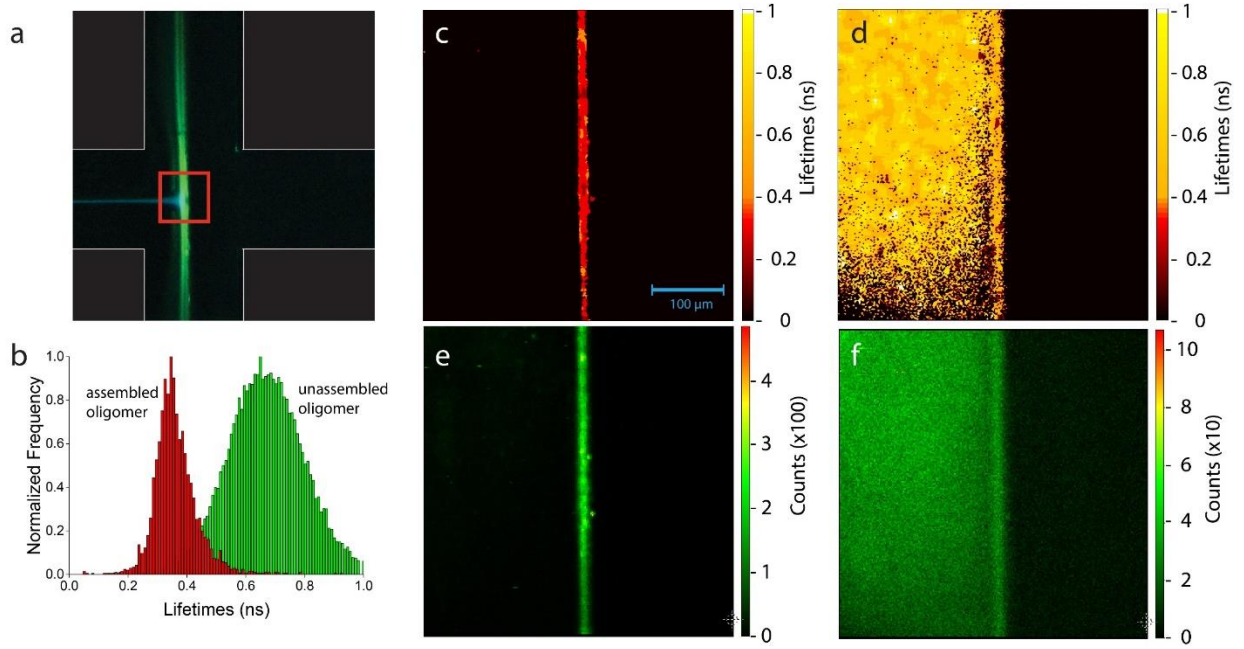

Figure 2.11 In situ *FLIM for fluidic-directed assembly of oligopeptides with 4T cores. (a) False color image of the assembly process at device cross slot (green shows unassembled peptide and red shows assembled peptide). Blue square indicates position and field of view for* in situ *measurements with respect to the device cross slot. (b) Histograms showing fluorescence lifetimes from two detector channels. Fluorescence lifetimes were normalized with respect to their highest values, thereby revealing a bimodal lifetime distribution. Red represents channel 1 and green represents channel 2 (Table 1). (c) Two-dimensional spatial map of assembled oligomer fluorescence lifetimes. Color represents lifetime and is scaled the same for both (c) and (d). (d) Two-dimensional spatial map of unassembled oligomer fluorescence lifetimes. (e) Assembled oligomer fluorescence intensity map. Color represents intensity as number of photon counts on the detector. (f) Unassembled oligomer fluorescence intensity map. Note that color scale is an order of magnitude lower than for (e).*

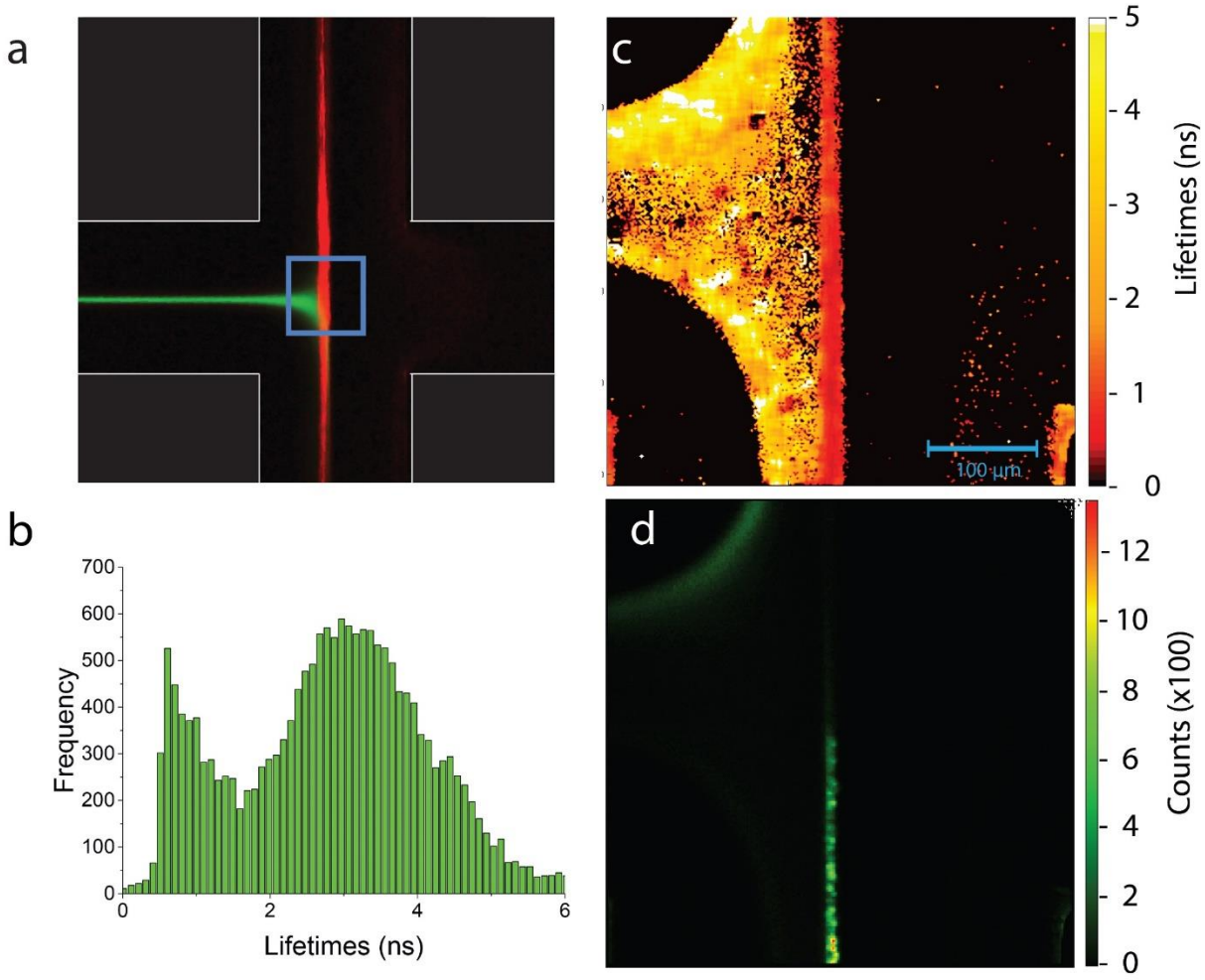

Figure 2.12 In situ *FLIM for fluidic-directed assembly of oligopeptides with PDI cores. (a) False color image of assembly process at device cross slot. Blue square indicates position and field of view for* in situ *measurements with respect to the device cross slot. (b) Histogram of fluorescence lifetimes shows a bimodal distribution due to unassembled and assembled oligopeptides. (c) Fluorescence lifetimes for both assembled and unassembled oligomer. Color map represents lifetime and clearly indicates the spatial locations of unassembled peptide (orange, longer lifetimes) and spatial locations of assembled peptide (red, shorter lifetimes). (d) Fluorescence emission intensity map corresponding to the same physical region as part (c). The color map represents intensity as number of photon counts on the detector, demonstrating that fluorescence lifetime information can be used to inform the assembly process despite potentially uninformative fluorescence emission intensity data.*

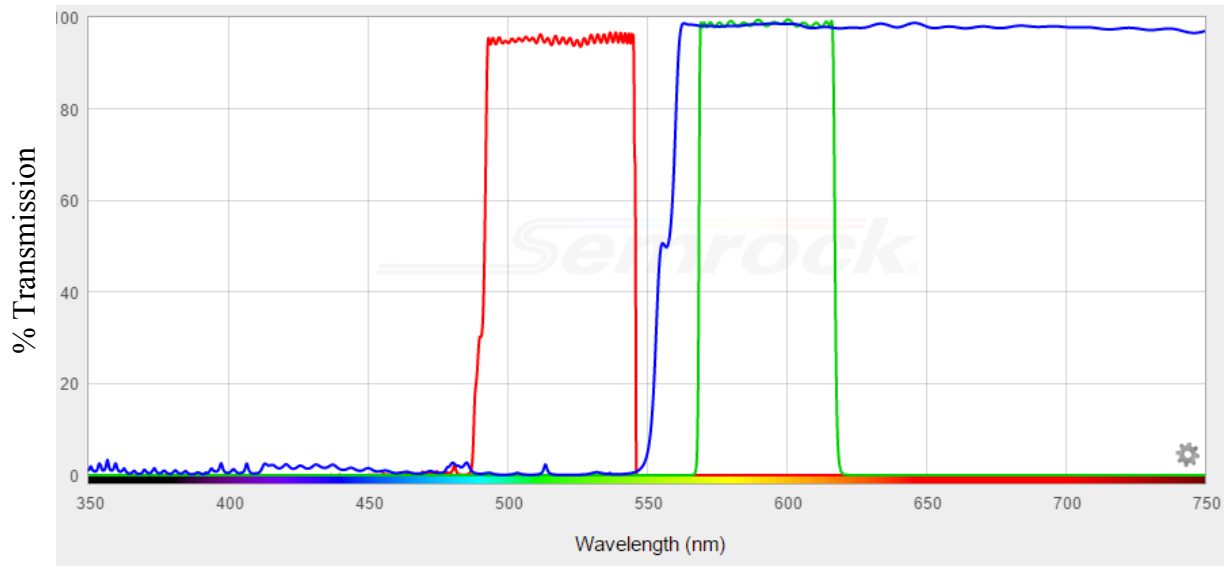

Figure 2.13 Transmission profile of filters and dichroic mirror for in-situ *FLIM system. Red is channel 1. Green is channel 2. Blue is the dichroic separating the two channels.*

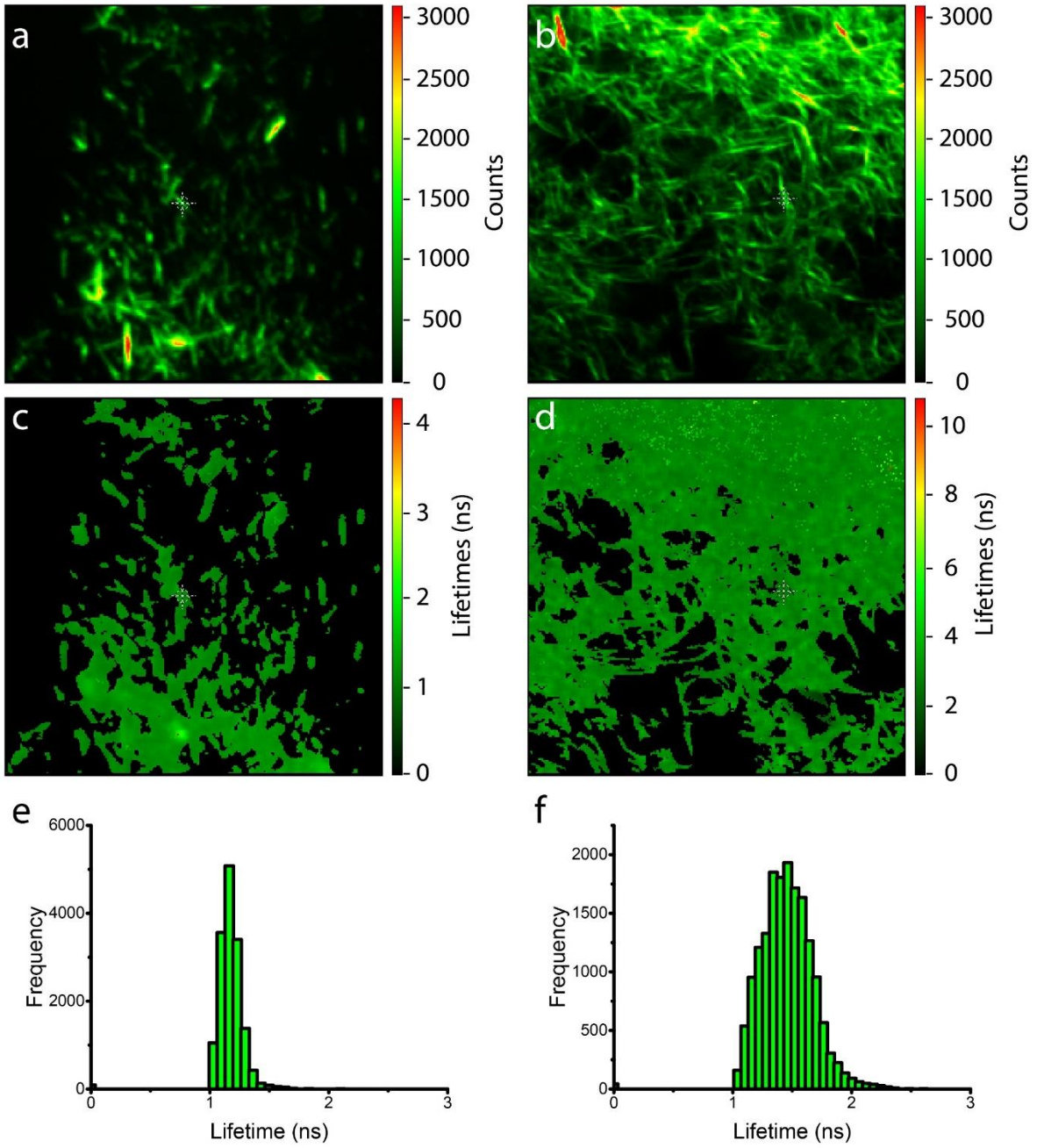

Figure 2.14 Fluorescence lifetimes of assembled material collected from effluent streams in devices without and with chevrons for OPV3 synthetic peptides. (a) and (b) show fluorescence intensity maps of assembled oligopeptide from a device without chevrons and a device with chevrons, respectively. (c) and (d) show fluorescence lifetime maps of assembled oligopeptide from a device without chevrons and a device with chevrons, respectively. (e) and (f) show histograms of fluorescence lifetimes for (c) and (d), respectively. In all cases, nearly Gaussian distributions of fluorescence lifetimes indicate highly uniform aligned oligopeptide.

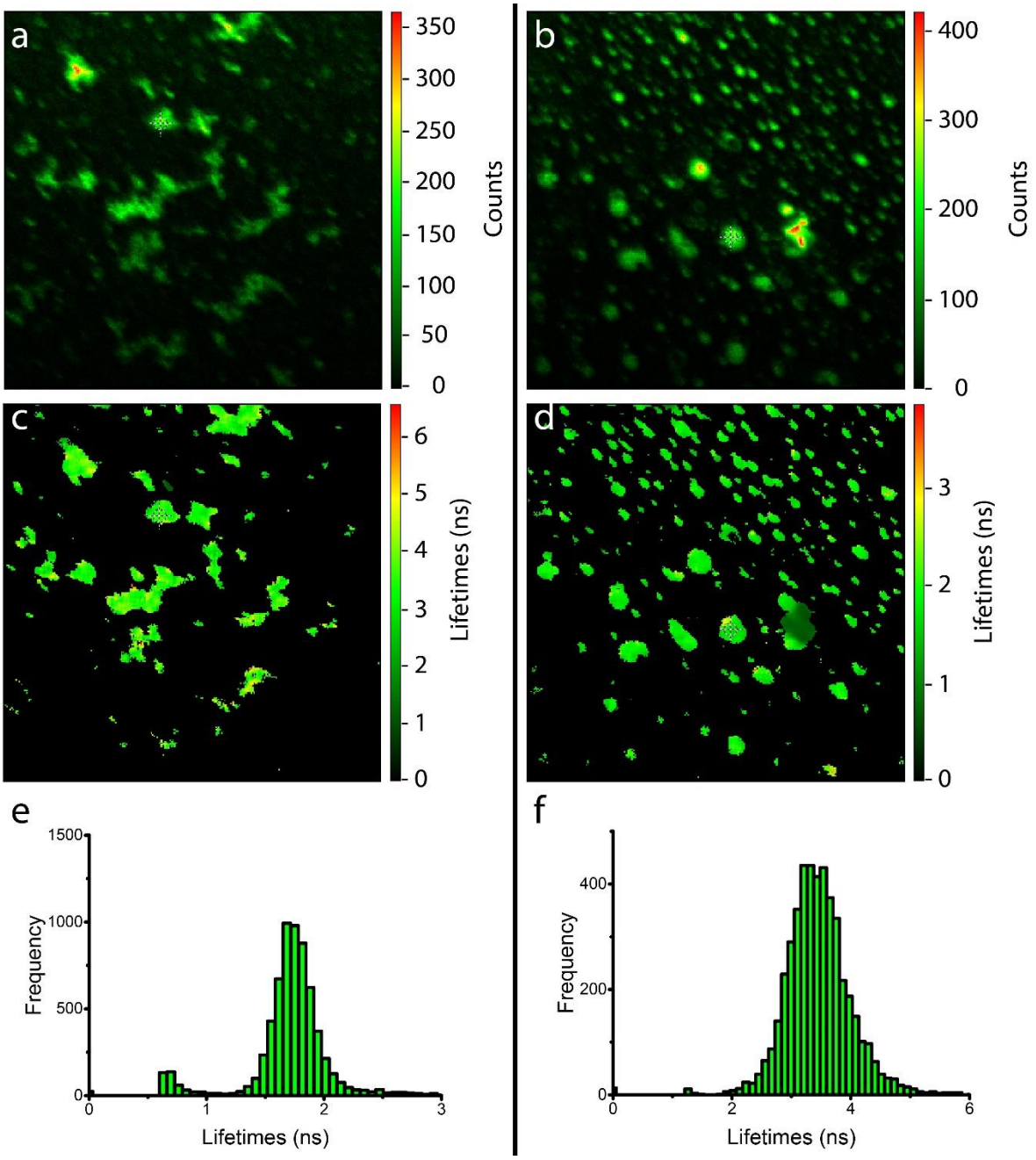

Figure 2.15 Fluorescence lifetimes of PDI assembled material collected from effluent streams in microdevices without and with chevrons. (a) and (b) show fluorescence intensity maps of collected aligned oligopeptide from a microdevice (a) without and (b) with chevrons. (c) and (d) show fluorescence lifetime maps of collected aligned oligopeptide from a microdevice (c) without and (d) with chevrons. (e) and (f) show histograms of fluorescence lifetimes for (c) and (d) respectively. In all cases, nearly Gaussian distributions of fluorescence indicate highly uniform aligned oligopeptide.

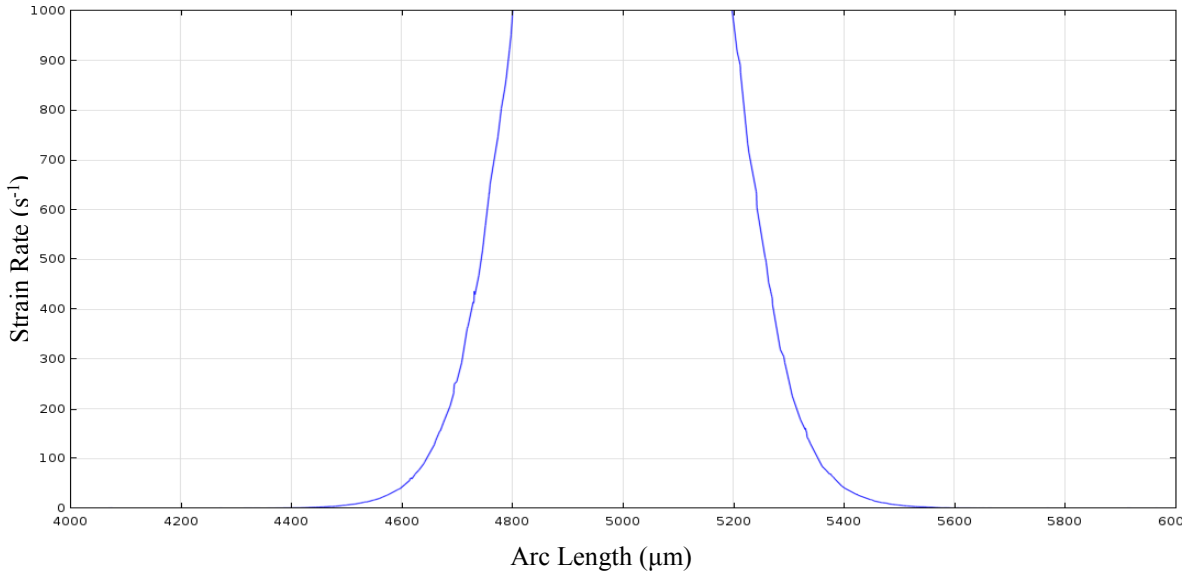

Figure 2.16 Strain rate along the center of a cross-slot with center x = 5000 μm. Arc length is in units of microns and the cross-slot width is 400 μm, from 4800 μm to 5200 μm in the plot.

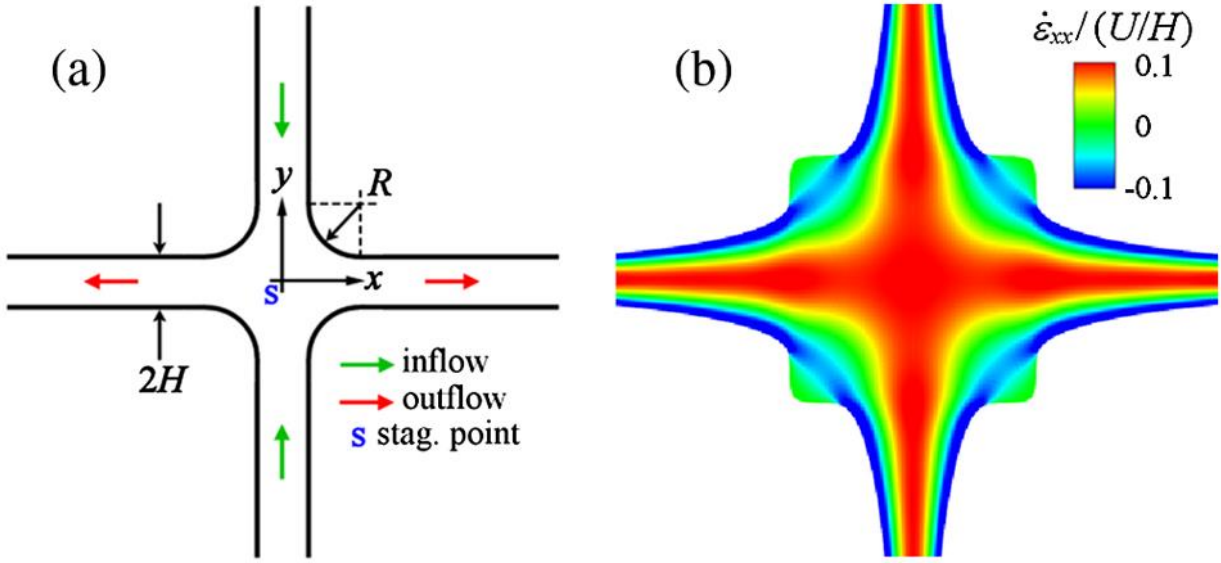

Figure 2.17 (a) Schematic representation of a cross-slot geometry, showing the coordinate system and characteristic dimension (H). (b) Strain rate field for numerically simulated Newtonian creeping flow in the optimized cross-slot geometry. Adapted from Haward et al. Phys. Rev. Lett. *2012 [80].*

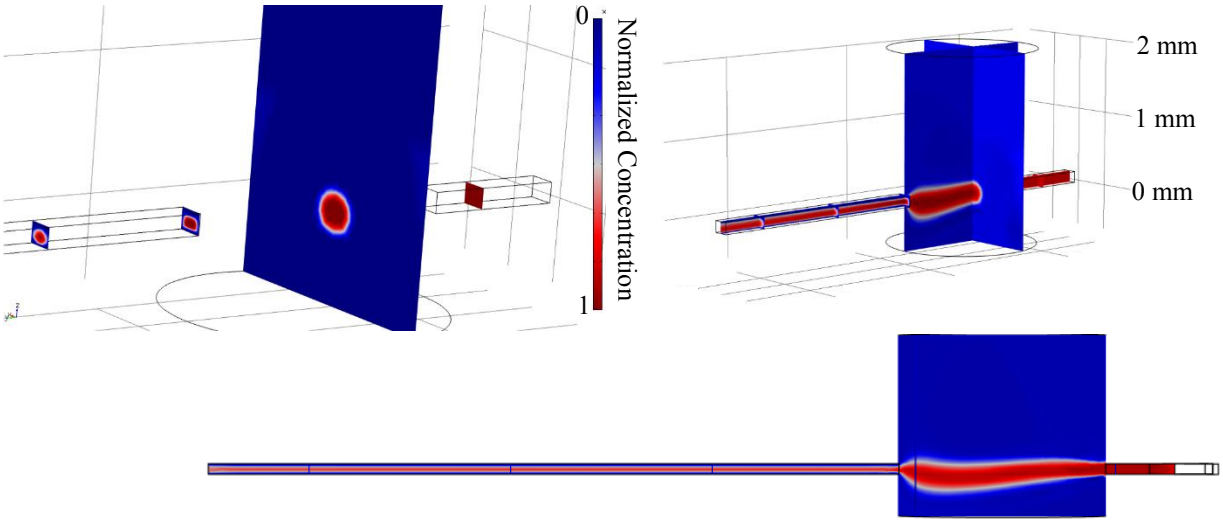

Figure 2.18 Single channel focusing design COMSOL simulation. Solution of species with normalized concentration (red) enters the focusing well from the right through a 100 µm x 100 µm channel and is coaxially concentrated in the exiting channel. Diagrams show concentration mapped onto a color scale of red meaning highest concentration and blue meaning lowest concentration.

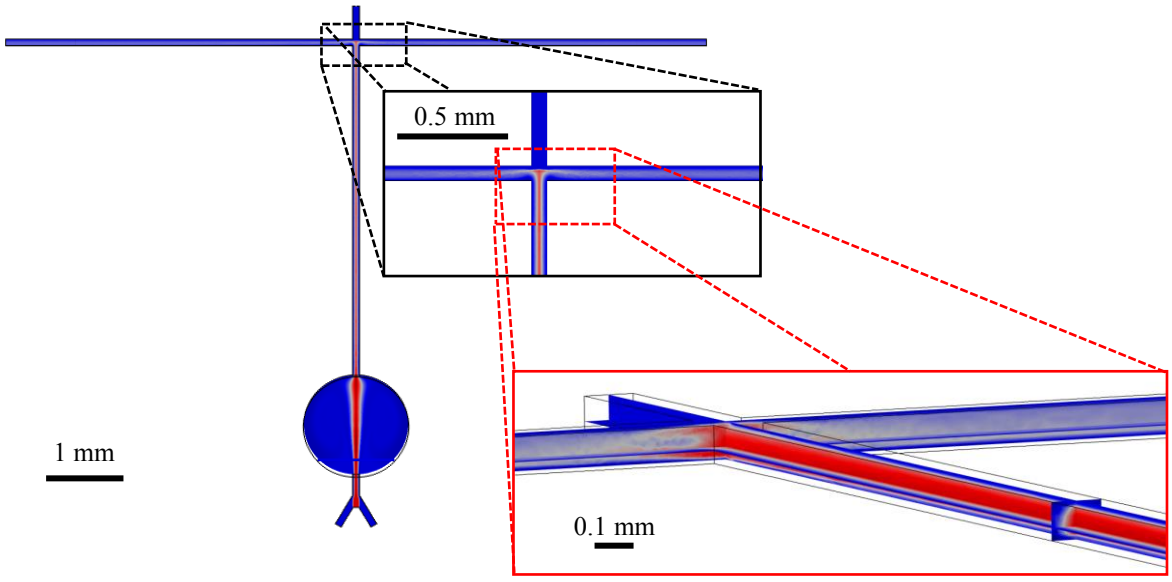

Figure 2.19 Cross-slot behavior of single channel focusing design COMSOL simulation. While vertical focusing appears to be maintained through the cross-slot (indicated by the remaining dark blue above near the ceiling and floor of the device), the vertical focusing seems to be significantly deteriorated after meeting the opposing stream.

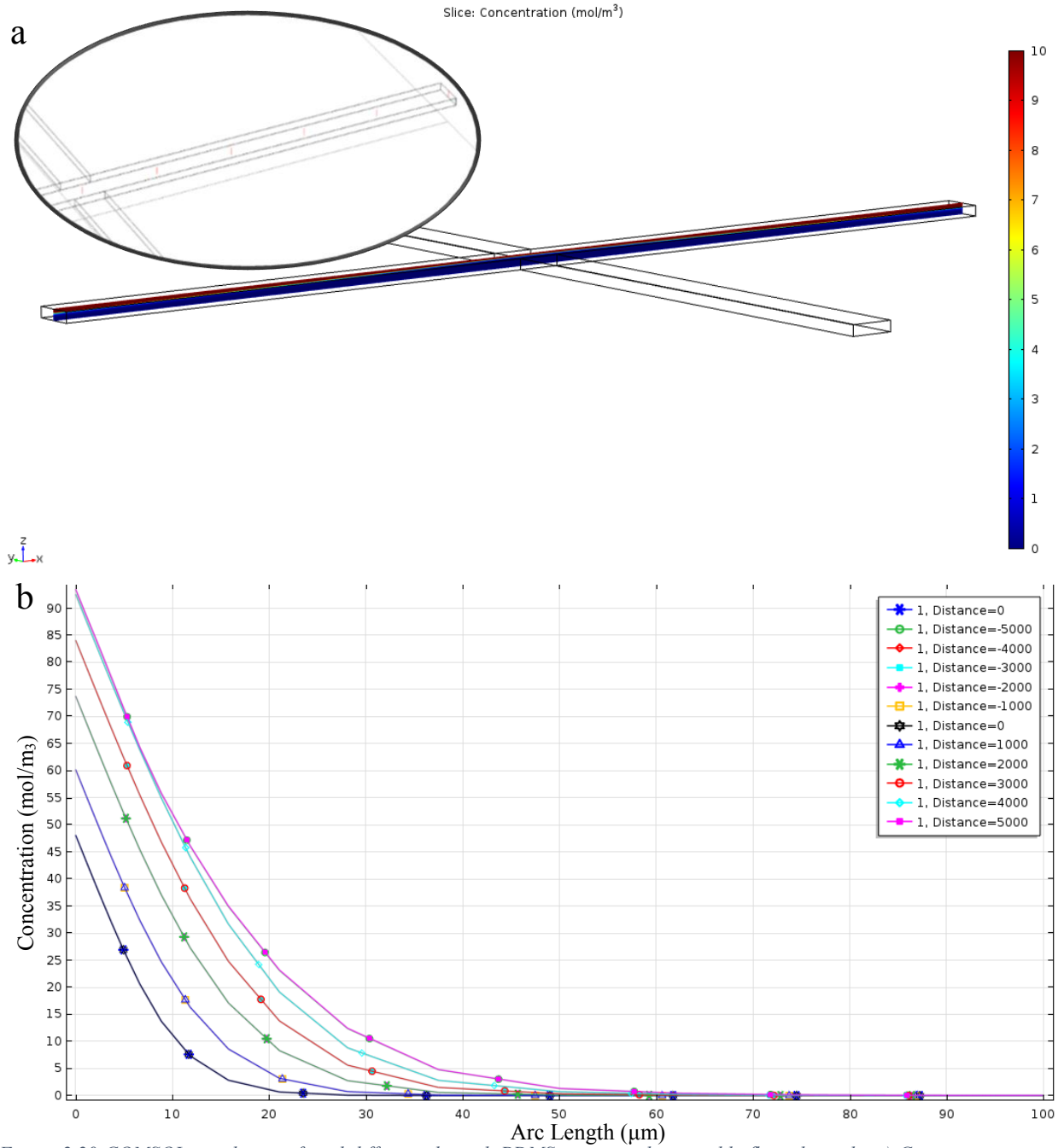

Figure 2.20 COMSOL simulation of acid diffusion through PDMS into peptide assembly flow channels. a) Concentration map displayed on cross-sectional plane of simulation volume. Inset: Red lines indicate locations of concentration measurements in (b). b) Concentration as a function of distance from ceiling to floor of device (in microns). Each line corresponds to line cut as shown in the inset above where the distance in the legend is the distance from the cross-slot center in microns.

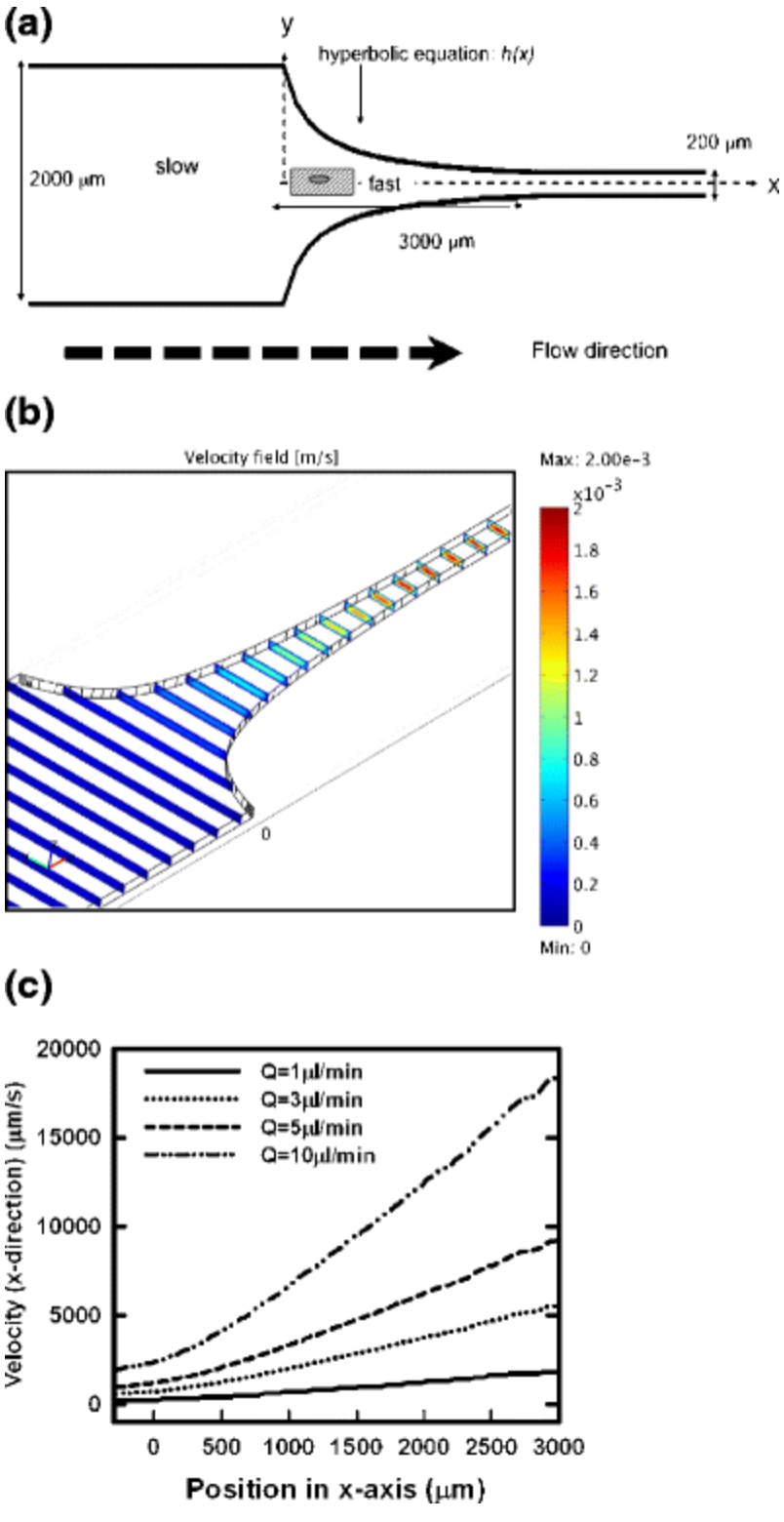

Figure 2.21 Tapered microfluidics for long channels with constant strain rate/linearly increasing velocity. Taken from Lee et al. Biomed Microdevices *2009 [85].*

CHAPTER 3:

DIRECT PRINTING FROM MICROFLUIDICS

INTRODUCTION

While the development of novel materials with enhanced properties for charge carrier transport, light conversion, and light emission is an important endeavor toward improving next generation organic semiconductor devices, the critical challenges of incorporating those materials into devices in a scalable and affordable manner cannot be neglected. Organic light-emitting diodes (OLEDs) have been particularly successful, gaining increasing market presence and effectively competing against established technologies such as liquid crystal displays. But organic materials have yet to make significant headway into the photovoltaic industry (OPVs), and flexible electronics still stand to benefit significantly from improvements in deposition resolution and morphological control of active materials. Furthermore, display technologies are pushing the limits of what can be achieved with conventional fine metal mask (FMM)-assisted vacuum evaporation as demand rises for larger areas and increased resolution [46].

Dovetailing nicely with the aforementioned challenges is the bourgeoning field of bioprinting. A wide variety of bioinks and printing methods—including droplet-based and extrusion-based approaches—are currently under development toward the goal of creating *in vitro* biological systems that optimally mimic their natural counterparts [43]. In fact, inkjet printing has been adapted from its traditional role in the graphic arts toward applications in bioengineering [43] and a variety of semiconductor electronics applications [45,88]. Inkjet printing's simplicity and

versatility combined with its high-resolution capability facilitate rapid prototyping and manufacturing without the poor thickness and roughness control of FMM-assisted vacuum evaporation or spin coating [45,48], ideally suiting it toward organic electronic and light conversion device fabrication. The π-bond-functionalized peptide materials we have investigated, in combination with the microfluidic devices we have developed for their continuous assembly and controlled alignment, are particularly well suited for integration with a printed deposition setup. The continuous assembly and flow characteristics of our device permit the high throughput manufacture of aligned material, a necessary prerequisite for conducting thorough material investigation through a large suit of techniques—including many described in this work—and for the ultimate scale up toward commercial manufacture of devices. As an added boon, material that is aligned in our devices can be directly flowed from the outlet to a print nozzle for direct writing on a substrate.

Our system spans both the challenges and opportunities afforded by printing biological and electronic materials. From high-resolution electrohydrodynamic jet (e-jet) printing to high-speed continuous jet modalities to the prolific, highly precise, and relatively simple drop-on-demand method, there are a variety of printing analogues available to match the specific ink and writing application desired [44,45]. In short, e-jet printing takes advantage of an applied back-pressure to bring ink to a metal-coated nozzle (which can be on the order of ten microns or several hundred nanometers). An electric field between nozzle and substrate pulls mobile ions to the droplet surface forming an equilibrium conical shape known as the Taylor cone. The electric field is modulated and at high enough fields, electrostatic stress surpasses surface tension and ink is ejected as droplets, a continuous jet, or many branched jets, depending on the field, flow rate, and fluid properties [44,89]. Continuous inkjet printing has the advantage of high speed and relative

immunity to clogging due to the continuous generation of droplets and the choice of volatile inks. This method writes by charging the ink and passing it through a controllable electric field to control the droplet deflection [45]. Finally, drop-on-demand printing is the method typically used in commercial printers. As in other methods, ink is maintained at the print nozzle by a balance of surface tension and internal and external forces, but in this case the ink reservoir pressure is increased in a controlled manner such that droplets are forced out when desired. This pressure control is typically achieved through either a piezoelectric plunger or micro bubbles created by local ink vaporization near an internal heating element [45]. In addition, surface energy relations and the choice of substrate and ink formulation are critical to achieving desired printing performance [43,45–48]. Water, which is the typical solvent used in our system, is incompatible with inkjet printing without the use of surfactants or other additives [43,45,48]. Ultimately, the choice of printing method, substrate wettability and other parameters, and ink rheology form a complex, interdependent optimization problem which is accomplished in practice through trial and error [45]. In this chapter I present a proof of concept demonstrating integration of the microfluidic device focused on in chapter 2 with an e-jet printing stage and controller for continuous assembly, alignment, and deposition of material under various conditions. Undoubtedly, a thorough investigation into printing this material should yield the correct parameters for the desire printing application; however, this optimization is best left off until we have determined the ideal devices and printing paradigms within which we would like to operate, and this determination should first be guided by more detailed material characterization such as follows in the succeeding chapters. The incorporation of microscale morphological control of continuously assembled organic material with a continuous printing framework presents exciting possibilities for future high-

throughput device fabrication. I am satisfied to present this demonstration as evidence of what can be achieved through future work.

METHODS

Given the very high resolution achievable with e-jet printing and the benefits of such high resolution to electronic applications, we chose to begin with e-jet printing. This investigation was dividing into three parts: 1. Compatibility of our material as an ink for e-jet and determination of an appropriate substrate. 2. Printing with a syringe pump-derived backpressure as opposed to the standard pneumatic backpressure. 3. Full device integration by supplying material and backpressure from the device outlet. Each step provided new insights into how best to print our material and the challenges that lie ahead.

Ink precursor synthesis

Sequence-defined synthetic peptides with π-conjugated cores were synthesized using solid phase peptide synthesis (SPPS), as previously reported [2]. The π-conjugated oligopeptides containing an oligo(p-phenylene vinylene) (OPV3), quaterthiophene (4T), or perylene-diimide (PDI) core were flanked by symmetric peptides with a primary amino acid sequence Asp-Phe-Ala-Gly (DFAG). The overall sequence of the π-conjugated oligopeptides the same except for the functional core and can be written as, for example, HO-DFAG-OPV-GAFD-OH, abbreviated as DFAG-OPV. In addition, PDI cores were synthesized with random side chain sequences consisting of the DFAG amino acids in no specifically controlled sequence. These materials are significantly

easier to synthesize and were thus best used to test experimental setups before using the sequence-defined peptides. All results are shown for the DFAG-4T and random sequence varieties.

Ink investigation for e-jet printing

Typical e-jet substrates are conductive materials such as doped Si or Si coated with gold due to the need for creating an electric field between substrate and print nozzle. However, given the optical properties of our materials, we also wanted a transparent substrate that would allow us to image and inspect printed samples on an inverted fluorescence microscope. Thus, we turned to indium tin oxide (ITO), a transparent conductive thin film material used in many commercial electronics including most touch screen devices, and we selected glass coverslips coated with ITO as the substrate (18 x 18 mm, #1.5, 8-12 Ω, Structure Probe Incorporated). The coverslips were fixed with the ITO side down on a grounded, five-axis stage using a vacuum pump with a line connected to holes beneath the stage. A pulled glass nozzle (World Precision Instruments), sputter-coated with a gold/palladium mixture, was held with a standoff height ~30 μm to ~50 μm and contacted to a voltage source which could be varied ±600 V relative to ground. Both the voltage source and the five-axis stage were connected to a computer running a LabView VI to coordinate printing and sample movement. All nozzles were treated for 10 minutes with either 0.1% perfluorodecanethiol (Sigma-Aldrich) in N,N-dimethylformamide (for metallic coated nozzles) or chlorotrimethylsilane (Sigma-Aldrich) vaporized in a vacuum chamber (for uncoated glass nozzles). Without these critical hydrophobic coatings adhesion would direct the ink up the nozzle side (Figure 3.1) rather than encouraging it to form droplets or a Taylor cone at the nozzle tip. Sample ink was placed in a syringe body with a luer lock connection to the nozzle and attached on the other end to an air pump for backpressure of 3-4 psi. We first used a standard silver ink to verify compatibility of ITO-coated glass with the e-jet. Due to the scarcity of peptide material

available, we troubleshot the system for peptide ink using DFAG nonsequence-defined peptide with PDI cores.

Syringe pump compatibility tests

After ink testing with the regular e-jet setup, we proceeded to attach a syringe pump system to the nozzle in lieu of the standard pneumatic backpressure. We used a single 10 ml glass syringe attached via plastic tubing to a luer lock attachment for the nozzle. Injection was controlled using a single Harvard Apparatus PHD ULTRA syringe pump holding a 10 ml syringe (SGE Analytical Science). We used nozzles with end diameters varying between 0.2 μm and 10 μm and flow rates ranging from 10 μl/min to 1000 μl/min while also varying the speed of the stage while printing between 10 mm/s and 1000 mm/s as controlled by the software. (It should be noted that despite the software allowing for a 1000 mm/s write speed, it appeared that the hardware had speed limit of ~200 mm/s which was not communicated to the software. For print substrate we also investigated regular #1.5 36 x 60 mm glass slides and filter paper.

Microfluidic device integration

Following optimization of the print parameters for device-compatible flow, a microfluidic device was set up as described in chapter 2 with the exception that instead of being mounted on a microscope stage with outlets draining to a collection reservoir, the device was situated to the side of the print stage with outlet tubing running to the print nozzle position. Printing was conducted both using pulled glass nozzles and by simply using the tubing outlet as a nozzle by positioning the end of the tubing directly above the print substrate. We also experimented with glycerol as an additive, mixing glycerol at 40% into the acid and the focusing water solutions.

Printed material characterization

In additional to optical photographs taken during printing, printed material was examined using a Zeiss LSM710 inverted microscope and imaged through a Zeiss Plan-Apochromat 20x objective (NA = 0.8). A Ti:Sapphire laser system (Mai-Tai, Spectra Physics) was used for two-photon illumination of the devices. Spectral information was collected using a QUASAR 34 channel spectral detector, consisting of two standard PMTs and a 32 channel PMT array.

RESULTS AND DISCUSSION

Using the metallic e-jet ink we were able to successfully print controlled lines. We could not, however, obtain repeatable results with our peptide ink. It was generally found that backpressure was either insufficient to allow electrohydrodynamic pulling of the ink or too great such that an uncontrolled jet of fluid was ejected from the nozzle. Occasionally, printing would work, likely due to ink contamination that modified its rheological properties. Thus, e-jet printing should work with these peptide solutions as inks given the correct choice of additives to allow high-resolution e-jet printing.

As it remains uncertain if the ultimate applications of these peptides will require the degree of resolution and control provided by e-jet methods, and given that our main goal for these experiments was to simply verify printability of material from the microfluidic device, we proceeded to attach a syringe pump system to the nozzle in lieu of the standard pneumatic backpressure, sacrificing the high degree of drop-on-demand control afforded by standard e-jet printing and investigating more facile methodology. Further motivation for this departure from e-

jet printing was the critical realization that any drop-on-demand printing is inherently incompatible with pump-controlled flow.

Pump-controlled flow with an incompressible fluid is unable to achieve a stable equilibrium of ink at the nozzle tip because when flow is stopped at the nozzle tip, additional material continues to flow toward the nozzle tip from farther upstream, leading to a monotonic increase in pressure until that internal pressure can overcome the atmospheric pressure and capillary forces keeping the fluid inside. Thus, pressure periodically builds and is released, creating a natural pulsatile ejection. This challenge could be overcome by switching to pressure driven flow mechanics instead of using syringe pumps. However, given the complexity of acquiring new equipment and debugging a new setup, we opted to choose a method more analogous to continuous jet printing, using the translating stage to direct writing rather than a varying electric field to deflect the ink stream.

Through an appropriate balance of nozzle size, flow rate and stage speed we were able to achieve lines as thin as ~10 μm and dot spacing as low as ~1/70 μm (Figures 3.2a-3.2c), and these write conditions can likely be further optimized. Watching the printing of larger lines with slower stage speed (~1 mm thick at 10 mm/s) we were able to observe that continuous lines were flowing out of the nozzle and adhering to the surface as a continuous line and quickly beading up into drops on the surface, resulting in printing like that seen in Figure 3.3a. This is likely due to a surface energy that is too high to allow adhesion to counteract cohesive forces in the printed solution.

The surface energy considerations are particularly interesting to this mode of printing and likely explain the observation that even when operating in a flow regime such that drops of ink periodically formed beads and fell from the nozzle, the frequency with which drops formed at the

nozzle was lower than the frequency of droplet spacing on the surface. Moreover, the highest flow speeds did not yield the highest printing resolution (Figure 3.3). During the transition from dripping to jetting modes [89] the deposited droplets change from regular sizing and spacing to more erratic deposition, although this may only be if the surface is far enough away from the nozzle outlet such that the Rayleigh limit is reached and the jet breaks up [43,45,89]. Ink properties could also be adjusted to maintain droplet integrity and negative effects of splashing behavior at higher speeds [43]. We also observed that ensuring a good hydrophobic coating on the print nozzle was essential for obtaining fine printing resolution with drops of regular size and spacing. It was also notable that turning corners when writing more complex designs results in larger droplets, imposing higher limit on resolution than would be expected by regular line widths. Notably, the large droplets only form when the stage changes direction and not when lines overlap, indicating that the larger droplet formation is less a function of interdrop cohesion and more related to the energy dynamics between the tip and substrate via the ink (Figure 3.3d). Thus, it appears that droplets are actually pulled off the nozzle by the surface as the surface moves below the dripping nozzle in a complex interplay between water-water, water-nozzle, and water-surface energies.

One observation which has eluded explanation is that nozzles appear to clog irreversibly after a certain pressure is reached. This occurred for all nozzles below 5 μm. For any nozzles in this size regime, there was a brief lag after flow was initiated at the syringe before outflow from the nozzle would commence, instantly in the jetting regime—as opposed to larger nozzles which would have an intermediary dripping regime. If flow was allowed to continue unhindered, the jetting would stop on its own on the order of several minutes, with smaller nozzles taking less time and 0.2 μm nozzles stopping flow usually within the first minute. Following this cessation of outflow, either the nozzle to tubing luer lock coupling would burst or the pump would stop and

warn that it had reached maximum torque. Any such nozzle could not be made to flow again. Furthermore, except for the occasional 2 μm diameter nozzle, for all instances in which flow was manually stopped by shutting off the pump after having achieved jetting, flow through the nozzle tip could not be reinitiated.

In addition to achieving very high dot resolution, we were able to print uninterrupted lines of the aligned material exiting the device. Such continuous lines are particularly desirable for maintaining peptide alignment from the device onto the printed structure. While continuous lines could be achieved using the widest nozzle diameters printing on glass, these lines did not have well controlled widths and could not be achieved with regularity (Figure 3.4), indicating a very high sensitivity to ink contaminants and/or variations in surface energy. Printing directly from the device outlet tubing onto filter paper, however, we were able to achieve continuous lines on the order of the tubing outer diameter (~1-2 mm) at 100 μl/min with a stage moving 10 mm/s (Figure 3.5). When printing on glass, however, the trailing end of lines would preferentially follow the printing direction rather than adhere to the surface.

An investigation of the theory behind printing and the associated literature revealed that ideal printing likely occurs in a parameter space of ideal drop formation defined by the inverse Ohnesorge number, also known as the *Z* parameter. The *Z* parameter can also be thought of as the Reynolds number divided by the square of the Weber number, or

$$Z = \frac{\sqrt{We}}{Re} = \frac{\eta}{\sqrt{\gamma \rho L}} \qquad (3.1)$$

where η is the dynamic viscosity of the fluid, γ is the surface tension, ρ is the fluid density, and ideally $1<Z<10$ [45]. The *Z* parameter of a regular aqueous solution is ~300, and the same solution

with a viscosity closer to that of glycerol would be much less than 1. Thus, it is unsurprising that much of the literature regarding the printing of proteins—which often must be kept in aqueous solutions—implements addition of 40% glycerol to shift the ink's rheological properties into the ideal printing realm [43,45,90–92]. We found this composition to yield a dramatic improvement in both filter paper and glass printing. On filter paper, lines smaller than the tubing outer diameter could be printed faster, 100 μl/min at 20 mm/s, and with very evenly sized lines. Furthermore, this method made printing on glass possible, although with a greater flow rate of 500 μl/min at the same stage speed of 20 mm/s (Figure 3.2d).

Imaging of the samples printed on filter paper (Figure 3.5) were made difficult by the absorptive spread of the liquid into the paper, resulting in a gradual transition between printed line and substrate background. The lines printed on glass, however, had clearly defined edges.

CONCLUSIONS AND FUTURE WORK

We hypothesize that an appropriate balance of surface energy and surface temperature should facilitate printing of continuous lines even with pure peptide solution, however the use of glycerol or similar additives will certainly improve this optimization. Increasing the hydrophilicity of the surface should encourage printed lines to remain intact by adhesion dominating over cohesion. However, using slides that had been treated with an oxygen plasma to increase the surface hydrophilicity resulted in the opposite extreme: printed lines rapidly spread to cover the entire slide. Furthermore, our earlier experiments with the e-jet modality exhibited drops so small as to evaporate on the order of seconds. For the larger droplets obtained during continuous jet-

style printing and due to the increased flow required for printing solution with 40% glycerol, a heated stage could make it easier to strike a right balance between adhesion and cohesion to allow continuous lines to persist until the ink evaporates and to have that ink evaporate as quickly as possible. There is ample room for experimentation in this regard as the peptides have been demonstrated to remain unaltered at temperatures as high as 200 °C.

An alternative tact that could significantly improve the consistency and confinement of printed lines would be to prepattern the surface with be hydrophilic where lines are desired and hydrophobic elsewhere. There are wide variety of chemical treatments available to increase the hydrophobicity of a substrate surface to varying degrees. An e-jet metallic tip could be used as the write nozzle, first passing over the substrate in the pattern that one wishes to print, not flowing ink but maintained at a high voltage so as to ablate the hydrophobic coating only in the vicinity of the pattern. Then nozzle would then make a second pass exactly as before but with the voltage turned off and the ink flowing. Along a similar vein, the surface energy could be greater controlled to test for factors such as relative humidity by enclosing the print setup in a controlled environment.

As demonstrated repeatedly throughout the literature, any printing system has many knobs to turn, including but not limited to ink rheology, printing mode, print speed, and surface energy. All these parameters must be calibrated through systematic trial and error in order to use a desired ink or to achieve a desired print speed or resolution on a chosen substrate. Modifying any of these goals alters the constraints of the problem and requires a different optimization with potentially vastly differing properties. We have thus refrained for placing excess emphasis on optimizing any particular printing regime for our aligned peptide assembly devices, finding it prudent to first determine the printing goals. What's more, the goals for how to print this aligned peptide will depend on its intended uses, which in turn depend on a more thorough characterization of the

material such as follows in the succeeding Chapters. We have herein demonstrated the ability to not only control the assembly and alignment of semiconducting synthetic peptides using a microfluidic platform, but also to directly print that material as it is synthesized in a continuous manner compatible with high throughput modalities. We have shown a variety of possible routes toward optimizing this printing process for one class of peptides. The microfluidic system can also be extended toward any chemical system where the designer would like to control the microscale morphology and, significantly, would like to do so in a continuous manner with high throughput deposition and patterning.

FIGURES

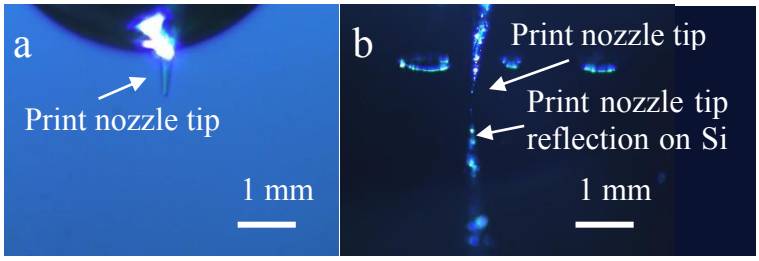

Figure 3.1 Optical micrographs showing impact of hydrophobic coatings. a) Adhesion-induced drop migration due to poor hydrophobic coating. Hydrophilicity can cause droplets to adhere above the nozzle tip. b) With proper hydrophobic coating, droplets should form at the tip and completely fall off, leaving the nozzle clean as in the image to the right.

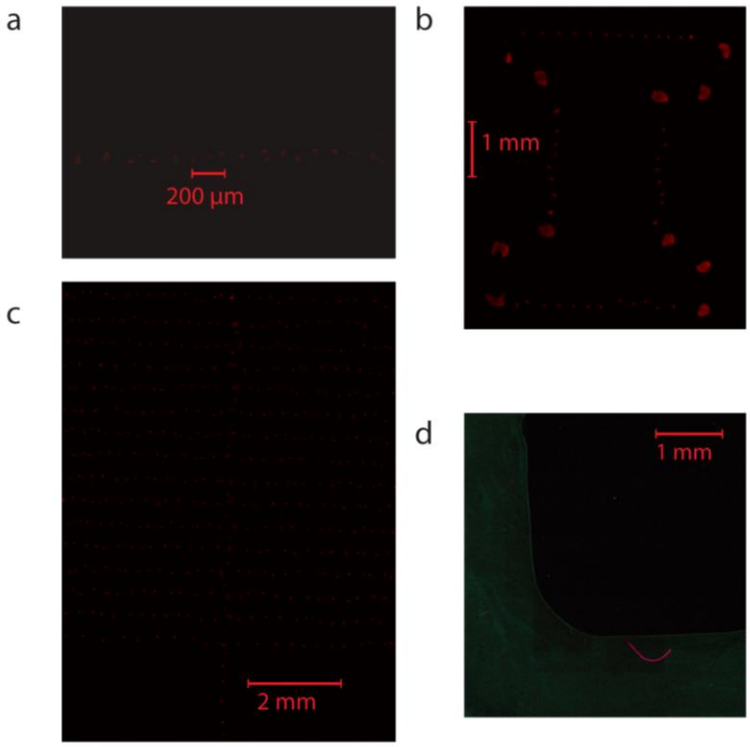

Figure 3.2 Results printing with fluorescent peptide. a) The best resolution achieved was through using material flowing through a 2 µm or smaller tip before clogging occurred. b) Complex shape writing is possible but resolution is limited by changing stage direction as indicated by larger drops at the corners of the block "I." c) Consecutive rows of relatively high resolution peptide printing. d) Printing results of assembled peptide from the microfluidic device with 40% glycerol on glass.

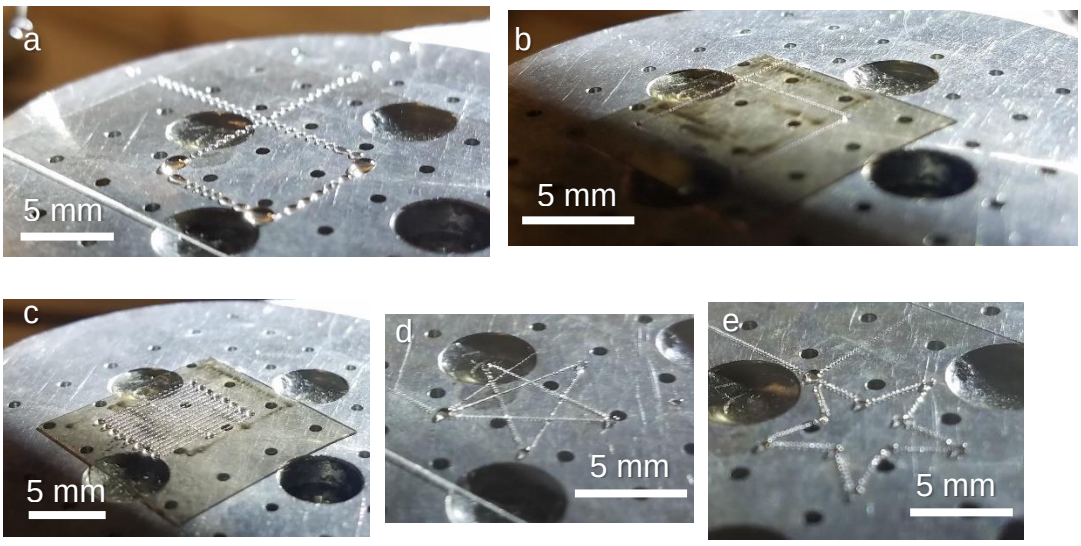

Figure 3.3 Comparison of printing results at different flow and stage speed ratios and in different patterns with 10 µm tips. a) Non-optimized droplet printing. b) Well optimized droplet printing with droplets very regularly spaced and sized. c) Rastered lines under the same parameters as (b) yield many large droplets at each point where the stage changes directions. d & e) Two star patterns written under the same parameters as (b) but with different print directions indicate the potential for writing complex patterns. The positions of the large droplets indicate that their formation is related to the energy dynamics of pulling fluid off the nozzle droplets rather than cohesion pulling droplets together after printing.

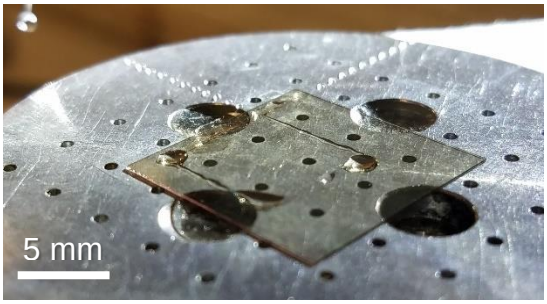

Figure 3.4 Uninterrupted line printing. Using 40% glycerol allows printing of continuous lines rather than separate droplets.

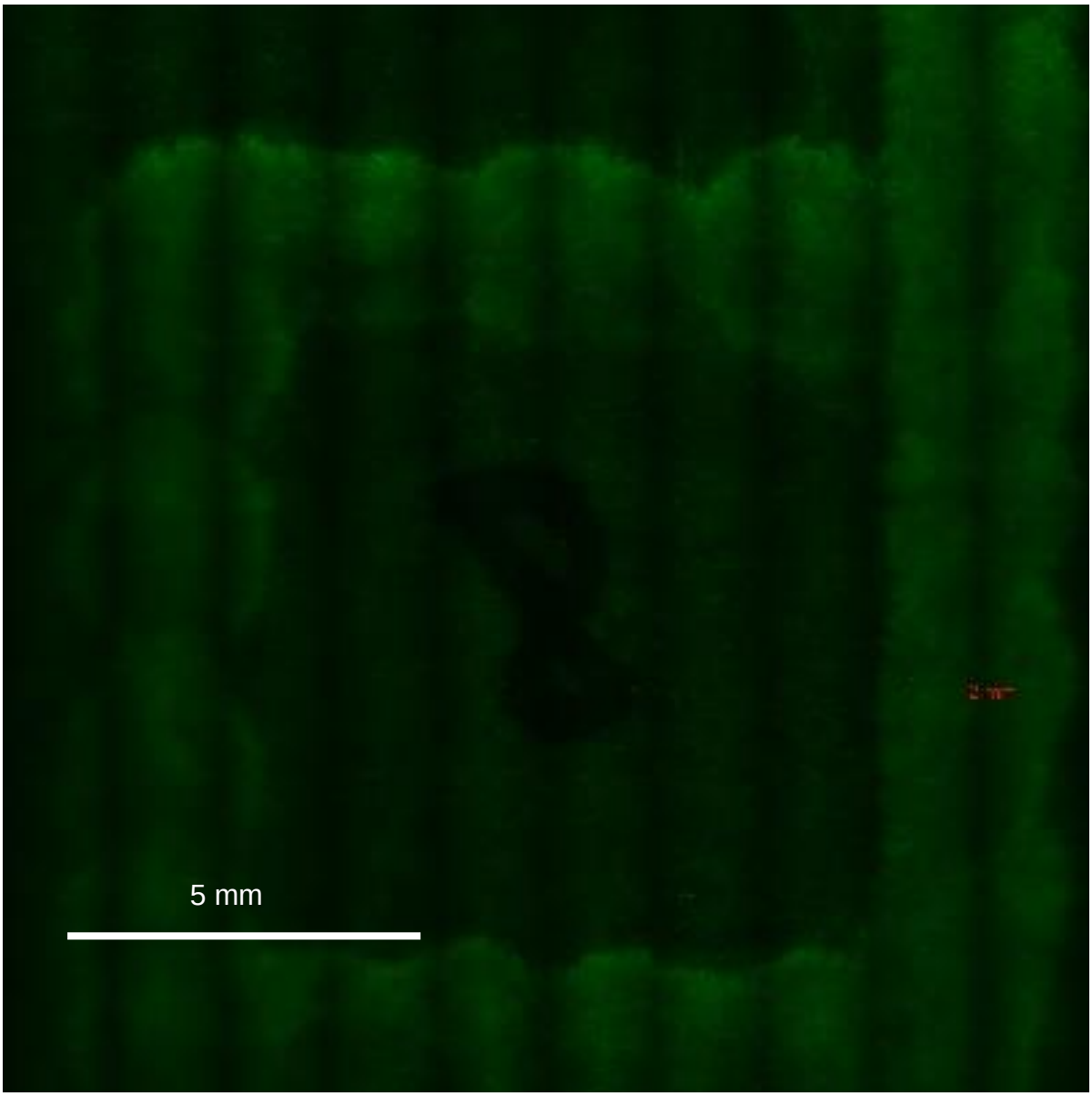

Figure 3.5 Continuous line printing on filter paper. Composite of 10 x 10 images showing a full printed square of fluorescent peptide on filter paper.

CHAPTER 4:

FLUORESCENCE CORRELATION SPECTROSCOPY

An important step in controlling biomimetic amyloid systems is understanding the self-assembly reaction kinetics. We are interested in a family of such materials characterized by symmetric sequences of amino acids flanking a π-conjugated functional core. Many of these materials rapidly self assemble into long fibers upon protonation in an acidic environment. Despite extensive investigation of these materials' properties, little is yet understood regarding their reaction kinetics. Based on previous studies we have chosen DFAG-4T-GAFD as a representative system and conducted molecular dynamics simulations, demonstrating that not only is assembly triggered by lowering a solution's pH, but also even in non-protonating environments some degree of aggregation is thermodynamically favorable. These results are consistent with findings for other systems such as DFAG-OPV-GAFD. The nonprotonated aggregation also appears to be concentration dependent, occurring at concentrations of 100 nM and above. Single molecule measurements using fluorescence correlation spectroscopy provide experimental support for these computational predictions. We find evidence of spontaneous aggregation in aqueous solutions of peptides with concentrations as low as 100 nM; however, 10 nM solutions appear to be homogeneous solutions of unassembled monomer. These results indicate that the simplest explanations for kinetics of acid-mediated assembly—protonation-induced nucleation by monomeric addition followed by subsequent stages of aggregation and elongation—are inappropriate in this system. In fact, the system only exists as pure monomer in very low concentrations, nucleation actually occurs in the absence of protonating elements at concentrations

typically used for experiments Furthermore, triggered assembly must be considered to operate outside the domain of nucleation-dependent models.

INTRODUCTION

Understanding the specific kinetics of assembly in amyloid-forming systems is a valuable step toward understanding how best to control such systems. This is especially true in bio-inspired materials attempting to harness the potential of natural self-assembly to create functionalized devices with microscale or nanoscale order. Such biomimetic materials are researched for, and implemented in, a wide suite of applications ranging from cell growth and bioengineering [2] to photovoltaics [5]. The synthetic oligopeptide system consisting of a π-conjugated core flanked by symmetric sequences of amino acids has been explored in various permutations [2,4,12,14,93], including recent work exploring the acid-mediated assembly of DFAG-π-GAFD, where π can be one of various π-conjugated systems including quaterthiophene (4T), oligo(p-phenylene vinylene) (OPV3), and perylene-diimide (PDI). The π-conjugated cores of these materials can be tuned for the specific applications desired, such as making p-type semiconductors with 4T and OPV3 cores and n-type with PDI. Upon introduction to an acidic environment the protonated aspartic acids on the outer ends of the unassembled oligomer interact via van der Waals forces to form beta sheets. Ideally these unassembled units would continue to stack in a ladderlike fashion with a helical twist (Figures 4.1A & 4.1B) ultimately forming long fibers. Although these fibers can be seen experimentally (Figure 4.1D), very little is understood about their assembly dynamics. Theoretical models suggest a variety of mechanisms by which these amyloid structures may form, with the

classic example being an initial nucleation stage followed successive elongation stages [49,50]. However, reaction speed upon introduction of acid to this system has made characterization of the initial stages difficult.

In an effort to better understand the smaller-scale, early time assembly behaviors of DFAG, we have previously employed molecular dynamics simulations to probe the smaller-scale early time assembly behaviors of DFAG-OPV-GAFD peptides. Simulations have analyzed the impact of peptide symmetry [16], concentration [51], pH, and fluid flow [52] on peptide assembly. Our simulations enabled probing of the thermodynamics, kinetics, and morphologies of peptide aggregation [49,50]. We observed a strongly favorable free energy well at ~15 k_BT for the dimerization of DFAG-OPV3-GAFD peptide in a low pH environment. Addition of each subsequent monomer was found to yield a further decrease in free energy of ~25 k_BT, indicating that monomeric addition of peptides beyond dimerization is increasingly favorable. Our simulations suggest that aggregates at the free energy minima exist as well-aligned stacks with significant π-stacking between cores. In addition, simulations probing the dynamics of assembly of protonated peptides beginning in the monomeric state indicated that peptides rapidly coalesce into spherical micelle-like structures, and then structurally ripen to form the well-ordered β-sheet stacks observed in free energy simulations on times scales larger than several tens of ns. The spontaneous formation of these self-assembled stacks in free energy simulations and the increasingly favorable changes in free energy upon further aggregation agree well with the suspected amyloid-like nucleation and monomeric addition and elongation into larger 1-D fibers that have been observed experimentally [4,12,14,53].

Surprisingly, simulations for high-pH conditions also exhibited favorable dimerization with a change in free energy of ~4k_BT due to hydrophobicity, π-stacking, and dispersion

interactions [53]. Furthermore, the formation of higher order structures such as pentamers remain thermodynamically favorable with free energy change of ~5k_BT, albeit aggregation is naturally decreasingly favorable with larger aggregates as negative charges increase in concentration over the growing oligomer [53]. These simulations suggest a paradigm in which early-stage assembly consists of light aggregates which rapidly assembly and subsequently reorganize into more thermodynamically stable beta-sheet-like structures, which in turn grow and elongate as further oligomeric units are added and structurally relaxed in a low-pH environment. *The high-pH assembly predicted furthermore implies that when acid-mediated assembly is induced, the peptide precursor solution exists in a pre-nucleated state, significantly impacting how one should view the assembly kinetics in acid-mediated assembly experiments when analyzing through the lens of amyloid formation dynamics.*

While most of the low-pH simulation observations support what has already been observed experimentally, other collaborators have only recently demonstrated support for the possibility of spontaneous assembly at high-pH [54]. These recent microrheological observations demonstrate peptide assembly only down concentrations of 0.1 mM with no evidence of assembly below that concentration. This lack of experimental evidence is in large part due to the length scales and numbers of molecules under consideration. Microrheology relies on large, brightly fluorescing probes to correlate observed fluorescence with material properties. The microrheologically observed critical fiber formation concentration is likely due to limitations of the technique rather than actual physical phenomena. Thus, we have turned to fluorescence correlation spectroscopy (FCS), a single-molecule technique that allows us to directly detect peptide fluorescence to measure molecule size and to distinguish between low order aggregates of different sizes. Additionally, as our experiments utilized a close cousin of the previously modeled peptides—

DFAG flanking sequences with a quaterthiophene instead of oligo(p-phenylene vinylene)3—we conducted additional simulations specific to the currently used peptide in order to verify consistency of the computationally observed phenomena.

METHODS

Experimental

Fluorescence correlation spectroscopy allows single-molecule observation by confocally focusing a laser spot down to a femtoliter-scale volume (Figure 4.1C). As fluorescent molecules diffuse into and out of this volume, the fluctuations in fluorescence intensity observed can be time-correlated to gain information about the diffusion characteristics of the molecular species. Aggregates at different stages of self-assembly will of course have different sizes and mass, differences which are detected as they pass through the beam spot (Figures 4.1B & 4.1C), and can be extracted from the correlation data. The intensity fluctuations are related by means of a normalized autocorrelation function $G'(\tau)$:

$$G'(\tau) = 1 + \frac{\langle \delta F(0) \delta F(\tau) \rangle}{\langle F \rangle^2} \qquad (4.1)$$

The autocovariance of $F(t)$ is the autocorrelation function of the fluorescence fluctuations and is conventionally referred to as the "autocorrelation function," $G(\tau)$:

$$G(\tau) = \frac{\langle \delta F(0) \delta F(\tau) \rangle}{\langle F \rangle^2} \tag{4.2}$$

where *F(t)* is the fluorescence intensity at time *t*, and τ is the time between measured fluorescence events. The δ refers to the fluctuation in intensity relative to the average value. Further, the measured intensity can be written as a function of brightness, *B*; collection efficiency, *CEF(r)*; excitation intensity, *I(r)*; and the distribution of fluorophores, *C(r,t)*:

$$F(t) = B \int CEF(r) I(r) C(r,t) dV \tag{4.3}$$

For conventional one photon FCS, the confocal volume is isolated using a pinhole. The experimental volume can be well approximated as a three dimensional (3-D) Gaussian ellipsoid with semi-minor axis—radius—*r* and semi-major axis—length—*l*. Assuming isotropic translational diffusion in such a volume for the distribution of fluorophores and plugging Eq. (4.3) into Eq. (4.2) yields an autocorrelation function:

$$G(\tau) = \frac{1}{N}\left(1 + \frac{\tau}{\tau_D}\right)^{-1} \left(1 + \left(\frac{r}{l}\right)^2 \frac{\tau}{\tau_D}\right)^{-1/2} \tag{4.4}$$

where *N* is the average number of particles in the observation volume, with 1/*N* being *G(0)*, and τ_D is the diffusion time for the volume:

$$\tau_D = \frac{r^2}{4D} \tag{4.5}$$

The average fluorophore concentration can also be gleaned from N via the relation

$$\bar{C} = \frac{N}{V_{\text{eff}}} \tag{4.6}$$

where V_{eff} is the effective volume. This effective volume is different from the actual volume for an ellipsoid in that it represents the observation volume—$\pi^{3/2}r^2l$ for a 3D Gaussian—and it is critical to know this geometry to extract an accurate measure of the diffusion coefficient, D, from the diffusion time using Eq. (4.5). Thus, all FCS experiments are first calibrated by measuring the effective volume via a fluorophore with known diffusion coefficient. We used a ~1 nM aqueous solution of Rhodamine 110, with known $D \approx 340$ $\mu m^2 s^{-1}$ to calibrate the system each new day an experiment was run (see Supporting Information) [94,95]. Other phenomena leading to signal depletion such as inter-system crossing to a triplet state, can be accounted for by incorporation into the correlation function. In general, these effects are negligible to the phenomenon of interest and can be filtered out through time-bracketing of analyzed data [96–98]. Furthermore, as the effects of multiple species on the autocorrelation function is linear, multiple components can be accounted for by summing over all species such that

$$G(\tau) = \sum_{i=1}^{m} a_i \left(1 + \frac{\tau}{\tau_{Di}}\right)^{-1} \left(1 + \left(\frac{r}{l}\right)^2 \frac{\tau}{\tau_{Di}}\right)^{-\frac{1}{2}} \tag{4.7}$$

and a_i represents the relative amplitude of each species.

Finally, while control of the confocal volume can be achieved using pinhole optics, two-photon illumination is often a better alternative when available. (Here the system is naturally confocal with volume defined by the nonlinear excitation dependence. Only molecules near the opticical excitation focus contribute to the detected signal. No pinhole is needed.) Operating at such low concentrations increases the importance of each fluorescence photon and inclines the experimenter to use a larger pinhole aperture to reject fewer photons; however, as aperture increases so does the danger of optical artefacts skewing observations in ways that are mitigated by two-photon illumination, such as the false appearance of multiple species [99]. The illumination volume of a two-photon system is also advantageously smaller than the one photon case and is more accurately modeled by a 2D Gaussian in the plane of observation but a Lorentzian in the axial direction. It should be noted, though, that the Gaussian-Lorentzian model is a complicated solution without a closed form equation and can usually be approximated well enough by a 3D Gaussian for the sake of data analysis [100].

All FCS experiments were performed on a Nikon Eclipse Ti inverted microscope equipped with an ISS Alba FCS scanning mirror module, using a 60x (1.2 NA) water immersion lens. Pinhole confocal experiments utilized a 470 nm diode laser with 3 mW power at the objective and two-photon excitation was accomplished using a mode-locked Ti:Sapphire laser system (Tsunami and Millennia, Spectral Physics) with 80 MHz pulse repetition rate and ~100 fs pulse width. The system has both a TCSPC board and ISS FastFLIM card for time-tagged-time-resolved data acquisition. Autocorrelation functions were analyzed using the ISS Vista software. Samples were contained in μ-Slide 8-well glass slides (Ibidi). Wells coated with bovine serum albumin (BSA) or with aminosilane were compared to uncoated slides with no significant difference found. Thus,

uncoated well slides were used for all experiments. Due to limitations of detectable fluorescence intensity, peptide concentrations below 10 nM were not investigated.

Computational

In considering the reactions under observation, we note that for the reaction

$$A + B \leftrightarrow AB$$

the equilibrium constant can be calculated as [101,102]

$$K^{\ominus} = Kc^{\ominus} = \frac{1}{v^{\ominus}\sigma_{AB}} \int_0^{r_b} dr\, 4\pi r^2 e^{-\beta F(r)} \qquad (4.8)$$

where σ_{AB} is is the symmetry number (2 for A=B, 1 otherwise), r_b is the center of mass cutoff distance below which an aggregate is considered to have formed, $\beta = (k_B T)^{-1}$, $F(r)$ is the potential of mean force at a center of mass separation value of r, and $c^{\ominus} = 1/v^{\ominus}$ is the standard number concentration. The equilibrium constant may be related to the concentrations of the reactants and product as

$$K^{\ominus} = \frac{c^{\ominus}[AB]}{[A][B]} \qquad (4.9)$$

where [X] is the number concentration of species X and $c^{\ominus} = 1/v^{\ominus}$ is the standard concentration. So, by combining Eqs. (4.8) & (4.9), given the potential of mean force (PMF) for the aggregation of A and B to form complex AB, we can predict equilibrium constants,

$$K = \frac{[AB]}{[A][B]} = \frac{1}{\sigma_{AB}} \int_0^{r_b} dr\, 4\pi r^2 e^{-\beta F(r)} \qquad (4.10)$$

For a system of monomeric self-assembly, by conservation of mass we have that the concentration of peptide in the system can be expressed as

$$[P] = [M] + 2[D] + 3[T] + \cdots \qquad (4.11)$$

where $[P]$ is the total peptide concentration, $[M]$ is the concentration of peptides that exist as monomers, $[D]$ is the concentration of peptides that exist as dimers, $[T]$ is the concentration of peptides that exist as trimers etc. From Eqs. (4.10) & (4.11) we then have

$$[P] = [M] + 2K_2[M]^2 + 3K_2K_3[M]^3 + \cdots \qquad (4.12)$$

where K_2 is the equilibrium constant for the formation of dimers by $M + M \leftrightarrow D$, K_3 is the equilibrium constant for the formation of trimers by $D + M \leftrightarrow T$, etc. Eq. (4.12) defines a polynomial in the peptide monomer concentration that can be solved for $[M]$ and from which all higher aggregate concentrations can be computed using the calculated values of K_2, K_3, etc. The equilibrium concentrations of aggregates heavier than six peptides is so low that the root of the polynomial is insensitive to truncation of the polynomial beyond the 6th term, so it is only necessary to compute equilibrium constants for the hexamers and lighter aggregates. We have verified the insensitivity of the polynomial solution by incorporating terms up to 200 employing extrapolated equilibrium constants, and find that the computed value of $[M]$ changes by less than 0.01%.

We use GROMACS 4.6.7 [103,104] to conduct all molecular dynamics simulations, with the AMBER99SB force field [105,106] and used the GlycoBioChem PRODRG2 Server [107] to obtain initial peptide geometries. Asp residues on either side of all peptides were fully deprotonated in order to simulate a neutral pH environment. We conducted explicit solvent

simulations in TIP3P water [108] with initial velocities generated from a Maxwell-Boltzmann distribution. Electrostatics were treated using the Particle Mesh Ewald scheme [109] with a cutoff of 1.0 nm and a 0.12 nm Fourier grid spacing. Lennard-Jones interactions were smoothly shifted to zero at a cutoff of 1.0 nm. Bond lengths were fixed using the LINCS algorithm [110], and Lorentz-Berthelot combining rules were used to determine interaction parameters between unlike atoms [111]. The system was integrated using the leap-frog algorithm with a 2 fs time step [112].

Energy minimization was conducted using the method of steepest descents until the maximum force on any atom was less than 1000 kJ mol^{-1} nm^{-1}. The system was then equilibrated in an NVT ensemble using a stochastic velocity rescaling thermostat [113] to a constant temperature of 298 K. Further simulations were conducted in an NVT ensemble using a Nosé-Hoover thermostat [114,115] with a time constant of 0.5 ps.

Following our previous approach [53] we also conduct molecular dynamics simulations in implicit solvent with a modified model that rescales interactions to more accurately match explicit solvent. Polar interactions between solute and solvent are treated with the Generalized Born model while nonpolar interactions are implemented with a solvent accessible surface area approximation [116]. An analytical continuum electrostatic (ACE) type approximation [117] with a value of 2.259 $kJ/mol.nm^2$ for the surface tension [118] is made in treating nonpolar interactions. We calculated Born radii using the method of Onufriev, Bashford, and Case with a relative dielectric constant of 78.3 and with the standard parameter set of $\alpha = 1$, $\beta = 0.8$, and $\gamma = 4.85$ [119]. Since the peptides are not neutrally charged, implicit solvent simulations are conducted without the use of periodic boundary conditions. Coulombic and Lennard-Jones interactions are smoothly shifted to zero at the large cutoff value of 3.4 nm for the sake of stability.

We utilized the method of umbrella sampling [120] to compute the PMF as a function of center of mass separation between peptide aggregates. To compute the PMF for the formation of an *n*-mer from an (*n*-1)-mer and a monomer, the initial geometry of an *n*-mer aggregate is obtained by stacking *n* peptides at a core-core separation of 0.45 nm. The system was first equilibrated using the method of steepest descents until the maximum force on any given atom was less than 1000 kJ/mol.nm. Initial velocities of atoms were then drawn from a Maxwell-Boltzmann distribution and the system was equilibrated for 20 ps with the positions of the cores restrained in an NVT ensemble at a temperature of 298 K using a Langevin integrator as a thermostat with a friction constant of 0.5 ps^{-1} [118], and for another 20 ps with unrestrained cores under the same conditions. The system was then simulated for 1.5 ns and the configuration at the end of each 0.5 ns served as the initial configuration for a series of three independent simulations. Each initial configuration was then pulled both closer together and farther apart at a rate of 0.04 nm/ps using a harmonic biasing potential with a spring constant of 1000 $kJ/mol.nm^2$ between the center of mass of (*n*-1) peptides and the center of mass of the remaining monomer. These simulations were run for a sufficiently long time to allow the monomer to reach a distance from the (*n*-1)-mer at which the two were no longer able to interact. From these three separate pulling simulations, we then conducted three different umbrella sampling simulations by utilizing configurations over the course of each pulling simulation as the initial geometries for the restrained umbrella sampling. Windows were selected at evenly spaced intervals of 0.1 nm, were restrained using the same harmonic potential as the pulling simulation, and were run for 20 ns each. The first nanosecond of each simulation at each window was discarded to allow the system to equilibrate. We then used the weighted histogram analysis method (WHAM) [121,122] to reconstruct the unbiased PMF. Statistical errors in each PMF were computed using 100 bootstrap resamples of the data, and

sampling errors were computed as the standard of deviation between each of the three umbrella runs. In each case, the $-2kTl\log r$ non-interacting entropic contribution to the PMF was removed in order to give the PMFs a well-defined plateau and in order to avoid double counting this entropic contribution which is already contained in the $4\pi r^2$ Jacobian of Eq. (4.8) [118,123].

RESULTS AND DISCUSSION

Computing the PMF for the formation of aggregates of sizes 2-6 by means of monomeric addition at neutral pH (Figure 4.2), we observe free energy changes favoring aggregation on the order of 10 k_BT in each case. The dimerization of two peptides exhibits the largest free energy change at $\Delta F = (-15.2 \pm 1.1)\ k_BT$, while larger aggregates exhibit smaller free energy changes, indicating a decreasing degree of favorability of aggregation. The decreasing favorability of aggregation with increasing aggregate size explains why peptide in neutral solution appears to be unassembled at typical experimental length scales. Nevertheless, the formation of larger aggregates remains thermodynamically favorable. Despite repulsion between negatively charged termini, the minimum free energy configurations for each aggregate size exhibit a high degree of core-core stacking. Aggregates of 4 or fewer peptides also display a high degree of alignment in this stacking and frequently adopt linear stacks of parallel peptides. Aggregates of 5-6 peptides often favor configurations of 2-4 peptides existing in the same well aligned linear stacks with the remaining peptides stacking with one another. These results indicate that hydrophobic and π-π stacking interactions between the conjugated cores mean that it is favorable for peptides to form

oligomeric aggregates even at neutral pH where the deprotonated Asp termini mediate substantial electrostatic repulsion.

From Eq. (4.8), the equilibrium constants for the formation of aggregates are computed from these PMFs (Table 4.1). Since K is related to the exponential of the free energy, propagation of the uncertainties in the PMF values yields errors in K that are larger than the computed values for K. In order to better quantify this uncertainty, we compute 90% confidence intervals for each equilibrium constant. Intervals are computed by randomly generating 10^6 PMFs by shifting each point on the PMF by the product of the error at that point with a single number randomly generated from a gaussian distribution of mean zero and standard deviation one. In this way, the variation in the estimated error in the value of the PMF as a function of r is maintained, while nonphysical discontinuities that would be obtained by generating a separate random number for every point are avoided. Each PMF is then integrated over the binding region to obtain 10^6 different values for each equilibrium constant, the middle 90% of which determines the confidence interval. We observe that the value of these equilibrium constants, in general, decreases significantly with increasing aggregate size, indicating a decreased propensity for the formation of heavier aggregates.

Table 4.1 *Equilibrium constants for the formation of an aggregate of size n from a tightly-bound (n-1)-mer and a monomer.*[a]

Aggregate size	Equilibrium constant, K (M^{-1})	Confidence Interval, (M^{-1})
2	1.8×10^{6}	$(5.1\times10^{5}, 6.4\times10^{6})$
3	6.6×10^{5}	$(1.2\times10^{5}, 3.9\times10^{6})$
4	4.7×10^{4}	$(4.9\times10^{3}, 4.7\times10^{5})$
5	2.8×10^{4}	$(3.9\times10^{3}, 2.1\times10^{5})$
6	1.0×10^{5}	$(9.7\times10^{3}, 1.1\times10^{6})$

[a]*The equilibrium constants are in units of M^{-1}, or, equivalently, are unitless with a reference concentration of 1 M (see Gilson et al. 1997) [102] for example). Errors are reported as a 90% confidence intervals due to the high variance.*

Despite the favorable PMFs, low overall peptide concentrations favor light aggregate distributions. From Eqs. (4.8) & (4.12), we calculate the predicted distribution of aggregate sizes in deprotonated peptides from the computed PMFs based on the overall peptide concentration (Figure 4.3). Errors estimates are obtained by randomly generating equilibrium constants from each 90% confidence interval obtained by the propagation of error PMFs as previously described. Each set of samples yields one value for the relative concentration of each aggregate size. We compute 10^{6} such samples and plot the mean and standard of deviation. We predict that at a concentration of 10 nM the vast majority of the peptide tends to exist as isolated monomers. In such a scenario, the loss of entropy in bringing two peptides separated by a large distance together to aggregate makes the formation of larger aggregates unfavorable despite the favorable peptide interactions. When the peptide concentration is increased to 100 nM we observe a significant shift in the distribution of peptide sizes that indicates an appreciable amount of aggregation of peptide into larger aggregates. Such a transition is in qualitative agreement with what is observed experimentally.

Measurements of peptide in aqueous solution at 10 nM reveal diffusion coefficients on average (300 ± 50) $\mu m^2 s^{-1}$ (Figure 4.4a, Table 4.2). These are consistent with particles on the order of 1 nm assuming the Stokes-Einstein equation,

$$r_h = \frac{kT}{6\pi\eta D} \tag{4.13}$$

provides a reasonable underestimate of particle size, where r_h is the hydrodynamic radius, k_B is Boltzmann's constant, T is the temperature, η represents the fluid viscosity, and D is the diffusion constant. As an added check, we utilize explicit solvent molecular dynamics simulations to compute the diffusion constant of the peptide monomer by means of the Einstein diffusion equation:

$$\frac{\partial\langle r^2(t)\rangle}{\partial t} = 2dD \tag{4.14}$$

where $\langle r^2(t)\rangle$ is the mean-squared-deviation (MSD) of the molecule as a function of lag time, and d is the dimensionality of the system. A 50 ns unbiased simulation is conducted, the first ns of which is ignored to allow the system to equilibrate. From this we compute the MSD as a function of lag-time, and the linear regime of the MSD is determined to occur for lag-times from 1 to 9 ns. The diffusion constant for peptide monomers is then computed to be (330 ± 10) $\mu m^2/s$ using the program g_msd [118], in good agreement with experiment. Furthermore, the measured concentrations for these diffusion coefficients are ~1.78±0.36 nM, which correspond reasonably well with the intended concentrations when achieved by manually pipetted dilutions.

Table 4.2 *Comparing values for 10 nM vs 100 nM.*[b]

Sample		D (um2/s)	C (nM)	Percent of Solution
10 nM Solution		191	2.29	
		320	1.42	
		317	1.59	
		288	2.14	
		338	1.48	
		325	1.75	
100 nM Solution	Species 1	3.78	0.0229	
		4.31	0.0563	
		4.05	0.0597	
		4.94	3.12	
		6.33	3.09	
		5.01	3.07	
	Species 2	0.125		85.7 %
		0.0193		77.0 %
		0.162		81.1 %
		651		49.1 %
		337		41.8 %
		446		40.8 %

[b]*Data from six FCS curves each are shown for 10 nM and 100 nM samples. The 10 nM data are fit with one species for each curve and thus show one value for each of the six curves under the diffusion coefficient (D) and concentration (C) columns. The 100 nM solutions are fit using two species, with one diffusion coefficient tabulated in each of the "Species 1" rows and the other in each of the "Species 2" rows. Meanwhile concentrations for the 100 nM data are tabulated for each dataset's species 1. And for each species 2, its percentage of the total solution is tabulated in the last column.*

Interestingly, peptide solutions of concentrations ten times greater, at 100 nM, can often no longer be fit to a 1-species autocorrelation model. Furthermore, when fitting data to 2-species models we find average diffusion coefficients ranging from ~0.1 to ~5 to ~500 $\mu m^2 s^{-1}$, often with the same species overlapping multiple datasets (Figures 4.4b & 4.4c). These correspond to particles ranging in size from monomeric to 1000 times larger coexisting within the sample volume. Thus, we are able to experimentally support computational predictions that at concentrations as low as 100 nM the peptides spontaneously assemble small aggregates even in the absence of a protonating acid solution.

The discrepancy in aggregate sizes between simulation predictions and experimental measurements is understandable given that this computational approach does not account for every possible method of forming aggregates. The method utilized in computing equilibrium constants implicitly assumes that *n*-mers are formed only by the addition of a monomer to a pre-existing, tightly bound (*n*-1)-mer; it does not allow for the possibility of a chain of weakly interacting, smaller aggregates despite the previously established importance of these alternate assembly pathways [49,50,124]. These predictions of aggregate sizes then only include tightly stacked aggregates, and thus we expect this treatment to be useful in quantifying well-aligned aggregates, but to underestimate aggregate sizes by ignoring the existence of a larger, weakly interacting network of peptide oligomers.

Finally, when acid is directly added to any of the aforementioned solutions the result is a rapid and dramatic fluorescence quenching and decrease in the $G(0)$ intercept of the autocorrelation curves, indicating a rise in measured concentration. While these effects are apparently contradictory—with quenching associated with assembly but assembly associated with decreased concentration—we are inclined to conclude that assembly occurs, given the known

phenomenon of quenching as a result of assembly and assembly being triggered or significantly catalyzed by the addition of acid. Meanwhile, an alternative explanation for the increased concentration is readily available in consideration of the decreased fluorescence signal. The decreased fluorescence intensity also dramatically lowers the signal to noise ratio, making it likely that the correlations observed are artefacts of the system rather than true events. For this reason autocorrelation fitting and derived parameters are not provided for these curves. Thus, the FCS data for these ultra-low concentration solutions nicely overlap with computational predictions, indicating that the peptide exists in a monomeric state in non-protonating conditions at concentrations of 10 nM and lower. While the rapidity of acid-triggered assembly has precluded the detection of any lag phase, computations in this work as well as coarser-grained simulation from collaborators corroborate the lack of any lag phase [51]. Simulation indicates that nucleation-dependent models are unlikely to accurately reflect this system's kinetics. Finally, experimental results from FCS indicate, in agreement with simulation, that assembly is not truly acid-triggered, rather it is acid-mediated, and the fibrils formed upon introduction of acid are beginning from a pre-nucleated state.

CONCLUSIONS

We have conducted molecular dynamics simulations to confirm the consistency of assembly behavior between previously computer DFAG-OPV3-GAFD peptides and their DFAG-4T-GAFD cousins. These simulations demonstrate that for both materials, not only is macroscopically observable assembly triggered by lowering a solution's pH, but also even in non-

protonating environments some degree of aggregation is thermodynamically favorable. In addition, simulation predicts a critical transition at or around concentrations of 10 nM for which entropic losses in uniting such distant monomers makes aggregation unfavorable despite the favorable interpeptide interactions. Single molecule measurements using fluorescence correlation spectroscopy provide experimental support for these computational predictions. We find that aqueous solutions of peptides in concentrations as low as 100 nM will spontaneously aggregate to form heterogeneous solutions with sizes ranging from monomeric to 1000 times larger. However, below 100 nM solutions appear to be homogeneous solutions of unassembled monomer. These results indicate that previously assumed paradigms of acid-mediated assembly in this system whereby monomer aggregates upon protonation were incomplete. In fact, the system only exists as pure monomer in very low concentrations, and under experimental conditions the untriggered solution already exists in a pre-nucleated state.

FUTURE WORK

The experiments detailed in this chapter were intended as the initial stages of a larger experiment whereby we would take advantage of techniques developed with coworkers as described in Li et al. *ACS Appl. Mater. Interfaces* 2017 [87] to slow down the rate of acid transport into the sample and shift the assembly from a reaction-dominated to a diffusion-dominated regime. The hope is that by slowing down the reaction we can use FCS to record the assembly transition that happens so quickly under simple acid vapor induced assembly conditions. Li et al. found that the slower assembly led to longer, more homogeneous fiber assembly, and using silicon oil as an

isolation layer between the unassembled peptide and the acid vapor triggering assembly led to the slowest assembly of all isolation layers tested. We thus designed an experiment whereby unassembled peptide was placed in one well of an 8-well glass slide, but before the introduction of concentrated HCl solution to the adjacent wells a layer of silicon oil was pipetted onto the peptide sample (Figure 4.5). Care was taken to not inject the silicon oil with too much force such that it would penetrate in the peptide fluid. We also allowed the system approximately 30 min to equilibrate and properly phase separate each time the silicon oil was added for a new sample. Measurements immediately after adding silicon oil often had some anomalous spikes in fluorescence intensity that would stop happening after ten to twenty minutes. We measured the FCS signal at regular intervals (initially taking three 60 s integrations and two 120 s integrations every 20 minutes) in hopes of measuring the concentration and mass of reactants as a function of time for which we could use standard amyloid assembly kinetics relations to estimate the reaction stages and rates [49].

Unfortunately, initial implementation of this experiment can be long and tedious because reaction under such conditions happens on the order of days. Furthermore, the long timescales for reaction under these conditions poses other difficulties. For example, the FCS setup uses water immersion optics and the layer of water between the objective and sample evaporates over several hours. This evaporation can scatter light and lead to artifacts in the data. Furthermore, experiments were conducted in a shared user facility which meant that samples needed to be regularly unmounted and remounted on the microscope, increasing the risk changing the acid transport rate due to turbulent mixing caused by physically moving the sample.

Despite the challenges associated with this experiment, the underlying principle is sound and the experiments would be interesting to see carried through to completion. In the future, care

should be taken to ensure that the peptide solution and silicon oil have not mixed and to minimize movement of the sample, perhaps by even implementing a water injection system to keep the system properly immersed on the objective without having to move the sample. Also, the ratio of peptide solution to silicon oil could be varied to find the ideal isolation layer thickness to slow the reaction just enough to measure the kinetics. It must be noted that each well is limited to approximately 400-500 μl.

Finally, the work in this chapter demonstrates that as triggered assembly begins there will actually be a distribution of sizes for the assembled material and this distribution may even broaden as assembly continues. As such, 2-species fits to the data will be insufficient toward making more quantitative conclusions from the data. Thus, it would be interesting to implement and compare the results from two modified FCS formulae: Maximum Entropy Method FCS (MEMFCS) [125] and a 5-component Gaussian Distribution Method (5GDM) [126]. For MEMFCS a basic GDM is used which entails setting a_i from eq (4.7) equal to a Gaussian distribution such that

$$a_i(\tau_{Di}) = A_i \exp\left[-\left(\frac{\ln(\tau_{Di}) - \ln(\tau_p)}{b}\right)^2\right] \qquad (4.15)$$

where A_i represents the relative amplitudes of these subcomponents of a_i, τ_p is the peak diffusion time, and b is a free parameter that defines the distribution width. A probability function, p_i, is then defined as

$$p_i(\tau_{Di}) = \frac{a_i(\tau_{Di})}{\sum a_i(\tau_{Di})} \qquad (4.16)$$

with a corresponding entropy function

$$S = -\sum p_i \ln(p_i) \tag{4.17}$$

where entropy, S, is maximized at the same time the χ^2 values are minimized for fitting the regular autocorrelation function, thus finding a size distribution without any *a priori* assumptions as to what that distribution should be. Alternatively, the 5GDM method compromises between regular GMD and MEMFCS by hypothesizing that there are a certain number (in this case, five) predominant species which may present themselves each as a Gaussian distribution (due to slight variations in size or how the species intercept the observation volume, for example). Instead of defining and maximizing an entropy for the system, this method would entail simply modifying Eq. (4.15) to sum over the distributions as

$$a_i(\tau_{Di}) = \sum_{n=1}^{k} A_n \exp\left[-\left(\frac{\ln(\tau_{Di}) - \ln(\tau_{pn})}{b_n}\right)^2\right] \tag{4.15}$$

where k is the number of peaks chosen. In the case of 5GDM, k equals 5, representing the populations of completely unassembled oligomer, very low order oligomer, larger oligomer, small fibrils, and large fibrils. Future studies could experiment with varying the number of Gaussian distributions in the fit. All in all, these more powerful FCS analysis methods combined with more time using the silicon oil isolating layer could prove very promising for measuring the distribution of species as a function of time over assembly and using that to gain significant insight into the rate equations and constants governing the kinetics of these assembly reactions.

FIGURES

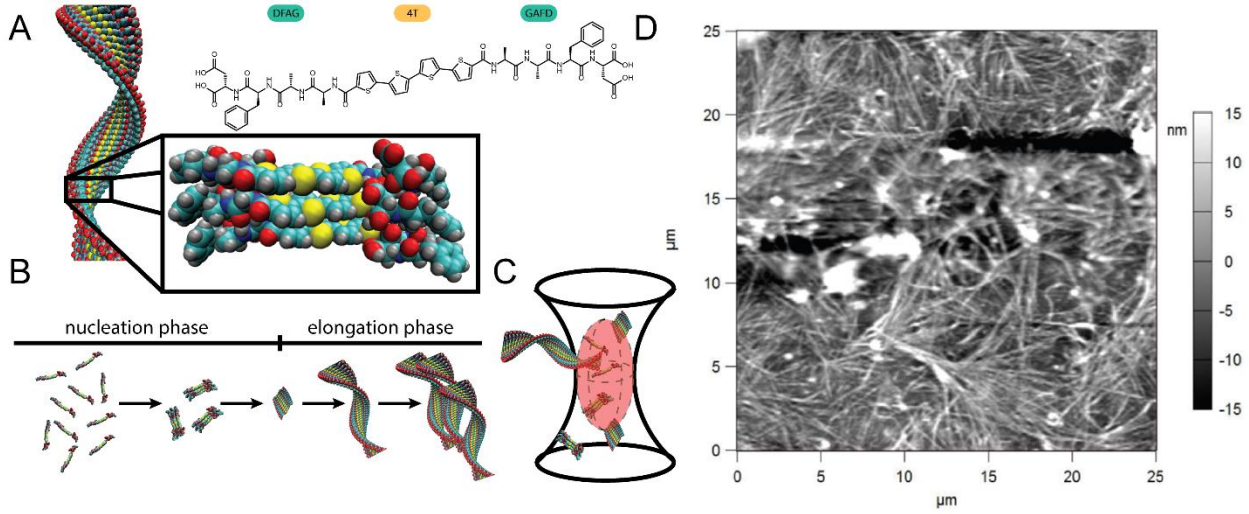

Figure 4.1 Illustration of DFAG-4T structure, aggregation, and FCS detection. A) Chemical structure and idealized stacking behavior of DFAG-4T. B) Standard model for amyloid formation via nucleation-dependant aggregation. C) Confocal spot and observation volume (elipsoid) used for FCS. As aggregates of various sizes pass into and out of the observation volume fluctuations in fluorescence intensity are detected. D) Atomic Force Microscope (AFM) image of DFAG-4T fibers deposited on Si.

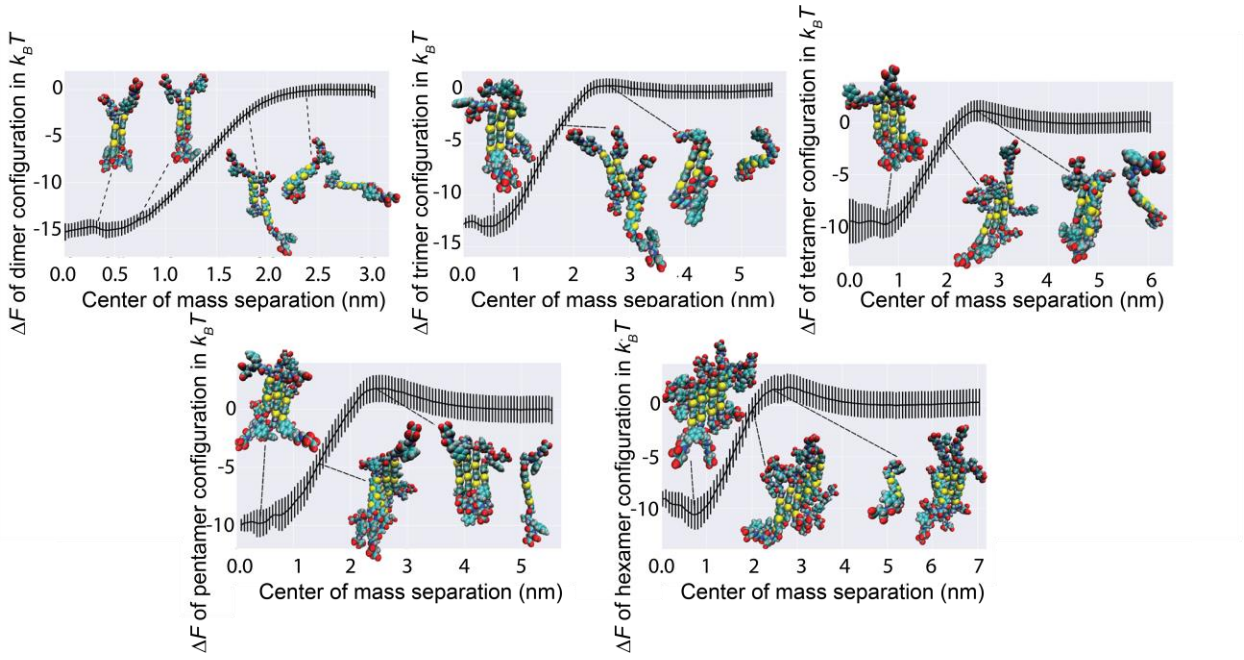

Figure 4.2 Computational prediction for pi-pi stacked bonding when deprotonated for a) dimers, b) trimers, c) tetramers, d) pentamers, and e) hexamers with representative configurations of aggregates at various points along the reaction coordinate.

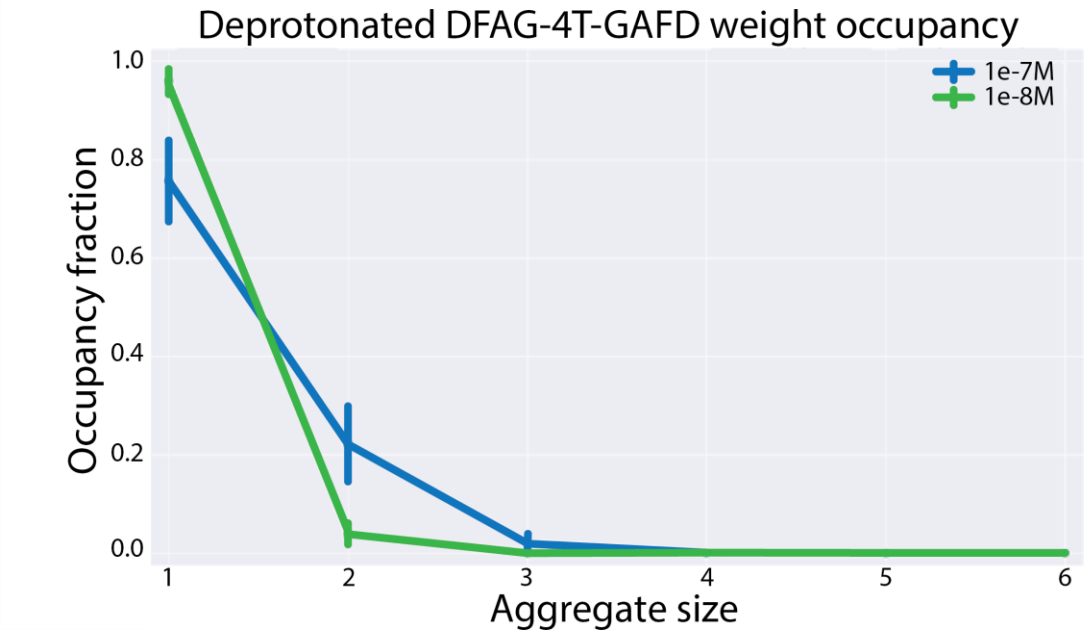

Figure 4.3 Predicted fraction of peptide existing in various aggregate sizes as a function of peptide concentration. Lines are drawn to guide the eyes. Errors are obtained from random sampling of K values within 90% confidence interval.

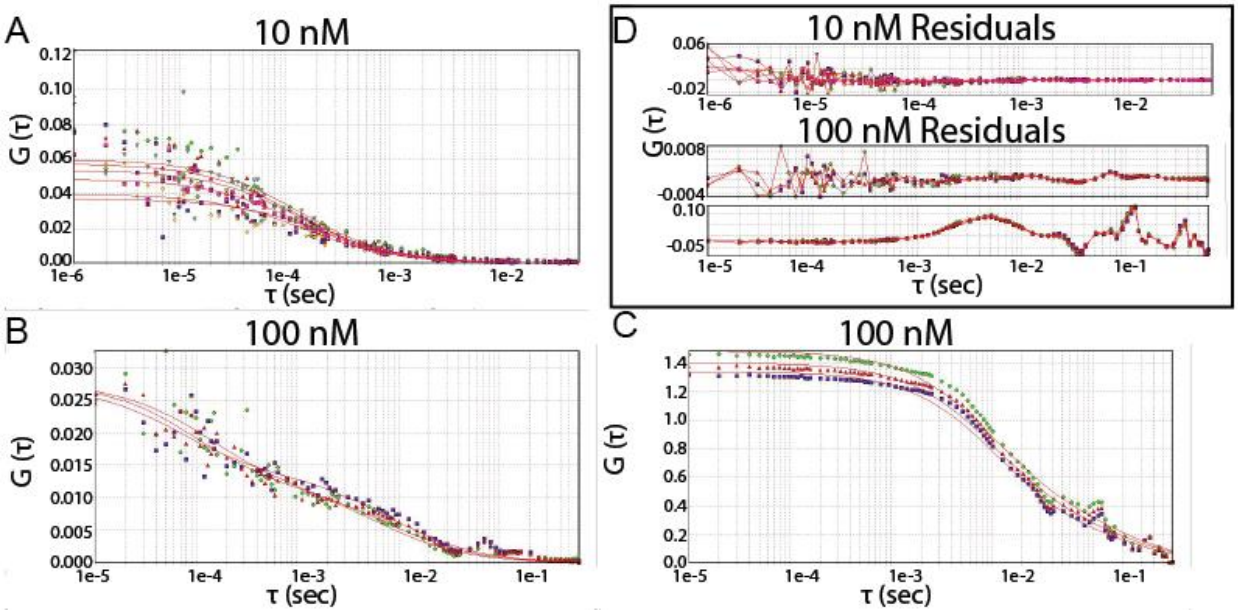

Figure 4.4 FCS data for comparison of 10 nM vs 100 nM samples. A) Six experiments at 10 nM. B) Three experiments at 100 nM C) Three other experiments also at 100 nM D) Residuals for the fitted curves in (A)-(C).

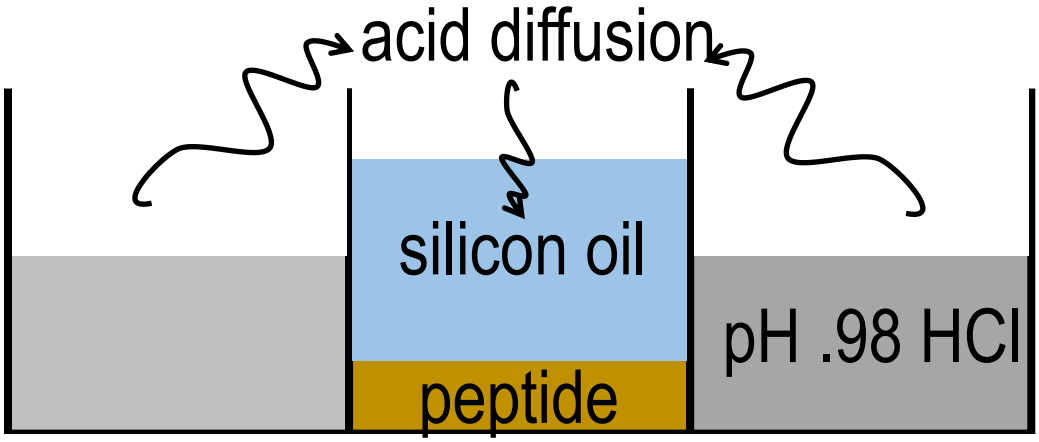

Figure 4.5 Experimental setup for slow triggered assembly using a silicon oil isolation layer.

CHAPTER 5:

NANO FOURIER TRANSFORM INFRARED SPECTROSCOPY

INTRODUCTION

The 20 characters of the amino acid alphabet allow for a staggering degree of complexity in the structures they create. This complexity it not only due to the myriad permutations of the amino acids available, but also compounded by the manifold conformations those structures can take. Each nuanced change in structure can drastically influence the function of a given protein complex. As such, when investigating a new system it is important to elucidate the unique structures at play. This can be accomplished through a variety of techniques depending on the specific system. Some of the techniques available to today's scientist are molecular coordinate approaches, Fourier transform infrared (FTIR) spectroscopy, nuclear magnetic resonance (NMR) spectroscopy, and X-ray diffraction. FTIR spectroscopy has proven itself to be a comfortable compromise between accuracy and ease of use compared to other methods [55] and thanks to advances in Michelson interferometers as well as applications of the fast Fourier transform algorithm and band-narrowing methods [56] FTIR has emerged as a prolific technique to the extent that collection of FTIR spectra is often considered standard practice.

Our recent investigation into the family of materials defined by symmetric sequences of amino acids flanking a functional π-conjugated core has involved several assumptions with regards the ultimate structure, namely β-sheet fibrils hypothesized as the outcome upon peptide assembly. While atomic force microscopy (AFM) and scanning electron microscopy (SEM) demonstrate

fibers on the order of several nanometers wide by several microns long, and optical spectroscopy and fluorescence lifetime imaging (FLIM) of the samples imply β-sheet H-stacked material (see chapter 2 for a detailed discussion [87]), FTIR could provide substantial evidence of these properties as well as more nuanced and detailed structural information. Furthermore, while some of these materials or their close cousins have been characterized by bulk FTIR [2,4,13] these measurements only provide an average of the properties over a relatively large observation volume. As recent investigations have shown (see chapter 4 for more detail) the assembly process of this material is polydisperse at the molecular level, necessitating hitherto unprecedented molecular-level measurements of the fibers.

The chemical bonds in protein structures generally vibrate with frequencies between 10^{13} and 10^{14} Hz, and light at those frequencies corresponds to wavelengths between 2.5 and 50 μm (this range of the electromagnetic spectrum is often referred to by wavenumber, corresponding to 4000 to 200 cm^{-1} in this case), which is known as the mid-infrared (mid-IR) band [57]. The amide I band, related to C=O stretching vibrations coupled with N-H bond in-phase bending and C-N bond stretching is located between 1700 and 1600 cm^{-1} and is of particular interest as these vibrational modes are directly related to backbone conformation and are the least complex, highest intensity of the Amide bands [55–59]. The amide II band, which derives from C-N-H bending and stretching vibrations, is also conformationally sensitive but is little-used, more complex, and might not be visible in many cases with s-SNOM techniques discussed below due to the strong orientation dependence of detection [56,59].

Infrared radiation at the same frequency as one of a protein's vibrational modes can induce a vibrational energy transition if the molecular dipole moment changes when vibrated at resonance, and the strength of this absorption is greater with bonds that are more polar [57]. As will be

expounded in more detail below, these molecular vibrations are geometry-dependent because adjacent vibrational dipoles can couple. That coupling can be detected via the IR absorbance, and this is the key to gaining detailed chemical bond, morphological, and/or secondary structural information from FTIR spectra [59]. However, FTIR spectroscopy is typically conducted with solutions or bulk surface-deposited samples and precludes single-molecule measurements due to the diffraction limited resolution of optical light (especially true for large IR wavelengths). And while X-ray diffraction can provide very detailed, single molecule structural information, such studies are only useful for assessing crystal structures [58]. Yet, recent developments in scattering, or apertureless, scanning near-field optical microscopy (s-SNOM) have led to the development of new techniques for measuring IR spectra at 10 to 20 nm spatial resolution [59,60] (where that resolution becomes mostly a function of mechanical, rather than optical properties of the setup). The crux of these developments is the integration of the laser system and optical components with a vibrating sharp metal probe. This is typically implemented by shining the illumination beam at a metallic or metalized AFM tip which acts as an antenna. The incident electromagnetic field components polarized along the same axis as the tip induce a corresponding movement of free electrons in the tip, leading to optical field enhancement confined at the tip's nadir on the scale of its radius of curvature [61]. This confined field leads to localized polarization of the sample which in turn has a near-field interaction with the tip leading to varying degrees of elastic and inelastic scattering, depending on the sample material [60].

Nonetheless, using an AFM tip as an antenna alone is not enough to measure the near-field interactions because of the overwhelmingly large scattering background signal. That background signal can be significantly reduced by oscillating the AFM tip with a frequency Ω, usually the resonant frequency, and an amplitude $\Delta z \ll \lambda$, where Δz is the height oscillation and λ is the

wavelength of light. While the background signal is on the scale of λ, Δz almost exclusively affects the near-field signal, which drops off drastically away from the tip on a length scale closer to the tip radius. By probing the scattered signal only at higher harmonics of the tip oscillation, $n\Omega$, the background signal becomes increasingly negligible at higher harmonics, with n representing integer multiples of the base harmonic, Ω. Although, it should be noted that the absolute signal also decreases with increasing harmonic, so a balance must be made between the two competing factors [60,127,128].

Yet this higher harmonic demodulation technique falls prey to the fact that measured light intensity, I, is always proportional to the square of the electric field and the scattered background signal must still be mixed with the near-field signal as

$$I = \langle \left(E_{nf} + E_{bs}\right)^2 \rangle = \langle E_{nf}^2 \rangle + \langle E_{bs}^2 \rangle + 2\langle E_{nf} E_{bs} \rangle \qquad (5.1)$$

where E_{nf} and E_{bs} are the near field and background scattering field respectively. Thus while the additive components of the background are eliminated, the multiplicative components remain [60,128]. When measuring such small signals as those caused by the near-field interactions, minimization of the signal to noise ratio (S/N) is critical and this multiplicative coupling of the fields is intolerable for accurate measurements. Heterodyne interferometric detection can fully eliminate the background signal by using a reference wave that is slightly frequency-shifted with respect to the illumination wave. But heterodyne detection requires a reference beam whose alignment changes with wavelength, making the method intractable for spectroscopic applications. So-called pseudoheterodyne detection is the critical development which has allowed for the recent burgeoning application of nanoscale infrared spectroscopy and commercialization of several table-top systems using only slight variations of the heterodyne technique. Pseudoheterodyne detection

uses only a Michelson interferometer with one beamsplitter and one vibrating mirror to introduce a sinusoidal phase modulated reference beam in place of the heterodyne frequency shifted beam [60]. This accomplishes the same goal as classical heterodyne detection but is immensely more practical to implement.

The pseudoheterodyne technique makes achieving theoretical electronic limits in noise possible, and liquid nitrogen cooling of the detectors means that the largest impact on S/N comes from the laser source. Thus, it is critical to minimize intensity fluctuations from the source. While advanced techniques—such as a secondary beam path with a voltage divider—can be used to divide out fluctuations, such techniques have limited application and can end up introducing more noise than they seek to eliminate. Therefore, the simplest method to optimize S/N from the laser source—much like the choice for which probe harmonic to use—is to attenuate the beam by just the right amount that the loss of overall signal is counteracted by the lower background noise contributions [61]. These various external sources in aggregate form a separate noise term which must be added to the unwanted background signal when determining the true S/N such that

$$S/N_{true} = \frac{\sigma_{N,n}}{\sigma_{B,n} + D_n} \tag{5.2}$$

where $\sigma_{N,n}$ is the Fourier component of the Near-field scattering signal at the nth harmonic, $\sigma B_{,n}$ is the corresponding term for the Background signal, and D_n represents the Fourier component for the aggregate Disturbance contributions from all other noise in the system at the given harmonic. If the total system noise, his disturbance contribution, exceeds the absolute magnitude of the signal at a given harmonic, even if the near field signal is well isolated from the background, no measurements of the sample are possible. Thus, at smaller probe amplitudes, it's possible that the system noise can cause the third or even the second harmonic to have the optimal S/N despite the

signal-isolating effect of moving to higher harmonics. Further, as the total energy of the system noise contributions doesn't change, one can increase the S/N by integrating for a longer period of time, thus subdividing the frequency space such that a smaller component of noise contributes at each frequency band measured [61,128].

Finally, while the tunability afforded by quantum cascade lasers (QCLs) provides invaluable benefit to s-SNOM techniques by facilitating nanoscale probing with very fine spectral resolution across a wide range of wavenumber, the pulsed nature of these light sources must be accounted for to avoid digitization noise [61]. In short, care must be taken to operate within the Nyquist limit constraints by tapping at a higher frequency than twice the laser pulse rate while also maintaining high enough laser pulse rate such that higher order harmonics of the probe oscillation frequency can be sampled.

Through the use of both broadband continuous wave and QCL laser sources pseudoheterodyne detection can be used to take point spectra analogous to classical FTIR (nano-FTIR spectral mode) or to image optical absorbance as a function of position with spatial resolution independent of the wavelength (s-SNOM imaging mode). Thus, through the use of a recently developed s-SNOM system we are able measure the mid-IR spectral properties of individual nanoscale fibers.

METHODS

Materials Synthesis

Sequence-defined synthetic peptides with π-conjugated cores were synthesized using solid phase peptide synthesis (SPPS), as previously reported [2]. The π-conjugated oligopeptides containing an oligo(p-phenylene vinylene) (OPV3), quaterthiophene (4T), or perylene-diimide (PDI) core were flanked by symmetric peptides with a primary amino acid sequence Asp-Phe-Ala-Gly (DFAG). The overall sequence of the π-conjugated oligopeptides the same except for the functional core and can be written as, for example, HO-DFAG-OPV-GAFD-OH, abbreviated as DFAG-OPV.

Sample preparation

All samples were prepared by evaporation on silicon wafers. All samples except the DFAG-4T sample with acid-triggered assembly were prepared by dilution in deionized water to a concentration of 0.05 mg/ml. Solution was deposited on the silicon wafer and allowed to dry overnight. The acid-triggered assembly DFAG-4T sample was prepared in the same way except that a drop of concentrated (pH << 0) HCl solution was placed nearby with the sample and acid covered by a glass petri dish to allow acid vapor from the HCl solution to trigger assembly before evaporation.

s-SNOM nanoFTIR

We used a system comprised of a central AFM and microscope core with modular attachments for s-SNOM imaging and spectroscopy (Neaspec GmbH, Germany). The AFM is operated in tapping mode using PtIr5 coated arrow-head tips (NanoWorld, Arrow NCPt) vibrating

at the cantilever resonance frequency, 240-380 kHz. The system allows for coupling a QCL illumination source on one end or a broadband continuous wave light source on the other for imaging and spectral modes, respectively.

Imaging mode and imaging spectra

We used a quantum cascade laser (QCL) tunable between 890 and 1890 cm^{-1} passed through a Michelson interferometer for signal demodulation and pseudoheterodyne detection allowing us to measure optical near-field scattering amplitude and phase up to order n=4. As the system is subject to thermal drift on the order of nanometers per minute, we could not measure point spectra of single fibers with high confidence when the measured signal was coming from tip-fiber interactions. Rather, we collected spectra for individual peptide fibers by imaging a 5 μm by 5 μm region at a single wavenumber. Images were taken every 5 cm^{-1} between 1600 and 1710 cm^{-1} with the exception of 1700 cm^{-1} and 1705 cm^{-1}. Images were taken at 1702 cm^{-1} in lieu of 1700 cm^{-1} due to the very strong water absorption line at that wavenumber. We used an integration time of ~19 ms per pixel for 100x100 pixel images. Because laser alignment can change slightly when tuning the QCL to different wavenumber and because the range of interest for these experiments spans the spectral output of two of the QCL's three chips—for which drastic alignment changes can occur when switching chips—the system's optical alignment had to be adjusted between each successive scan in order to optimize the signal at each wavenumber. In additional to recording the Z-height for each image, the system records mechanical and optical amplitude and phase up to the fourth harmonic. As discussed below, our use of the imaging mode to collect scattering spectra in combination with uncertainties about baselining spectroscopy prompted us to investigate optical properties at demodulation orders n = 2, n=3, and n=4.

Spectroscopy mode

For point-spectroscopy measurements the system is equipped with two broadband lasers joined in a fiber-laser system for difference frequency generation (FemtoFiber pro IR and SCIR, Toptica Germany) tuning between 700 and 2,500 cm^{-1}, grouped into five distinct output bands (Figure 5.1). As we were most interested in the amide I band between 1600 and 1700 cm^{-1}, we used the "D" range exclusively. Interferograms were collected by measuring the demodulated detector signal as a function of reference mirror position, and fast Fourier transformation yielded spectra with a resolution comparable to that collected via imaging (5 cm^{-1}) for a 20 ms pixel integration time over 4500 pixels. Each spectrum is averaged at least 10 times.

RESULTS AND DISCUSSION

Nanoscale FTIR spectroscopy

We first measured bulk FTIR spectra of the material for the amide bands and attempted to compare with broadband infrared spectra of relatively thick samples prepared using the polystyrene crack alignment method, starting with DFAG-4T. The polystyrene crack method is discussed in greater detail in chapter 7. Briefly, this method entails the creation of many aligned microscale cracks in a film of polystyrene beads. Unassembled peptide solution is then drop cast onto the sample and allowed to infiltrate the cracks via capillary forces. Fibers are then evaporatively assembled inside the cracks and samples are soaked in toluene. The peptide fibers are insoluble in toluene and remain adhered to the surface while the polystyrene material is completely dissolved and removed. The bulk broadband spectra for all compounds reveal clear

peaks in the 1700-1600 cm^{-1} and 1600-1500 cm^{-1} regions which likely correspond to the amide I and amide II bands, respectively (Figure 5.2). To collect nanoscale broadband FTIR spectra we first imaged the sample using our system's AFM capabilities. Scans revealed lines in pairs corresponding to material accumulation along the inner corners of the cracks (Figures 5.3a & 5.3b). We chose to investigate these thick accumulations of hundreds of fibers before tackling individual fibers because of concerns over thermal drift of the system and the necessity of constant contact between tip and peptide over the course of each spectrum integration. We acquired ten spectra in this manner at the location indicated in Figure 5.3b. We also acquired reference amplitude and phase spectra on a clean area of SiO_2. (It is assumed that as these measurements are not conducted in an environmentally controlled chamber, all Si wafers have a thin oxide layer on top and the extreme spatial confinement s-SNOM means that we are not probing beyond that surface SiO_2 layer.) These reference spectra are used to normalize all spectra from the peptide and assume a relationship between the scattering signal and absorption spectra, a_n, of each harmonic n such that

$$a_n(\lambda) = \frac{s_n}{s_{n,r}} \sin(\varphi_n - \varphi_{n,r}) \qquad (5.3)$$

where s_n and $s_{n,r}$ represent the sample and reference scattered field respectively while φ_n and $\varphi_{n,r}$ represent the corresponding phases.

The finite optical path of any physical system inherently limits the resolution of Fourier transform-based spectroscopy. The optical path length effectively multiplies the actual wave function being observed by a step-wise function corresponding to the path length, truncating the otherwise infinite wave. The result is that peaks are widened and additional oscillations are introduced as artefacts. Furthermore, the discrete nature of digitally sampling the signal means that adjacent data points in the Fourier transform are spaced at the inverse optical path length. This

means that two resolved peaks in frequency space may not be apparent as separate data points if they are immediately adjacent. Thus, the nanoFTIR system's software automatically performs apodization and zero padding on all nano FTIR spectra. Apodization entails multiplying the interferogram by a Gaussian function as wide as the interferogram, resulting in slightly lowered spectral resolution due to peak broadening but in return eliminating artefact oscillations. Zero padding means that we add zero values to either end of the untransformed interferogram which artificially increases the number of data points in the transformation. This does nothing to improve actual resolution, but it makes closely separated peaks more discernable by weighting the transformed function back toward zero between the real data points. Two data points belonging to two separate peaks will thus have a small intervening valley as opposed to appearing to exist on the same slope a larger convolved peak [127].

There is significantly less dramatic structure in the nanoscale FTIR spectra compared to the bulk spectra (Figure 5.3c) with regards identifying amide bands. This is due in part, however, to the fact that bulk measurements are necessarily averaging over the spectra of all the material in the beam path. The nanoscopic spectra will, thus, tend to have smaller, sharper peaks corresponding to the specific structure attributes of each fiber within an amide band, such as specific signatures for parallel or anti-parallel β-sheet stacking [58,59]. Given the anticipated structural similarity of the fibers we measured, and the fact that the thicker samples inherently entail some degree of averaging, we calculated the average over ten individual spectra in order to identify significant peaks across all the measured fibers (Figure 5.3d). Additionally, we cross referenced all the spectra to identify peaks that occurred most frequently among all the measurements. The histogram in Figure 5.3d represents the confidence in our identification of a given peak, with the height of each bar indicating the percentage of spectra with a peak within 10

cm^{-1} of that bar's location. Although relatively weak, the peak near 1630 cm^{-1} may be indicative of β-sheet structures [56,59] as we expect to see for our fibrils. As explained in more detail in chapters 2 & 4, we expect DFAG-4T material to self-assemble into H-stacked or slip-stacked β-sheet fibrils due to the H-bonding of the aspartic acids compounded with π-stacking and hydrophobic interactions of the cores. For DFAG-PDI we would expect similar structures, although with perhaps smaller or less cleanly aligned fibers due to the steric hindrance from the larger PDI moiety. However, for the nonsequence-defined peptides such as Glu-PDI we expect more α-helix or random coil behavior. The peak near 1650 cm^{-1} could be related to a 1660 cm^{-1} α-helix signature but it more likely due to adsorbed water, which has a very strong absorption at 1645 cm^{-1} [57]. Although one can generally ascribe absorption around 1633 cm^{-1} to β-sheets, absorption near 1654 cm^{-1} to α-helices, and features around 1672 cm^{-1} to β-turns, there is also additional, weaker β-sheet signature around 1684 cm^{-1} and nuances in the molecular structures such as the number of strands or the parallel versus antiparallel ratios in a β-sheet or the number of α-helix residues can shift the absorption bands anywhere from a couple to several tens of wavenumber [57]. These nuances make it difficult to ascribe specific structural properties to measured nanoscopic samples without a proper reference, even without the complication of water absorption features. Nonetheless, one could measure the properties of different peptide material created in similar conditions to ascribe a fingerprint to each structure, allowing the fibers of various materials to be distinguished.

However, the true power of this nanoFTIR technique lies in the potential to resolve IR spectra at single-fibril spatial resolution. Although pseudoheterodyne detection theoretically provides nanometer spatial resolution in the system's optics, mechanical constraints limit that resolution through sample drift. Regardless of AFM cantilever motion, the sample may change

position relative to the AFM tip as a function of factors that are outside of experimental control in the current experimental configuration, such as environmental humidity and temperature changes. We were fortunate to attempt broadband FTIR spectra of single fibers on a day when the sample drifted by only a couple nanometers over the course of a ~13 min, 10 spectrum averaged data acquisition, allowing us to acquire ten such averages (Figure 5.4). With the AFM tip positioned at the intersection of two fibers, we observed just enough drift such that the tip appeared to move across the area of the crossed fibers (Figure 5.5a). These spectra show reasonable overlap with the previously acquired spectra shown in Figure 5.3, in particular with regards the likely water absorption feature. However, the spectra shown in Figure 5.4 contain much more well-defined and self-consistent features. This discrepancy is likely due to the fact that the spectra of Figure 5.4 are from only two fibers at a very specific spot. Meanwhile, the spectra of Figure 5.3, while not from such a polydisperse sample as a bulk spectrum, are nonetheless from a relatively thick sample with many fibers that are not individually distinguishable, leading to more averaging-induced broadening. An additional contribution to the discrepancy may also come from the fact that the laser used in these experiments was replaced due to instabilities that were discovered in the intervening time between the experiments for Figures 5.3 and 5.4. These instabilities in the old laser may have been present and contributed to the noise in the earlier experiments.

We conducted several control experiments for the data acquired from the two crossed fibers discussed above, such that the entire experiment consisted of five stages (Figure 5.5): 1. A reference spectrum consisting of 10 averaged spectra was measured on a plain SiO_2 reference sample. 2. Nine additional analogous spectra were acquired on the same reference sample. 3. Ten spectra were acquired on a clean SiO_2 region on the corner of the sample containing peptide fibers. 4. Ten spectra were acquired in the region between fibers. 5. Ten spectra were acquired on the

intersection of two fibers. We took an image of the sample area before and after every 3 data acquisitions to check for sample drift with the exception of the measurements on the intersecting fibers themselves, for which we imaged between every single data acquisition. The same initial reference spectrum was used for all subsequent spectra.

The rationale for acquiring spectra in the order described above was to mitigate contamination by moving from the cleanest sample, to a region that should be clean but might be compromised by its proximity to deposited peptide, to a region that would ideally be clean but likely contains some deposited contamination from solution such as poorly formed peptide species below the AFM detection limit, and finally directly on the sample peptide which could potentially stick some material to the AFM tip. We thus intended to test the suitability of using spectra acquired in the manner of experiment 3 in liu of the dedicated reference sample used in experiments 1 and 2 as well as test our assumption that the region between fibers should be spectrally similar to plain SiO_2. Finally, we expected to see the unique spectral signatures of the fibers featured in the spectra from experiment 5 and absent in spectra of the previous stages.

For each of the stages above we further combined the spectra, taking the data from each acquisition, which consists of 10 averaged spectra, and averaging the data from a single stage to obtain one curve corresponding to an average of 100 spectra. We plot the results from each experiment in Figure 5.5 and it becomes clear that something is amiss. The two remarkable curiosities of the spectra in Figure 5.5 are: 1. The spectra corresponding to the reference sample are so different as compared to the self-referenced line when all these spectra are taken from the same sample. 2. The spectra from all stages of the experiment are remarkably similar, implying that the peptide fiber is spectrally identical to the background SiO_2, which is known to be false. Further investigation into the manner of using a reference spectrum to calibrate all spectra with

respect to the background signal is required. Possible solutions are discussed at greater length along with similar issues of noise and background compensation in Appendix B.

Imaging-based spectra

Given the challenge of obtaining accurate spectra for individual fibers with diameters on scale of a few nanometers because of thermal drift sufficient to shift a fiber out from below the probe tip, we developed an alternative method to acquiring the nanoscale infrared scattering absorption spectrum that does not use a Fourier transform. In addition to using a broadband laser source, we can tune a QCL laser source with incredible accuracy to image the scattering absorption of the sample at specific wavenumber. By imaging an entire region at different wavenumber we are thus able to measure scattering as a function of position and topography with nanoscale spatial resolution. Some material inevitably remains in the field of view from image to image. We thus created effective spectra of our samples by imaging at increasing wavenumber between 1600 cm^{-1} and 1710 cm^{-1}. As laser power and alignment varies with each tuning of the QCL, we compared the absorbance amplitude and phase of the fibers relative to the substrate at each wavenumber before concatenating a single-fiber absorbance spectrum over the spectral region imaged. We accomplished this through two methods. We compared the average values of an area of background pixels to the average values of pixels for a line drawn along the length of a fiber (Figure 5.6b), and we took the ratio of those two values to yield the spectra shown in green in Figure 5.6a. As a second method, for images at each wavenumber we took a histogram of the scattering field, which could typically be fit to two Gaussian curves. We then took the peak to peak difference between the two curves to be the difference of the scattering field between the fibers and the SiO_2 substrate [58] (Figures 5.6a & 5.6c).

We note that there is general agreement between the two methods across all DFAG-4T spectra with β-sheet peak features both in the 1630 cm^{-1} region and in the 1675 cm^{-1} region as well as what is very likely to be water absorption around 1650 cm^{-1}. It is more difficult to ascertain if there is unexpected α-helix behavior in the peaks closer to 1660 cm^{-1}, or if those peaks are simply shifted from the β-sheet peaks. Furthermore, we notice that for several images, the intensity ratio method yields curves that appear to be only noise for much of the measured band, yet the Gaussian difference method for those same images yields more identifiable structure in line with the other spectra measured. Half the spectra collected were from DFAG-4T assembled via evaporation alone and half were assembled through an acid-triggered process from HCl vapor diffusion. We compared averages of the two sets and there appears to be little difference between the two with the exception of what is perhaps a more prominent peak around 1665 cm^{-1} in the evaporatively assembled sample (Figure 5.7a). This may indicate a tendency for peptide that is allowed to slowly assemble via evaporation to form some α-helix or random coil-like structure where acid triggered assembly does not. It would be unsurprising to find such structures only in the nonacid-triggered assembly given the relative strength of H-bonding in the protonated samples, where the aspartic acids in the residues exert more control over fiber structure in an acidic environment. All these measurements were conducted using images from the fourth harmonic optical scattering absorption amplitudes.

In addition to measuring scattering absorption spectra for DFAG-4T, we also measured samples of the same amino acids but not sequence-defined and containing a PDI core rather than 4T. Previous studies of this random sequence residue PDI material indicated that the material has a stronger tendency to form α-helices than β-sheets and thus cannot form fibers (Figure 5.8). Indeed, AFM topography maps of these samples show no indication of fiber formation (Figure

5.9). Moreover, the scattering absorption spectra we collect exhibit a much stronger peak in the α-helix region than do the DFAG-4T samples (Figure 5.9). These imaging-based spectra indicate the power of this nano s-SNOM technique for acquiring detailed spectra of nanoscopic samples with similarly nanoscopic spatial resolution while also providing a sharper view of detailed features within the amide bands that is more difficult when averaging over large ensembles of material as well as avoiding the pitfalls associated with Fourier transform techniques with limited optical paths.

The method of acquiring spectra where the data at each wavenumber correspond to images taken at only that wavenumber appears to be advantageous over typical spectra acquired from the Fourier transform of an interferogram. Beyond the original motivations with respect to spatial resolution and drift for small fibers, the imaging spectra appear to do a better job of identifying specific structural peaks within the amide I band and are not complicated by apodization and zero-filling. There are, however, complications unique to this method which must be accounted for. For instance, Figure 5.10 demonstrates that there is very consistent correlation between the height trace and optical scattering data. This correlation alone should not be cause for concern, as there will always be some correlation between sample thickness and absorption, and the height data at different wavenumber should have no systematic variation as do the corresponding optical data [58,59,129]. Although what should be true theoretically is not always the case and there is certainly some convolution of the height or sample thickness signal with the scattering field signal. These complications are discussed in greater depth in Appendix B.

Obtaining optical properties via scattering/absorption conversion

Moreover, the imaging spectra are not true absorption spectra as they are actually measurements of the scattered field. While there is some validity to using the scattering spectra as

an equivalent analogue to the absorption spectrum, given the qualitative agreement between certain features and bulk FTIR absorptions features [59]. Further, the identification of spectral features is essentially a function of the second derivative of the spectra, hinging on the identification of the locations for local extrema, which should be the same for scattering or absorption. Nonetheless, it is important to understand that the measured scattering field is a function not just of the absorption spectrum, but also of the material's dielectric constant and index of refraction [58]. The *z*-motion of the tip can also introduce artefacts into the scattering, although this can be corrected for [130]. For these reasons we have been careful to refer to the imaging spectra as scattering absorption, rather than true absorption spectra. The scattering loss is actually proportional to the imaginary part of the effective polarizability, א, in the tip-sample interaction which is related to the scattered field phase shift, φ, by

$$\mathrm{Im}(\text{א}) \propto A\sin(\varphi) \tag{5.4}$$

where A is some constant. Electromagnetic field interactions between an AFM tip and sample are often approximated as a sphere above a plane [58,59,66,131] and the polarizability can similarly be described for this geometry by a dipole and its image as a function of tip and sample electronic properties by

$$\text{א} = \frac{\text{ג}}{1 - \frac{\text{בג}}{16\pi(r-d)^3}} \tag{5.5}$$

where r is the tip radius, d is the half distance between the dipoles, and ג and ב are functions of the tip and sample dielectric constants, ε_t and ε_s, respectively such that

$$\text{ג} = 4\pi r^3 \frac{\varepsilon_t - 1}{\varepsilon_t + 2} \tag{5.6}$$

and

$$\text{ב} = \frac{\varepsilon_s - 1}{\varepsilon_s + 1} \tag{5.7}$$

and the dielectric constant of the sample links the scattering spectrum to the absorption spectrum via the index of refraction, $n(\lambda)$, as $n^2 = \varepsilon$, (or more accurately, $\mathrm{Re}(\varepsilon) = \mathrm{Re}(n)^2 - \mathrm{Im}(n)^2$ [61]) where λ is the wavelength of light. The imaginary part of the index of refraction is a function of absorption spectrum and the optical path length, L, by the simple relation

$$\mathrm{Im}\big(n(\lambda)\big) = \frac{\lambda a(\lambda)}{4\pi L} \tag{5.8}$$

and we can obtain the rest of the index of refraction using the Kramers-Kronig relationship

$$\mathrm{Re}\big(n(\lambda)\big) = n_b + \frac{2\lambda^2}{\pi} P \int \frac{\mathrm{Im}(n(\lambda'))}{\lambda'(\lambda^2 - \lambda'^2)} \mathrm{d}\lambda' \tag{5.9}$$

where n_b is the visible range index of refraction and P signifies the Cauchy principal value for the proper contour integral [58]. Thus, the measured scattering absorption spectra can be quantitatively linked to the corresponding traditional absorption spectrum and in the process we determine valuable information about the sample's optical properties.

Signal-to-noise considerations

At this point it is important to note that although there is extensive discussion in the literature with regards achieving optimum S/N and choosing the optimal harmonic for near field imaging [60,61,127,128], there is little discussion with respect to harmonic choice and S/N as they

relate to baselining spectroscopy. There is a tendency to use the highest harmonic at which an optical signal can still be discerned because the higher the harmonic, the more spatially confined the measurement is to the region near the probe tip and the higher the ratio of near field signal to background scatter. However, as one probes higher harmonics, the absolute intensity of the scattering signal decreases such that eventually the gains of higher harmonics are counterbalanced by approaching the noise floor. Thus, with respect to imaging, the ratio of near field signal to noise makes the third or even the second harmonic preferable to the fourth [61]. However, while, these lower harmonics yield better images, it's uncertain how they affect measurements of the scattering absorption compared across multiple wavenumber. For every measurement, the system automatically records all mechanical and optical amplitude and intensity for each harmonic up to the fourth. Thus, it was a simple extension of previous work to calculate the same spectra as above for both the second and the third harmonics (Figure 5.11). As might be expected, the absolute value of the scattering difference decreases with increasing harmonic. However, normalizing all spectra to a highest peak value of 1 reveals almost identical behavior regardless of harmonic (Figure 5.12).

CONCLUSIONS AND FUTURE WORK

We have demonstrated the efficacy of using an s-SNOM system paired with Michaelson interferometers as well as both broadband and QCL laser sources to probe infrared scattering behavior of material with nanoscale spatial resolution. The recent innovation of pseudoheterodyne detection allows one to truly isolate the near field scattering signal from scattered signal originating

at the sample substrate by only observing signals that are at the side bands of harmonics of the probe tip oscillation frequency of order $n \geq 2$. We have demonstrated that in addition to acquiring broadband point spectra through Fourier transformation of scattered absorption signal at the AFM tip, we can also acquire analogues of absorption spectra by measuring the scattered signal at images collected for a single sample at multiple wavenumber to achieve truly nanoscale spatial resolution regardless of thermal drift.

We have further demonstrated the value of this technique by distinguishing spectroscopic signals of differences in structure for sequence-defined DFAG-4T peptide fibers versus PDI based peptide aggregates with nonsequence-defined DFAG residues. Furthermore, we have elucidated subtle differences in the structure that are indistinguishable via existing nanoscale topographic probing techniques for DFAG-4T fibers formed via evaporation versus acid-triggering.

Yet there is significantly more information available to collect from the systems studied above. The absorption spectra for each sample should be calculated from the image-based scattering spectra using the above relations and compared to bulk IR spectra. This would allow us to quantitatively measure for the first time the dielectric constants and indices of refraction for all the peptide materials we are considering. Similarly, it could be instructive to see if calculating those values the opposite direction, deriving the expected scattered spectra from the bulk absorption, gives similar results. Alternatively, Raman, and particularly tip enhanced Raman spectroscopy (TERS) could be useful measurements to crosscheck the chemical signatures we hope to identify. Although the highly fluorescent nature of the sample might make Raman spectroscopy unfeasible, if Raman spectra could be acquired, the method's ability to essentially disregard signal from water could be valuable in eliminating that one source of background signal as the water absorption line is positioned right near the center of the amide I band.

Also note that from Eq. 5.4 it is imperative to not only measure and analyze the scattering amplitude, but also the scattering phase of each image. The 2π periodicity of phase measurements poses a challenge to this method because phase can only be interpreted within a single image. Given that only differences in phase and not absolute phase are used for the dielectric constant calculations, and phase differences are all calculated internal to a specific image, this concern might be irrelevant, although a more detailed investigation is required.

It is possible to acquire bulk IR spectra with spectral resolution more than twice as detailed as the 5 cm^{-1} resolved imaging spectra we acquired. We could attach greater significance to our results if we redo analogous measurements to those already made but at 2.5 cm^{-1} spacing. Imaging spectra are extremely time-consuming (average ~5 hrs per spectrum) because of the integration time required for each image compounded with the time required to realign the interferometer optics between each scan. The time challenge might be mitigated by scanning a smaller area with the same pixel density, although care would have to be taken that thermal drift over the course of the experiment does not push all material outside the initial field of view. Obtaining a 2.5 cm^{-1} resolution would also make the imaging method of spectral acquisition superior to the Fourier transformed point spectra. Although the imaging spectra have thus far proved more promising than point spectra for these samples, the globular, lower aspect ratio of the structures from the PDI-based material might be more amenable to point spectra, with comparison of those nanoFTIR point spectra to the nanoscale imaging spectra. Furthermore, such point spectra may provide fingerprints to distinguish various similar samples.

We intend on investigating sequence-defined DFAG-PDI fibers as well as peptide constructed of only PDI cores with Glu residues. The residues for these materials should give them predominant β-sheet and α-helix structure, respectively. It will be interesting to see if we can

distinguish sequence-defined peptides with only different cores or PDI cores with different residues from each other based solely off of nanoFTIR or s-SNOM image-based spectra.

Ultimately, recent developments in near field signal enhancement and detection have facilitated remarkable characterization of nanoscopic material using methods that hitherto were diffraction limited to less informative bulk ensemble measurements. We now have the ability for unprecedented characterization of structural and optoelectronic properties of self-assembling functional biohybrid materials at the single molecule scale. Moreover, these experiments are only a taste of the plethora of potential investigations into our material. These techniques should prove useful not only as outlined above, but also as we increase the scale of order with our material. We could investigate flow-aligned fiber bundles and quantify the effects of that alignment. Finally, these characterization techniques can inform the development of our material toward device applications.

FIGURES

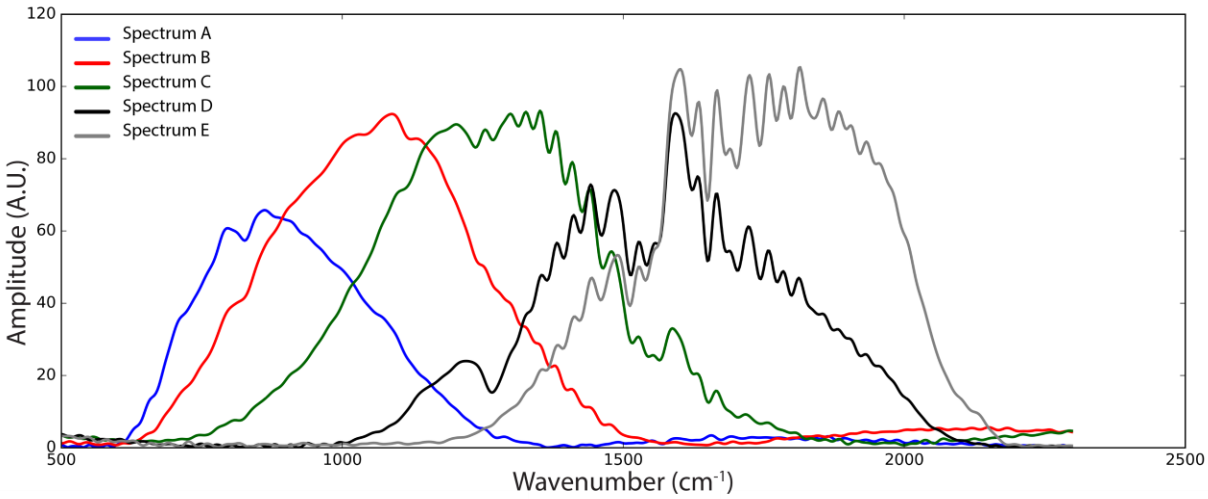

Figure 5.1 Neaspec spectroscopy laser output bands. Spectra A through E represent the SiO_2 background spectrum for each band.

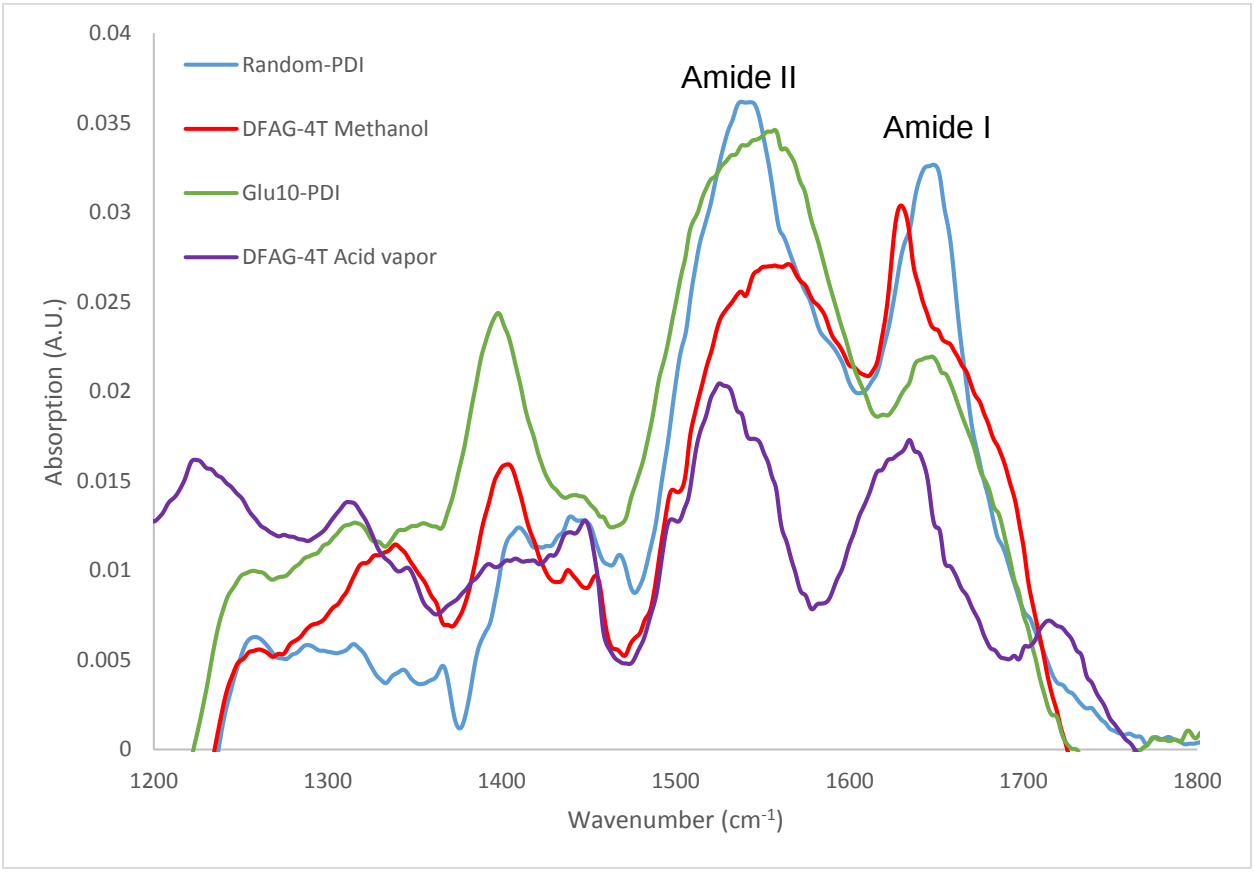

Figure 5.2 Bulk FTIR data. All samples exhibit absorption peaks in the amide I and amide II regions.

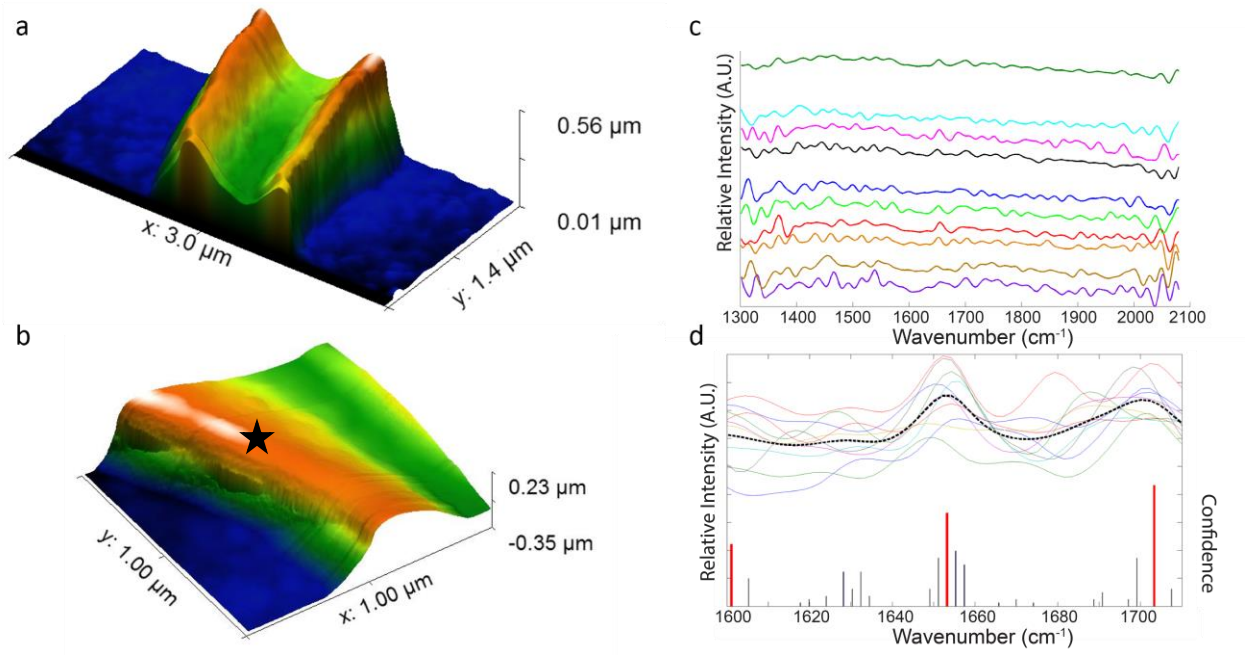

Figure 5.3 Nanoscale imaging and spectroscopy of polystyrene crack-aligned peptide fibers. a) Crack-aligned peptides topography. b) Topography of one side of a line of deposited peptide. Spectra were acquired at the location of the black star. c) We acquired 10 spectra at the same location, all of which are plotted here, offset to show detail. d) Detail of the spectra in the amide I region. All 10 spectra from (c) are plotted together with the average spectrum shown in black, bold and dashed. Histogram shows locations of peaks with magnitude reflecting confidence in the peak location. The three most significant peaks are highlighted in red.

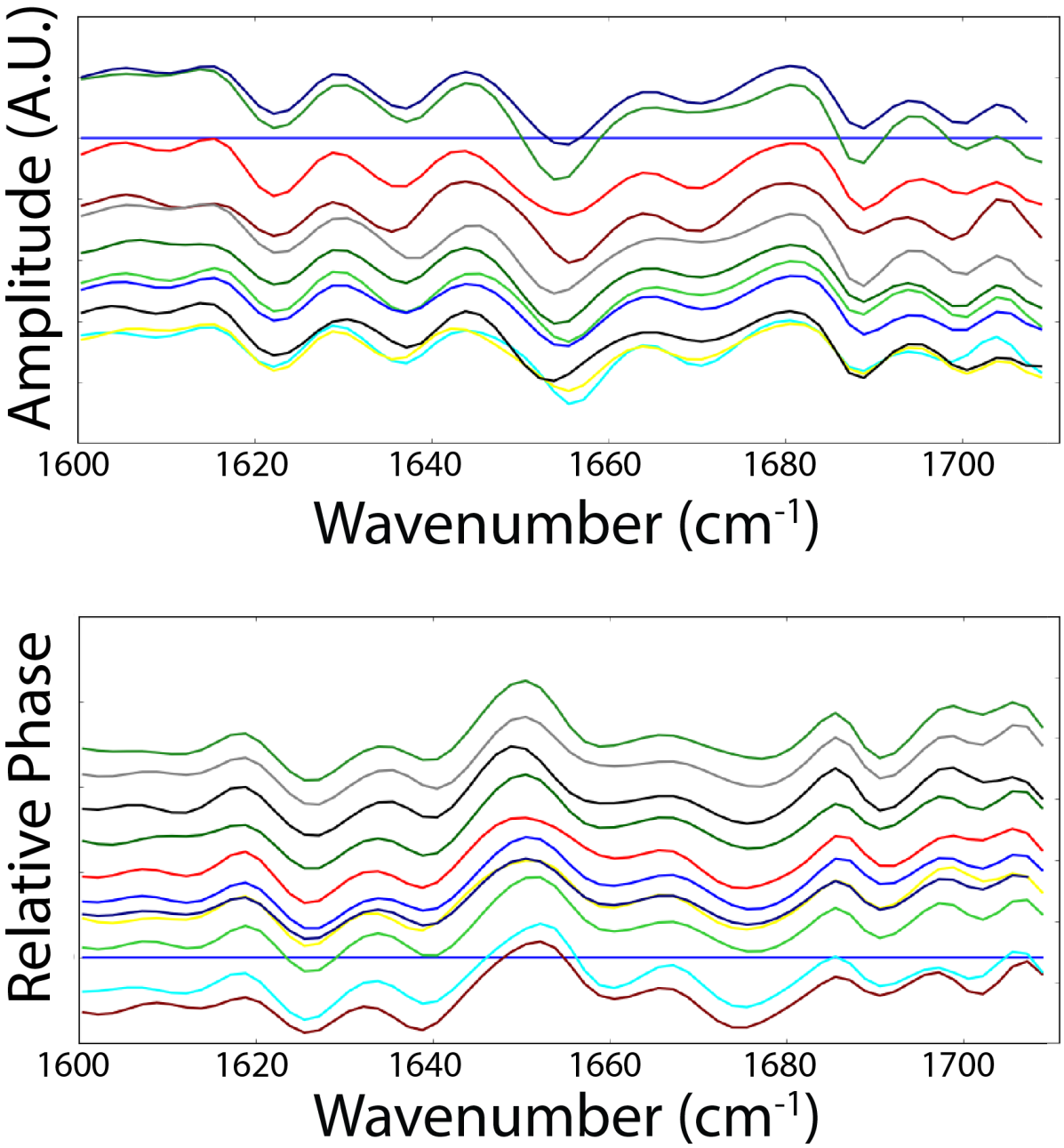

Figure 5.4 Amplitude and phase spectra for the intersection of two overlapping peptide fibers. Each curve corresponds to one set of data acquisition consisting of 10 spectra acquired and averaged over the course of ~13 min. All curves are offset from each other for comparison. Such a method of comparison is particularly valid due to the arbitrary absolute scale for each graph. There appear to be distinct features at approximately 1620, 1635, 1650, 1665, and 1685 which remain consistent across all curves.

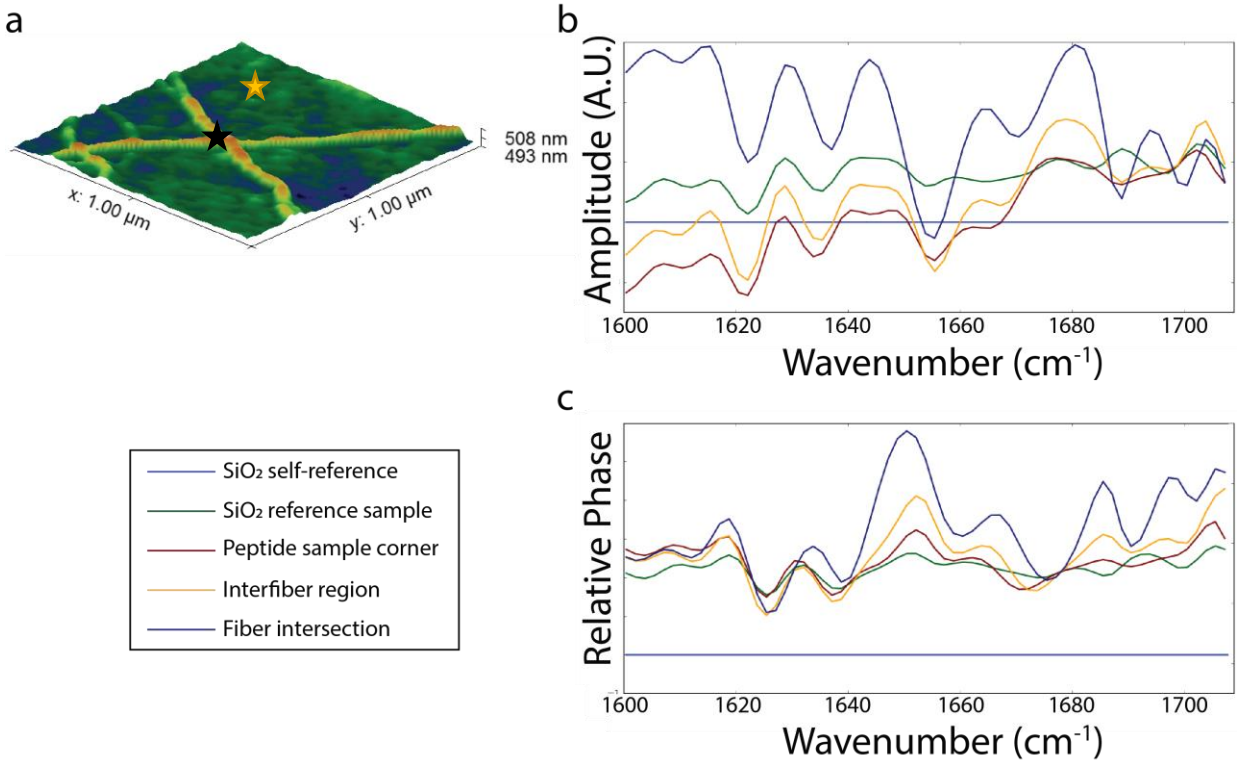

Figure 5.5 Nanoscale imaging and spectroscopy of individual fibers on SiO_2 substrate. a) Three dimensional topographical reconstruction of the sample region for interfiber and on-fiber curves in (b) and (c). The gold star indicates the AFM tip position for interfiber spectra and the black star indicates the tip position for the on-fiber measurements. b) Scattering absorption amplitudes and c) scattering absorption phase measured for a bare SiO_2 reference sample (green), a region of clean SiO_2 on the corner of the peptide sample (red), a region between individual fibers (yellow), and the intersection of two individual fibers (dark blue). All spectra are calibrated with a single reference spectrum acquired on the bare SiO_2 reference sample. The light blue horizontal line in both graphs represents the reference spectrum calibrated against itself.

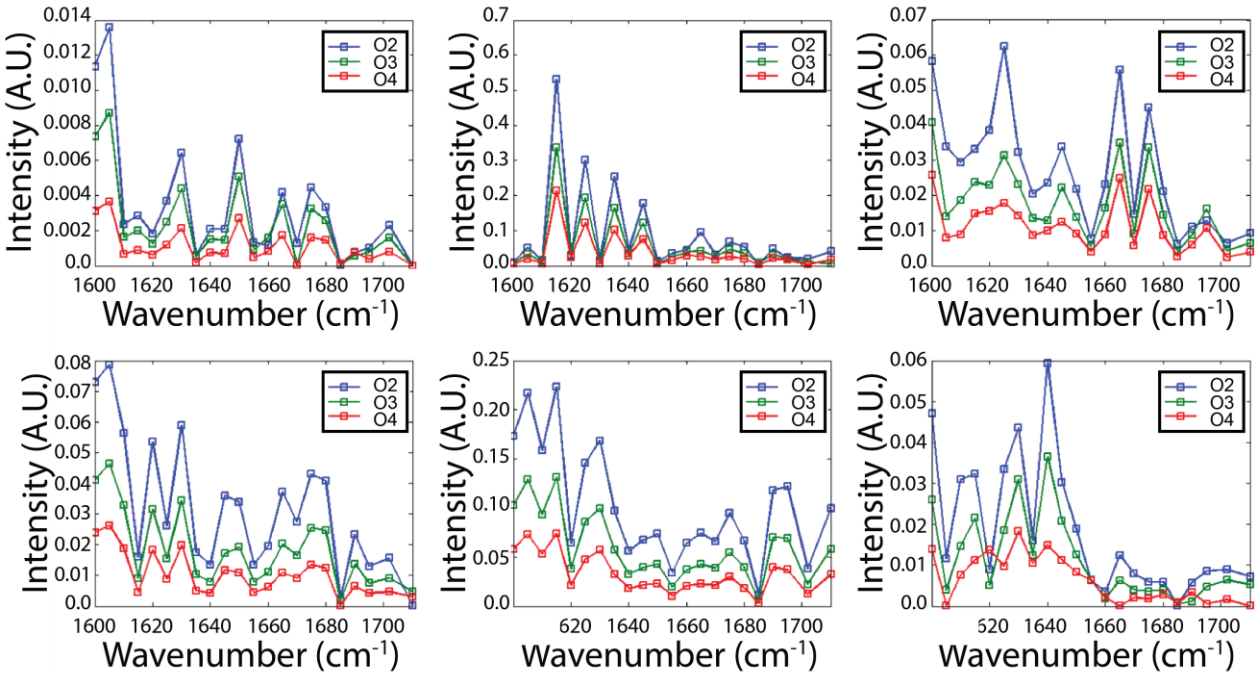

Figure 5.6 Comparison of scattering absorption imaging spectra measured at n=2,3,4 optical harmonics using the Gaussian difference method. Intensity decreases with higher harmonic, however overall structure remains nearly identical. The vertical axis in each graph is plotted in the raw measurement scale with arbitrary absolute value. Rather, the relative values compared proportionally within one dataset are what is being compared, and these are consistent with each image. In other words, all data are comparable to within a scaling factor.

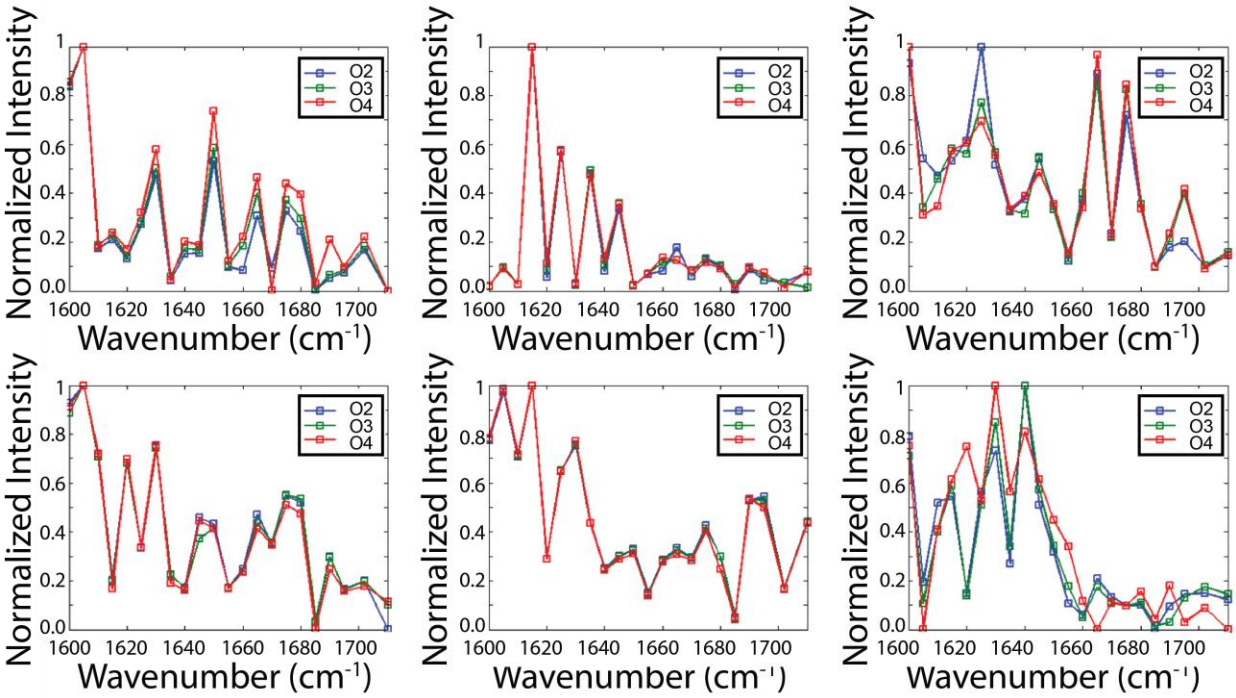

Figure 5.7 Normalized comparison of spectra at different optical harmonics indicate the high degree of similarity between different harmonics.

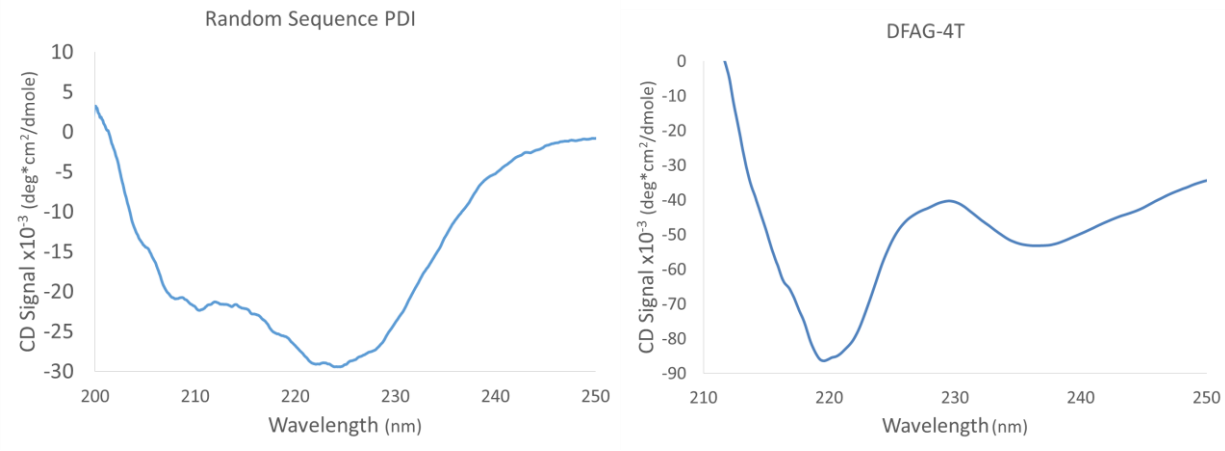

Figure 5.8 Circular dichroism spectra for PDI sample versus 4T sample.

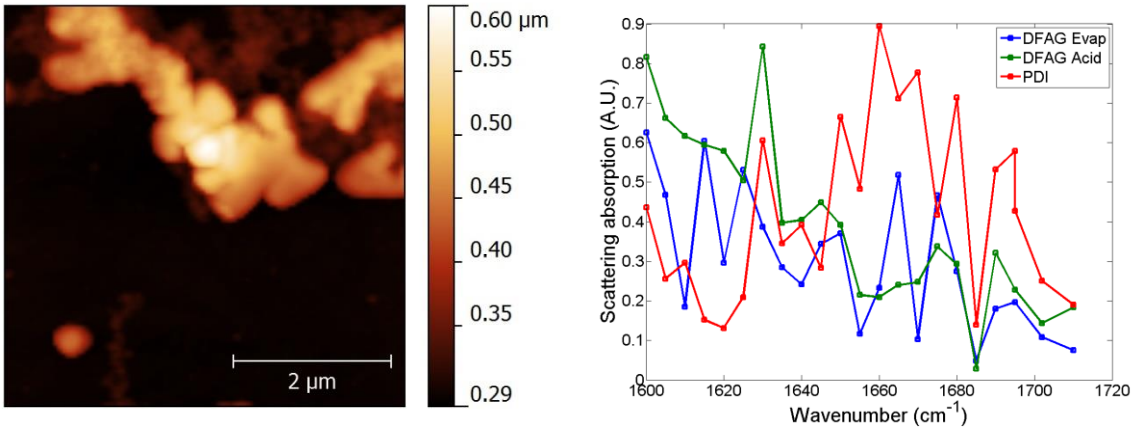

Figure 5.9 Analysis of nonsequence-defined PDI peptide vs DFAG-4T peptide. Left: AFM topography image shows the absence of fiber formation. The image has been linearly extrapolated to 5x magnification for display purposes only. Right: Comparison of averages for DFAG-4T and nonsequence-defined DFAG-PDI scattering absorption spectra. Each spectrum is averaged over three imaging spectra collected in different regions for each of the three different samples. All spectra indicate the expected peaks for β-sheets, water absorption, α-helices, and random coils. The more structured DFAG-4T fibers formed by acid-mediated assembly have the strongest β-sheet character while the PDI with random side chains, which does not form fibers, has strong absorption in the α-helix region of the spectrum.

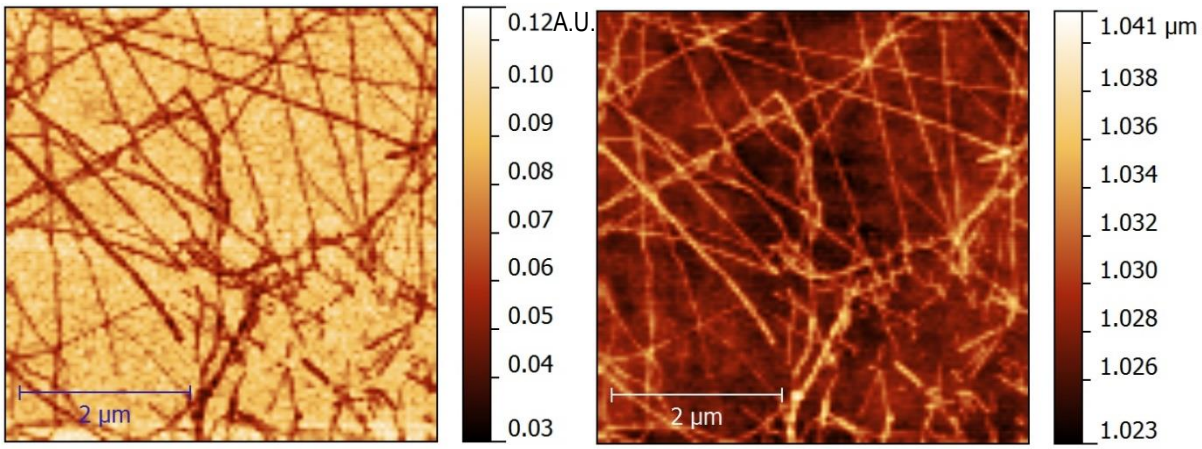

Figure 5.10 Optical scattering absorption versus height data for DFAG-4T at 1600 cm^{-1}. Left: Fourth harmonic optical scattering amplitude. Right: Tapping mode AFM height trace. Both images were acquired simultaneously on the nanoFTIR system. Both images were acquired at 100 x 100 pixels and linearly extrapolated to 5x magnification solely for the purpose of illustration in this figure. All data analysis was carried out on the original 10 kilopixel images.

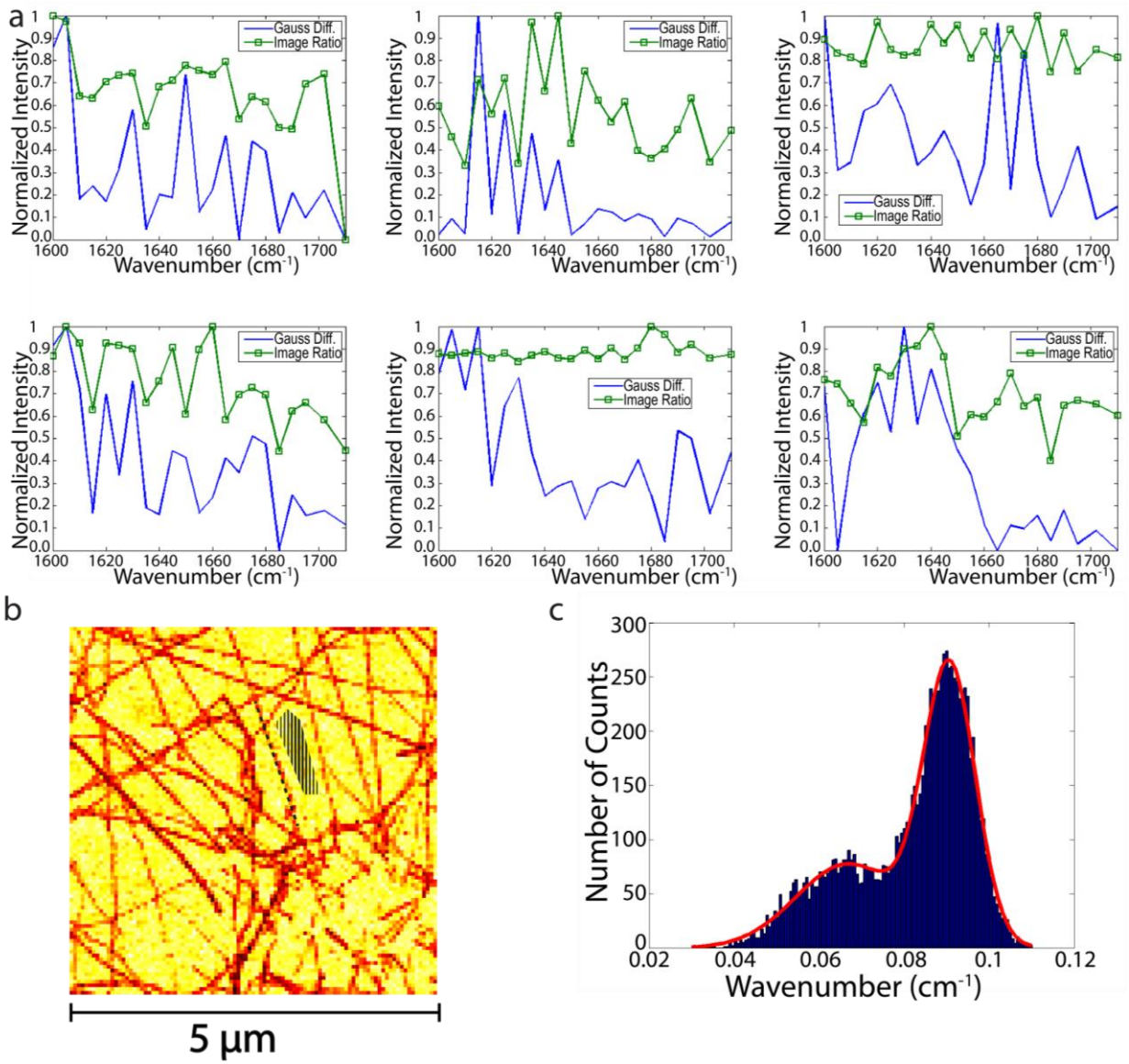

Figure 5.11 Imaging spectra for DFAG-4T samples. a) Green lines with square markers represent scattering measured taking the ratio of fiber to background intensity in each image as in (b). Blue lines represent scattered measured by taking the peak to peak distance of two Gaussians fit to each images intensity histogram. The top three spectra are from evaporatively assembled peptide and the bottom three are from peptide assembled via acid vapor diffusion. b) Scattering absorption image of DFAG-4T fibers at 1600 cm^{-1}. We measured scattering absorption by taking the ratio of pixel intensity averaged over the dotted line on one of the fibers relative to the average over the hatched region on the background SiO_2. c) Histogram of raw data in image (c). The red line shows a two-Gaussian fit to the histogram data, indicating the scattering intensity of background versus sample.

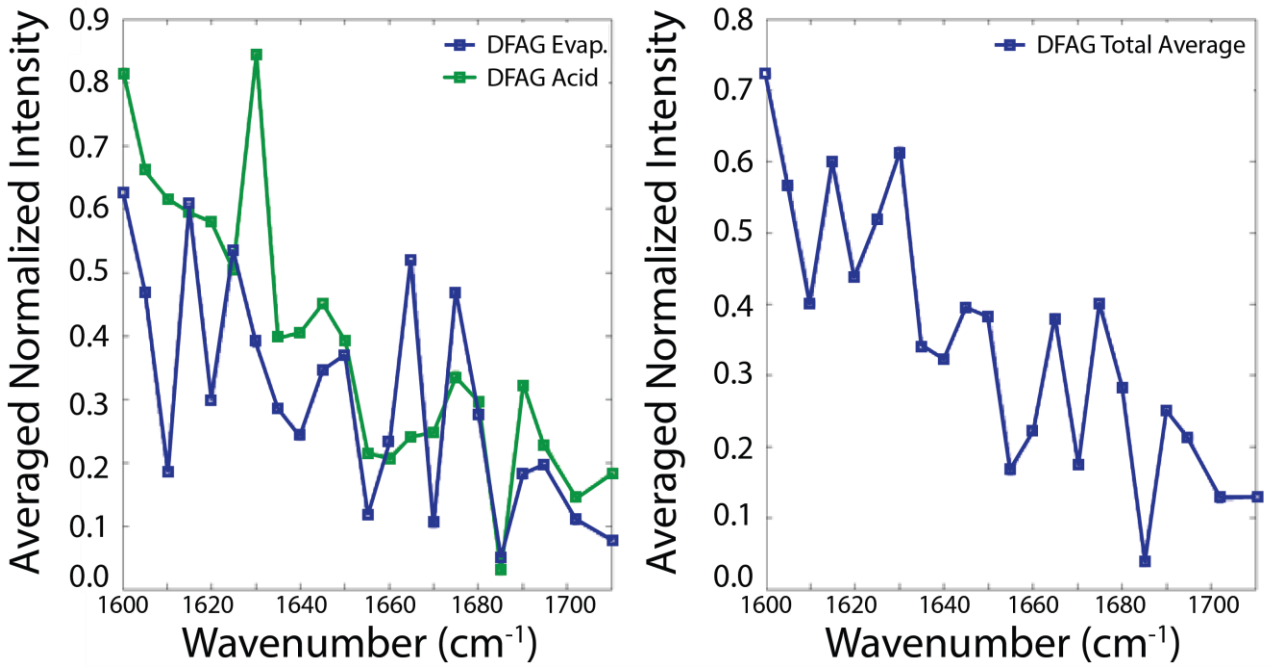

Figure 5.12 Comparison of averages for imaging scattering spectra from DFAG-4T. Left: Evaporatively assembled peptide compared to peptide fibers formed via acid-mediated assembly. Right: Average over all DFAG-4T peptide fiber measurements.

CHAPTER 6:

CONDUCTIVE PROBE ATOMIC FORCE MICROSCOPY

INTRODUCTION

As our ultimate intention behind developing self-assembling functionalized oligopeptides is to create semiconductor devices, it is imperative to thoroughly characterize their optoelectronic properties. My predecessors have conducted preliminary investigations of the unique characteristics displayed specifically when shear-flow is used to prepare peptides very similar to those we have been using. These experiments were the first indications that shear-flow could induce optical properties such as uniform polarization and electrical properties such as increased conductance in these systems [5]. However, these early experiments were done by hand and the results are difficult to repeat consistently. While these enhanced properties are consistent with what we would expect from increased intermolecular π-stacking and aligned microdomains given the current understanding of organic semiconductors [62,63], demonstration of consistent assembly via microfluidics leading to consistently reproducible optoelectronic properties represents a significant boon for device-oriented applications.

Further, collaborators have engaged in valuable research on characterizing self-assembling π-conjugated peptide nanostructures like those we have used, most notably through thin film field-effect transistor (FET) architectures to characterize hole transport and voltage equilibrium in drop cast films [17]. However, these are bulk measurements of randomly oriented fibers. Bulk measurements of organic thin films are analogous to those of amorphous semiconductors in that

measurements of the bulk are highly dependent of the order at different scales and can have very little indication of the material's intrinsic properties [62,132]. Continuing the analogy, morphological factors such as grain boundaries and local defects have a marked impact on optoelectronic properties, especially charge carrier mobility [133]. Compared to the free electron wavefunctions and densely populated energy bands of traditional semiconductors, organic materials have discrete energy states and localized charge carriers, like solitons caused by isolated charges between different segments of an oligomer chain adopting different conformations. Otherwise, charge transport within organic molecules occurs as separated charge pairs called excitons or as polarons or bipolarons caused by the addition or removal of electrons which result in local lattice distortions [132].

Additionally, the overall transport of an organic material versus an individual molecule must not only account for intramolecular conformational changes and charge transport, but also intermolecular charge carrier hopping, which usually happens less frequently [132] and can approximately modeled by

$$k_{et} = \left(\frac{2\pi}{\hbar}\right)\frac{H^2}{\sqrt{4\pi\lambda k_B T}}FC \qquad (6.1)$$

where k_{et} is the hopping rate, $\hbar$ is the reduced Planck's constant, H is the matrix element describing donor and acceptor state overlap—higher for stronger intermolecular electronic coupling, λ is the reorganization energy—a function of bond length changes, FC is a sum over exponentials representing all possible vibrational overlap due to the Franck-Condon principle [11,134,135], and k_BT is the thermal energy. In the language of solid state devices, charge carrier transport in the bulk

material occurs between discreet states and transitions must be phonon-assisted; thus, charge transport can have a strong dependence on temperature [135]. Thermal considerations aside, the highest mobilities are achieved with largely overlapping orbitals and highly delocalized π-electrons. These maximize Eq. 6.1 by satisfying higher molecular charge coupling along with small reorganization energy, respectively [11,134].

By extension, the band gaps and energy levels of organic semiconductors are more accurately represented by the separation between their highest occupied molecular orbital (HOMO) and lowest unoccupied molecular orbital (LUMO) with discrete energies on either side of the gap which can be approximated as two Gaussian distributions (Figure 6.1) [136] rather than wide, essentially continuous valence and conduction bands. This also means that the line between HOMO/LUMO levels and trap states can be blurred as many sources of localized trap states are inherently connected to the overall discrete nature of charge transport. In addition to solid state-type sources of charge carrier trapping such as impurities, polaron/bipolaron self-trapping and structural defects such as variations in effective conjugation length can hinder charge transfer. Another peculiarity of organic semiconductor charge transfer are excitons that can't recombine due to selection rules but remain unseparated, also known as Germinate pairs. Localized states often hinder charge transport and can give rise to hysteretic effects in switching devices and limit switching speed, a critical challenge to organic transistors [137]. Herein also lies the importance of achieving order consistently across as many length scales as possible. The carrier mobilities and other transistor properties measured for drop cast films [17] only represent the properties of the material with that microscale morphology and may not be the same for the same material deposited via other means. Different microscale ordering can influence the degree of intermolecular orbital overlap and electronic coupling, significantly impacting the ultimate charge separation and transfer

characteristics, even leading to enhanced mobility and band-like transport of delocalized charge carriers [138]. Understanding the properties of a specific system at the molecular level can inform what sort of order is ideal at larger and intermediate scales. Variations on scanning probe microscopy, such as scanning Kelvin probed microscopy (SKPM) [139] scanning tunneling microscopy (STM), mechanically controlled break junctions, STM break junctions and CP-AFM [140] represent techniques that should allow us to characterize individual fibers and anticipate the device-scale properties achievable with aligned fibers.

A final consideration that must be taken into account in the proceeding section is the importance of not only characterizing the current-voltage (*I*-*V*) characteristics of the material in question, but also characterizing the interactions between the material and the electrical contacts. Molecule-electrode coupling and electrode material choices can dramatically impact the measured *I*-*V* characteristics [133]. These contact effects can dominate behavior in the ballistic regime and are otherwise difficult to parse from the material characterization measurements [141], which is unfortunate given the difficulty of achieving ohmic contact between an organic semiconductor and a metallic contact [11]. Instead, most organic semiconductor to metal junctions form Schottky barriers with diode characteristics. Most metals have work functions that are too high relative to an organic semiconductor's HOMO, and most organic semiconductors rely upon injection of electrons from the metal. When the Fermi energy of the metal lies right in the semiconductor bandgap the easiest solution is often to preferentially dope the semiconductor near the contact interface [11]. Conduction at the contacts must thus occur through carrier diffusion, thermionic emission, or quantum tunneling. The dominant mechanism is determined by the specific materials, doping concentrations, applied bias, etc. These contact effects are compounded with the fact that with ideal contacts the actual *I*-*V* behavior is only ohmic at the lowest bias because current is

limited by carrier injection from the electrode. At higher voltages current becomes trap-limited and transfer properties follow a power law where $I \propto V^p$, where $p > 2$. And at high enough fields $p = 2$ and the current transition to the space-charge-limited current (SCLC) regime [66].

For CP-AFM operation, conductive tips—most commonly made by coating standard tips with gold or platinum—are mounted to the AFM using a specialized holder with an electrical connection to operating controls allowing the user to bias the tip-sample system to induce electrical current. Typical AFM tips are on the order of 10-20 nm in diameter, leading to tip contact areas with the sample on the order 100 nm^2 [64,65]. The complex morphology of the tip-sample interaction region means that assumptions must be made with regards the electric field at the tip [66], and geometrical effects must be taken into consideration. For example, mobility measurements in fibers that are wider than the tip-sample interaction area are significantly complicated unless fiber length>>width, and even then the mobility measurements must be underestimates [138].

There are three fundamental measurements that can be done with CP-AFM. First, if the sample is deposited on a conductive substrate, the probe tip can be scanned across the sample in contact or tapping mode to create a map of transverse conductivity and/or to collect *I*-*V* curves for the properties in the transverse direction. Second, if the sample is deposited such that it contacts an electrically conductive terminal on one end but primarily rests on an insulating substrate, then the probe tip can be used as a movable electrode for longitudinal electronic transport measurements [142]. Third, an expansion of the second method, the insulating substrate below the sample is itself deposited on a conducting substrate—a layer of SiO_2 on a highly n-doped Si wafer for example—and, thus, creates a FET with the AFM tip operating as source or drain. This nanoFET permits

valuable mobility measurements in organic fibers. In the latter two cases, electrode pads are typically first deposited on the insulating substrate and the semiconducting material is drop cast or otherwise placed on top of the conductive pad. The sample is then scanned to reveal regions where sample material is draped over the electrode. Collecting *I-V* curves for different gate and drain voltages would facilitate calculating electron mobility of the sample and help inform its suitability for creating organic FETs.

For FET measurements, care must be taken to account for shifts in threshold voltage due to weak gating efficiency when there is an air gap between fibers—especially stacked fibers—and the electrode pads upon which they sit [138]. Furthermore, the extremely small contact area implies very high contact resistance. Luckily the contact resistance and the intrinsic mobility can be separately extracted via the transmission line method in which transistor properties are measured at successive points along the fiber, essentially varying the channel length, L with each measurement. The channel length is linearly related to both resistances as

$$R = R_{Ch} + R_C = \frac{L}{W\mu_i C(V_G - V_T)} + R_C \qquad (6.2)$$

where R_{Ch} and R_C are the channel and contact resistances, respectively, W is the channel width, μ_i is the intrinsic charge carrier mobility, C is the capacitance per unit area, and V_G and V_T are the gate and threshold voltages, respectively [138]. Thus, the contact resistance is simply the *y*-intercept of the resistance as a function of L. The primary parameter of interest, μ_i can also be obtained from the slope of this line given known values for the other parameters.

Furthermore, there is a well-established Arrhenius relation for conductivity in both n-type and p-type organic semiconductors [143]. That relation guides the use of a method for determining the free carrier mobility, μ_0, known as the multiple trapping and release (MTR) model:

$$\mu = \mu_0 \exp\left(\frac{-E_a}{k_B T}\right) \tag{6.3}$$

where μ is the observed mobility, and E_a is the energy difference between a trap state and the conduction band edge or LUMO. This model assumes that the observed mobility is a result of charge carrier trapping in shallow localized states, reducing the free carrier mobility [138]. In such temperature dependent measurements, however, one must not neglect that the possibility of high contact resistance also means a possibility of significant Joule heating. While unintentional Joule heating can obscure measurements and damage a sample, in other situations the tip can be deliberately used for local sample annealing [65].

One may also extract the transverse charge carrier mobility from known parameters and measured quantities using a modified version of the Mott-Gurney model [66]. The need for modification arises from the complicated tip-sample geometry compared to the planar geometry of typical thin film transistors (TFTs) for which the model is intended. It's further necessary to convert measured currents into current densities, J using geometric assumptions. Wood et al. (*J. Phys. Chem. C*, 2015) introduce a modified version of a semiempirical formula introduced by Reid et al. (*Nano Lett.* 2008) for use in the SCLC regime

$$J = \alpha \epsilon \epsilon_0 \mu_0 e^{0.89\gamma\sqrt{V/L}} \frac{V^2}{L^3} \delta_J \left(\frac{L}{2r_c}\right)^{1.6\pm0.1} \tag{6.3}$$

where ε and ε_0 are the relative and vacuum permittivity, respectively, L is the channel length (thickness in a thin film), α is a numerically defined prefactor to account for nonuniform electrical field, $\delta_J = 7.8 \pm 1$ is an empirically derived constant determined by Reid et al., r_c is the contact radius, μ_0 is the mobility at zero bias, and γ is the strength of the mobility's field dependence [66,131]. A detailed explanation of how this equation modifies the Mott-Gurney model to account for the conical and spherical nature of the AFM probe and tip can be found Reid et al [131]. The last two parameters, μ_0 and γ are free parameters to fit the experimentally measured current densities.

METHODS

Materials Synthesis

Sequence-defined synthetic peptides with π-conjugated cores were synthesized using solid phase peptide synthesis (SPPS), as previously reported [2]. The π-conjugated oligopeptides containing an oligo(p-phenylene vinylene) (OPV3), quaterthiophene (4T), or perylene-diimide (PDI) core were flanked by symmetric peptides with a primary amino acid sequence Asp-Phe-Ala-Gly (DFAG). The overall sequence of the π-conjugated oligopeptides the same except for the functional core and can be written as, for example, HO-DFAG-OPV-GAFD-OH, abbreviated as DFAG-OPV.

Sample substrate and electrode preparation

We purchased interdigitated array (IDA) electrodes with a 2 μm gap from ALS Co. (Catalog No. 012257). These electrodes are Pt on a glass substrate. In addition, we prepared custom

electrodes on chips separated from regular Si wafers as well as highly n-doped (0.001-0.005 Ohm-cm) with 300 nm wet thermal oxide purchased form University Wafer (Catalog No. 2373). We deposited Au electrodes between 10 nm and 50 nm thick on top of a 2 nm Ti adhesion layer per the literature for similar electrode setups [144,145] using a Temescal six pocket E-beam evaporation system. Electrodes were patterned with both shadow mask and photolithographic techniques to achieve optimally smooth and sharp electrode edges for ideal draping of peptide fibers from electrode to substrate. The two primary designs were a single large pad (~1 cm^2) and an array of small (~50 μm) square pads achieved by using a transmission electron microscopy (TEM) sample support grid mesh as a shadow mask. The rational behind using smaller pad sizes is to minimize the chance of shunt short circuits through pinhole defects in the SiO_2 layer.

Electrical and structural characterization

Macroscopic conductive probe *I-V* measurements were carried out with a Keysight B1500A under a nitrogen atmosphere. We tested the structural integrity of the fibers using an Asylum Research MFP-3D AFM with contact mode tips (k ≈ 0.2 N/m) with a 5nm Cr and 25 nm Pt coating (BudgetSensors, ContE-G). These were also used or subsequent electrical measurements as well as various solid Pt tips (20 nm tip radius with k ≈ 0.8 N/m & 8 N/m, 10 nm tip radius with k ≈ 0.3 N/m) (Rocky Mountain Nanotechnology, 12Pt300B, 24Pt400B, 12Pt400B-10). For CP-AFM we used the ORCA conductive AFM accessory. The ORCA tip holder keeps the tip at ground while applying a bias through an external wire which must be attached to an electrode on the sample. Samples were mounted on glass slides and silver paint was used to draw a conductive path from the sample electrode pads to the glass slide periphery for easier connection to ORCA electrode. For transistor samples using the highly doped Si substrate, we use common adhesive tape at the wafer chip edge to prevent short circuiting connection. We further employed

adhesive tape when contacting to pads made by the TEM grid shadow mask in order to minimize the chance of point defects in the SiO_2 contacting the n-Si to the silver paint. Finally, the AFM system is enclosed in a housing that can be flushed with N_2 gas. We experimented with both N_2 flushing and heating with the BioHeater and Environmental Controller accessory to reduce humidity and surface water layers.

Additional structural characterization was conducted using Hitachi S-4800 and S-4700 high resolution scanning electron microscopes (SEM).

For transfer property measurements using the CP-AFM-based transistor architecture using a Keithley 2412 source measure unit (SMU) to provide the gate bias. An SMU was used as opposed to a standard power supply because the SMU allowed us to limit current to 20 nm, the same limit for the ORCA AMF accessory, thus preventing damage to the ORCA tip holder. An equal ground reference to that used by the ORCA and MFP-3D electronics was established by connecting the LO pin to the grounded exterior cladding of a coaxial input connection on the MFP-3D controller.

RESULTS AND DISCUSSION

Macroscale electronic probe measurements

Before beginning CP-AFM measurements, I worked with collaborators to attempt probe-station-scale electronic characterization of the fibers. We deposited DFAG unassembled peptide solution in methanol into IDA electrodes with 2 μm spacing and allowed the material to evaporatively assemble. Methanol was chosen as a highly volatile compatible solvent that accelerate evaporative assembly. Given the nanoscale by microscale aspect ratio of the fibers, we

deemed the 2 μm electrode spacing to be sufficiently narrow for individual fibers to span the gap from anode to cathode. This allowed, if not single fiber measurements, at least measurements of many single fibers in parallel. Measuring the *I-V* response in a two-point probe geometry, we obtained roughly antisymmetric curves with apparently one regime from -5 V to 5 V and another from -10 V to -5 V and from 5 V to 10 V (Figure 6.2a). The overall structure is like that of a rectifier or back-to-back diodes [141]. As the material is at best a p-type semiconductor, there is no obvious diode behavior coming from the material itself. Rather, contact effects must be dominating in the form of a Schottky barrier at each fiber-electrode contact [10,11,141]. Notably, the open loop hysteresis of the *I-V* curves may indicate capacitive charging and the resistive random-access memory (ReRAM) effect [146]. Furthermore, there was a reduced current response for measurements made over a bias range of ±40 V and above (Figure 6.3). Similarly, curves I6 and I7 of Figure 6.2a demonstrate that after an exceedingly high bias was applied (100 V in this case) the previous *I-V* activity could not be recovered at lower bias sweeps.

CP-AFM conductive imaging

Concurrent to the aforementioned probe measurements we began investigating the material on a true single-fiber level with CP-AFM. The first step of this process was to verify that the AFM could be operated in contact mode without damaging the fibers or plowing them around the substrate. While resolution is inferior to tapping mode, contact mode is preferred for CP-AFM measurements to maintain consistent electrical contact [138]. While the upper layers of thickly deposited fibers clearly shifted between scans, sparsely deposited fibers in contact with the substrate (electrodes or insulating portions) for the length of the fiber remained in place after multiple scans (Figure 6.4).

We thus turned to investigating the samples used previously in the probe measurements. Surprisingly, we found that the electrodes had trenches deeper than 0.1 μm (Figure 6.5), making it nearly impossible to trace a single fiber from one electrode to the other. Further investigation of the electrodes revealed that not only are the electrodes separated by deep trenches, but also the electrodes have a mounded topography on top and sit at a lower height than the background glass material (Figure 6.6). This realization cast serious doubt onto our ability to accurately correlate any probe-scale measurements with the actual fiber properties by introducing too many unknowns to the surface geometry. We thus abandoned these electrodes and investigated custom electrodes made of 10-50 nm Au on 2 nm Ti.

The first step in measuring conductive properties of the fibers was to start with the easier transverse conductivity measurements. It should be noted that one useful feature of the IDA electrodes was their function as a good standard for testing our ability to measure current independent of topography with the ORCA accessory (Figure 6.7). For these measurements we looked at regions where fibers were simply drop cast onto a Au substrate. We performed two types of measurements: imaging and point. For imaging measurements we operated the AFM in contact mode with a 0.5 Hz scan frequency in a 25x25 μm region to find areas of well-formed, sparsely deposited fibers. We then operated between 0.5 Hz and 1 Hz in 5 μm regions while applying a bias between 50 mV and 4 V. Initial scans on Au revealed a high degree of correlation between the Au layer topography and the current measurements (Figure 6.8) and after several scans looking for a relevant region it would become impossible to measure any current at reasonable voltages. Likely explanations for these various difficulties include erosion of the metallic coating at the tip apex by successive scans [147], melting of the conductive coating at high voltages due to Joule heating, and removal of the conductive coating by stray shocks of static electricity. With the conductive

coating removed it can be hard to tell if measured diode behavior is due to the sample or to the interactions between the Si of the exposed tip bulk between the conductive coating the conductive substrate. Given the initial difficulties of finding an appropriate scan region and determining if the probe was on a fiber only nanometers thick, we decided to eliminate these additional sources of error by purchasing solid Pt tips. The advantage of solid Pt tips is that even though the tips may dull or become contaminated after multiple uses as any tip may, there is no concern of losing the ability to establish an electrical connection with the sample and surface features. (Granted, significant contamination could serve as a boundary to electrical contact, but by the time this would happen it's likely that the tip would perform so poorly in imaging that it would be discarded anyway.)

By scanning slowly over small regions we were able to conclude that without any gate potential, the fibers act as electrical insulators on the Au substrate (Figure 6.9). The best images were acquired using the solid Pt tips. This is unsurprising given the fact that a classic semiconductor should also be insulating unless a high enough bias is applied as well as the fact the primary conductive pathway—that with the longest stretches of π-orbital overlap—extend along the length of the device, but the amino acid side chains that give the fibers structure are themselves insulating. We did however have difficulty with achieving good conduction contrast in many samples such as those shown in Figure 6.10. While some fibers are clearly visible, the background also has a cloudy appearance, indicating diffusely deposited fine material. We have not found a suitable explanation for the craterlike structures. All these structures were visible in some samples regardless of substrate, indicating that they are not simply artefacts related to the substrate itself. The situation appeared to have ameliorated in later samples. The most likely explanation is that early samples contained some form of contamination, but the source of that

contamination remains a mystery. Finally, one question that remains to be answered is if these insulating side chains make the fibers analogous to wires cladded in insulation, or if the pitch of the helical turns is wide enough such that regions where monomeric units are parallel to the surface permit easy carrier injections from a conducting substrate to the semiconductor.

CP-AFM single-point I-V *curves*

The second form of measurement, point measurements of *I-V* spectra, were significantly more challenging because of the very narrow fiber widths, on the order of 5 nm. Following a protocol similar to that conducted on similarly small fibers [144,145] we scanned a zoomed in region near a fiber 2-3 times to ensure no change in topography, directed the AFM tip to sit on the fiber, collected *I-V* data, then reimaged the same region to ensure no changes. Fibers would often not conduct until a bias of at ~3-4V was applied. After reaching that bias threshold, the fibers not only exhibited Ohmic behavior, but the resistance seemed to decrease with each successive sweep of the applied bias (Figure 6.2b). We found that the same behavior could be achieved by sweeping at a slower rate (slower the rate, more quickly the onset of current flow) or by sitting on the wire with a steady 4V bias applied. Curiously, this behavior is reversible up to a point. For example, sweeping the bias across ±3 V will yield an Ohmic response after the first few sweeps, but subsequently sweep over just ±1 V the material will return to higher resistance and/or insulating behavior.

Eventually, however, after the bias is raised the material will stop conducting altogether. A possible explanation for this behavior is that Joule heating from the enhanced electric field is pushing the material above its glass transition temperature and drastically increase the free carrier mobility [143]. The cessation of electrical conduction is occasionally accompanied with a visible break in the fiber near the tip location that did not exist in scans prior to voltage sweeping. This

behavior may be indicative of rupturing due to excitation of vibrational modes of the material at resonance [140,148]. If the rupture was entirely due to a thermally activated process or mechanical instability of the tip, then rupture should occur with equal probability regardless of applied voltage. The fact that rupture appears to be voltage-dependent indicates electrical bond interactions such as voltage-induced bond weakening [140,148]. However, if the increased voltage is causing significant Joule heating then it could be difficult to parse the effects.

We also noticed that when imaging at elevated voltages, the fibers appeared to be dragged across the surface when they would not at lower voltage. One possibility is that the enhanced electric field created at the tip apex interacts with dipole moment of the fibers, which is transverse to their length, and creates an attractive force strong enough to overcome van der Waals forces keeping the fibers on the substrate.

Longitudinal conductance and nano FET architecture

After establishing generally semiconducting transverse behavior for the fibers we proceeded to measure longitudinal properties. Creating appropriate custom electrodes became a significant challenge as a clean edge is necessary for fibers to nicely lay across the electrode onto the insulating surface below. Conventional photolithographically defined features were challenging to make because photoresist removal would often cause Au liftoff near the electrode edges (Figure 6.11) and for the finer features of the TEM grid (when used as a photomask rather than a shadow mask) it was difficult to not leave behind excess photoresist on the one hand or remove too much from the features on the other (Figure 6.12). Furthermore, electrodes created by shadow masks tended to have faded edges that very gradually sloped from full height down to the SiO_2 layer, making it difficult to discern the true edge (Figure 6.13). We were ultimately able to

make the best measurements by using centimeter-scale Au pads that were defined with photolithography using paper adhesive tape as a photomask.

The approach we used for measuring longitudinal conductivity was to image at zero applied bias near the electrode edge until finding a region with several long, isolated fibers extending across the Au-SiO_2 interface. Then we would zoom the scan area such that the electrode was excluded just beyond the image frame. Finally, we would apply a bias between 50 mV and 4V then scan the same region, measuring any current. The expectation was that if there is longitudinal conduction, the fibers in contact with the electrode should be visible in the conductivity map and that visibility should decrease along the length of the fiber away from the electrode edge [144,145]. However, we were unable to measure any such conductivity.

Given that similar material in the literature also showed no conductivity at zero gate bia [144,145] we continued to set up the transistor architecture to apply a gate bias and measure the material's transfer properties. Unfortunately, we were unable to measure any fibers with an applied gate bias of ±6V. One possible reason could be poor connection and increased threshold voltage due to the dielectric water monolayer that will form on nearly any surface not in a dry environment [131,133]. For this reason, all samples were stored when not in use in an N_2 dry box. We thus flushed the chamber containing the AFM system with N_2 gas. We also tried mounting samples on the BioHeater accessory to simultaneously bake off the water layer. Interestingly, measuring the transverse electrical properties when applying a +6 V gate bias with a positive drain bias (V_D) we noticed a change in the current flowing proportional to the change in V_D; lowering V_D resulted in lower measured current between the Au pad (source) and AFM tip (drain) (I_{SD}). Furthermore, applying an equal but opposite V_D saw a similar trend but with significantly lower magnitude. This seemed to indicate that the positive gate bias was effective; however, flipping the gate bias to -6

V did not change the previously observed trend in V_D, which would indicate a poor gate connection. Thus, a more reasonable explanation for the difference in response for varying positive V_D vs negative V_D is that while the gate electrode is poorly connected, hole injection is more efficient than electron injection at the tip-peptide interface, which is consistent with the p-type nature of the peptides' quaterthiophene cores [66].

CONCLUSIONS AND FUTURE WORK

We have established the semiconducting nature of drop cast DFAG-4T fibrils in the transverse direction; however, there is significant room for further investigation into the properties of that semiconducting behavior as well as deeper probing of their longitudinal electrical properties. Scanning tunneling microscopy (STM) is a common analogue of, and complement to conductive AFM measurements and is often used to determine a material's density of states (DOS). Such DOS measurements could be invaluable toward mapping the energy levels of our samples, determining their bandgap as well as HOMO and LUMO levels [149]. However, STM measurement may prove intractable as our materials seem to be dominantly resistive, and many organic thin films are too resistive for STM probing [147].

In addition to STM, there are several other AFM-based scanning probe measurements which could prove useful. For example, electrostatic force microscopy (EFM) can be a valuable non-invasive method of probing fiber current as well measuring sample capacitance [150,151]. If fibers are connected between two electrodes on the substrate surface and an alternating current is applied at a different frequency from the tip oscillation, sample capacitance and charge transport

can be extracted through sum and difference frequency analysis of changes in force as a biased tip is passed over the sample [151]. Unfortunately, EFM has several drawbacks including the need for a more complicated experimental setup including a lock-in amplifier as well as decreased resolution due to potential interactions of the electrical field with the cantilever and to electric field spreading between tip and sample [133]. However, the ability to probe the fibers without physically contacting and disturbing them as well as the possibility of extracting capacitance information warrant further consideration of EFM.

Given the ultimate LED or PV potential applications of these materials, it will also be important to test their photoresponsivity. Preliminary evidence from probe station measurements indicate that the DFAG-4T fibers are photoresponsive because the *I-V* curves changed when the sample was illuminated. Such properties can be probed in more detail at the single-fiber level using Kelvin probe microscopy (KPM). In particular, intensity modulated scanning KPM (IM-SKPM) can provide a valuable measure of charge carrier lifetime by measuring the time averaged tip-sample contact potential difference in response to a more rapidly modulated illumination source [139]. The easiest first step toward measuring the photoexcitation response of the fibers would be to make the same measurements as done with regular CP-AFM but with an external excitation source such as a solar lamp and to compare the results. Yet, a supplemental technique dubbed time resolved EFM (trEFM) combines EFM with an external excitation source in order to measure induced photocurrents that require attoamp sensitivity in the ORCA accessory [139]. On the other hand, in all such photoresponse measurements it's important to account for the possibility of photoinduced electron emission due to the conductive tip acting as an antenna for the incident radiation energy [133].

In addition to branching out to more characterization techniques, there are many ways we could improve our current experimental setup. As one of the greatest sources of uncertainty is proper contact between the fibers and electrodes, we could further investigate the apparently clean and abrupt transitions from contact to insulating substrate seen in Figure 6.13 to deliberately create such scratches. The best idea might to use a nanoindentor or a dull AFM tip so as to minimize the risk of scratching off the SiO_2 layer as well and shorting the device circuit. Alternatively, first drop casting the fibers and afterward depositing electrodes with shadow mask patterning could significantly improve our ability to measure currents [133]. Moreover, placing the Au pads on top of the fibers could mitigate the uncertainty of where the Au-SiO_2 edge is with respect to where along the fiber can be considered to be in direct electrode contact. In the same vein, applying more pressure with the conductive probe tip might improve contact at the fiber-tip electronic interface. Throughout all the experiments in this chapter, tip forces were kept at a minimum (maintaining a 0.2 V deflection set point); rather than actually increasing the scan pressure directly, we resorted to rotating the scan direction by 90° to take advantage of the higher torque when we needed to correct poor tip tracking to the surface. While higher forces during contact mode still pose a problem of dragging more of the sample across the surface, increasing the force used in point scans could ensure that the delocalized electrons from the fiber core can communicate with the conductive probe. We could even use load forces to test the mechanoelectrical response of the material [133]. For the most reliable results it would be best to acquire many *I-V* curves for the above-mentioned methods such that statistical tools could be used [133].

Finally, the ultimate goal of this work has been to investigate the potential improvements in microscale to mesoscale semiconductor performance of controllably aligned, self-assembled peptide fibers with π-functionalized cores. Thus, the ultimate intention of all the work conducted

and proposed above for drop cast material would be to apply the same analysis techniques to aligned material assembled and deposited through the methods developed in the previous chapters. We believe with good electrical contact, the <4 Å core-to-core distances between stacked monomeric units along the length of the fibers should have band-like, rather than thermally activated hoping transport along the length of our fibers [152] and alignment of the fibers through to the microscale will give rise to large, well-connected electronic domains, ultimately yielding valuable enhanced charge carrier mobilities useful for many future device applications.

FIGURES

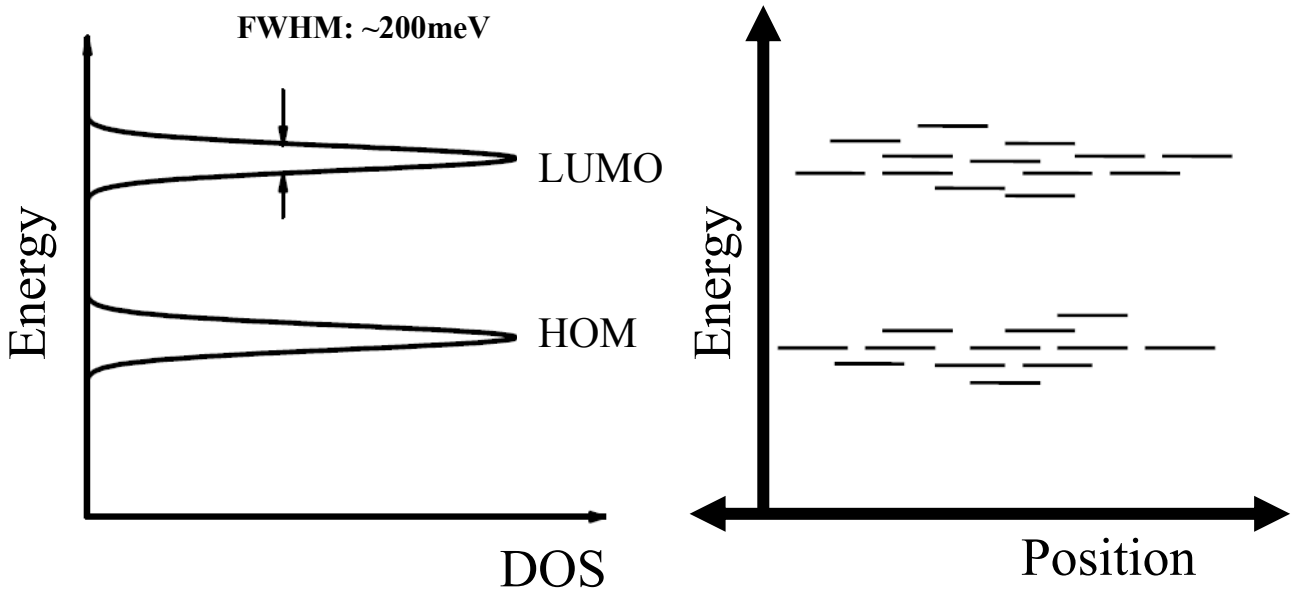

Figure 6.1 Organic semiconductor bandgap analogue. Right: Simplified representation of distribution of states in organic semiconductor. Left: Approximation of energy levels by density of states (DOS) as a function of energy. Adapted from Kondo 2007 [11].

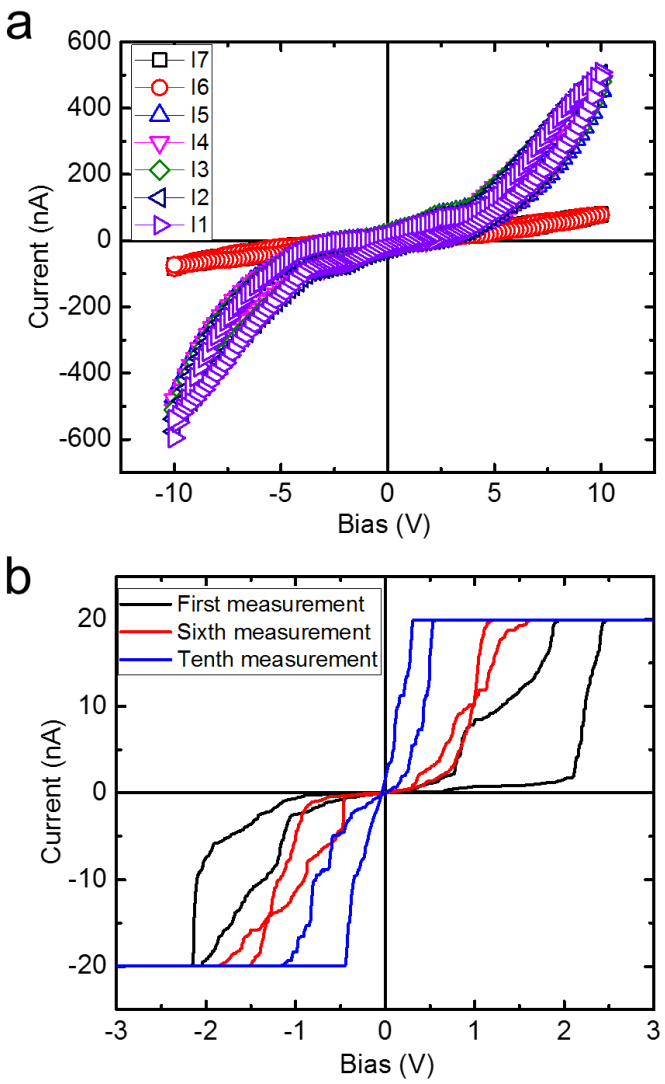

Figure 6.2 Conductance I-V *curves for evaporatively assembled DFAG-4T. (a) Probe station* I-V *measurements using IDA electrodes. The bias was ramped from -10V to 10V over multiple iterations before (I1-I5) and after (I6-I7) applying 100V. After application of high voltage, the* I-V *curves show a dramatic change, suggesting structural rearrangements under high bias. (b) Single point conductivity measurements of DFAG-4T fibers using CP-AFM show a tendency toward lower resistivity with consecutive sweeps in voltage.*

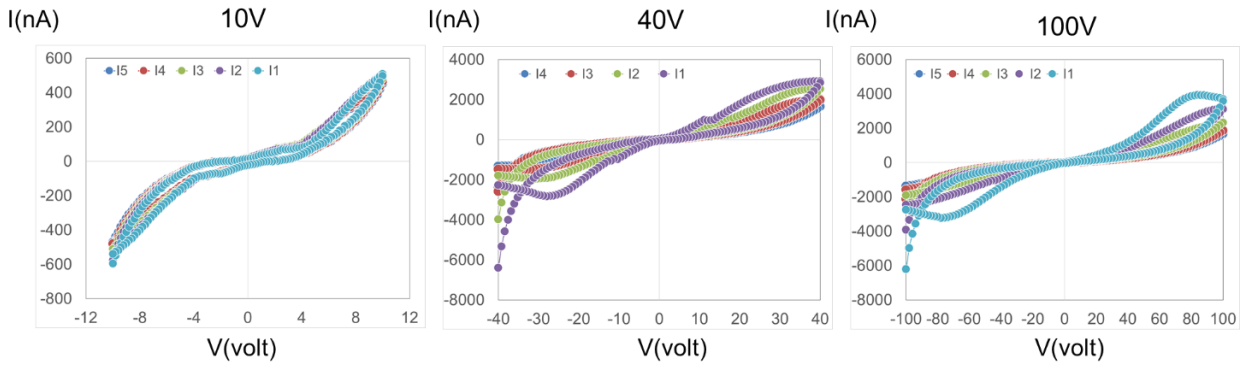

Figure 6.3 Charge transport properties of vaporatively assembled DFAG-4T characterized over varying bias ranges. From left to right, the plots show conductivity measurements of DFAG-4T fibers with decreasing current response upon increasing the bias from 10 V to 40 V to 100 V.

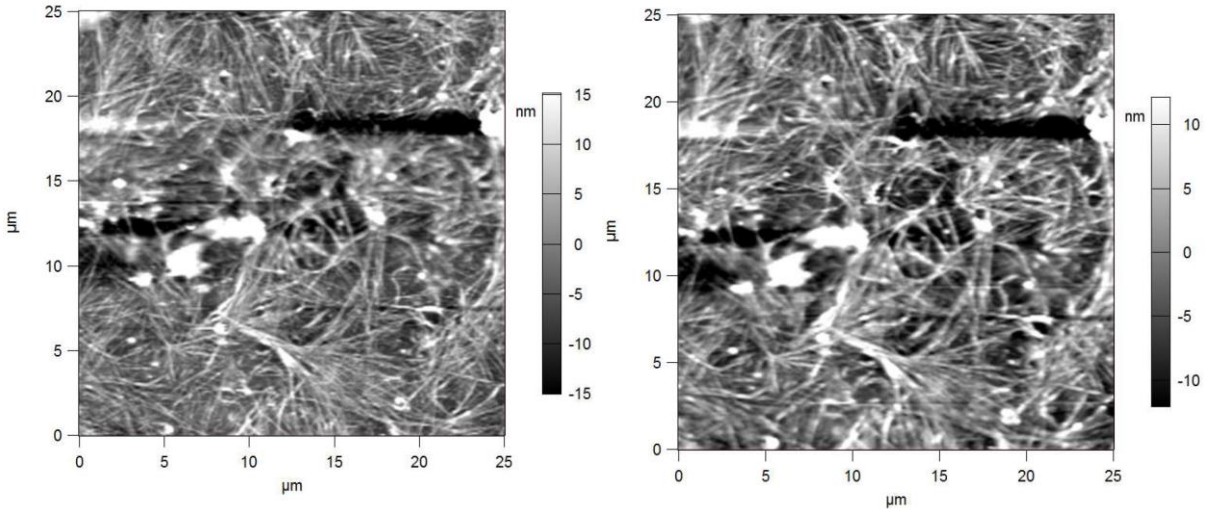

Figure 6.4 Contact mode disturbance test. Most fibers remain in place between before (left) and after (right) scans, but those that loosely rest upon other fibers get dragged away.

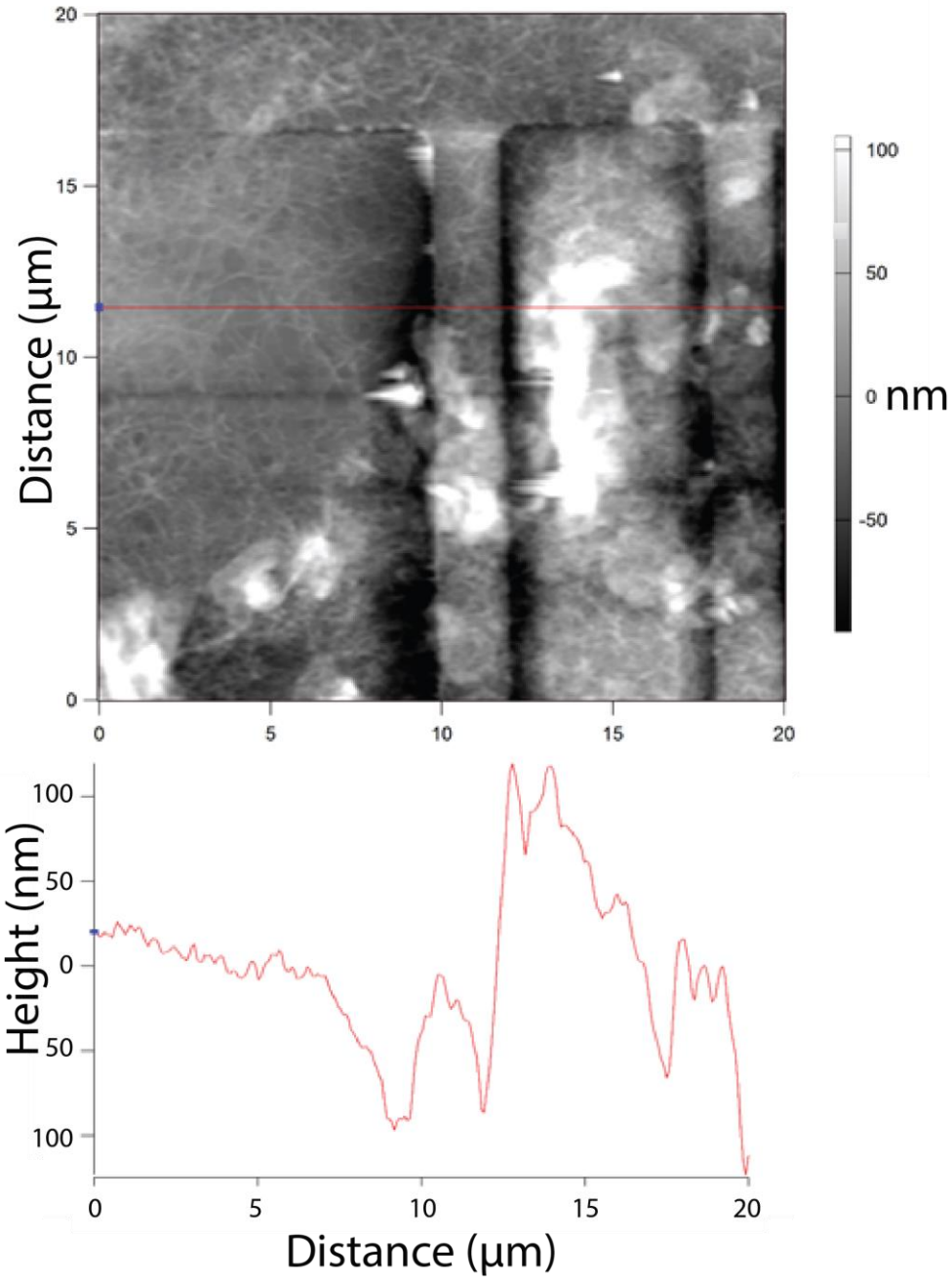

Figure 6.5 DFAG-4T samples on IDA. The bottom graph is height trace of the line cut shown in red on the top image. Deep trenches on either side of each electrode make it difficult to ascertain if fibers are truly draped from electrode to electrode, from electrode to substrate, or otherwise.

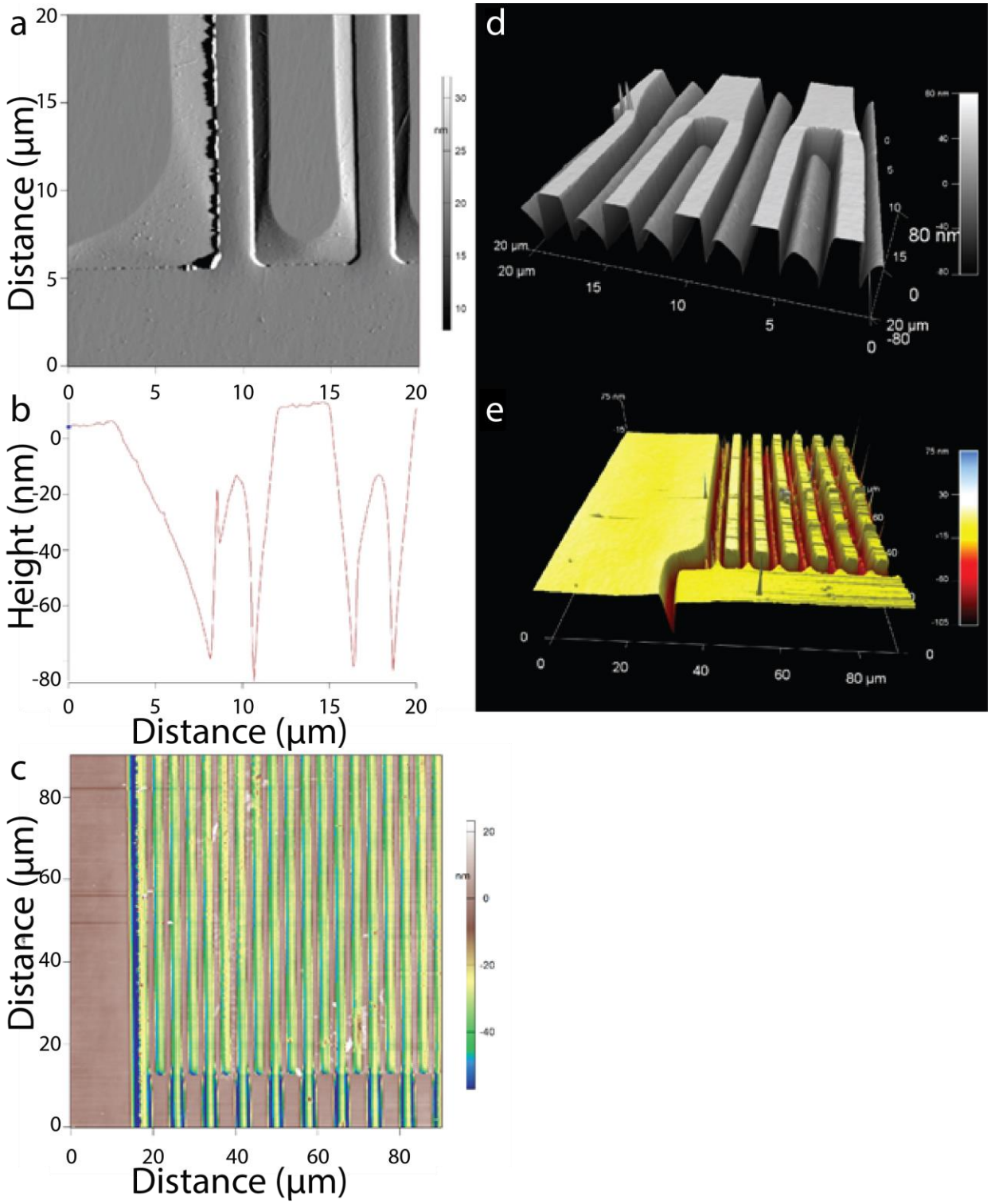

Figure 6.6 Trenching in IDA electrode. a) Topography at the base for electrode digits. b) Height profile of horizontal line cut across (a). c) Two dimensional representation of the base region for the digits of one side of the electrode with height mapped to color as indicated. d) Three dimensional reconstruction of electrodes where opposing digits terminate near base of other digits. e) Three dimensional reconstruction of (c).

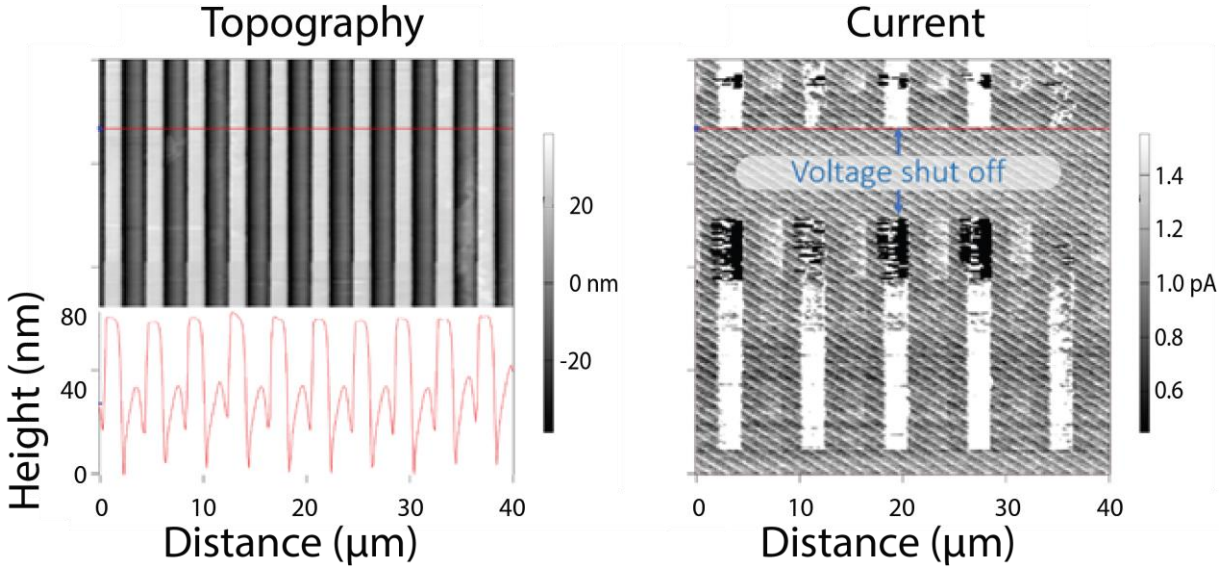

Figure 6.7 Corresponding topography and current maps demonstrate that we can accurately correlate conductive elements in an image with their physical position and that electrical measurements are not merely artefacts of physical topography. Notably, in the region where bias was reduced to 0, the current topography disappears while physical topography remains.

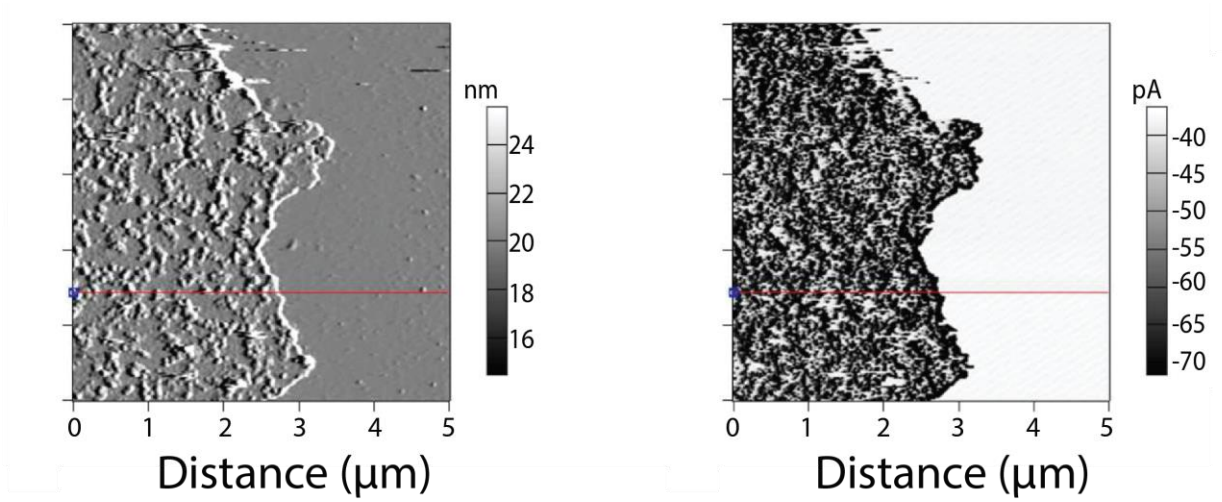

Figure 6.8 Corresponding topography and current maps as in Figure 6.7 of a custom made Au electrode edge. While the Au region is clearly distinguishable from the substrate, there also appears to be a high degree of correlation between the internal topography of the Au region and the corresponding current map, indicating the possibility of tip artefacts such as erosion of the metallic coating at the tip apex and selective conduction where convoluted surface features contact the tip sides that still retain their metallic coating.

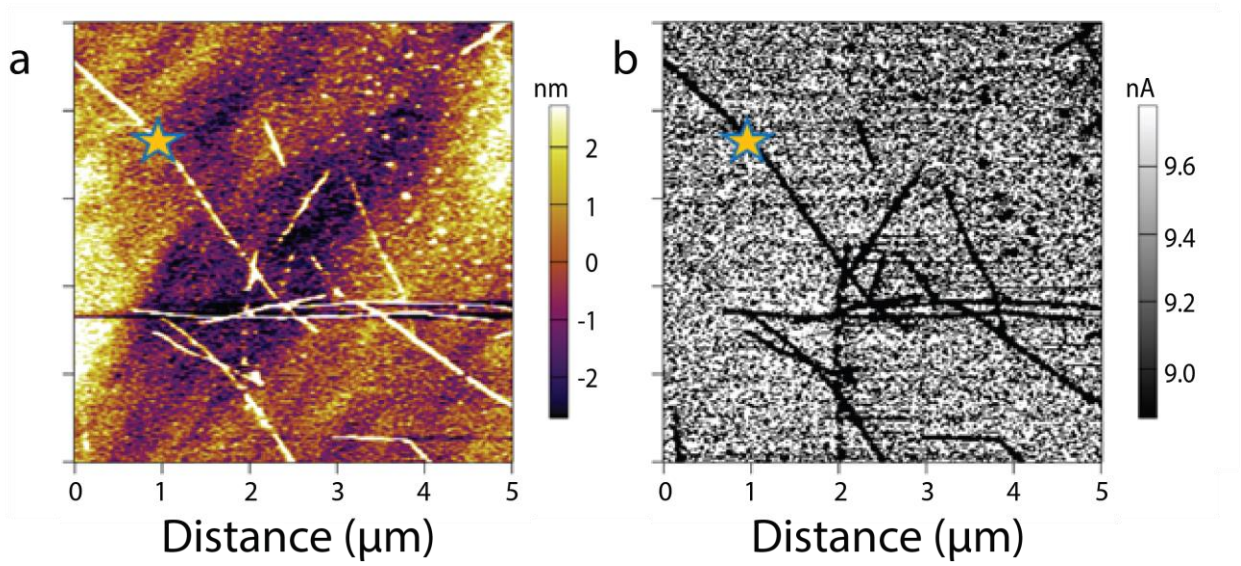

Figure 6.9 Charge transport properties of assembled DFAG-4T characterized using conductive AFM. (a) AFM height and (b) conductivity map of DFAG-4T fibers deposited on gold substrate using methanol as solvent. The star indicates where the point conductivity measurements of Figure 6.2b were made.

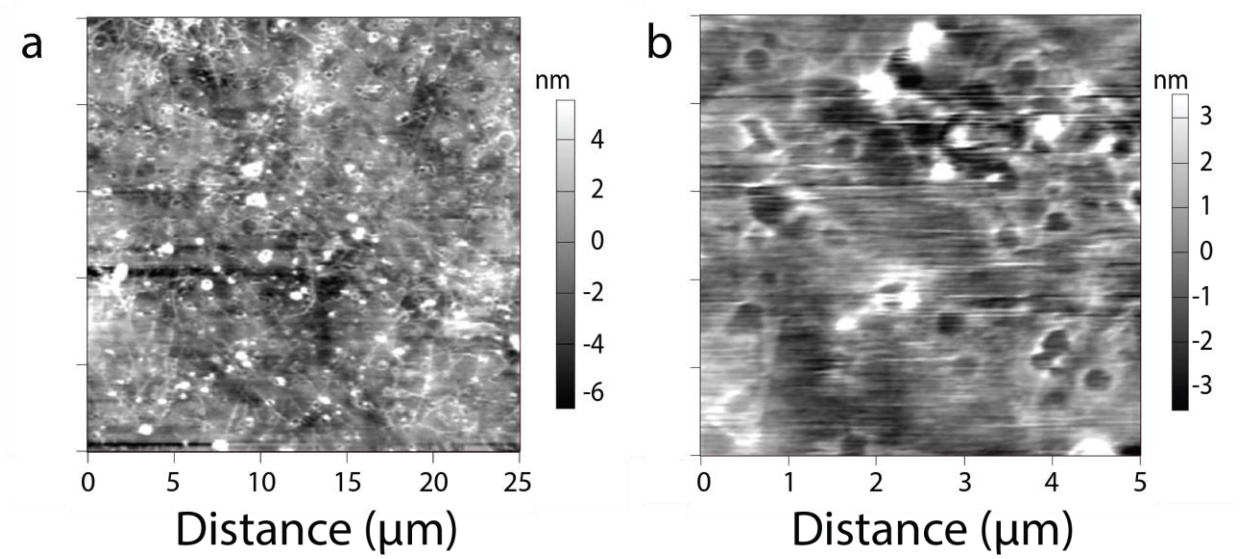

Figure 6.10 Possible evidence of contamination film in some samples. a) Wide-field scan on Pt substrate showing cloudy background and anomalous crater structures. b) Zoomed in region on Si substrate showing the same anomalous features as in (a).

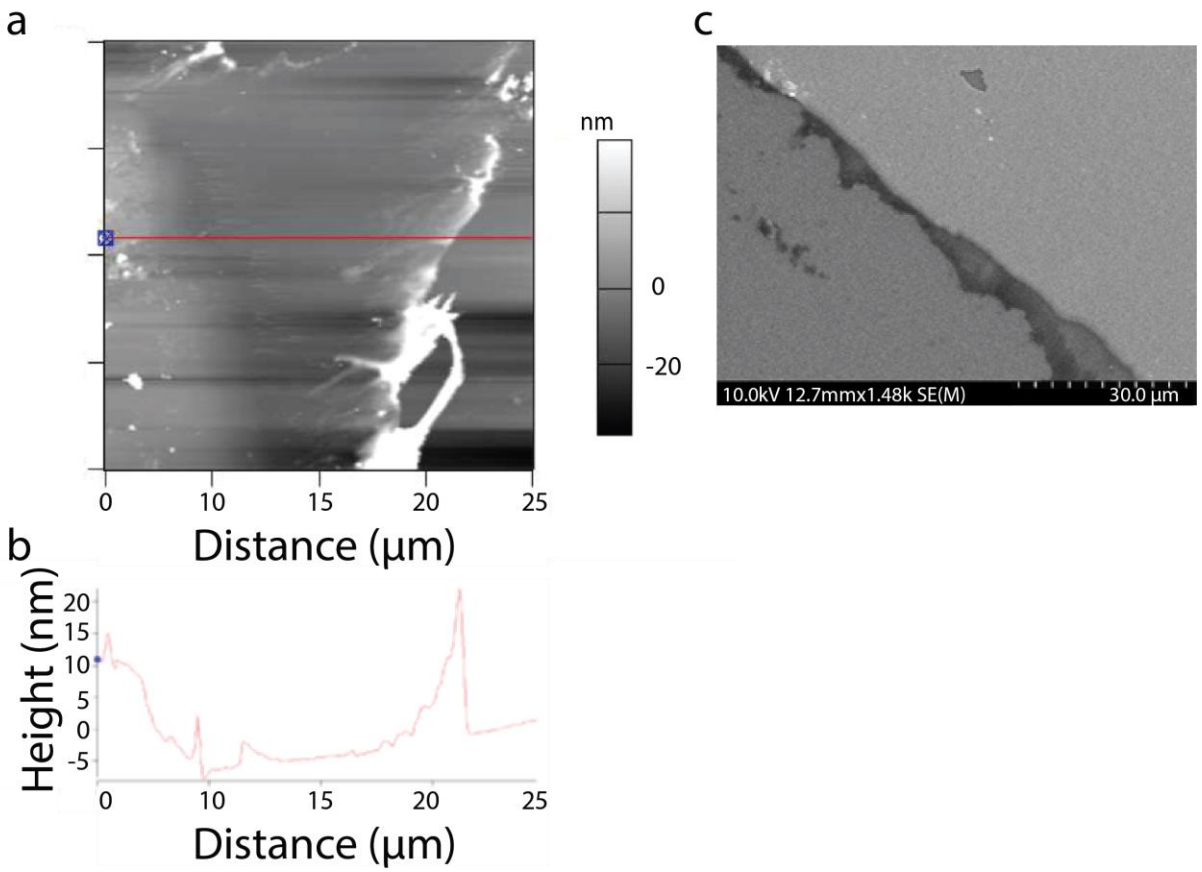

Figure 6.11 Electrode edge liftoff. a) AFM height retrace image. b) Height profile of horizontal line cut at the red line in (a). c) SEM image showing rough edge topography.

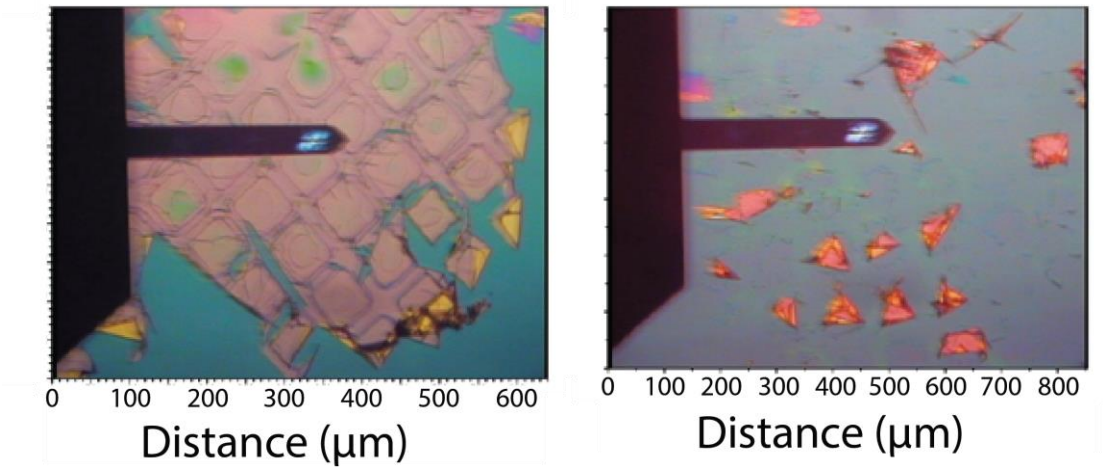

Figure 6.12 Optical micrographs of failed photolithographically defined electrodes.

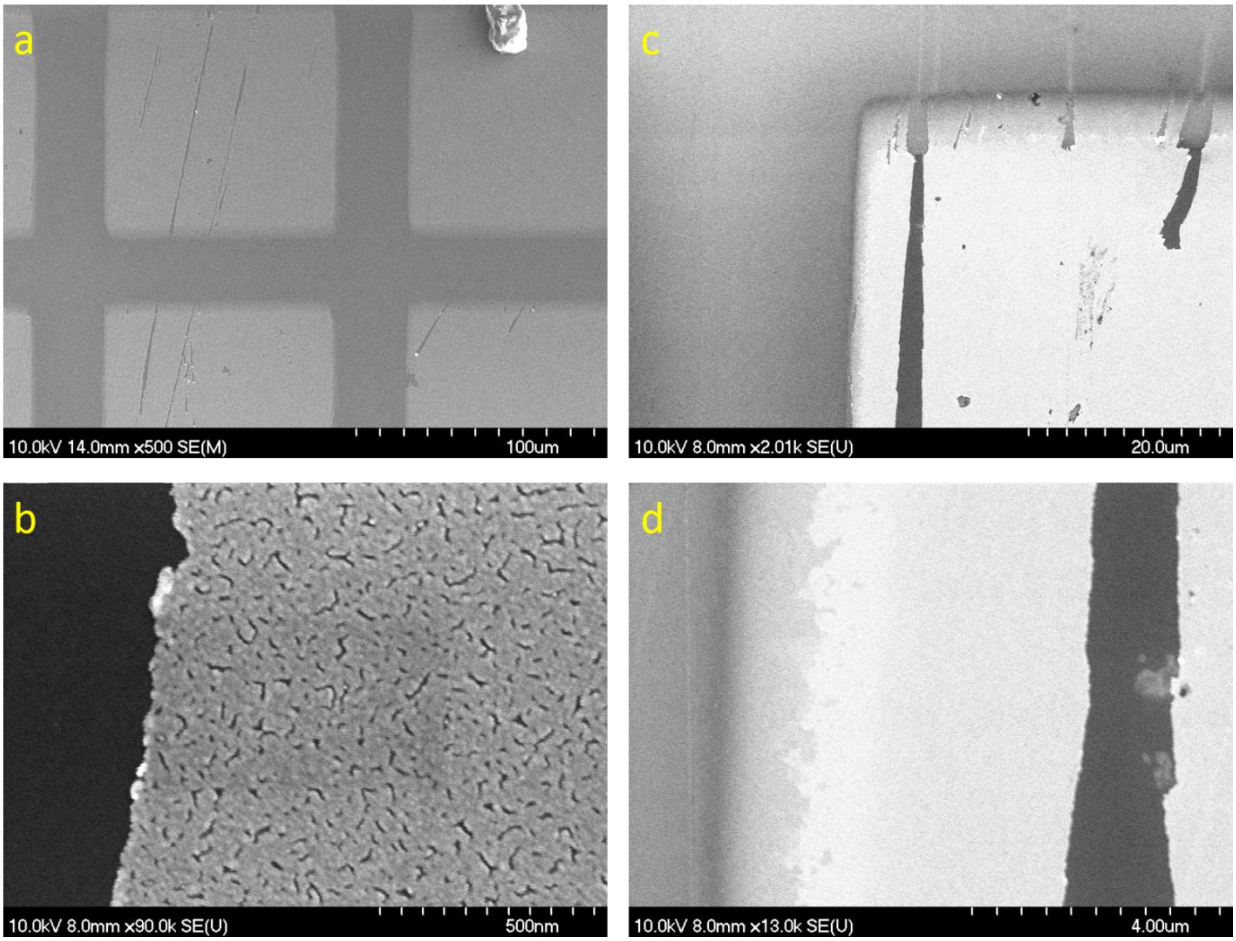

Figure 6.13 SEM micrographs of Au electrodes on SiO_2 substrate deposited via E-beam evaporation using a TEM grid as a shadow mask. a) From a wide vantage point the grid topography is clearly visible. b) Zooming in very close to the Au pad surface reveals granular structure that may be due to the 10 nm thinness of the pad. c) Closer inspection of the pad edges reveals that the definition at each edge is different, likely shadow effects due to the direction from which the evaporated Au was deposited and incomplete contact of the mask with the surface. d) Closer inspection of what appear to be scratches in the pads that extend down to the substrate show much more defined edges than those provided by the shadow mask.

CHAPTER 7:

POLARIZATION OF MACROSCOPICALLY ALIGNED PEPTIDE

As has been elucidated in detail in preceding chapters, the performance of semiconductor devices using organic materials has much to be gained through greater control over alignment during assembly and deposition of active materials. The electronic coherence length of organic semiconducting nanomaterials is directly related to alignment at all scales, and while the relationship between nano- to microscale and ultimate device performance are not yet fully understood, greater control over this ordering is the key deepening that understanding and ultimately crafting higher performance devices [153].

While biomimetic materials take advantage of naturally occurring self-assembly phenomena to achieve order at the molecular scale, there remains a critical gap in lengths scale over which order is controllable. Most organic functional materials are deposited using one of a variety of methods including spin coating, electrospinning, and reel-to-reel printing [4,10] as well as vacuum vapor deposition, electrochemical deposition, and Langmuir-Blodgett techniques [11], but none of these methods preserves any nanoscale order that may exist, fundamentally limiting the coherence lengths and levels of electronic communication achievable with nano-ordered materials. Our work as described in chapters 2 & 3 is one recent novel approach toward extending the order of 1-D semiconducting nanowires to the micro scale.

Meanwhile, through recent collaborations we have also investigated the use of sacrificial microchannels to achieve long-range macroscopic order deposited peptide nanofibers. The microchannels are created by drying a film of polystyrene latex nanoparticles on a solid substrate

(in this case silicon). Capillary stresses during drying causes the nanoparticles to aggregate into highly ordered microchannels generally oriented along the direction of evaporation—this yields a pattern of radiating spokes for droplets and can be adjusted through careful printing techinques to form parallel lines [154] over relative large distances. Solutions of unassembled peptide are then deposited on the microchannel arrays. The peptide solution infiltrates the channels via capillary action and peptide is evaporatively assembled and deposited in the microchannels. Finally the sample is soaked in toluene overnight, which selectively dissolves the nanoparticles but leaves the deposited peptide intact.

Collaborators investigated the deposited material through a variety of metrological techniques including atomic force microscopy (AFM), photo-induced force microscopy (PiFM), IR-AFM (related to, but distinct from the technique described in chapter 5), and electron microscopy. In addition, I used fluorescence polarization microscopy to confirm microscale alignment of the material. I conducted these experiments using a Zeiss LSM 710 confocal scanner equipped with a Spectraphysics Mai-Tai Ti-Sapphire Deep See eHP laser tuned to 780 nm at a 70 fs pulse rate for polarized two-photon illumination. By inserting a rotatable half-wave plate into the beam path immediately outside the laser source, I was able to rotate the excitation polarization. I imaged each region 18 times, rotating the half-wave plate by 5° each time to achieve a polarization resolution of 10°.

The individual peptides from which these fibers are formed have a dipole moment parallel to the peptide length, perpendicular to fiber length, and this dipole moment makes the fluorescent response of the fibers isotropic as well. As Figure 7.1a demonstrates, regions of parallel lines exhibit similar fluorescence polarization. Meanwhile, looking at a microchannel defect region containing lines at 45° to each other reveals a preference for one set of lines at 90° polarization and

a preference for the other at 135°. It is important to note that absolute intensity as a function of polarizer angle alone cannot be used to determine sample polarization because the intensity of the beam as it passes through the system optics will invariably be polarization-dependent due to polarization-dependent systemic imperfections. Thus, one approach to making polarizations measurements is to take a corresponding series of images of a completely anisotropic material such as a small-molecule dye solution and use the variations in intensity as a function of polarization for that sample to calibrate all data from the same system. Alternatively, a circularly polarized sample such as starch grains can be used to measure the intensity of response at each polarization angle. However, if one is interested primarily in the angular dependence of the polarization response as opposed to the magnitude of fluorescence intensity at each polarization, it is easiest to measure a region such as that in Figure 7.1c. As Figure 7.1b demonstrates, intensity varies as a function of polarization with different phase depending on which subregion is chosen. If the polarization response were merely an artifact of the system optics, the intensity would change uniformly across the image as a function of polarization angle. The different phases in Figure 7.1b demonstrate that different regions are in fact polarized at different angles.

The fact that these changes in polarization correspond to the same angular variation of the microchannel geometry of the sample indicates that this microchannel alignment method is deserving of further investigation. It would be particularly interesting to make conductive probe measurements of these samples as described in chapter 6 and to compare the electrical response of peptide aligned via this method versus simple drop-cast material (both by evaporatively assembly and acid-vapor triggered assembly) and material from microfluidics.

FIGURES

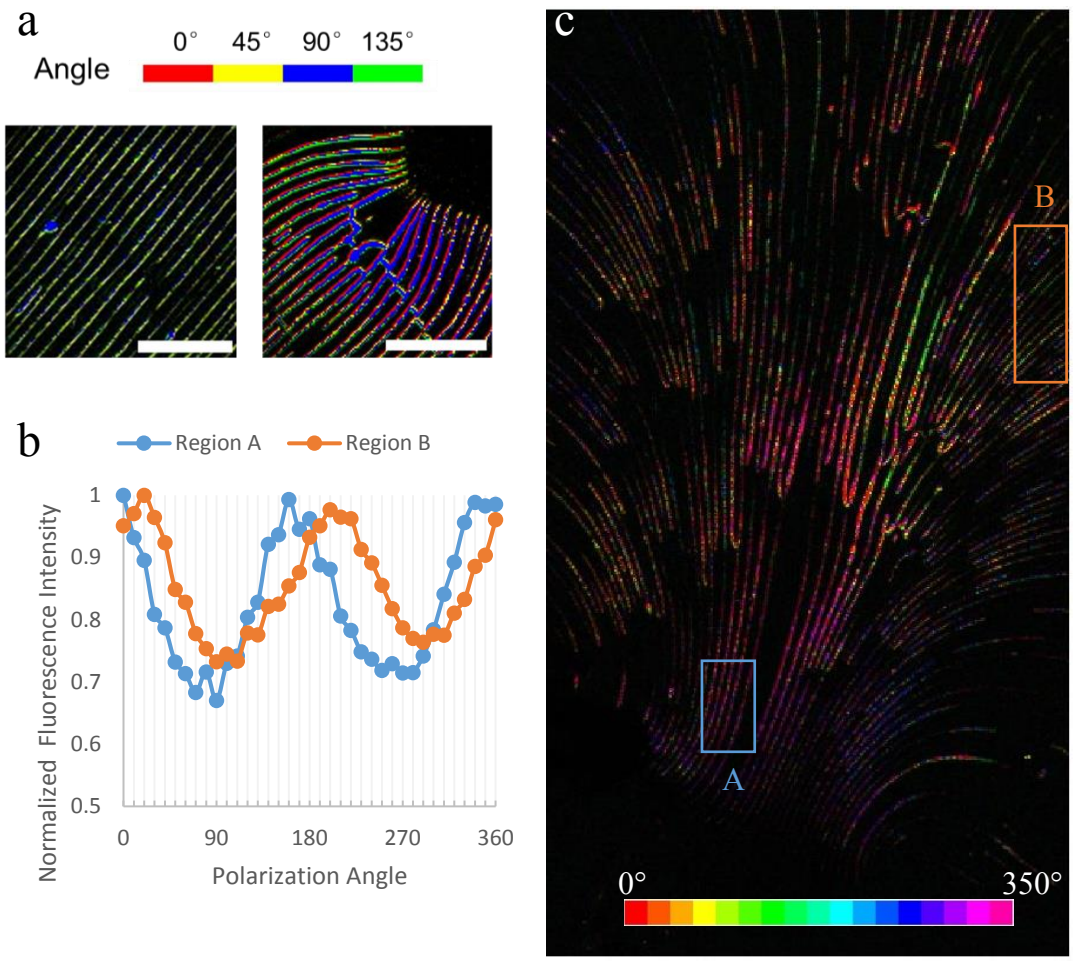

Figure 7.1 Demonstration of fiber alignment via fluorescence polarization. a) Regions of parallel lines and lines with 45° offset demonstrate markedly different polarization. b) Average intensity as a function of polarization angle for two regions from image (c). The difference in phase strongly indicates sample polarization to the exclusion of polarization-dependent artifacts in the optical setup. c) Defect region containing lines at various angles. Color of each pixel corresponds to the polarization of greatest intensity with 10° resolution.

CHAPTER 8:

CONCLUSIONS

The purpose of the work presented in this dissertation began with dreams of a budding scientist to change the world for the better by developing novel organic photovoltaic or LED devices with unprecedented light collection and conversion efficiencies. This expanded to encompass potential applications in organic transistors and the world of biosensors that follows. I was presented with an exciting new material: self-assembled biomimetic fibers whose amino acid residue sequences could be tuned to control their final structure and whose core moieties could be swapped for countless compounds to achieve a desired optoelectronic function. What's more, recently developed microfluidic techniques used the mechanical forces of the flow itself to physically manipulate these fibers as they assemble, aligning them. I had dreams of modified devices for joining p-type and n-type functionalized fibers, creating p-n junctions with controlled order near the single-molecule level. The aligned fibers presented immense potential for charge carrier transport given the control over microscale domains.

While this scientist's dreams remain, and the far-reaching potential applications of these biohybrid semiconductors remain as well, the work presented here has taken a two-pronged approach toward tackling what are still the very early stages of developing these materials for device applications. On the one hand, I worked to improve the simultaneous assembly and alignment process by developing new microfluidic designs and exploring printing-based deposition techniques. On the other hand, I not only used time-resolved and spectrally resolved fluorescence techniques to characterize the aligned material we were creating, but I also used the more easily assemble and deposited, drop-cast analogues of our materials to set the groundwork

for advanced optoelectronic materials characterization and comparison against their aligned counterparts.

In chapters 2 & 3, I describe how I took what had been promising, although limited and batch-process constrained microfluidic device and demonstrate new devices for continuous assembly, extrusion, and deposition of aligned oligopeptide fibers. Through confocal fluorescence microscopy I demonstrate how chevrons incorporated to the peptide inlet streams create coaxially focused streams of DFAG-OPV3, -4T, and -PDI material that assemble at the extensional flow axis of a cross-slot device. As peptide material never touches the devices surfaces, this process can be run continuously for as long as desired. Indeed, the devices can be used for any such material that one would want to assemble using microfluidics and the continuous flow operation makes it very easy to explore a wide chemical parameter space in a rapid, high-throughput manner. The rapid production of fibers whose assembly is controlled in device also makes it easy to create sufficient quantities of assembled material for use as organic electronic ink in a variety of printer set ups. Moreover, the outlets of the microfluidic devices can be directly coupled into print nozzle arrangements for immediate direct transfer of material to a substrate. I avoided fully optimizing any one specific printing technique as that is inevitably a time-consuming process of trial and error to find the ideal ink rheological properties, printing mode, print speed, surface energy, etc. But several proof of concept experiments demonstrate that the technology is primed for optimization as soon specific applications are determined.

Meanwhile, materials characterization via fluorescence correlation as well as polarization microscopy, near field IR spectroscopy, and conductive probe AFM set the groundwork for determining the future uses to which we might apply these specially aligned organic semiconductors. The initial goal was to characterize both quiescently assembled, drop-cast

material as well as aligned, printed material and to compare the measured optoelectronic properties. However, the great complexity of single-molecule characterization, as well as the novelty and relative lack of understanding specifically surrounding near field IR measurements, limited my investigations to single-fiber measurements of quiescently assembled drop cast material. Nonetheless, the progress made with these techniques as well as the developments in printing aligned material have prepared the stage for these materials comparisons.

Single molecule measurements in chapter 4 using fluorescence correlation spectroscopy provide experimental support for computational predictions that DFAG-OPV3 and DFAG-4T oligopeptides assemble not only via acid-triggering and protonation, but also begin aggregation even in non-protonating environments. Experiments also confirm a transition concentration around 10 nM below which no nucleation occurs. The critical discovery in this collaboration with peers running molecular dynamics simulations is that both simulation and experiment challenge the previous understanding of acid-mediated assembly that assembly begins at the moment of protonation. Rather, the system only exists as pure monomer at extremely low concentrations, but under experimental conditions the untriggered solution already exists in a pre-nucleated state.

Near field infrared spectroscopy—conducted both in a nanoFTIR mode as well as in a s-SNOM imaging-based mode—and conductive probe microscopy in chapters 5 and 6 facilitate identification of molecular secondary structure at a single-fiber level and identification of molecular scale optoelectronic properties. The measured IR scattering absorption for samples of evaporatively assembled DFAG-4T, DFAG-4T assembled via acid-triggering, and evaporatively assembled nonsequence-defined PDI analogues all demonstrate unique signatures indicative of their microstructure. The sequence-defined 4T samples show predominantly β-sheet signatures while PDI material is predominantly α-helical. Impressively, even the differences between acid

mediated assembly and evaporative assembly are evident by greater α-helix presence in the evaporatively assembled samples due to the less strongly deterministic assembly relative to protonated material. Meanwhile although longitudinal measurements were unsuccessful, transverse electrical measurements of all 4T samples imply semiconducting p-type characteristics.

Finally, chapter 7 elucidates some alignment properties of the same sequence-defined DFAG-4T oligomers but aligned not in microfluidic flow, but assembled and aligned by capillary flow into, and evaporative assembly within microcracks on a polystyrene film. This last project highlights the immense possibilities for controlling this material and the importance of the above characterization techniques for comparing material assembled through various means and assessing their respective virtues.

REFERENCES

1. Y. Sun, L. Jiang, K. Schuermann, W. Adriaens, L. Zhang, F. Boey, L. De Cola, L. Brunsveld, and X. Chen, Chemistry - A European Journal **17**, 4746 (2011).

2. S. Diegelmann, J. Gorham, and J. Tovar, Journal of the American Chemical Society **130**, 13840 (2008).

3. E. Ruiz-Hitzky, M. Darder, P. Aranda, and K. Ariga, Advanced Materials **22**, 323 (2010).

4. A. B. Marciel, M. Tanyeri, B. D. Wall, J. D. Tovar, C. M. Schroeder, and W. L. Wilson, Advanced Materials **25**, 6398 (2013).

5. B. Wall, S. Diegelmann, S. Zhang, T. Dawidczyk, W. Wilson, H. Katz, H. Mao, and J. Tovar, Advanced Materials **23**, 5009 (2011).

6. F. Hoeben, P. Jonkheijm, Meijer, and A. Schenning, Chemical Reviews **105**, 1491 (2005).

7. Hill, Mio, Prince, Hughes, and Moore, Chemical Reviews **101**, 3893 (2001).

8. S. Hecht, Materials Today **8**, 48 (2005).

9. G. M. Whitesides and B. Grzybowski, Science **295**, 2418 (2002).

10. G. Horowitz, Advanced Materials **10**, 365 (1998).

11. T. Kondo, Georgia Institute of Technology (2007).

12. J. Tovar, Accounts of Chemical Research **46**, 1527 (2013).

13. T. Kale and J. Tovar, Tetrahedron (2016).

14. B. Wall and J. Tovar, Pure and Applied Chemistry **84**, 1039 (2012).

15. B. Wall, A. Zacca, A. Sanders, W. Wilson, A. Ferguson, and J. Tovar, Langmuir **30**, 5946 (2014).

16. B. Wall, Y. Zhou, S. Mei, H. Ardoña, A. Ferguson, and J. Tovar, Langmuir **30**, 11375 (2014).

17. K. Besar, H. Ardoña, J. Tovar, and H. Katz, ACS Nano **9**, 12401 (2015).

18. F. Spano and C. Silva, Annual Review of Physical Chemistry **65**, 477 (2014).

19. F. Spano and H. Yamagata, The Journal of Physical Chemistry B **115**, 5133 (2010).

20. J. Chan, J. Tischler, S. Kooi, V. Bulović, and T. Swager, Journal of the American Chemical Society **131**, 5659 (2009).

21. J. Lakowicz, H. Szmacinski, and K. Nowaczyk, Analytical Biochemistry 316 (1992).

22. K. Suhlinga, L. Hirvonena, J. Levitta, and Chunga, Handbook of Photonics for Biomedical Engineering 1 (2015).

23. G. Whitesides, Nature **442**, 368 (2006).

24. A. Stroock, S. Dertinger, G. Whitesides, and A. Ajdari, Analytical Chemistry **74**, 5306 (2002).

25. A. D. Stroock, S. K. Dertinger, A. Ajdari, I. Mezić, H. A. Stone, and G. M. Whitesides, Science **295**, 647 (2002).

26. E. Mansur, Y. Mingxing, and W. Yundong, Chinese Journal of Chemical Engineering **16**, 503 (2008).

27. J. Howell, D. Mott, S. Fertig, C. Kaplan, J. Golden, E. Oran, and F. Ligler, Lab on a Chip **5**, 524 (2005).

28. H. Wang, P. Iovenitti, E. Harvey, and S. Masood, Smart Materials and Structures **11**, 662 (2002).

29. C. Schroeder, H. Babcock, E. Shaqfeh, and S. Chu, Science **301**, 1515 (2003).

30. A. Thangawng, P. Jr, J. Richards, J. Erickson, and F. Ligler, Lab on a Chip **9**, 3126 (2009).

31. D. Boyd, A. Shields, P. Howell, and F. Ligler, Lab on a Chip **13**, 3105 (2013).

32. P. Paiè, F. Bragheri, R. Vazquez, and R. Osellame, Lab on a Chip **14**, 1826 (2014).

33. N. Hashemi, J. Howell, J. Erickson, J. Golden, and F. Ligler, Lab on a Chip **10**, 1952 (2010).

34. S.-C. Lin, P.-W. Yen, C.-C. Peng, and Y.-C. Tung, Lab on a Chip **12**, 3135 (2012).

35. P. Howell, J. Golden, L. Hilliard, J. Erickson, D. Mott, and F. Ligler, Lab on a Chip **8**, 1097 (2008).

36. J. Golden, G. Justin, M. Nasir, and F. Ligler, Analytical and Bioanalytical Chemistry **402**, 325 (2011).

37. M. Nasir, D. Ateya, D. Burk, J. Golden, and F. Ligler, Biosensors and Bioelectronics **25**, 13631369 (2010).

38. G. Justin, A. Denisin, M. Nasir, L. Shriver-Lake, J. Golden, and F. Ligler, Sensors and Actuators B: Chemical **166-167**, 386393 (2012).

39. A. Shields, C. Spillmann, J. Naciri, P. Howell, A. Thangawng, and F. Ligler, Soft Matter **8**, 6656 (2012).

40. M. Daniele, K. Radom, F. Ligler, and A. Adams, RSC Advances **4**, 23440 (2014).

41. J. Golden, J. Kim, J. Erickson, L. Hilliard, P. Howell, G. Anderson, M. Nasir, and F. Ligler, Lab on a Chip **9**, 1942 (2009).

42. J. Puigmartí-Luis, D. Schaffhauser, B. Burg, and P. Dittrich, Advanced Materials **22**, 2255 (2010).

43. I. Donderwinkel, J. Hest, and N. R. Cameron, Polymer Chemistry **8**, 4451 (2017).

44. H. Gudapati, M. Dey, and I. Ozbolat, Biomaterials **102**, 20 (2016).

45. J. Li, F. Rossignol, and J. Macdonald, Lab on a Chip **15**, 2538 (2015).

46. K. Kim, G. Kim, B. Lee, S. Ji, S.-Y. Kim, B. An, M. Song, and J.-U. Park, Nanoscale **7**, 13410 (2015).

47. Kim, Friend, and Cacialli, (1999).

48. D. McManus, S. Vranic, F. Withers, V. Sanchez-Romaguera, M. Macucci, H. Yang, R. Sorrentino, K. Parvez, S.-K. Son, G. Iannaccone, K. Kostarelos, G. Fiori, and C. Casiraghi, Nature Nanotechnology **12**, 343 (2017).

49. T. Michaels and T. Knowles, American Journal of Physics **82**, 476 (2014).

50. S. Cohen, Vendruscolo, and Dobson, *The Kinetics and Mechanisms of Amyloid Formation* (2013).

51. R. Mansbach and A. Ferguson, The Journal of Physical Chemistry B (2017).

52. R. Mansbach and A. Ferguson, Organic & Biomolecular Chemistry (2017).

53. B. Thurston, J. Tovar, and A. Ferguson, Mol Simulat **42**, 955 (2016).

54. Y. Zhou, B. Li, S. Li, H. Ardoña, W. Wilson, J. Tovar, and C. Schroeder, ACS Central Science (2017).

55. M. Jackson and H. H. Mantsch, Critical Review in Biochemistry and Molecular Biology **30**, 95 (1995).

56. H. Yang, S. Yang, J. Kong, A. Dong, and S. Yu, Nature Protocols **10**, 382 (2015).

57. A. Barth, Biochimica et Biophysica Acta **1767**, 1073 (2007).

58. M. Paulite, Z. Fakhraai, I. Li, N. Gunari, A. Tanur, and G. Walker, Journal of the American Chemical Society **133**, 7376 (2011).

59. I. Amenabar, S. Poly, W. Nuansing, E. Hubrich, A. Govyadinov, F. Huth, R. Krutokhvostov, L. Zhang, M. Knez, and J. Heberle, Nature Communications **4**, (2013).

60. N. Ocelic, A. Huber, and R. Hillenbrand, Applied Physics Letters **89**, 101124 (2006).

61. E. Yoxall, Applications of Scattering-Type Scanning Near-Field Optical Microscopy in the Infrared, Imperial College, n.d.

62. D. deQuilettes, S. Vorpahl, S. Stranks, H. Nagaoka, G. Eperon, M. Ziffer, H. Snaith, and D. Ginger, Science (New York, N.Y.) **348**, 683 (2015).

63. Hiszpanski, Saathoff, Shaw, and Wang, (n.d.).

64. A. Seko, Y. Watanabe, H. Kondo, A. Sakai, S. Zaima, and Y. Yasuda, Japanese Journal of Applied Physics **44**, 7582 (2005).

65. Yang, Xu, Chen, Xu, Yu, and Ma, (2015).

66. D. Wood, I. Hancox, T. Jones, and N. Wilson, The Journal of Physical Chemistry C **119**, 11459 (2015).

67. H. Ardoña, K. Besar, M. Togninalli, and H. Katz, Journal of Materials Chemistry C **3**, 6505 (2015).

68. S. Hecht, Materials Today **8**, (2005).

69. S. Zhang, M. Greenfield, A. Mata, L. Palmer, R. Bitton, J. Mantei, C. Aparicio, M. de la Cruz, and S. Stupp, Nat Mater **9**, 594 (2010).

70. S.-Y. Min, T.-S. Kim, B. Kim, H. Cho, Y.-Y. Noh, H. Yang, J. Cho, and T.-W. Lee, Nature Communications **4**, 1773 (2013).

71. Y. Cheng, F. Zheng, J. Lu, L. Shang, Z. Xie, Y. Zhao, Y. Chen, and Z. Gu, Advanced Materials **26**, 5184 (2014).

72. A. Campo and C. Greiner, Journal of Micromechanics and Microengineering **17**, R81 (2007).

73. M. Unger, H.-P. Chou, T. Thorsen, A. Scherer, and S. Quake, Science **288**, 113 (2000).

74. D. Duffy, C. McDonald, O. Schueller, and G. Whitesides*, Anal Chem **70**, 4974 (1998).

75. M. Zhang, J. Wu, L. Wang, K. Xiao, and W. Wen, Lab on a Chip **10**, 1199 (2010).

76. H. Fidder, J. Knoester, and D. Wiersma, Chemical Physics Letters **171**, 529 (1990).

77. D. Möbius and H. Kuhn, Israel Journal of Chemistry **18**, 375 (1979).

78. S. Boer and D. Wiersma, Chemical Physics Letters **165**, 45 (1990).

79. A. Fitzpatrick and G. Debelouchina, Proceedings of the National Academy of Sciences **110**, 5468 (2013).

80. S. Haward, M. Oliveira, M. Alves, and G. McKinley, Physical Review Letters **109**, (2012).

81. C.-H. Hsu, C. Chen, and A. Folch, Lab on a Chip **4**, 420 (2004).

82. B. Casavant, E. Berthier, A. Theberge, J. Berthier, S. Montanez-Sauri, L. Bischel, K. Brakke, C. Hedman, W. Bushman, N. Keller, and D. Beebe, Proceedings of the National Academy of Sciences **110**, 10111 (2013).

83. Pinnau and He, (2004).

84. Merkel, Bondar, and Nagai, (2000).

85. Lee, Yim, Ahn, and Lee, (2009).

86. B. Smit, J. Reimer, C. Oldenburg, and I. Bourg, World Scientific **1**, (2014).

87. B. Li, S. Li, Y. Zhou, H. Ardoña, L. Valverde, W. Wilson, J. Tovar, and C. Schroeder, ACS Applied Materials & Interfaces **9**, 3977 (2017).

88. J.-U. Park, M. Hardy, S. Kang, K. Barton, K. Adair, D. Mukhopadhyay, C. Lee, M. Strano, A. Alleyne, and J. Georgiadis, Nature Materials **6**, 782 (2007).

89. Onses, Sutanto, Ferreira, and A. Small, (2015).

90. K. Shigeta, Y. He, E. Sutanto, S. Kang, A.-P. Le, R. Nuzzo, A. Alleyne, P. Ferreira, Y. Lu, and J. Rogers, Analytical Chemistry **84**, 10012 (2012).

91. M. Poellmann, K. Barton, S. Mishra, and A. Johnson, Macromol Biosci **11**, 1164 (2011).

92. Sutanto, Shigeta, Kim, Graf, Hoelzle, Barton, Alleyne, Ferreira, and Rogers, Journal of Micromechanics and Microengineering **22**, 045008 (2012).

93. H. Ardoña and Tovar, (2015).

94. Gendron, Avaltroni, and Wilkinson, (2008).

95. P. Kapusta, Absolute Diffusion Coefficients: Compilaton of Reference Data for FCS Calibration, PicoQuant Application Note (2010).

96. J. Enderlein, I. Gregor, D. Patra, and J. Fitter, Current Pharmaceutical Biotechnology **5**, 155 (2004).

97. J. Enderlein, I. Gregor, D. Patra, and Fitter, Current Pharmaceutical Biotechnology **5**, 155 (2004).

98. Grunwald, Cardoso, and Leonhardt, Current Pharmaceutical Biotechnology **6**, 381 (2005).

99. S. Hess and W. Webb, Biophysical Journal **83**, 2300 (2002).

100. A. Nagy, J. Wu, and K. Berland, Biophysical Journal **89**, 2077 (2005).

101. J. Jeon and M. S. Shell, Biophys J **102**, 1952 (2012).

102. M. K. Gilson, J. A. Given, B. L. Bush, and J. A. McCammon, Biophysical Journal **72**, 1047 (1997).

103. H. J. C. Berendsen, van der Spoel, and van Drunen, Computer Physics Communications **91**, 43 (1995).

104. D. Spoel, E. Lindahl, B. Hess, G. Groenhof, A. Mark, and H. Berendsen, Journal of Computational Chemistry **26**, 1701 (2005).

105. J. Wang, P. Cieplak, and P. Kollman, J Comput Chem **21**, 1049 (2000).

106. V. Hornak, R. Abel, A. Okur, B. Strockbine, A. Roitberg, and C. Simmerling, Proteins Struct Funct Bioinform **65**, 712 (2006).

107. A. W. Schüttelkopf and D. M. F. van Aalten, Acta Crystallographica Section D: Biological Crystallography **60**, 1355 (2004).

108. W. Jorgensen, J. Chandrasekhar, J. Madura, R. Impey, and M. Klein, J Chem Phys **79**, 926 (1983).

109. U. Essmann, L. Perera, M. Berkowitz, T. Darden, H. Lee, and L. Pedersen, The Journal of Chemical Physics **103**, 8577 (1995).

110. B. Hess, H. Bekker, H. Berendsen, and J. Fraaije, J Comput Chem **18**, 1463 (1997).

111. Allen, Tildesley, and J. Banavar, Physics Today **42**, 105 (1989).

112. R. . Hockney, S. . Goel, and J. . Eastwood, J Comput Phys **14**, 148 (1974).

113. G. Bussi, D. Donadio, and M. Parrinello, The Journal of Chemical Physics **126**, 014101 (2007).

114. W. Hoover, Phys Rev A **31**, 1695 (1985).

115. S. Nosé, Molecular Physics **52**, 255 (2006).

116. C. Still, A. Tempczyk, R. Hawley, and T. Hendrickson, Journal of the American Chemical Society **112**, 6127 (1990).

117. M. Schaefer, C. Bartels, and M. Karplus, Journal of Molecular Biology **284**, 835 (1998).

118. D. van der Spoel, E. Lindahl, B. Hess, and GROMACS development team, *GROMACS User Manual Version 4.6.7* (2014).

119. A. Onufriev, D. Bashford, and D. Case, Proteins: Structure, Function, and Bioinformatics **55**, 383 (2004).

120. G. M. Torrie and J. P. Valleau, Journal of Computational Physics **23**, 187 (1977).

121. S. Kumar, J. Rosenberg, D. Bouzida, R. Swendsen, and P. Kollman, J Comput Chem **13**, 1011 (1992).

122. J. Hub, B. Groot, and D. Spoel, Journal of Chemical Theory and Computation **6**, 3713 (2010).

123. R. Neumann, American Journal of Physics **48**, 354 (1980).

124. T. Mason, T. Michaels, A. Levin, E. Gazit, C. Dobson, A. Buell, and T. Knowles, J Am Chem Soc **138**, 9589 (2016).

125. N. Pal, S. Verma, M. Singh, and S. Sen, Analytical Chemistry **83**, 7736 (2011).

126. J. Mittag, S. Milani, D. Walsh, J. Rädler, and J. McManus, Biochem Bioph Res Co **448**, 195 (2014).

127. F. Huth, Nano-FTIR: Nanoscale Infrared Near-Field Spectroscopy, Euskal Herriko Unibertsitatea - Universidad del Pais Vasco, 2015.

128. N. Ocelic, Technische Universität München (2007).

129. F. Huth, A. Govyadinov, S. Amarie, W. Nuansing, F. Keilmann, and R. Hillenbrand, Nano Letters **12**, 3973 (2012).

130. K. Mueller, X. Yang, M. Paulite, Z. Fakhraai, N. Gunari, and G. Walker, Langmuir : The ACS Journal of Surfaces and Colloids **24**, 6946 (2008).

131. O. Reid, K. Munechika, and D. Ginger, Nano Letters **8**, 1602 (2008).

132. J. Bredas and B. Street, Accounts of Chemical Research **18**, 309 (1985).

133. C. Musumeci, A. Liscio, V. Palermo, and P. Samorì, Materials Today **17**, 504 (2014).

134. P. Barbara, T. Meyer, and M. Ratner, The Journal of Physical Chemistry **100**, (1996).

135. R. Marcus, Reviews of Modern Physics **65**, 599 (1993).

136. Bässler, Phys Status Solidi B **175**, 15 (1993).

137. R. Schmechel and H. von Seggern, Physica Status Solidi (a) **201**, 1215 (2004).

138. J. Mativetsky, E. Orgiu, I. Lieberwirth, W. Pisula, and P. Samorì, Advanced Materials **26**, 430 (2014).

139. R. Giridharagopal, P. Cox, and D. Ginger, Accounts of Chemical Research **49**, 1769 (2016).

140. T. Su, M. Neupane, M. Steigerwald, L. Venkataraman, and C. Nuckolls, Nature Reviews Materials **1**, 16002 (2016).

141. Zhang, Yao, Liu, Jin, Liang, Chen, and L. -M. Peng, Advanced Functional Materials **17**, 2478 (2007).

142. K. A. Walsh, Scanning Probe Microscopy of Protein Nanowires, Michigan State University, 2013.

143. S. Saito, H. Sasabe, T. Nakajima, and K. Yada, Journal of Polymer Science Part A-2: Polymer Physics **6**, 1297 (1968).

144. J. Bolsée, W. Oosterbaan, L. Lutsen, D. Vanderzande, and J. Manca, Advanced Functional Materials **23**, 862 (2013).

145. J.-C. Bolsée, W. Oosterbaan, L. Lutsen, D. Vanderzande, and J. Manca, Organic Electronics **12**, 2084 (2011).

146. Müller, Naulaerts, Billen, Genoe, and Heremans, Applied Physics Letters **90**, 063503 (2007).

147. T. Kelley, E. Granstrom, and D. Frisbie, Advanced Materials **11**, 261 (1999).

148. H. Li, T. Su, V. Zhang, M. Steigerwald, C. Nuckolls, and L. Venkataraman, J. Am. Chem. Soc **137**, 5028 (2015).

149. M. Oehzelt, N. Koch, and G. Heimel, Nature Communications **5**, 4174 (2014).

150. H. Dai, E. Wong, and C. Lieber, Science **272**, 523 (1996).

151. P. Girard, Nanotechnology **12**, 485 (2001).

152. T.-Q. Nguyen, R. Martel, M. Bushey, P. Avouris, A. Carlsen, C. Nuckolls, and L. Brus, Physical Chemistry Chemical Physics **9**, 1515 (2007).

153. Z. Henson, K. Müllen, and G. Bazan, Nature Chemistry **4**, 699 (2012).

154. B. Li, W. Han, B. Jiang, and Z. Lin, ACS Nano **8**, 2936 (2014).

155. M. Eddings, M. Johnson, and B. Gale, Journal of Micromechanics and Microengineering **18**, 067001 (2008).

156. B.-H. Jo, L. Lerberghe, K. Motsegood, and D. Beebe, Microelectromechanical Systems, Journal of **9**, 76 (2000).

157. T. Ishibashi, Y. Cai, Nano Express **10**, 375 (2015).

APPENDIX A:

MICROCHANNEL DEVICE FABRICATION AND OPERATION

Most of the literature on microfluidic devices dismisses the fabrication step with a standard reference to standard soft-lithography methods; however, I would like to use this appendix to expand upon some of the quirks in the process, especially with regards the assembly of multilayer devices, and methods I found for addressing some of challenges particular to this process.

Bonding

One of the easiest ways of making microfluidic devices involves creating a Si and photoresist-based master mold and free-pouring or spin-coating PDMS on to this mold. Once the PDMS has cured, it can be removed from the mold to reveal channels on the bottom of the PDMS slab, a negative relief of whatever was patterned on the mold. Those channels can then be completed and sealed by bonding the bottom of the PDMS slab to a piece of glass—for our purposes this glass was always a long (50 - 60 mm) coverslip. This bonding is accomplished by stripping the hydrogen atoms from both surfaces via an oxygen plasma and allowing the exposed charges to create strong hydrogen bonds between the two materials when placed in intimate contact. It should be noted that although plasma treatment is often used as a sample cleaning method, bonding is significantly enhanced when the glass to be bonded has been precleaned by sonication in isopropanol (IPA) or simply treating the surface with successive rinses of IPA, water, and IPA again.

However, multilayer devices can require multiple stages of alignment and bonding and often require the bonding of PDMS to PDMS. While PDMS can be bonded to itself using the same

plasma bonding technique as used with PDMS and glass, this is often problematic when there is an alignment step. The plasma bonding occurs effectively instantaneously so the layers must be perfectly aligned before coming into contact in order to achieve a well aligned, undamaged sample with proper bonding. Alignment—especially when done by hand—can be made much easier by being able to move one layer around on top of the other layer; this is possible when instead of plasma bonding two cured layers of PDMS, the PDMS is layers are aligned before the PDMS has fully cured. In this manner, the PDMS layers that need to be joined will finish curing together, thus bonding via the same cross-linking reactions that provide the PDMS bulk with its ultimate cured properties. I found this curing-based bonding to be preferable to plasma bonding for device layering because of the ease of being able to finely manipulate one layer of PDMS while in contact with another layer without the concern of instantaneous bonding. This preference comes with the caveat, though, that the bonding is weaker than plasma bonding of PDMS to glass (although not necessarily weaker than plasma bonding of PDMS to itself [155]). The initial standard procedure I used involved mixing PDMS in a 1:10::cross-linker:base ratio, curing in a 60 degree Fahrenheit oven for 30 min before aligning layers, and then returning to the oven for an overnight bake before use. I found that reducing the prealignment bake time to as little as 20 minutes increased the probability of a good PDMS to PDMS bond. Baking for less time than that did not allow the PDMS to sufficiently cure to be able to remove the thicker channel layer and punch the necessary inlet and outlet holes.

While I did find other techniques that might have yielded reliable alignment of 3D channels, they were either equally or more complicated than the hand alignment I did or akin to using a table saw to cut a stick of butter [32,156].

Alignment

The chevrons devices I created involved two alignment steps: one alignment of top chevrons with the main channels at the master fabrication step and one alignment of bottom chevrons with the main channels/top chevrons mold for each device created. As mentioned in the main body of this text, the first alignment was significantly aided through the use of FeO on glass masks instead of laser-printed masks using regular black ink. Each master contains the designs for four microdevices arrayed on a single 3 in. wafer (Figure A.1). As such, chevrons needed to be aligned on all four devices at once, leaving far less tolerance for error than if only one device were being aligned at a time because a small deviation in alignment angle at, for example, the top left design could lead to a very large offset in the designs for the bottom right design. Being able to see through the mask design allowed for much easier fine manipulation of the mask over the existing patterns.

For the second alignment step, the PDMS mold was first removed from the master for punching inlet and outlet holes and in the same step the four devices were separated from each other and excess PDMS was cut away using a razor blade. This allowed each device to be aligned individually, which was significantly easier than trying to align all four at once, especially given the stickiness and elasticity of the partially cured PDMS. Nonetheless, alignment was not facile and one technique that I used to aid the process (based on discussion with Dr. Jeff Erickson at the Naval Research Lab) was to place a drop of alcohol on each device pattern before alignment. The alcohol lubricated the surfaces, making it extremely easy to line up the patterns very accurately. Furthermore, PDMS is porous and permeable to gas exchange, allowing alcohol vapor to escape so that the PDMS could come into intimate contact for bonding. Unfortunately, I found that the alcohol (even methanol, which is the lightest, most volatile alcohol available) seemed to interfere

with bonding and I could never achieve proper bonding in this manner alone. I did find that using methanol and punching many holes around the device pattern seemed to allow the methanol to evaporate and escape sufficiently quickly to achieve good bonding most of the time. Perhaps better bonding could have been achieved by curing the PDMS at room temperature, which would be more slow than in the oven and allow the methanol more time to evaporate.

Bubbles

An ever-present challenge to proper microfluidic device operation is the elimination of unwanted material phases in the working fluid. In other words, I had to keep the bubbles out. Elimination of bubbles could be achieved by taking the following precautions with most devices:

- Before connecting the syringes to fluid lines bubbles should be eliminated from the syringe. This can be accomplished by repeatedly rapping the syringe, plunger side down, against something somewhat forgiving, like a finger or the top of a cardboard box, until the bubbles have risen to the top and coalesced. Then the bubble can be forced out of the syringe.
- Flow fluid through the lines to eliminate any bubbles caused by the initial connection at the syringe-line interface and ensure they are pushed out of the lines.
- Flow devices with water first.
- Increase pressure in device by increasing flow rate and/or plugging outlets. The increased pressure will force the air bubbles to escape through the PDMS walls.

While the above precautions are effective for typical, single layer devices, multilayer devices pose an additional challenge due to the weaker PDMS to PDMS bonding. Increasing the pressure too high causes the PDMS layers to delaminate. I found that flow rates above 4000 μl/min consistently

broke the devices and decided on a safe rule of 3000 µl/min max for eliminating bubbles. Furthermore, bubbles are a particularly egregious problem in the chevron devices due to the many small angled corners in where the chevrons meet the channel walls. Flowing at 3000 µl/min can eliminate bubbles, but it can take several minutes. Thus, it is important to have a large reservoir for the water syringe to have enough fluid remaining after bubble elimination for the rest of the experiment.

FIGURE

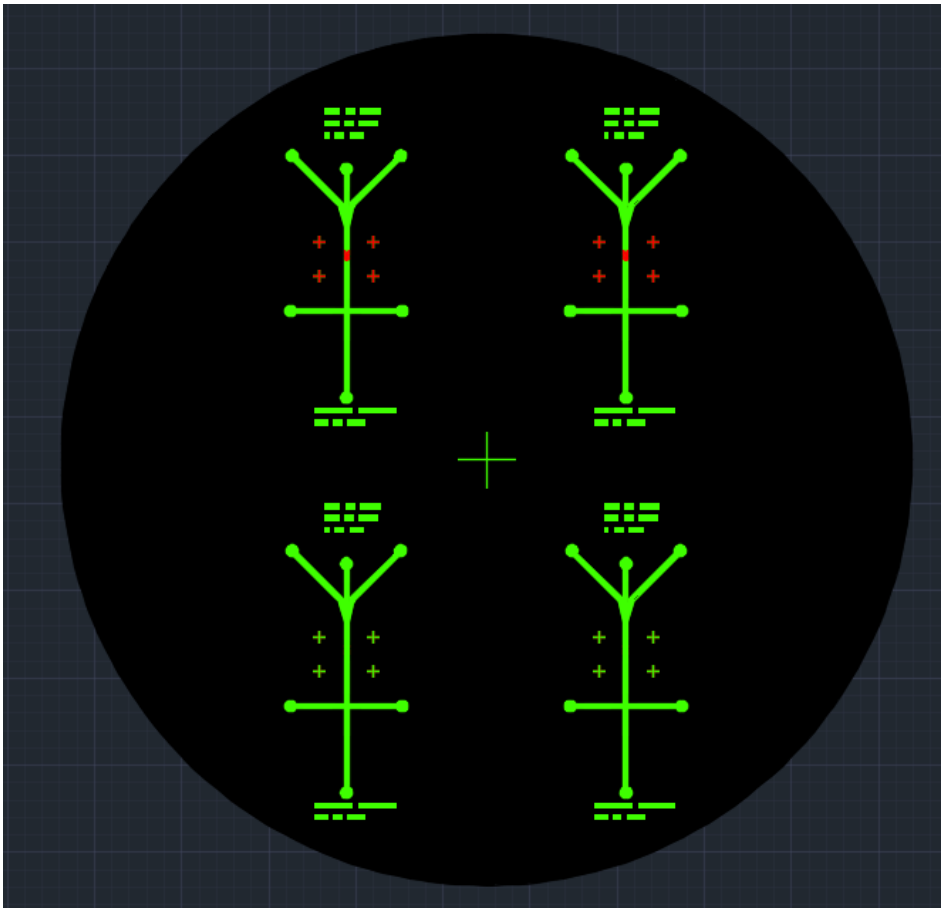

Figure A.1 Example pattern for microfluidic mold master design. Green corresponds to the central channel layer and red corresponds to the chevrons. Crosses serve as guides to the eye for alignment.

APPENDIX B:

NANOSCALE INFRARED SPECTROSCOPY EXPERIMENTAL DESIGN LIMITATIONS AND RESOLUTIONS ROADMAP

The recently developed pseudoheterodyne techniques for near-field scattering-based detection of infrared (IR) spectra in single macromolecules present exciting potential for heretofore unheard of combinations of spectral information and spatial resolution. However, despite the theoretical capability to completely eliminate background excitation and scattered beam signals from the desired near-field scattered signal, systemic limitations in current experimental designs require important caveats to be considered when analyzing data acquired through these means.

As discussed in Chapter 5 of this work, liquid nitrogen cooled detectors put thermal noise at or below the shot noise of the system, both of which are tolerable and negligible in comparison to noise form the laser source. Practical complications in separating the desired signal from laser background as well as mechanical influences of the system are also more important issues to address. Granted, it is important to make sure that the liquid nitrogen reservoirs are kept full, especially over the several hours long experiment sessions that are often required. Over such long times, the liquid nitrogen reservoirs must be regularly topped off to keep detector noise at a minimum. Chapter 5 also touches upon issues of proper background subtraction/division technique for calibrating collected interferograms as well as the issue of topographical information being convolved into measured IR absorption maps. Both of these issues relate to broader questions of how to properly calibrate for background and disturbance signals for optimal signal to noise ratio (S/N) in the context of a real system. In this appendix I will present the various limitations of the

current experimental design and, where possible, a roadmap toward potential resolution of these issues.

FTIR SIGNAL NOISE: LASER STABILITY AND BACKGROUND SUBTRACTION

Recalling that the largest source of systemic noise in s-SNOM measurements are from laser fluctuations, it is of utmost importance to characterize the laser system with a known sample before attempting to characterize unknown material. This concept is manifest in the broadband point spectra we collected and discussed in Chapter 5. The discrepancy between spectra collected with the two different lasers may simply be due to the different types of sample analyzed, but the doubts as to the influence of having an unstable laser for the first set of spectra (collected on the peptide in polystyrene nanoparticle cracks) make extensive comparisons between the data sets dubious. The new laser should be used to analyze the original sample of the first set of spectra to see if the results more closely match the spectra in Figure 5.3 or those in Figures 5.4 & 5.5. It would furthermore behoove future experimentalists to carefully characterize the laser power as a function of both wavelength and time and to ensure stability in both before making any sample measurements. And while attenuation of the reference laser power can improve the signal to noise ratio by reducing beam artifacts relative to sideband measurements, it's important to not attenuate the power so much as to lower the signal intensity to a level comparable with other sources of systemic noise [127].

Nonetheless, even a system with the most stable of lasers will have undesirable background signal from a variety of sources which can obfuscate the signal one would like to measure.

Pseudoheterodyne detection significantly reduces such background signal by eliminating both the additive and multiplicative components of the scattered excitation beam such that we only measure the near field signal and the miniscule portions of the background that coincidentally coincide with the near field detection frequency. Nonetheless, even in the near field, with sufficiently small samples such as the peptide fibrils of interest in this work, there will be scattering contributions from both the peptide sample and the substrate upon which it is deposited. We assume a linear relationship between the signal contribution from the substrate and the contribution from the peptide. Thus, it is common practice to collect a reference spectrum from a region where we are certain that the only near field contribution is from the substrate. This reference spectrum is then subtracted from all subsequent spectra to remove the background inference and find the true absorption signal of the sample alone.

Yet, the FTIR spectra from Chapter 5 indicate that simply taking one reference spectrum and using it to subtract all subsequently collected data will not always properly account for the background. It would be instructive to take a dataset such as that illustrated in Figures 5.4 and 5.5 and to use each of the spectra collected on the SiO_2 reference sample as references against each other to identify any anomalous spectra that should be excluded from the dataset due to unknown signal contamination. Ideally, there should be minimal variation in all spectra calibrated with any of the reference sample spectra. Further, using an average of all reference sample spectra as the reference may be the best choice. If the average of all the reference spectra is more reliable than any individual spectrum, this begs the question of how long one should integrate for each spectrum versus how many spectra to average and where increases in experimental observation time offset the likely diminishing returns of moving to longer integration time for each spectrum. For certain, longer integration time is favorable as energy conservation for the system noise means that longer

integration times divide the transformed frequency space into smaller units which each must have smaller noise contributions. However, the concern with longer observation times is not only an issue of time value with regards opportunity cost in forgone other experiments or the cost of paying experimentalists. Longer observation times also aggravate our initial concerns of laser stability and noise. Longer data acquisition times lead to longer experiments over which the laser has more time to deviate from its initial state at the beginning of the experiment. Thus, a balance must be struck between extending observation time to reduce the influence of background noise and limiting the duration of experiments to avoid laser stability issues.

S-SNOM IMAGING NOISE: IMAGE BACKGROUND VS SPECTRA BACKGROUND

One of the most confusing aspects of the literature with respect to near-field IR spectroscopy is the relationship between noise in the sense of the previous section as it relates to a spectrum from a Fourier transformed interferogram and noise in the context of imaging. The terms "noise" and "background" are used interchangeably with respect to both modes of operation [58-61, 127-129]. However, clearly the noise that is reduced in FTIR spectra by integrating for longer times cannot be correspondingly reduced in s-SNOM images or spectra derived thereof. Alternatively, the background signal that is subtracted out of FTIR spectra is not exactly the same as the background of an s-SNOM image and cannot be accounted for in the same way. The limited literature on this subject explains that while imaging at increasingly higher harmonics should give increasingly better S/N due to increasingly localized near-field measurement, the monotonic decrease in absolute signal intensity with higher harmonics means that operating at a harmonic

that is too high will result in a noisier image due to the addition of systemic fluctuations that are otherwise negligible at higher overall signal strengths [61]. Nonetheless, as Figures 5.6 & 5.7 demonstrate, a noisier image does not necessarily translate to a noisier spectrum extracted from that image. The noise across a series of images taken at different wavenumber but at the same harmonic may make any individual image less sharp as compared to the same image at the same wavenumber but a different harmonic. But when comparing the difference between background and sample intensity across images at one harmonic, by virtue of the fact that we are only measuring differences between images within the same set, those noise contributions seem to self-correct.

In the course of extracting spectra from image series we have, however, noticed flaws that must be addressed before we can confidently make conclusions about spectral features measured in such a manner. Figure B.1 illustrates that our method of extracting sample signal from the background of the images for comparison across the spectrum yields very consistent results. The rationale seems reasonable and is well founded in the literature [58] that by subtracting the substrate signal from the fiber signal in each image we are effectively removing the uninteresting background information from the fiber data to get a true measure of changes in scattering absorption by the material as a function of wavenumber. However, subsequent experiments seeking to quantify the systematic variation of the system's QCL output power as a function of wavenumber reveal that there is, in fact, a significant amount of background signal that is not removed via the Gaussian differencing method (Figure B.2). We measured these variations by cropping a portion from an image at each wavenumber containing only the substrate. We then measured a histogram of the cropped, sample-less region and fit it to a single Gaussian. Using the peak position of the Gaussian fit as a representation of the average intensity of the scattered signal,

we proceeded to plot these values against the corresponding wavenumber at which they were acquired in order to construct a background spectrum. The result has almost the exact shape of the previously measured sample spectra. Thus, it is possible that spectra measured earlier using this method, both in by us and in previous work (cite again) are not indicative of the sample at all and are, rather, a measure of laser variability.

Upon further consideration, there are two possible sources of the structure observed in the background spectrum of Figure B.2b. One explanation is as put forth above, that the variations in amplitude with different wavenumber are representative of the laser's power variability. An alternative explanation is that the measured signal is from a different source of background noise: the SiO_2 substrate itself. Silicon dioxide will certainly have its own absorption spectrum which should be revealed by such a measurement. Thus, Figure B.2b is likely a convolution of laser power fluctuation and the native SiO_2 spectrum. Moreover, it is clear from visual inspection of optical scattered signal amplitude maps at different wavenumber that the sample does indeed absorb more or less at different wavenumber (Figure B.3). The signal measured in Figure B.1 is furthermore likely a convolution of the laser power fluctuation, SiO_2 spectrum and the spectrum of the fibers in which we are interested.

All these data are in the images, but we have yet to find the best way of isolating the fiber data from the other background information. Borrowing from signal processing and image analysis techniques, we hope to isolate this signal by means such as choosing threshold values for each image to remove the background signal and reanalyze only the pixel values corresponding to fiber locations. Another method which may be used alternatively or in conjunction with more advanced signal processing techniques is to take advantage of the inherent polarity of the sample by using an aperture-type fiber-based tip design rather than the current apertureless method which relies on

surface plasmon resonances. An aperture-type design would sacrifice some S/N with respect to system noise unrelated to the substrate signal due to the extreme signal attenuation as a single mode optical fiber is used to guide the light toward the sample [157]. However, the aperture design would allow us to maintain some of the light polarization and improve S/N as it relates to separation of fiber signal from substrate signal because we could align the probe polarization with the axis of polarization of the fibers (transverse to the fiber length) to preferentially measure signal only with that orientation. Although aperture-type methods have relatively poor spatial resolution typically greater than 50 nm [157] due to the necessity of a flat tip apex with metallic coatings over the fiber optics, if used on samples with sufficiently sparse distributions of fibers individual fibers should still be identifiable based on their unique polarization responses.

One might suggest at least removing the component due to laser power fluctuation by simply measuring output intensity versus wavenumber using a simple photodetector. This, however, fails to take into account all the components of the system which might influence the scattered signal, a concern which could be addressed by instead using a fully reflective calibration sample for the spectral regime of interest. And yet any such calibration fails to address that fact that fluctuations in laser power are of large enough magnitude that it is necessary to change the power manually at different wavenumber in order to either obtain sufficient signal from a sample or to avoid burning the sample. Thus, even if the laser power is calibrated for, that calibration will not account for the deliberate manipulation of the laser power over the course of an experiment. One possible way to address this issue is to optimize laser choice and design such that maximum and minimum values of output power fall within an acceptable range for nondestructive sample interaction and detection. This still does not address the issue of changes in power due to alignment, which changes every time the QCL is tuned. Thus, the best method of subtracting

background still likely lies within the realm of data analysis and proper baselining derived from the sample images themselves.

DECONVOLVING OPTICAL AND TOPOGRAPHICAL DATA

As mentioned in the previous section, the spectra we have measured via topographical and optical scattering/absorption maps contain a combination of both the sample information and the latent spectrum of the SiO_2 substrate. This is unsurprising given the extended interaction volume around the tip. In other words, even if the AFM tip rests entirely on the sample, the evanescent wave at the probe is interacting with some material off to the sides. Furthermore, even neglecting the imperfect anisotropy of the interaction volume, the linear interaction depth immediately below the tip extends beyond the height of a fibril whose diameter is no more than a few nanometers. Scattering signal, even that which is confined to the near field directly above the sample, will thus inevitably contain some influence from both the sample and the underlying substrate.

All the above is further complicated by the fact that the scattered signal we detect with the current experimental design, even for a completely homogeneous sample, will change with topography. We devised a simple experiment to determine the transformation that relates variations in sample thickness to optical scattering absorption amplitude and phase detection. Using a standard AFM calibration chip with a triangle wave surface pattern, we filled the gaps on the chip with a polymer of known IR absorption spectrum (AZ5214 photoresist) (Figure B.4a). The surface should ideally be polished to ensure that it is topographically smooth and featureless. The linearly varying depth of the polymer should be a sufficient mimic of a sample that is varying

linearly in height. If the scattering signal is linearly dependent on the sample thickness then we should expect to see a correspondingly linear change in scattering signal alongside a featureless height signal as the tip scans the surface (Figure B.4b & B.4c). If the scattering absorption pattern is more complex, we should be able to use the known linear variation in sample depth to back calculate the transformation relating sample depth to signal attenuation.

Furthermore, this test could allow us to characterize the depth to which the s-SNOM measurement reaches at different harmonics. The peak to trough amplitude of the triangle wave grating is approximately one micron while the near field measurements should be spatially limited to the order of ten nanometers. Thus, the signal should plateau between peaks regions of minimum polymer depth and the position of that plateau should also change as a function of the harmonic under consideration (Figure B.4d). Higher harmonics, with more localized interaction volume, should have wider plateaus, corresponding to reaching maximum detection depth earlier, than those of lower orders.

These measurements for a sample of linearly varying depth contain an additional complication because the angle of the SiO_2 substrate itself, or general variations in the topography of even a homogeneous sample can themselves influence the absorption spectrum. We have tested this influence of pure topography on the measured IR scattering absorption by first imaging an uncoated version of the aforementioned AFM calibration chip. This sample should have a completely uniform IR response because it is composed of one material and is of sufficient depth to certainly exceed the interaction depth of the AFM tip. The only variation we would expect to see would by a slight decrease in interaction at the triangle peaks, and a slight increase at the trough nadirs. This is because at the peaks there is less opportunity for isotropic interaction with the sample. Likewise, at the troughs the tip can interact isotropically with the material of the trough

walls on either side of the tip. However, what we actually see is an IR map with significantly more correlation to the topographical map. Many more such experiments should be conducted with the same type of sample as well as other samples with well characterized variable topography in order to build up a significant dataset with which to construct a reliable transformation to calibrate an IR map for topographical variation.

ENVIRONMENTAL CONTROL

As a final consideration, many of the problems detailed above could be mitigated through proper environmental control. Fluctuations in temperature can drastically influence sample drift, and environmental contaminants can obscure the IR signals measured. The primary environmental contaminant is water, which invariably adsorbs to the sample surface. There might be some benefit to this contaminant because the adsorbed water will also absorb at certain specific regions in the IR and detection of these absorption lines can be a helpful reference to verify that the system is working properly. However, any such benefit could be negligible compared to the aforementioned complications. While the current experimental design is incompatible with significant environmental control, it should be possible to, at a minimum, run a nitrogen supply line into the system enclosure to approximate a dry air environment.

FIGURES

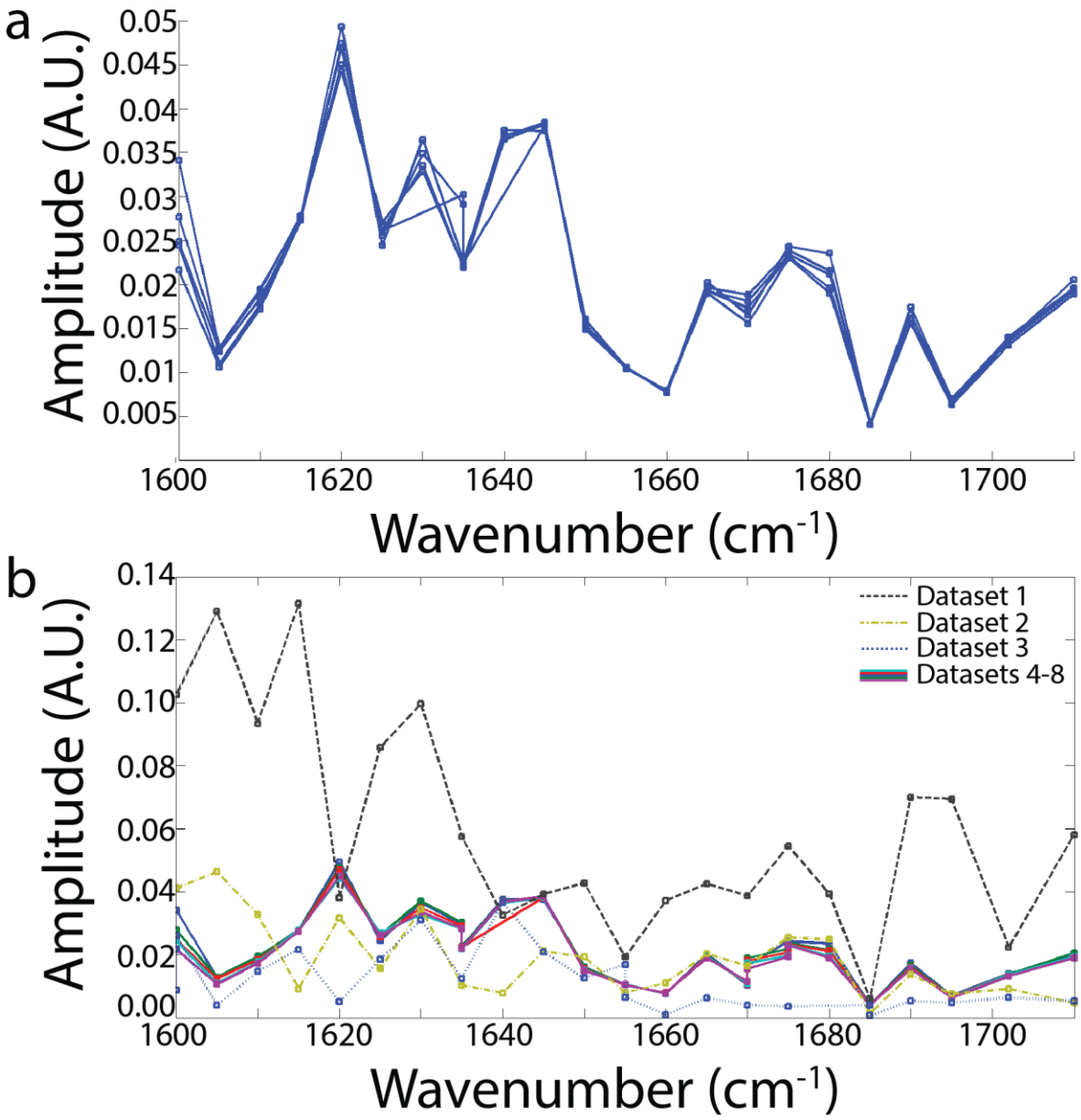

Figure B.1 Imaging-based spectra for DFAG-4T fibers formed via acid vapor. a) Five images were recorded at every five wavenumber with the exception of 1700 (using 1702 instead due to a precipitous drop in laser power at exactly 1700) and 1705. The scattering absorption amplitude was calculated using the Gaussian difference method described in Chapter 5, whereby the histogram of the image is fit to two Gaussians and the peak to peak distance is used as the scattering absorption. There is very good agreement between all five spectra thus acquired. b) The five spectra of (a) are designated Datasets 4-8 and compared against the three previously collected spectra for the exact same sample. Datasets 1 and 2 likewise show good agreement with the spectra from Datasets 4-8. Dataset 3 seems to be anomalous and may have been subject to disproportionately higher noise during acquisition as compared to the other datasets.

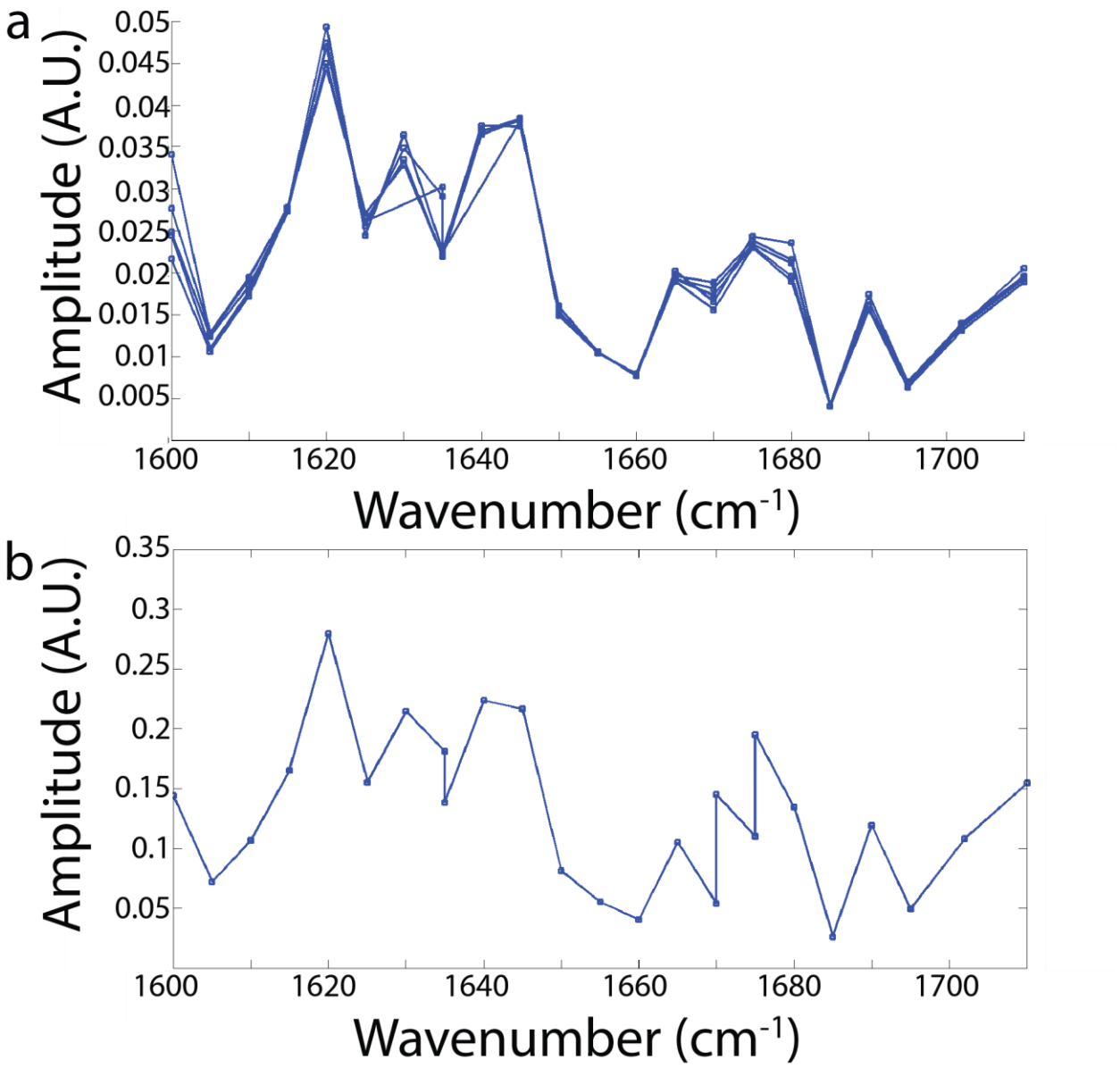

Figure B.2 Predominance of background substrate signal in imaging-based spectra. a) Imaging-spectra from five datasets as displayed in Figure B.1. b) Substrate signal as a function of wavenumber. A histogram for a cropped area containing only the substrate for an image at each wavenumber was fit to a single Gaussian and the peak position of each is plotted. There is remarkable agreement between the spectra in (a) and (b), seeming to indicate that background signal dominates the spectra as acquired for (a).

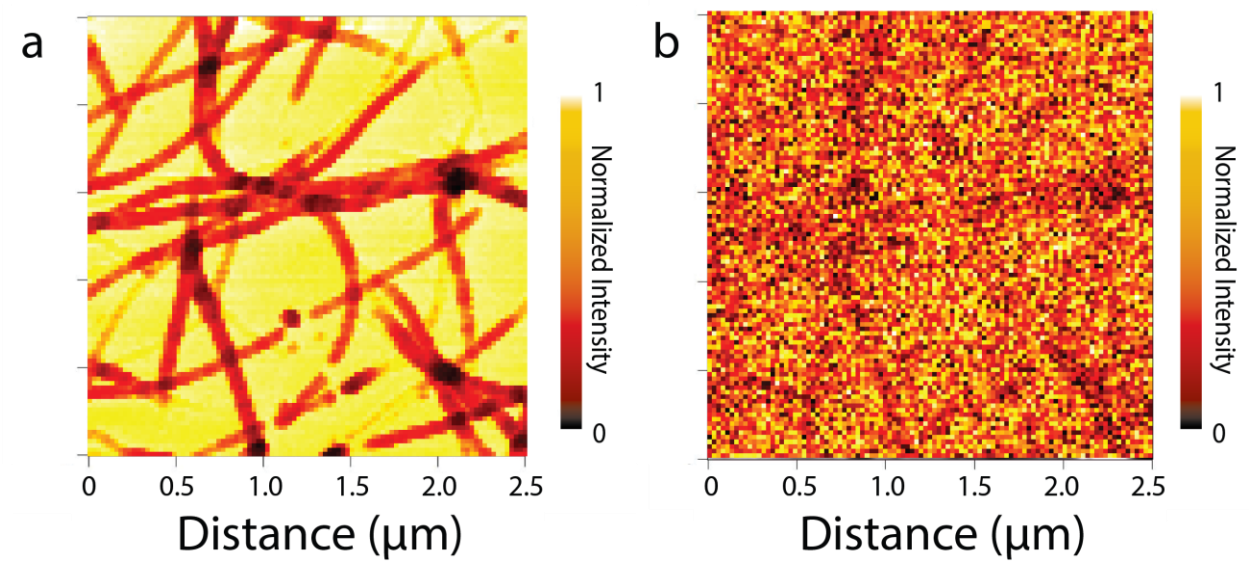

Figure B.3 Images for 4th optical harmonic amplitude of DFAG-4T acid vapor assembled fibers taken at different wavenumber. a) Scattering absorption at 1600 cm^{-1}. b) Scattering absorption at 1690 cm^{-1}. There is a clear difference in contrast between images (a) and (b). Thus, despite the similarity between the spectra for the fibers and background as shown in Figure B.2, there is a clear variation in the scattering absorption of fibers as a function of wavenumber independent of laser power fluctuations with wavenumber.

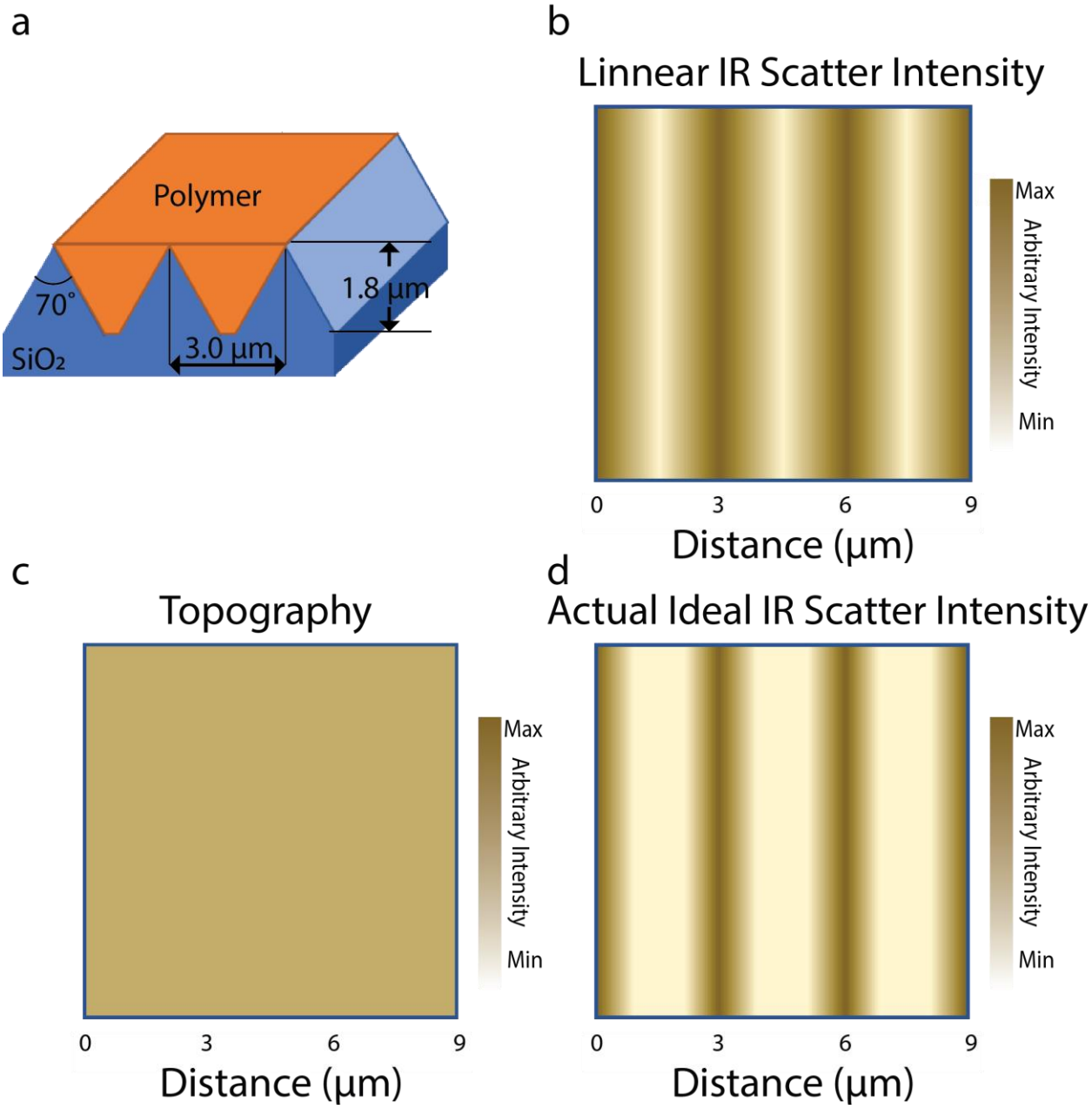

Figure B.4 Test sample for deconvolving thickness from IR data. a) Schematic of SiO_2 AFM calibration chip filled with polymer material. b) Idealized expected linear variation in IR scattering map for a wavenumber with selective absorption by polymer. c) Idealized expected topography map of the same sample. d) Idealized expected IR scatter map taking into account the finite near field interaction volume and signal penetration depth.

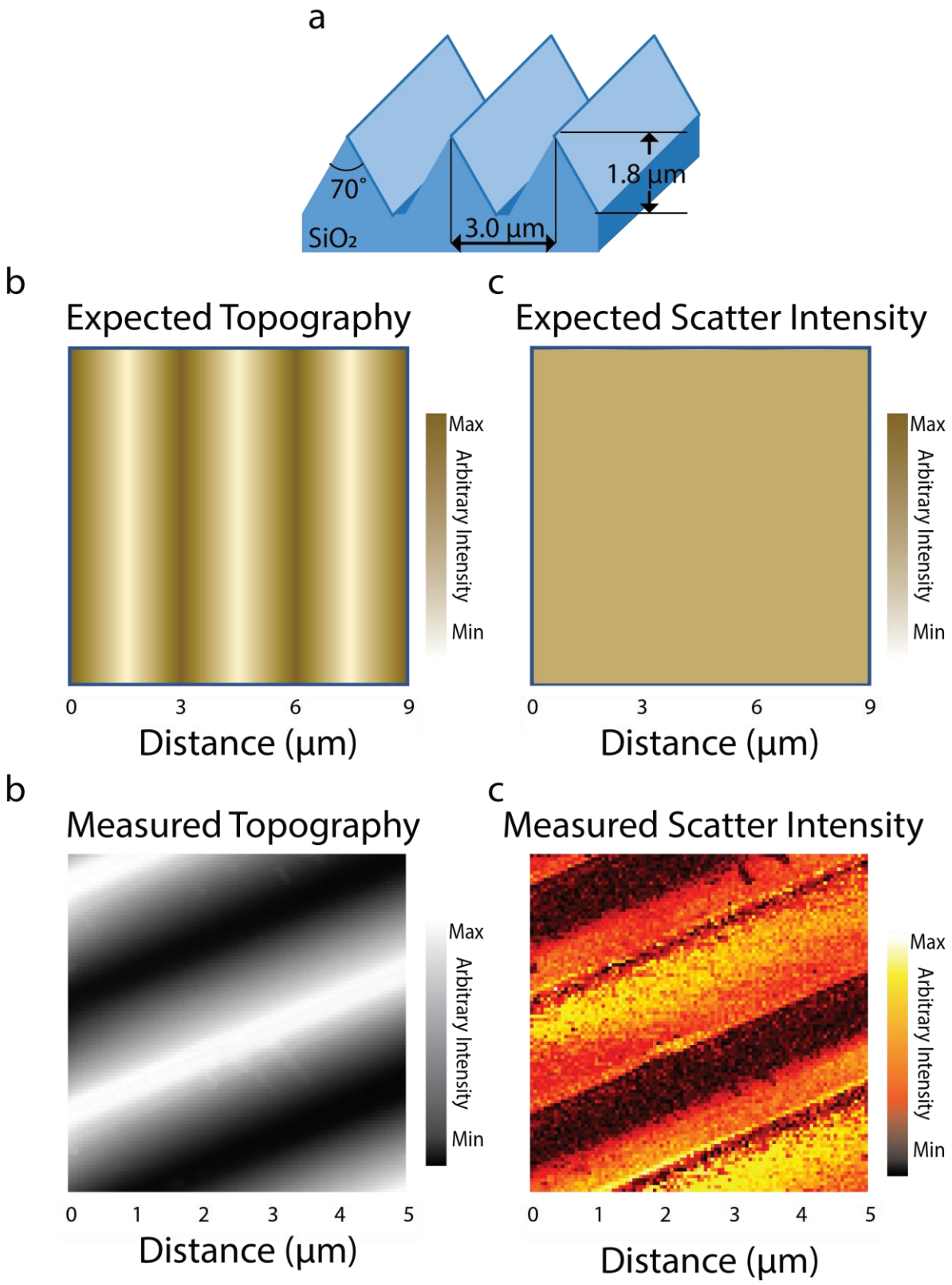

Figure B.5 Test sample for deconvolving topography from IR data. a) Idealized expected linear variation in topography. b) Idealized expected IR scattering for a homogeneous sample. c) Measured topography data consistent with expectation. d) Measured IR scattering map shows unexpected correlation with topography.